Karen Bokeloh

Calibration of hot and cold dark matter experiments: An angular-selective photoelectron source for the KATRIN experiment and an apparatus to determine the reflection properties of PTFE for vacuum UV light

– 2013 –

Experimentelle Physik

Dissertationsthema

Calibration of hot and cold dark matter experiments: An angular-selective photoelectron source for the KATRIN experiment and an apparatus to determine the reflection properties of PTFE for vacuum UV light

Inaugural-Dissertation
zur Erlangung des Doktorgrades
der Naturwissenschaften im Fachbereich Physik
der Mathematisch-Naturwissenschaftlichen Fakultät
der Westfälischen Wilhelms-Universität Münster

vorgelegt von
Karen Anna Bokeloh, geb. Hugenberg
aus Ankum

– 2013 –

Dekan:	**Prof. Dr. M. Donath**
Erster Gutachter:	**Prof. Dr. Ch. Weinheimer**
Zweiter Gutachter:	**Prof. Dr. J. P. Wessels**
Tag der mündlichen Prüfung:	**22.11.2013**
Tag der Promotion:	

Summary

Measurements of the Cosmic Microwave Background and of other observables show that the matter density of the universe is dominated by a non-luminous part, the so-called dark matter. The relic neutrino background of 336 neutrinos and anti-neutrinos/cm^3 contributes to this part as neutrinos do not interact electromagnetically and strongly. Due to their small mass, the neutrinos were relativistic at the time of the structure formation and thus suppressed the generation of small scale structures. As small scale structures exist today, neutrinos can, although they have a large number density, only contribute a small part to the total dark matter density, which is instead dominated by cold dark matter. Still the determination of the absolute neutrino mass forms an important science goal in its own right, not only because they still influence structure formation depending on the size of the neutrino mass, but also because the origin of neutrino mass is a very relevant question for particle physics. At the same time searches are ongoing to determine what makes up the major part of dark matter. The Weakly Interacting Massive Particle is a candidate particle for cold dark matter, which is being looked for in current experiments.
In this thesis experimental studies have been conducted for the calibration of the neutrino mass experiment KATRIN and of the dark matter experiment XENON.
The KATRIN experiment aims to determine the neutrino mass m_{ν_e} to an upper limit of 0.2 eV at 90 % confidence level by precisely measuring the shape of a β-spectrum at its endpoint using a MAC-E filter (magnetic adiabatic collimation with electrostatic filter). Due to possible imprecisions in the installation of the complex wire electrode system as well as the need to know the electromagnetic properties of the spectrometer precisely, thorough test and calibration measurements need to be conducted before measurements can take place. In the scope of this thesis, the prototype of an angular-selective, quasi mono-energetic electron source has been developed for the KATRIN experiment. Idealized design simulations have been conducted. On this basis a prototype has been built and measurements have been conducted at the MAC-E filter setup in Mainz. The analysis of the measurements has shown that the electron source works and electrons can be produced with with tunable pitch angles covering the full required angular range and with a reasonably small angular spread.
The XENON experiment aims to measure WIMP interaction rates by detecting nuclear recoils from elastic WIMP - nucleus scattering reactions. The XENON detector is a dual phase time-projection chamber with liquid Xenon as target material. It uses the direct scintillation light produced in the recoil reaction in the liquid phase as start signal and the charge signal drifted by an applied electric field to the gaseous phase, where proportional amplification takes place, as stop signal. The photons produced in these reactions are detected with two PMT arrays, one each at the top and the bottom of the chamber. To increase the light collection, PTFE panels have been implemented on the borders of the TPC volume. In order to simulate the response of the XENON detector, the exact reflection properties with information about the spatial distribution of the reflected light need to be known. For the next stage, XENON1t, different PTFE batches, different production processes and surface treatments need to be investigated. An experimental setup with a vacuum UV light source, a vacuum monochromator and a separate vacuum chamber for sample and detector has been designed and was set up for measuring the reflection pattern from materials. Two samples with different surface preparations have been measured. A method to analyze the data by fitting simulated reflection models has been presented and was used for the sample measurements. In addition a first test measurement of the wavelength dependence of the reflectance has been conducted, showing a decrease in reflectivity as function of decreasing wavelength in addition to a changed reflection pattern. The setup also offers the opportunity to address various other important questions.

Zusammenfassung

Messungen der kosmischen Mikrowellenhintergrundstrahlung und weitere Beobachtungen haben gezeigt, dass die Materiedich-te des Universums von einem nicht-leuchenden Anteil, der sogenannten Dunklen Materie, dominiert ist. Der kosmische Neutrinohintergrund mit einer Dichte von 336 $\nu + \bar{\nu}/cm^3$ trgt zur Dunklen Materie bei, da Neutrinos nicht stark oder elektromagnetisch wechselwirken. Jedoch sind Neutrinos aufgrund ihrer kleinen Masse zur Zeit der Strukturbildung relativistisch und unterdrücken Strukturen auf kleinen Skalen. Aus der heutigen Strukturverteilung sieht man, dass sie, trotz ihrer großen Anzahldichte, nur einen kleinen Teil zur Dunklen Materie beitragen, die stattdessen durch kalte Dunkle Materie dominiert ist. Trotzdem ist die Bestimmung der absoluten Massenskala der Neutrinomasse ein wichtiges wissenschaftliches Ziel, da die Frage nach dem Ursprung der Neutrinomasse sehr aktuell ist. Gleichzeitig finden zur Zeit Suchen nach Dunkler Materie, wie zum Beispiel dem Dunkle Materie Kandidat *Weakly Interacting Massive Particle* (schwach wechselwirkendes, schweres Teilchen) statt.
In dieser Arbeit werden experimentelle Studien, die im Rahmen des Neutrinomassenexperimentes KATRIN und des Dunkle Materie Experimentes XENON durchgeführt wurden, vorgestellt.
Ziel des KATRIN Exeriments ist es, durch die genaue Vermessung der Form eines β-Spektrums an seinem Endpunkt mit einem MAC-E Filter (magnetic adiabatic collimation with electrostatic filter), die Neutrinomasse bis zu einem oberen Grenzwert von 0.2 eV mit 90 % Sicherheit zu bestimmen. Da der Einbaus des komplexen Drahtelektrodensystems Ungenauigkeiten im elektromagnetischen Design hervorrufen kann und es für das Experiment wichtig ist, die elektromagnetischen Eigenchaften sehr genau zu kennen, müssen diese vor den Messungen gründlich gestestet und kalibriert werden. Im Rahmen der vorliegenden Arbeit wurde der Prototyp einer winkelselektiven, quasi monoenergetischen Elektronenquelle für das KATRIN Experiment entwickelt. für das Design wurden idealisierte Simulationen durchgeführt, auf deren Basis ein Prototyp gebaut und Messungen am MAC-E Filter Aufbau in Mainz durchgeführt wurden. Die Analyse dieser Messungen belegen, dass das Prinzip der Elektronenquelle funktioniert und Elektronen mit justierbaren pitch Winkeln im gesamt bentigten Winkelbereich mit schmaller Winkelbreite erzeugt werden.
Ziel des XENON Experimentes ist es, Interaktionsraten von WIMPs zu messen, indem Kernrückstöße von elastischen Streuungen von WIMPs an Kernen detektiert werden. Der XENON Detektor is eine Zwei-Phasen Zeit-Projektionskammer mit Xenon als Detektormedium. Das direkte Szintillationslicht aus der Rückstoßreaktion in der flüssigen Phase wird als Startsignal und das Ladungssignal, das mit einem angelegten elektrischen Feld zur Gasphase, in der Proportionalverstärkung stattfindet, geführt wird, als Stopsignal benutzt. Die in diesen Reaktionen erzeugten Photonen werden mit zwei Photomultiplierfeldern am Kopf und Boden der Kammer detektiert. Zur Erhöhung der Detektionseffizienz für Licht wurden die Seitenflächen des TPC-Volumens mit PTFE ausgekleidet. Um den XENON Detektor und seine Signale zu simulieren müssen die genaun Reflektionseigenschaften mit Informationen über die räumliche Verteilung des reflektieren Lichtes bekannt sein. Für den nächsten Experimentabschnitt XENON1t müssen verschidene PTFE Lieferungen, verschiedene Herstellungsverfahren und verschiedne Oberflächenbearbeitungen untersucht werden. Ein experimenteller Aufbau mit einer Vakuum-UV Lichtquelle und einer zweiten Vakuumkammer für das zu untersuchende Material und den Detektor wurde konziperiert und für die ortsaufgelöste Messung von reflektierten Licht von Mustermaterialien aufgebaut. Eine Methode um die Daten durch das Fitten von simulierten Reflektionsmodellen zu analysieren wurde vorgestellt und auf zwei Beispielmessungen angewandt. Zusätzlich wurde eine erste Testmessung der Wellenlängenabhängigkeit der Reflektivität durchgeführt, die einen Abfall der Reflektivität mit Abnahme der Wellenlänge zeigt. Der Aufbau bietet die Möglichkeit weitere wichtige Fragestellungen zu untersuchen.

Contents

1. Hot and cold dark matter

The Standard Model of particle physics successfully describes strong, weak and electromagnetic interactions of the twelve fundamental fermions and their antiparticles by mediation of the force carrying bosons. The particles are listed in figure 1.1.

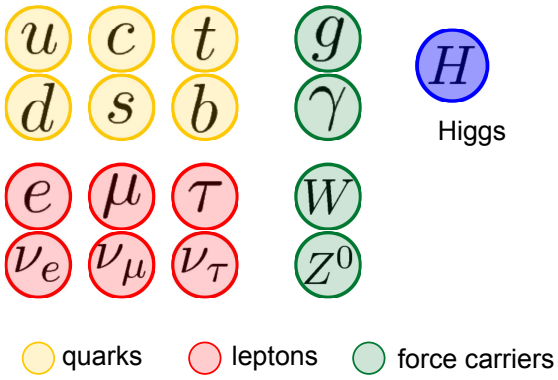

Figure 1.1.: Particle content of the Standard Model of particle physics. The six quarks ordered in 3 generations are marked yellow. The leptons are marked red. Each charged lepton e, μ and τ has a partner neutrino of the same generation. The force carrying bosons are marked in green. The gluon is the mediator of the strong force. The γ, W and Z^0 bosons are the force carriers of the electro-weak interaction. The Higgs particle responsible for the mass in the Standard Model is marked in blue.

Although the Standard Model with its 19 free parameters manages to describe many phenomena in elementary particle physics very well, observations as *e.g.* non-zero neutrino masses and the existence of dark matter point to physics beyond the Standard Model. In this chapter a short introduction into neutrino physics and the quest for the neutrino mass will be given in section 1.1. Evidence for the existence of dark matter as well as an introduction into searches for dark matter is given in section 1.2.

1.1. Neutrinos

The neutrino ν is the second most abundant particle in our universe after the photon γ, but due to its unique properties, the detection of neutrinos has proven to be difficult. As they carry no color charge, they do not interact strongly. In addition they have no electric or magnetic dipole moment and thus do not couple to the electromagnetic interaction, they couple only via the weak isospin I to the weak interaction. Due to the low interaction cross section σ of the weak force, the interaction rates are small and thus the probability to detect neutrinos, although they are there in large numbers[1], is very low. For neutrinos

[1]The number density of the cosmic neutrino background, that decoupled during the expansion of the universe, is $336\,\nu/\mathrm{cm}^3$, including neutrinos of all three flavors and both, ν and $\bar{\nu}$.

with energies in the region of $E_\nu \sim 1 - 100\,\mathrm{MeV}$ the cross section for charged current reactions on deuterium $\bar{\nu}_e + d \rightarrow e^+ + n + n$ is of the order $\sigma \approx 1 \cdot 10^{-44}\,\mathrm{cm}^2/\mathrm{fission}$, for the neutral current fission reaction $\bar{\nu}_e + d \rightarrow \nu_e + p + n$ the cross section increases to $\sigma_{NC} \approx 3 \cdot 10^{-44}\,\mathrm{cm}^2/\mathrm{fission}$ [For12].

The weak interaction exhibits maximum parity violation[2], it only couples to left-handed lepton doublets $\begin{pmatrix} l_L^- \\ \nu_{l,L} \end{pmatrix}$ and right-handed singlets l_R^-. Therefore, only left-handed neutrinos ν_L and right handed anti-neutrinos $\bar{\nu}_R$ are implemented in the framework of the Standard Model. As masses are acquired in the Standard Model formalism by Yukawa couplings of left- and right-handed fermion fields to the Higgs field, the neutrinos are massless in the Standard Model framework.

The Super-Kamiokande experiment is able to measure the flux of atmospheric neutrinos. The deviations of the measured from the expected flux can only be described consistently with neutrino oscillation[3]. The SNO experiment was able to verify neutrino oscillation by measuring the solar neutrino flux in all neutrino generations[4]. This has proven that the weak neutrino eigenstates $\mid \nu_\alpha\rangle$, $\alpha \in [e, \mu, \tau]$ are a superposition of mass eigenstates $\mid \nu_i\rangle$:

$$\mid \nu_\alpha\rangle = \sum_i U_{\alpha i} \mid \nu_i\rangle, \tag{1.1}$$

with the unitary matrix U representing the Pontecorvo-Maki-Nakagawa-Sakata mixing matrix. Due to the squared mass differences Δm_{ij}^2 between the mass eigenstates $\mid \nu_i\rangle$ and $\mid \nu_j\rangle$, the contributions have a different phase propagation and the probability to detect a certain neutrino flavor $P(\nu_\alpha \rightarrow \nu_\alpha, t)$ changes as a function of the energy E of the neutrino and the traversed distance L. The PMNS-matrix can, analogous to the CKM matrix in the quark sector, be decomposed into three rotation matrices:

$$U = \begin{pmatrix} 1 & 0 & 0 \\ 0 & \cos\theta_{23} & \sin\theta_{23} \\ 0 & -\sin\theta_{23} & \cos\theta_{23} \end{pmatrix} \cdot \begin{pmatrix} \cos\theta_{13} & 0 & \sin\theta_{13}e^{i\delta} \\ 0 & 1 & 0 \\ -\sin\theta_{13}e^{-i\delta} & 0 & \cos\theta_{13} \end{pmatrix} \cdot \begin{pmatrix} \cos\theta_{13} & \sin\theta_{13} & 0 \\ -\sin\theta_{13} & \cos\theta_{13} & 0 \\ 0 & 0 & 1 \end{pmatrix}. \tag{1.2}$$

A potential CP-violating Dirac phase, δ, has not be found experimentally up to now. If neutrinos are Majorana-particles, the matrix changes to $V = U \cdot M$ with the additional matrix

$$M = \begin{pmatrix} 1 & 0 & 0 \\ 0 & e^{i\alpha_1/2} & 0 \\ 0 & 0 & e^{i\alpha_2/2} \end{pmatrix} \tag{1.3}$$

and non-zero phases α_1 and α_2. Neutrino oscillation measurements are not sensitive to these phases.

[2] First experimental observation reported in [Wu57]

[3] The first indication of neutrino oscillation from atmospheric neutrinos was reported in [Fuk98], the latest Super-Kamiokande result on neutrino oscillation has been published in [Abe11].

[4] The SNO experiment is sensitive to elastic scattering, neutral current and charged current reactions by ν_e created in nuclear fusion reactions in the sun. The measured total solar neutrino flux from ^8B corresponds to the expected one from solar models, while the measured electron neutrino flux alone shows again the solar neutrino problem [Ahm02].

The probability to measure the weak flavor eigenstate $\mid \nu_\beta \rangle$ when starting with $\mid \nu_\alpha \rangle$ is given for the two-neutrino mixing by

$$P(\nu_\alpha \to \nu_\beta, t) = \sin^2(2\theta) \sin^2\left(\frac{\Delta m^2}{4}\frac{L}{E}\right) \tag{1.4}$$

and depends on the mixing angle θ, the squared mass difference $\Delta m^2 = |m_2^2 - m_1^2|$, the neutrino energy E and the distance L the neutrino has crossed.

Hints of the size of the neutrino mass can be extracted from cosmological data, from dedicated experiments searching for $2\beta0\nu$-decays or using the decay kinematics from β-decay.

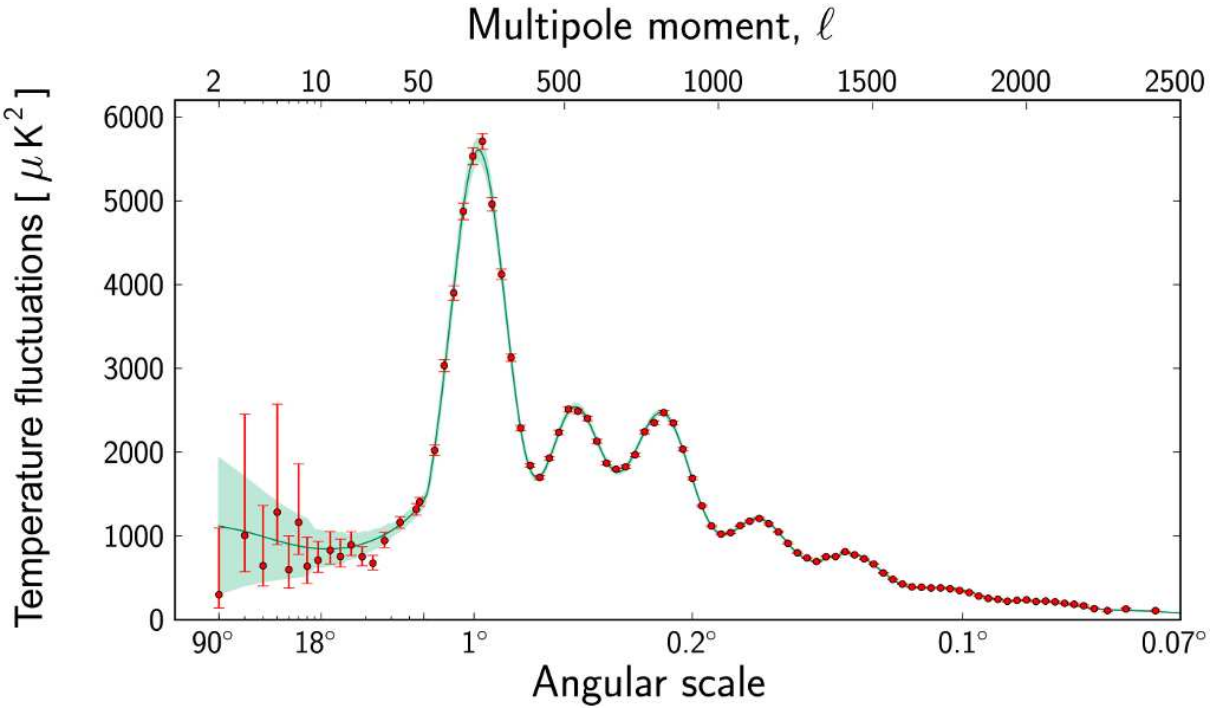

Figure 1.2.: The CMB power spectrum measured by Planck (figure taken from [Pla13a]).

The power spectrum of the cosmic microwave background (see figure 1.2) shows the directional density fluctuations at the time of the decoupling of the photons. The neutrino mass influences the power spectrum due to their *free streaming* properties. Because of their small cross section, neutrinos decouple at higher temperatures T_ν and thus earlier times t_ν than the photons (T_γ, t_γ). At the time of the structure formation, neutrinos are as low mass particles still relativistic (hot dark matter). Thus they smooth out fluctuations on small scales. Depending on the summed neutrino mass $\sum_i m_{\nu_i}$ the power spectrum changes at the first acoustic peak. Upper limits can be derived depending on the model assumption, the parameter range for the other fit parameters and the data sets[5] used in combination with the Planck data. A conservative upper limit for the sum over the three neutrino families has been derived combining Planck with a WMAP polarization

[5]In this context other data sets are measurements from different experiments delivering additional information as *e.g.* the high multipole data sets from the Atacama Cosmology Telescope and the South Pole Telescope, delivering complementary measurements for a multipole region in which Planck has to use foreground models.

low-multi-pole likelihood and data from high resolution CMB measurements assuming three species of degenerate massive neutrinos:

$$\sum_{i=1}^{3} m_{\nu_i} < 0.66\,\text{eV}\ 95\%;\ \text{Planck+WP+highL [Pla13]}. \tag{1.5}$$

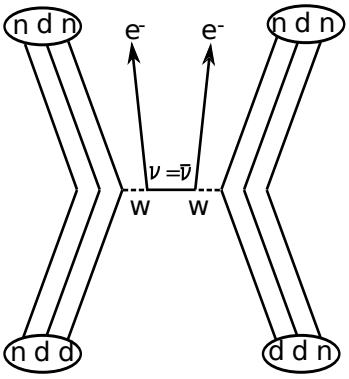

Figure 1.3.: Feynman diagram of the neutrino-less double β-decay.

If the neutrino is its own anti-particle $\nu = \bar{\nu}$, the double β-decay (see figure 1.3) has an additional mode in which the neutrino emitted in the first β-decay is absorbed as anti-neutrino in the second one (see figure 1.3). The neutrino is then virtual. The decay probability depends on the effective Majorana neutrino mass

$$\begin{aligned} m_{ee}^{\nu} &= |\sum_i V_{ei}^2 m_i| \\ &= ||U_{e1}|^2 m_1 + |U_{e3}|^2 e^{i\alpha_1} m_3 + |U_{e3}|^2 e^{i\alpha_2} m_3|. \end{aligned} \tag{1.6}$$

Due to the squared elements of the PMNS mixing matrix in the coherent sum of the mass eigenstates, the complex Majorana phases (see equation (1.3)) contribute differently than for the effective electron neutrino *mass*

$$m_{\nu_e} = \sqrt{\sum_i |U_{ei}|^2 m_i^2} \tag{1.7}$$

measured in the kinematic searches (see chapter 2) and the two masses are not directly comparable.

1.2. Dark Matter

In the previous section neutrinos have been discussed which belong to dark matter. In this section astrophysical and cosmological evidence for dark matter is presented, before possible dark matter particles and different approaches to detect them will be introduced.

1.2.1. Evidence

Hints for the existence of dark matter exist on a wide range of scales. Already in 1933 F. Zwicky measured the velocities of galaxies in the Coma Cluster and, by using the virial

theorem, calculated that the visible mass alone could not account for these velocities. He made the ansatz that there is non-luminous mass in the system and calculated that its density is a factor 400 higher than the visible luminous mass [Zwi33]. Since then the evidence for dark matter has been found in numerous observations on galactic and cosmological scales.

The influence of dark matter on galaxies is visible in rotation curves of spiral galaxies. Using the known mass distributions for the gas and the stars in the galaxies, the rotation velocity of stars is expected to decrease if the radius of their orbit exceeds a limit radius. Instead measurements show that the rotation velocity stays constant over a larger range[6] implying a significant part of the galaxy to be made of an unknown type[7].

In 2006 direct evidence for dark matter has been reported by D. Clowe *et al.* [Clo06]. This evidence is based on multi-wavelength observations of the *bullet cluster*, a galaxy cluster composed of two separate ones, who passed through each other. In the optical wavelength range the distribution of the galaxy's stars is observed. In addition the mass distribution of the galaxy can be derived using the weak gravitational lensing effect. The bending of the light emitted from background sources as *e.g.* galaxies depends on the mass of the foreground galaxy. The optical images (see figure 1.4(a)) point out that the centers of the cluster masses observed by weak gravitational lensing, passed through each other without interaction. In contrast to this the main part of the visible matter in clusters, the gas that can be observed in the X-ray region (see figure 1.4(b)), has interacted and is thus hotter and located closer to each other than the main masses seen with weak gravitational lensing. Meanwhile the stars have passed each other and are thus located in the region where the main mass was detected. The measurement shows without any model input

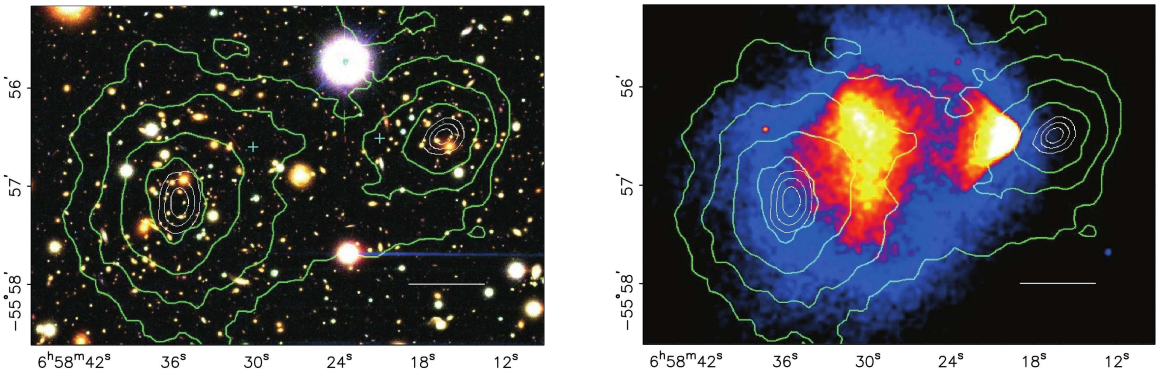

(a) Optical image. (b) X-ray image.

Figure 1.4.: The bullet cluster observed at different wavelength (figure taken from [Clo06]). The lines indicate the density profile of the gravitational mass measured with weak gravitational lensing.

that the main mass component of the cluster behaves collision-less like the stars, but does not coincide with the main baryonic mass.

Further evidence for dark matter comes from fits of the standard model of cosmology, the

[6]The first observations of flat rotation curves in the Andromeda nebula by V. Rubin and W. Ford were presented in 1970 [Rub70].

[7]An alternative approach is the modification of gravitation for this scale, as *e.g.* the **MO**dified **N**ewtonian **D**ynamics. They can be used to explain these observations, but fail to explain observations on different scales hinting at dark matter.

ΛCDM model, to a wide variety of data sets. The model uses the cosmological principle and the big bang as starting point and assumes that the total energy density Ω_{tot}[8] of the universe is composed of dark energy Ω_Λ, matter Ω_m which is divided into further components as cold dark matter Ω_{CDM}[9], neutrinos Ω_ν, baryonic matter Ω_b[10], radiation Ω_γ and a component Ω_k indicating the curvature k[11]:

$$\Omega_{\text{tot}} = \Omega_\Lambda + \Omega_{CDM} + \Omega_\nu + \Omega_b + \Omega_\gamma + \Omega_k \tag{1.8}$$

Additional parameters include the Hubble constant H_0 as a measure of the expansion rate of the universe. The results for the matter content of the universe by matching the ΛCDM model to the power spectrum measured with the Planck satellite (see figure 1.2) are listed in 1.1.

Table 1.1.: Matter content of the universe: Results for the six-parameter base ΛCDM model with Planck data alone [Pla13]. h is defined as $h = H_0/100\,\text{km}\cdot\text{s}^{-1}\cdot\text{Mpc}^{-1}$.

Parameter	Planck, 68 % limits
Ω_Λ	0.686 ± 0.020
Ω_m	0.314 ± 0.020
H_0	$(67.4 \pm 1.4)\,\text{km}\cdot\text{s}^{-1}\cdot\text{Mpc}^{-1}$
$\Omega_b h^2$	0.02207 ± 0.00033
$\Omega_{CDM} h^2$	0.1196 ± 0.0031

1.2.2. Dark matter candidates and detection

Different models have been constructed to explain the dark matter problem of the universe. In the most favored models, dark matter is made up by predominantly one type of particle[12], which is motivated to solve a different physical problem and meets the following requirements along the way: In order to be classified as dark matter, a particle should

- be non-bayonic,
- be cold, *i.e.* non-relativistic, at the time of structure formation[13],
- have no color charge and
- have no electric charge.

The most prominent suggestion is the **W**eakly **I**nteracting **M**assive **P**article. Instead of identifying one particular particle species, the abbreviation merely stands for a collection of properties required of particle matter to act as the sought-after dark matter: Its interaction cross section is of the size of the weak scale, it is massive, stable and slow (cold).

[8] Ω_i is defined as the relation of the density of the component i to the critical density $\rho_{\text{crit}}(\text{today}) = \frac{3H_0^2}{8\pi G}$: $\Omega_i = \frac{\rho_i}{\rho_{\text{crit}}}$.

[9] Cold dark matter indicates non-baryonic matter which is non-relativistic at the time of the decoupling.

[10] Electrons are counted to the baryonic matter as charge neutrality fixes their number density to be equal to the baryonic number density. Thus the contribution from electrons with $m_e \ll m_p$ is negligible.

[11] The measurements up to now indicate a flat universe, thus $\Omega_k = 0$.

[12] This assumption is an economical assumption.

[13] The free-streaming length is essential for structure formation. Hot dark matter as *e.g.* neutrinos, have a large free-streaming length, suppressing the structure formation on small scales in disagreement with observations.

The particle density of the WIMP depends on the freeze-out that takes place when the interaction rate Γ is smaller than the expansion rate given by the size of the Hubble parameter H at that temperature and their relative velocity v:

$$\Omega h^2 \approx \frac{1}{\left\langle \left(\frac{\sigma_{\text{ann}}}{10^{-38}\,\text{cm}^2}\right)\left(\frac{v/c}{0.1}\right)\right\rangle}. \tag{1.9}$$

For annihilation cross-sections σ_{ann} of the order of the weak interaction the resulting density has the correct abundance to fit with the ΛCDM model.

The neutralino χ is the lightest supersymmetric[14] particle. It is a superposition of neutral supersymmetric states

$$\chi = a_1\tilde{Z} + a_2\tilde{\gamma} + a_3\tilde{H}_1 + a_4\tilde{H}_2 \tag{1.10}$$

and belongs to the class of WIMPs. The hypothetic sterile neutrino[15] is another WIMP candidate.

Further hypothetic candidate particles for dark matter are the axion a, the axino $\tilde{a}$, the gravitino $\tilde{G}$ and many more. Of these the WIMP and the axion are experimentally accessible. Cosmological arguments have already excluded a wide span of axion masses, leaving only a mass range between μeV and several 100 μeV as possible window.

There are different detection modes for WIMPs:

- *Production:*
  Dark matter particles can be produced in collider experiments if the energy is above the production threshold. The signature of the particle is missing mass in the reaction.
- *Indirect detection:*
  If WIMPs annihilate, high energy secondary particles can be produced. An excess of these particles from high density regions as the sun or the galactic center are hints for dark matter. The γ-ray satellite Fermi, the earth-bound telescope array H.E.S.S. and the neutrino detector ICECUBE are among the detectors looking for these signals.
- *Direct detection:*
  WIMPs are expected to have a small cross section σ. They can interact with atomic nuclei by scattering elastically off them. Due to the rotation of the earth around the sun while the sun moves around the galactic center, the earth speed relative to a static galactic halo modulates. Assuming a static WIMP distribution, the WIMP scattering rate should show an annual modulation.
  In the scattering reaction the nucleus gains recoil energies of the order of a few 10 keV to several 100 keV, loosing it again by further scattering reactions in the detector medium. The deposited energy can be detected in phonon, charge or scintillation light signals (compare figure 1.5). The expected signal rate per unit mass of the detection medium depends on the number density of the WIMPs $n_\chi = \rho_0/m_\chi$, with

[14] Supersymmetry is an extension of the Standard Model of particle physics introduced to solve the hierarchy problem. The neutralino is a byproduct of the model that fits the conditions for dark matter.

[15] A sterile neutrino does not interact via the weak interaction and would therefore not be visible in the Z^0 resonance.

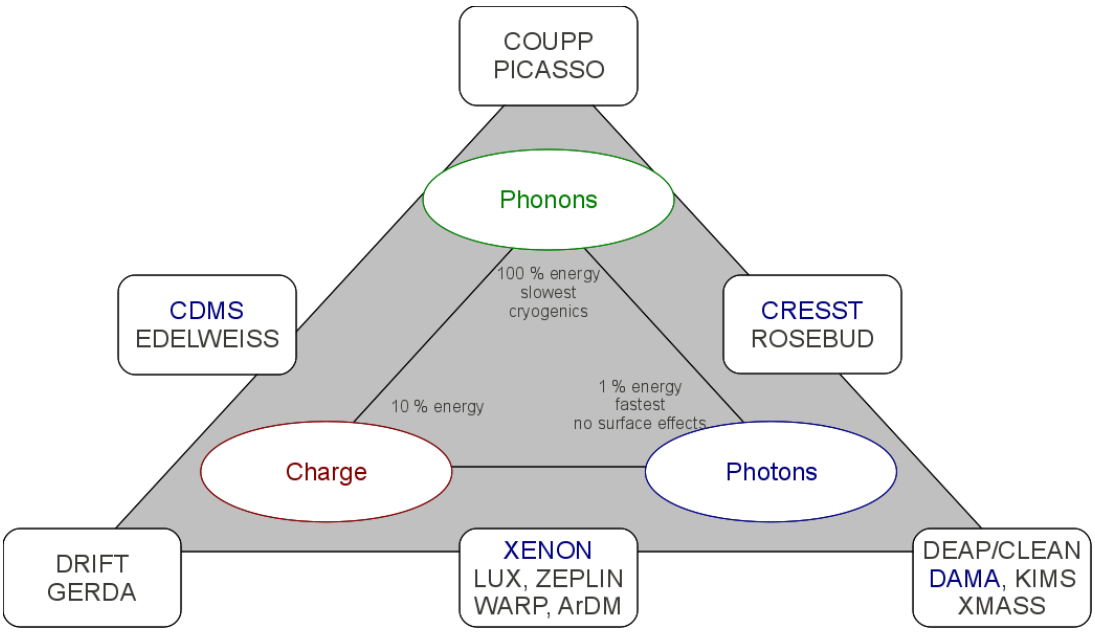

Figure 1.5.: Distribution of the WIMP signal into phonons, charge and photons. On the outside a list of experiments is given working with one or two of these signals.

ρ_0 the local WIMP density and m_χ their mass, the elastic scattering cross section σ_χ, their average velocity $\langle v \rangle$ with respect to the target and the mass of the target nucleus m_N:

$$R \approx \frac{\rho_0 \sigma_\chi \langle v \rangle}{m_\chi m_N}. \tag{1.11}$$

To calculate it, astrophysical model input is needed for the WIMP velocity distribution $f(\vec{v}, \vec{v}_E)$ with $\vec{v}$ the WIMP velocity relative to the earth and $\vec{v}_E$ the velocity of the earth relative to the galaxy, and the local WIMP density ρ_0. The expected recoil spectra from WIMP-nucleon scattering depend on the detector material. The cross section $\sigma_\chi(qr_n)$, with the momentum transfer q and the effective nuclear raduis r_n, can be expressed as

$$\sigma(qr_n) = \sigma_0 F^2(qr_n), \tag{1.12}$$

where σ_0 denotes the cross section at zero momentum transfer and $F(qr_n)$ the nuclear form factor. The form factor takes into account that the nucleus is not point-like, but has a certain structure. Further details can be found in [Lew96] and [Jun96]. A target nucleus of larger mass enhances the rate at low recoil energies for spin independent interactions as at low momentum transfer the scattering amplitudes of protons and neutrons would add in phase resulting in $\sigma \propto A^2$. The expected event rates for cross sections of about $10^{-44}\,\mathrm{cm}^2$ are of the order of $10^{-5} - 10^{-3}\,\frac{\text{events}}{\text{keV}\cdot\text{kg}\cdot\text{d}}$, therefore, background suppression plays an important role for these experiments. To suppress background from cosmic rays the experiments are located in underground laboratories.

Several experiments use only one of the three possible signals and focus their technical layout and analysis on good background suppression and the search for an annual modulation signal (see figure 1.5). The other experiments currently use two

of the three possible signals with the advantage that electron recoil background events show different characteristic distributions when comparing signal 1 to signal 2, than a nuclear recoil.

To detect phonons from the nuclear recoil, cryogenic calorimeters are used, measuring the temperature rise due to the deposited energy. To detect the expected temperature differences of the order mK, the detectors are cooled to temperatures below 10 mK. In this region the Debye model rules the behavior of the heat capacity $c \propto T^3$ and the change is measurable.

To collect charges from the interactions in bolometers, an electric field is applied across the volume and the drifted charges can be collected at the surface with charge sensors. This is done by the CDMS collaboration and by the EDELWEISS experiment.

In contrast to this the CRESST collaboration uses in addition to their calorimeter a light absorbing detector to measure the photon signal.

Liquid nobel gas experiments as ArDM and XENON (see section 4) aim to measure the light and the charge signal.

If the direct detection experiments detect WIMP-like signals, they can determine from their known detector properties and with the astrophysical input parameters some bounds on the WIMP mass m_χ and interaction cross section σ_χ. If no candidate events are detected, upper bounds, also called exclusion curves, can be calculated, excluding regions with combinations of WIMP mass m_χ and interaction cross section σ_χ that would have been visible in the detector at the given exposure time. The most recent exclusion curve published in 2012 is shown in figure 1.6 [Apr12b]. It is visible that there are contradictory results from different experiments claiming the detection of dark matter interactions and experiments excluding this parameter space.

Outline

This thesis consists of experimental work conducted for two different experiments in different fields of astro-particle physics. The two topics are closely related as neutrinos belong to dark matter although they can only account for a tiny fraction of the total dark matter density. The angular-selective electron source for the KATRIN experiment is a continuation and completion of a topic I worked on in my diploma thesis, the pre-spectrometer electron source. Effects investigated in the simulations are now used for an angular-selective electron source for the KATRIN experiment. After the measurements for the angular-selective electron source have been completed, I worked on the design and commissioning of a reflection chamber to measure the reflectance from Teflon samples.

The thesis is structured as follows:

Part I deals with the KATRIN experiment. In chapter 2 a short introduction into the concept and status of the KATRIN experiment is given. In chapter 3 the reasons, why an angular-selective electron source is needed at the KATRIN experiment are presented. Design simulations and the resulting experimental setup are shown. The measurements act as proof-of-principle, indicating that the working principle is understood, while at the same time pointing out difficulties and possible improvements.

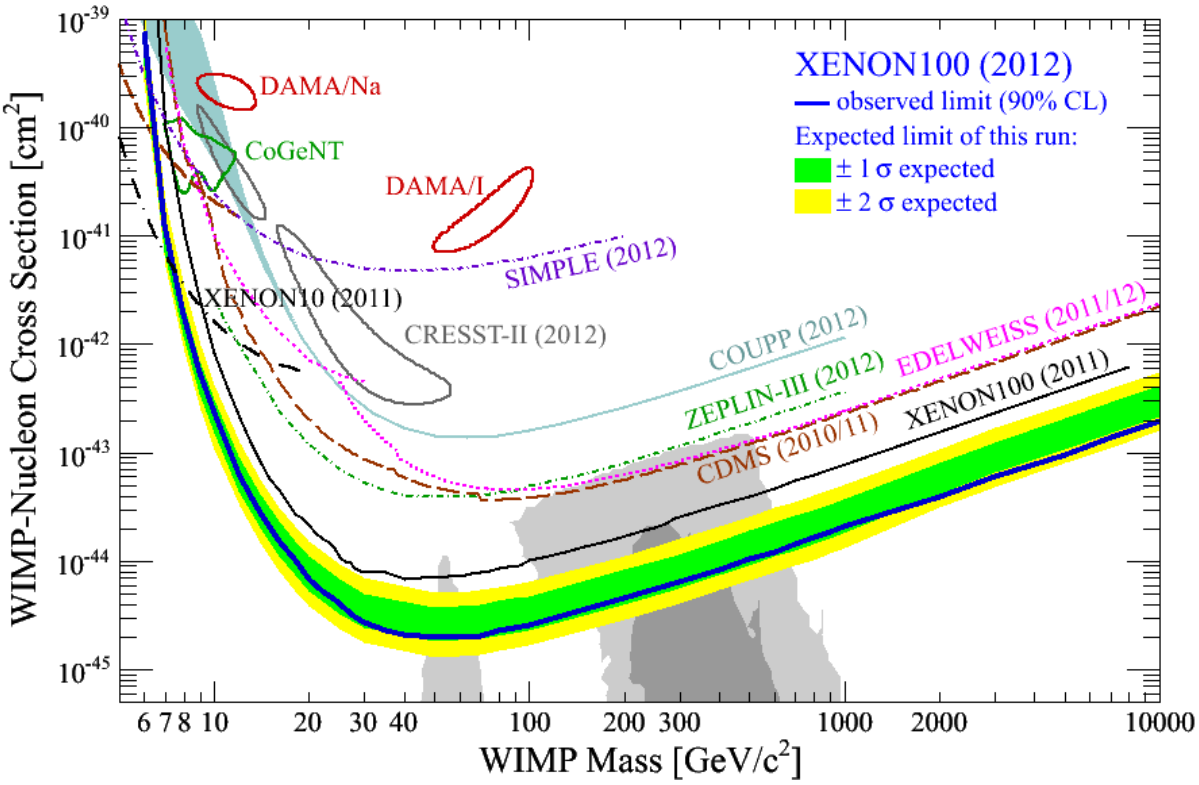

Figure 1.6.: Exclusion curves as published in [Apr12b]. Missing in this plot is the Si-CDMSII result recently published in [Agn12] which indicates a best fit WIMP mass of $8.6\,\mathrm{GeV/c^2}$ at a cross section of $1.9 \cdot 10^{-41}\,\mathrm{cm^2}$ (analyzed with a profile likelihood approach) in contrast to the XENON100 result excluding this parameter range.

In the second part of this thesis the work conducted for the dark matter experiment XENON is presented. After a shot introduction into the XENON detector and its results, the question of the size of the reflectance and the shape of the reflected light pattern is asked with focus on vacuum UV light from Teflon. Different stages of a setup to measure the pattern of reflected light are presented. A set of sample measurements has been taken and an analysis program has been written to analyze the reflectance.

The complete work is summarized in chapter 6.

An angular defined photoelectron source for the KATRIN experiment

2. The KATRIN experiment

The **K**arlsruhe **TRI**tium **N**eutrino experiment aims to determine the *m*ass of the electron neutrino m_{ν_e} of $m_{\nu_e} = 0.3\,\mathrm{eV/c^2}(0.35\,\mathrm{eV/c^2})$ with $3\sigma(5\sigma)$ significance or an upper limit of the neutrino *m*ass $m_{\nu_e} < 0.2\,\mathrm{eV/c^2}$ at 90 % confidence level by measuring the shape of the Tritium β-decay spectrum [KAT04].

2.1. β-decay

The β-decay is driven by the weak interaction which transfers a nucleus into an energetically beneficial state by transforming a neutron into a proton under the emission of an electron e^- and an anti-neutrino $\bar{\nu}_e$ and the release of energy Q:

$$(A, Z) \rightarrow (A, Z+1)^+ + e^- + \bar{\nu}_e + Q. \tag{2.1}$$

The energy Q is distributed between the total energy of the electron E_{kin}, the total energy of the neutrino $E_{\nu,\mathrm{kin}}$, the recoil energy of the daughter nucleus E_{rec} and the final state excitation of the daughter nucleus V_j. The neutrino mass has the largest influence on the β-decay spectrum $\frac{d^2N}{dEdt}$ at the endpoint region where the neutrino takes up a vanishing amount of kinetic energy and hence its energy share is dominated by the rest mass (see figure 2.1). Mathematically the kinetic energy spectrum of the electrons can be expressed

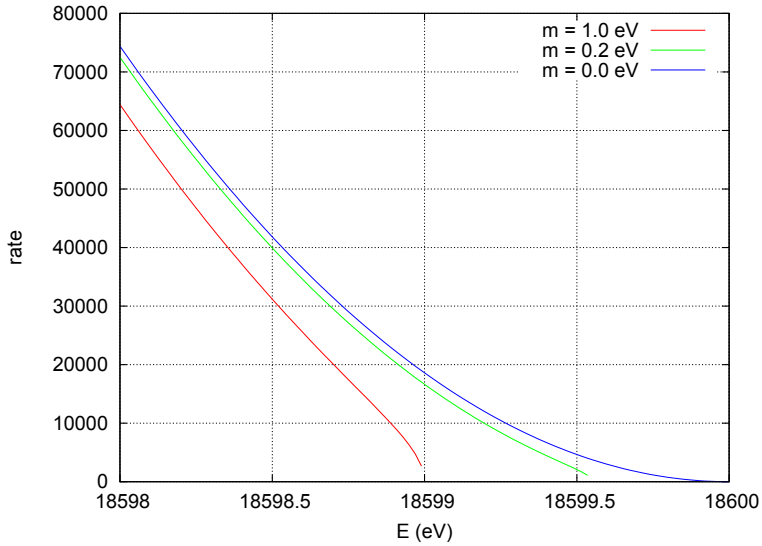

Figure 2.1.: Schematic presentation of the endpoint region of a β-spectrum for different neutrino masses.

according to [Ott08] as

$$\frac{d\Gamma}{dE} = R(E) \cdot \sum_i \sum_j |U_{ei}|^2 P_j(\epsilon - V_j)\sqrt{(\epsilon - V_j)^2 - m_i^2 c^4}\Theta(\epsilon - V_j - m_i^2 c^4). \tag{2.2}$$

Here the V_j denote different final states and P_j the probability of a decay into them, ϵ is the leftover energy $\epsilon = E_0 - E$ and $\Theta(\epsilon - V_j - m_i^2 c^4)$ ensures that the result stays in the physically meaningful range. The coefficient $R(E)$ contains the part of the spectrum not related to the neutrino mass:

$$R(E) = \frac{G_F \cos^2 \theta_C}{2\pi^3} |M_{\text{nuc}}|^2 F \cdot (E + m_e c^2)\sqrt{(E_0 + m_e c^2)^2 - m_e^2 c^4}, \tag{2.3}$$

with G_F the Fermi coupling constant, θ_C the Cabibbo angle, M_{nuc} the nuclear matrix element for the transition and F the Fermi function. Due to limitations in resolution the KATRIN experiment will not be able to differentiate between the contributions of the different neutrino mass eigenstates m_i, which show up as several steps in the β-spectrum, but will only see the combined influence of the incoherent sum

$$m^2(m_{\nu_e}) = \sum_i |U_{ei}|^2 m_i^2. \tag{2.4}$$

For convenience we define the effective superposition as the neutrino mass. Deteriming this mass will set the scale for all neutrino masses.

The KATRIN experiment uses ^{3}H as β-emitter as the decay is super-allowed and has a short half-live of 12.3 y. Therefore, the decay rate is relatively high. The nuclear matrix element for super-allowed decays shows no dependence on the energy of the electron. The simplicity of the $^3H_2$ molecule allows quantitative calculations of the final state spectrum.

A detailed discussion of the β spectrum and possible β emitters can be found in [Ott08].

The predecessor experiments in Mainz and Troitsk have likewise used ^{3}H as β-emitter and were able to set upper limits of $m_{\nu_e} < 2.3\,\text{eV}$ at 95 % confidence level [Kra05] and $m_{\nu_e} < 2.12\,\text{eV}$ at 95 % confidence level [Ase11], respectively.

2.2. The MAC-E filter

To measure the energy spectrum of the β-decay electrons, the KATRIN experiment uses a MAC-E filter (**M**agnetic **A**diabatic **C**ollimation with **E**lectrostatic **filter**, see *e.g.* [Pic92]). The electrons' energies are analyzed after parallelizing their momenta in a slowly decreasing magnetic field[1] using the conservation of the orbital magnetic moment[2]

$$\mu = \frac{E_\perp}{B} = \text{const}, \tag{2.6}$$

[1] The relative change of the magnetic field strength along one cyclotron loop must be small:

$$\left| \frac{1}{B} \frac{d\vec{B}}{dt} \right| \ll \omega_{\text{cyc}} = \frac{qB}{\gamma m_e}. \tag{2.5}$$

[2] In reality, the product of the orbital magnetic moment $|\vec{\mu}|$ and the Lorentz factor γ is the constant of the motion. In the case of ^3H decay $\gamma = 1.04 \approx 1$, thus it is sufficient to consider μ.

with $E_\perp$ denoting the energy stored in the cyclotron motion. The transversal energy[3] $E_\perp$ is converted into longitudinal $E_\parallel$ which can then be analyzed with an electric retarding potential U_0 that is applied at the position of the minimal magnetic field $B_{\min}$. Only electrons with

$$E_\parallel(B_{\min}) - qU_0 > 0\,\mathrm{eV} \tag{2.7}$$

can pass the spectrometer that thus acts as high-pass filter. The working principle of the spectrometer is illustrated in figure 2.2.

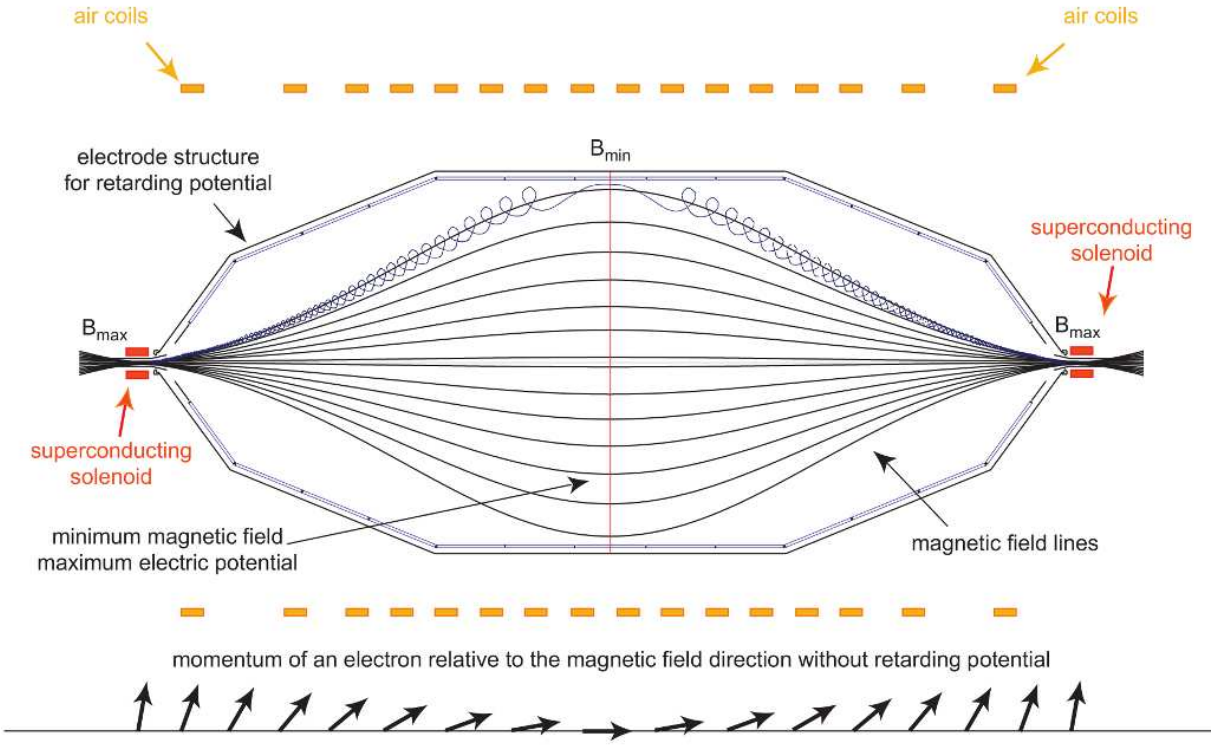

Figure 2.2.: Schematic drawing illustrating the working principle of the KATRIN main-spectrometer. Electrons are guided along magnetic field lines to the center of the spectrometer. Due to the decrease of the magnetic field strength the flux tube widens and the cyclotron radius increases. As the motion is adiabatic and therefore the magnetic moment conserved, the energy stored in the cyclotron motion is converted into longitudinal energy as shown with the arrows indicating the electrons' momentum at the bottom. The longitudinal energy is then analyzed with an electric retarding potential applied to the vessel and the wire electrode of the main spectrometer. Figure taken from [Hug08].

Using the angle θ enclosed by the magnetic field $\vec{B}$ and the momentum of the electron $\vec{p}$, the transversal and longitudinal energies can be expressed as

$$E_\perp = E_{\mathrm{kin}} \cdot \sin^2\theta \quad \text{and} \tag{2.8}$$

$$E_\parallel = E_{\mathrm{kin}} \cdot \cos^2\theta. \tag{2.9}$$

The magnetic field cannot be decreased to zero as the electrons still need to be guided. Therefore, electrons with kinetic energies barely sufficient for passing the filter $E_{\mathrm{kin}} \approx qU_0$,

[3] In the following the terms transversal and cyclotron are used equally.

but with nearly all their energy in the transversal component, will not cross the potential barrier. A residual of the transversal energy given by the magnetic field ratio is still in the transversal component. The energy resolution of the spectrometer at a fixed energy E_{kin} can be calculated with equation (2.6) to be

$$\Delta E = \frac{B_{\mathrm{min}}}{B_{\mathrm{max}}} E_{\mathrm{kin}}. \tag{2.10}$$

For an electron with the endpoint energy of Tritium β-decay of $E_{\mathrm{kin}} = 18.6\,\mathrm{keV}$, a minimal magnetic field of $B_{\mathrm{min}} = 3\,\mathrm{G}$ and a maximum magnetic field of $B_{\mathrm{max}} = 6\,\mathrm{T}$ this amounts to

$$\Delta E = 0.93\,\mathrm{eV}. \tag{2.11}$$

Due to the conservation of the orbital momentum (see equation (2.6)) the angle θ_f of the electron in the magnetic field B_f can be calculated if the magnetic field B_i and the angle θ_i at an initial position are known:

$$\sin^2\theta_f = \frac{B_f}{B_i}\sin^2\theta_i. \tag{2.12}$$

The transmission condition in equation (2.7) for one electron with energy $E_{\mathrm{kin}} \approx qU_0$ can now be expressed with the angle θ_{s} the electron has at its emission position in the magnetic field B_{s}.

$$\begin{aligned} 0 &< E_{\parallel}(B_{\mathrm{min}}) - qU_0 && (2.13)\\ &= E_{\mathrm{kin}} - E_{\perp}(B_{\mathrm{min}}) - qU_0 \\ &= E_{\mathrm{kin}} \cdot (1 - \sin^2\theta(B_{\mathrm{min}})) - qU_0 \\ &= E_{\mathrm{kin}} \cdot (1 - \frac{B_{\mathrm{min}}}{B_{\mathrm{s}}}\sin^2\theta_{\mathrm{s}}) - qU_0 && (2.14) \end{aligned}$$

One can thus see that the transmission function is not a step function but has a slope depending on the starting angle of the electron at its emission point. Solving the equation for the angle θ_{s} gives a direct correlation between the angle θ_{s} of an electron at its starting point and its energy E_{kin} and the applied retarding potential U_0. Electrons with angles below $\theta_{\mathrm{s}}^{\mathrm{max}}(E_{\mathrm{kin}})$ can pass the high-pass filter:

$$\theta_{\mathrm{s}} < \theta_{\mathrm{s}}^{\mathrm{max}}(E_{\mathrm{kin}}) = \arcsin\sqrt{\frac{E_{\mathrm{kin}} - qU_0}{E_{\mathrm{kin}}} \cdot \frac{B_{\mathrm{s}}}{B_{\mathrm{min}}}} \tag{2.15}$$

$$\overset{\text{if } B_{\mathrm{s}}=B_{\mathrm{max}}}{=} \arcsin\sqrt{\frac{\delta E}{\Delta E}}, \tag{2.16}$$

with $\delta E = E_{\mathrm{kin}} - qU_0$.

The normalized transmission function is the ratio of the intensity for one setting (E_{kin}, θ_{s}) to the maximum transmitted intensity. For an isotropic, monoenergetic electron source the maximum solid angle 2π emitted into the spectrometer is a measure of the maximum intensity and the solid angle restricted by the opening angle θ_{s}, $\Delta\Omega = \int_0^{2\pi}\int_0^{\theta_{\mathrm{s}}} \sin\theta d\theta d\varphi$, a measure of the intensity at the value E_{kin}. The transmission is thus given by their ratio, using the relation $\cos(\arcsin\sqrt{x}) = \sqrt{1-x}$.:

$$\frac{\Delta\Omega}{2\pi}(E_{\mathrm{kin}}) = 1 - \cos\theta_{\mathrm{s}}(E_{\mathrm{kin}}) = 1 - \sqrt{1 - \frac{E_{\mathrm{kin}} - qU_0}{E_{\mathrm{kin}}} \cdot \frac{B_{\mathrm{s}}}{B_{\mathrm{min}}}}. \tag{2.17}$$

If the retarding energy exceeds the the kinetic energy of the electrons $qU_0 > E_{\mathrm{kin}}$ no electrons can pass the filter. If the retarding energy is set below the kinetic energy minus the resolution of the spectrometer $qU_0 \leq E_{\mathrm{kin}} - \Delta E = E_{\mathrm{kin}}(1 - \frac{B_{\mathrm{min}}}{B_{\mathrm{max}}})$ all electrons can pass. In between these borders equation (2.17) is applied. In this region the angle θ_{s} is varied between $\theta_{\mathrm{s}} \in [0\,^\circ : 90\,^\circ]$. The transmission function is plotted in figure 2.3 for the KATRIN main spectrometer.

In section 3.1 electron sources with different emission characteristics and the respective transmission functions are discussed.

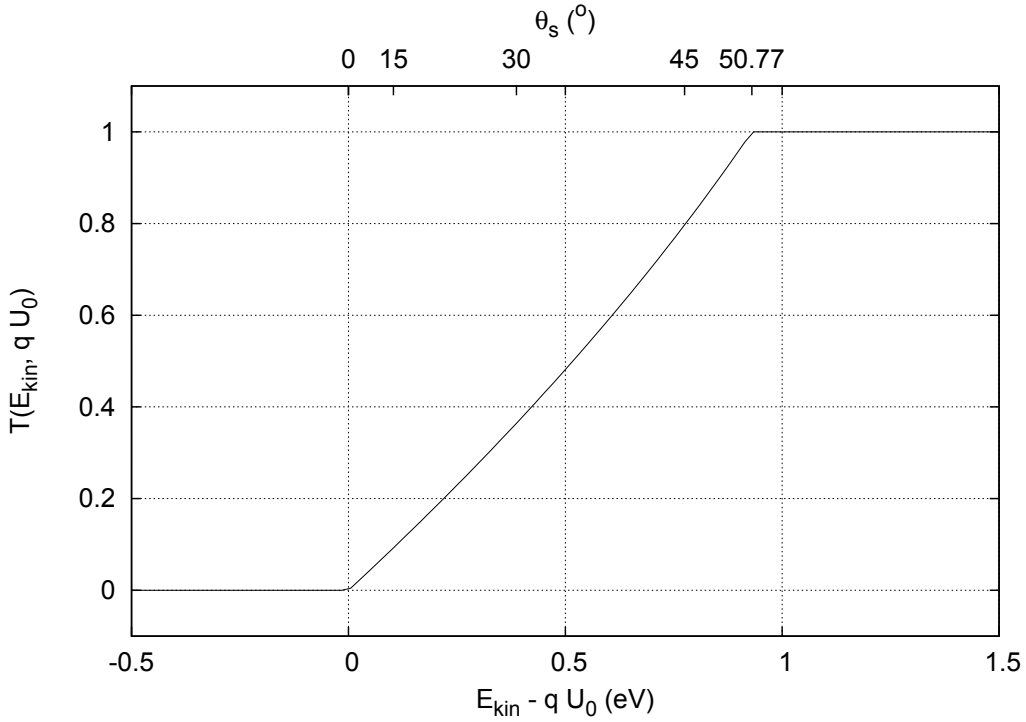

Figure 2.3.: Transmission function for the KATRIN experiment for a monoenergetic, isotropic electron source with settings $B_{\mathrm{min}} = 3\,\mathrm{G}$, $B_{\mathrm{max}} = 6\,\mathrm{T}$ and $B_{\mathrm{s}} = 3.6\,\mathrm{T}$.

In the KATRIN experiment the magnetic field inside the source section is with $B_{\mathrm{s}} = 3.6\,\mathrm{T}$ not equal to the maximum magnetic field which is applied as pitch field with $B_{\mathrm{max}} = 6\,\mathrm{T}$ in front of the detector. This leads to a rejection of electrons with high angles $\theta_{\mathrm{s}} > \theta_{\mathrm{s}}^{\mathrm{max}}$ that pass the filter, due to the magnetic bottle effect; the angle θ is increased according to equation (2.12) until the electrons are reflected. The maximum accepted angle $\theta_{\mathrm{s}}^{\mathrm{max}}$ decreases then from $90\,^\circ$ to

$$\begin{aligned} \theta_{\mathrm{s}}^{\mathrm{max}} &= \arcsin\sqrt{\frac{B_{\mathrm{s}}}{B_{\mathrm{max}}}} \\ &= 50.77\,^\circ. \end{aligned} \tag{2.18}$$

A transmission function for the idealized KATRIN main spectrometer is shown in figure

2.3. Mathematically it is described by

$$T(E_{\mathrm{kin}}, qU_0) = \begin{cases} 0 & \text{for} \quad qU_0 > E_{\mathrm{kin}} \\ \frac{1-\sqrt{1-\frac{E_{\mathrm{kin}}-qU_0}{E_{\mathrm{kin}}}\cdot\frac{B_{\mathrm{s}}}{B_{\mathrm{min}}}}}{1-\sqrt{1-\frac{B_{\mathrm{s}}}{B_{\mathrm{max}}}}} & \text{for} \quad E_{\mathrm{kin}} - \Delta E < qU_0 < E_{\mathrm{kin}} \\ 1 & \text{for} \quad E_{\mathrm{kin}} - \Delta E > qU_0. \end{cases} \tag{2.19}$$

It is important that the minimum of the magnetic field coincides with the maximum of the electric potential. For the standard configuration of the KATRIN experiment both lie in the center of the spectrometer, the plane is called the analyzing plane.

2.3. Overview of the KATRIN experiment

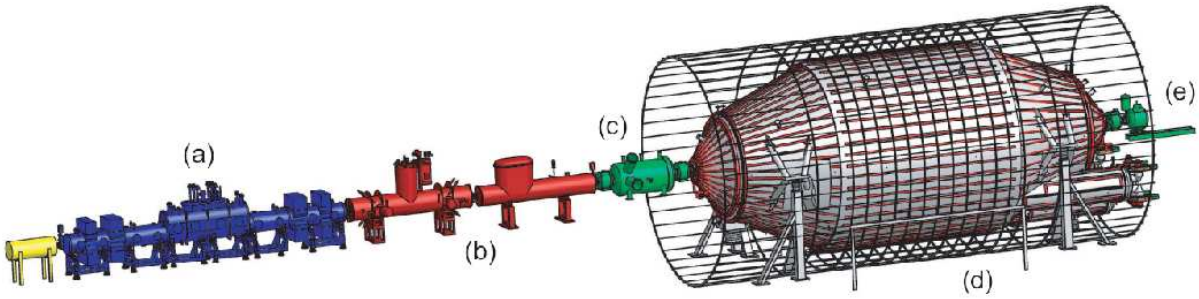

Figure 2.4.: Schematic drawing of the beam line of the KATRIN experiment. The rear section is shown in yellow, the WGTS is shown in blue (a), the Tritium retention system in red (b), the pre-spectrometer in green (c), the main spectrometer in grey (d) and the detector section in green (e).

$^3H_2$ is a gaseous molecule. To be able to measure the electrons emitted from its decay, the KATRIN experiment uses a **W**indowless **G**aseous **T**ritium **S**ource (see (a) in figure 2.4 and 2.5(a)) with a closed loop for continuous purification to maintain an isotope purity of $> 95\,\%$. The column density and thus the temperature T_{WGTS} and injection pressure p_{inj} are parameters directly influencing the systematic uncertainties at KATRIN. They are stabilized on a level of $\delta T_{\mathrm{WGTS}}/T_{\mathrm{WGTS}} \sim 10^{-3}$ and $\delta p_{\mathrm{inj}}/p_{\mathrm{inj}} \sim 10^{-3}$.

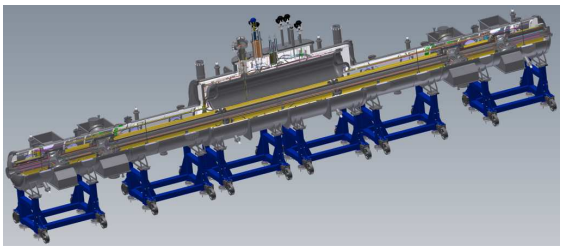

(a) CAD drawing of the windowless gaseous Tritium source.

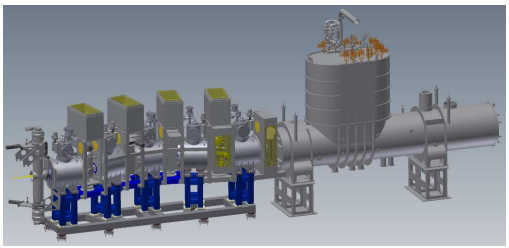

(b) CAD drawing of the transport section of the KATRIN experiment.

Figure 2.5.: CAD drawings of the source and transport section of the KATRIN experiment.

A constant magnetic field of $B_s = 3.6\,\mathrm{T}$ guides the electrons towards the spectrometer section where their energy will be analyzed. To detain the Tritium from passing into

the spectrometers, a transport section will be implemented. In the **D**ifferential **P**umping **S**ection the electrons are guided along a curved magnetic field. At the bends of the beam tubes turbo molecular pumps are placed which decrease the tritium pressure by 10^7. After the DPS a **C**ryogenic **P**umping **S**ection removes residual gas by covering the inner surface of the beam tube with Argon frost. The $^3H_2$ molecules will be absorbed on the cold surface decreasing the Tritium flow again by seven oders of magnitude. A drawing of the transport section is shown in figure 2.5(b).

The spectrometer section consists of a tandem setup of two spectrometers using the **M**agnetic **A**diabatic **C**ollimation with **E**lectrostatic **filter** principle. They act as high pass filter, letting only electrons with energies above their set energy barrier pass. The pre-spectrometer (see figure 2.6) is implemented to decrease the electron rate, its barrier is set to a value $\approx 300\,\mathrm{eV}$ below the endpoint, thus removing the uninteresting part of the spectrum, letting the electrons with energies in the endpoint region pass.

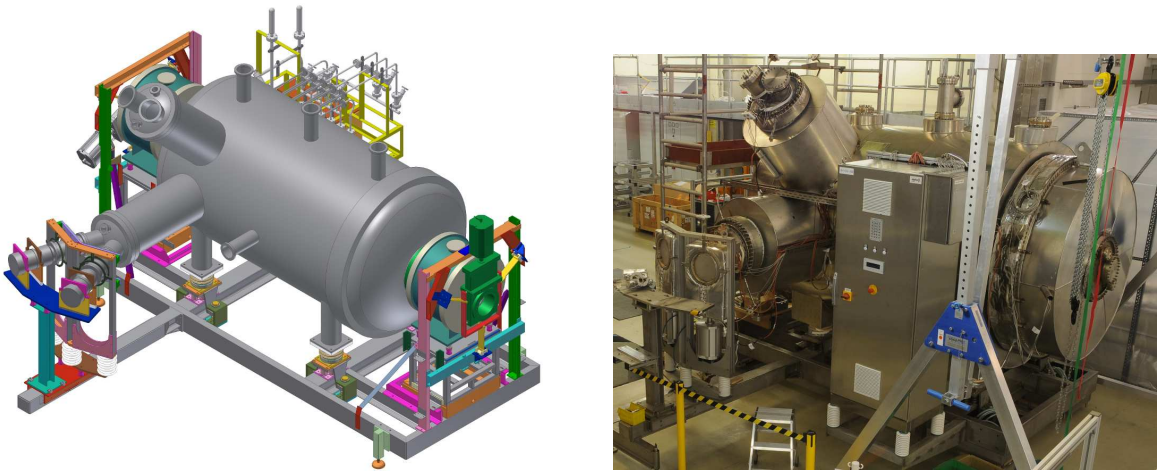

(a) CAD drawing of the KATRIN pre-spectrometer as stand alone.

(b) Picture of the KATRIN pre-spectrometer during build up in the KATRIN hall.

Figure 2.6.: The KATRIN pre-spectrometer.

The main spectrometer (see figure 2.7) analyzes the energy of the electrons. Its energy resolution is $\Delta E = 0.93\,\mathrm{eV}$ for electrons of energy $E_{\mathrm{kin}} = 18.6\,\mathrm{keV}$ (see equation (2.11)). A wire electrode system has been implemented inside the main spectrometer to fine tune the electric potentials and to reduce the background due to radioactive decays in the material of the vessel hull and cosmic radiation by electrically shielding the inside of the spectrometer from low energy electrons with a more negative potential.

The detector positioned downstream of the KATRIN main spectrometer counts the electrons passing the high pass filter. An additional magnet is used to reduce the diameter of the flux tube to fit on the 90 mm diameter disc of the detector. As signal rates in the mHz region are expected, active and passive shields are implemented, reducing the detector background to $< 1\,\mathrm{mHz}$. The detector system with its magnets is shown in figure 2.8(a).

Due to the ground potential applied at the entrance and exit of the main spectrometer and its large size, the potential in the analyzing plane is not homogeneous (see figure 3.5(a)). To account for the potential depression seen by electrons passing through the spectrometer for different radii, the detector is segmented (see figure 2.8(b)). The measurements will

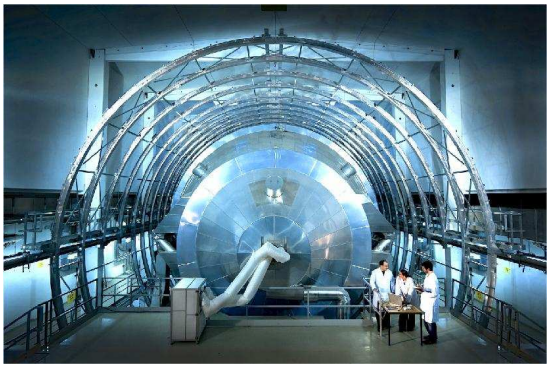

(a) Picture of the KATRIN main spectrometer with the installed air coil system.

(b) Picture inside the KATRIN main spectrometer with the wire electrode installed.

Figure 2.7.: The KATRIN main spectrometer with its wire electrode.

be analyzed separately for each segment.

(a) Picture of the assembled detector system.

(b) Picture of the segmented focal plane detector.

Figure 2.8.: The detector system of the KATRIN experiment.

3. An angular-selective electron source for the KATRIN experiment

Before the KATRIN experiment is ready to take Tritium data, thorough and elaborate tests of all components have to be conducted. To be able to interpret measurements correctly, different features of the KATRIN main spectrometer need to be investigated in detail. Electro-magnetic design simulations give a basis for the analysis, but cannot replace measurements at the setup with its hardware implementation. The KATRIN main spectrometer will be investigated with different custom-made electron sources. In this chapter an optimized source with which electrons of adjustable transversal energy at fixed total energy and thus adjustable angle θ_{mag} between the electron's momentum $\vec{p}$ and the magnetic field $\vec{B}$ in the entrance magnet can be produced, is presented.

In the first section the transmission function is reinvestigated with respect to the source properties. Resulting from this discussion the properties required of an electron source designed to characterize the transmission function of the main spectrometer are listed in section 3.2. The basic principle of the electron source, its realization and some simulations are presented in section 3.3. Measurements have been conducted with the electron source at the Mainz spectrometer. The experimental setup is described in section 3.4 and a measurement overview is given in section 3.5. The data are analyzed in section 3.6. A summary of the method and an outlook on ongoing investigations as well as on the implementation at the KATRIN experiment is given in section 3.7.

3.1. The transmission function of the KATRIN experiment: Considerations with respect to the source properties

A MAC-E filter acts as a high pass filter. Based on the initial conditions E_{kin} and θ_{s} of the electron source, electrons pass the filter (positive transmission condition, 1) or are reflected (negative transmission condition, 0). The function $t(E_{\mathrm{kin}}, \theta_{\mathrm{s}})$ describing the transmission condition thus maps a two-dimensional parameter space on two values:

$$t : \mathbb{R}^2 \to 0, 1$$
$$(\theta_{\mathrm{s}}, E_{\mathrm{kin}}) \mapsto \begin{cases} 0 \\ 1 \end{cases} .$$

Equation (2.15) gives the transmission condition as connection between θ_s and E_{kin} for the KATRIN experiment. It can be recast into the following form

$$t(\theta_s, E_{kin}, qU_0) = \begin{cases} 0 & \text{for} \quad \theta_s(E_{kin}) > \arcsin\sqrt{\frac{E_{kin}-qU_0}{E_{kin}} \cdot \frac{B_s}{B_{min}}} \\ 1 & \text{for} \quad \theta_s(E_{kin}) \leqslant \arcsin\sqrt{\frac{E_{kin}-qU_0}{E_{kin}} \cdot \frac{B_s}{B_{min}}} \end{cases} . \tag{3.1}$$

Figure 3.1 is a graphic representation of the transmission condition in the $E_{kin}(\cos\theta_s)$ parameter space, the shaded area covers combinations of $\cos\theta_s$ and E_{kin} for which $t = 1$, whereas for combinations falling in the blank area $t = 0$. Varying the potential U_0 applied to the spectrometer shifts the shaded area up and down.

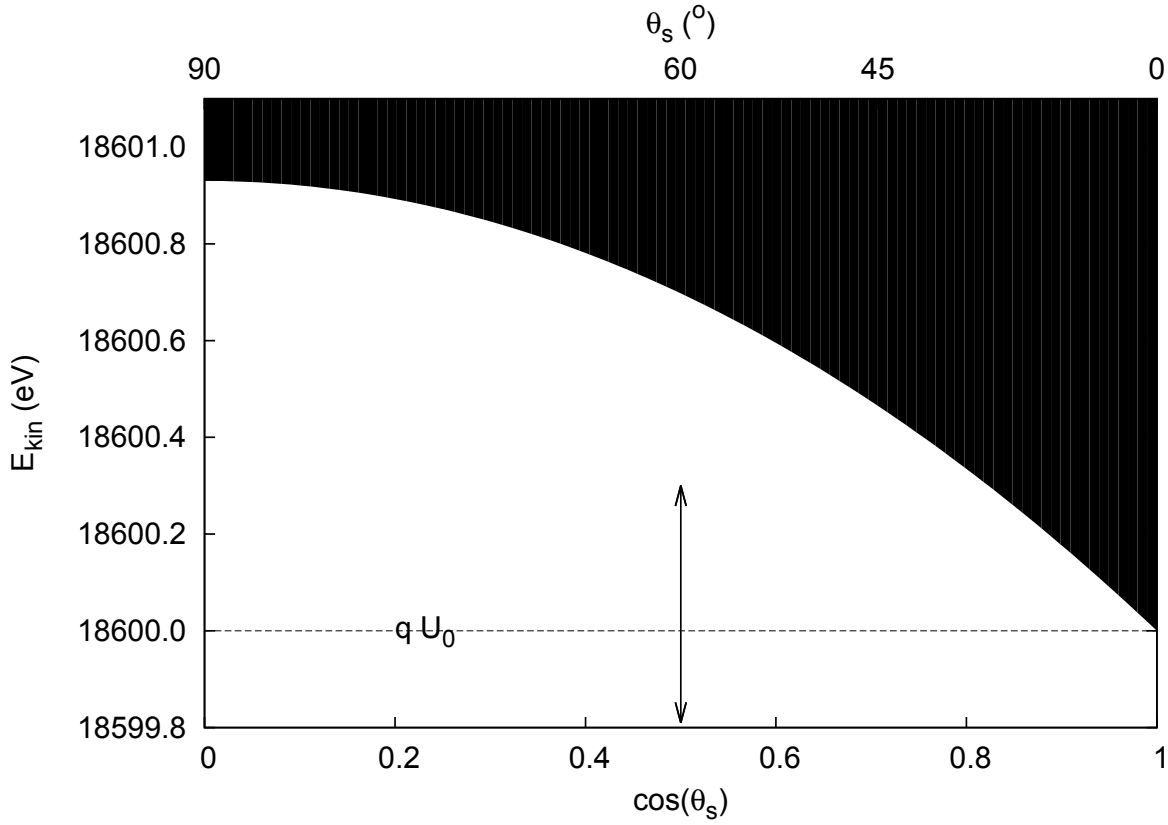

Figure 3.1.: Transmission condition of the KATRIN experiment (see equation (2.15)) denoted in the $E_{kin}(\cos\theta_s)$ parameter space. Electrons with an E_{kin} and $\cos\theta_s$ combination in the shaded area pass the filter, for all other combinations of E_{kin} and $\cos\theta_s$ the electrons are reflected. The horizontal line denotes the retarding energy qU_0, which is varied during the experiment. The shaded area moves accordingly.

The transmission function $T(qU_0)$ in this thesis is now defined as an integration of the product of the transmission condition $t(\theta_s, E_{kin})$ and the source function $f(\theta_s, E_{kin})$:

$$T(qU_0) = \int_0^{\pi/2} \int_0^{\infty} f(E_{kin}, \theta_s) t(E_{kin}, \theta_s, qU_0) dE_{kin} d\theta_s. \tag{3.2}$$

The source function $f(E_{kin}, \theta_s)$ can be separated into two parts $f_1(E_{kin})$ and $f_2(\theta_s)$ if the starting angle θ_s and the starting energy E_{kin} are decoupled:

$$f(E_{kin}, \theta_s) = f_1(E_{kin}) \cdot f_2(\theta_s). \tag{3.3}$$

This is the case for an isotropic electron source with $f_2(\theta_s)d\theta_s = \sin\theta_s d\theta_s \Leftrightarrow f_2(\cos\theta_s)d\cos\theta_s = 1$ and for electron sources with well-defined, non-isotropic angles. Figure 3.2 is a graphic representation of the integration of the product of the source function for an isotropic, mono-energetic electron source and the transmission condition resulting in the known transmission function of the KATRIN experiment. The width of the transmission function is the projection of the transmission condition onto the E_{kin}-axis.

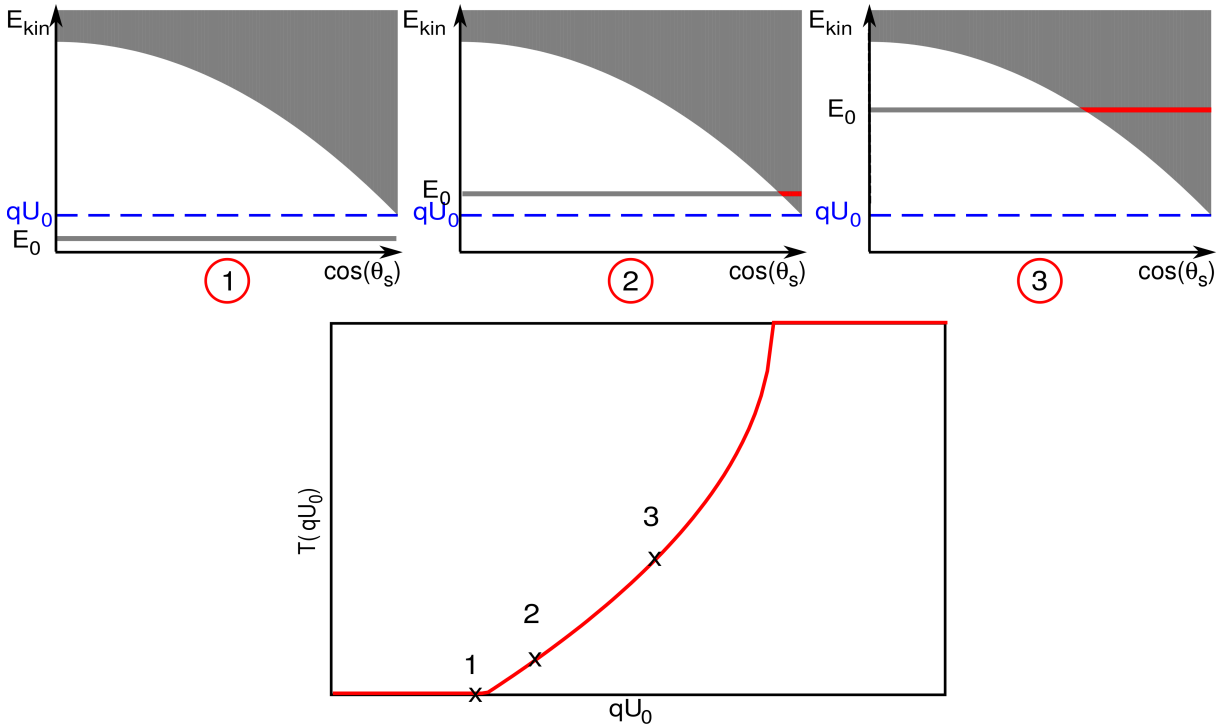

Figure 3.2.: Graphic representation of the integration of the product of the transmission condition and the source function of an isotropic, mono-energetic electron source. Steps 1 to 3 illustrate the transmission function for different values of E_{kin}.

In the case of a mono-energetic electron source with well-defined angular emission, the transmission condition tightens in the angular range. For a well defined angle the resulting transmission function is a step function (see figure 3.3).

Generally the energy distribution of the electron source can be correlated with the angular distribution. Figure 3.4 shows the construction of the transmission function for an example case.

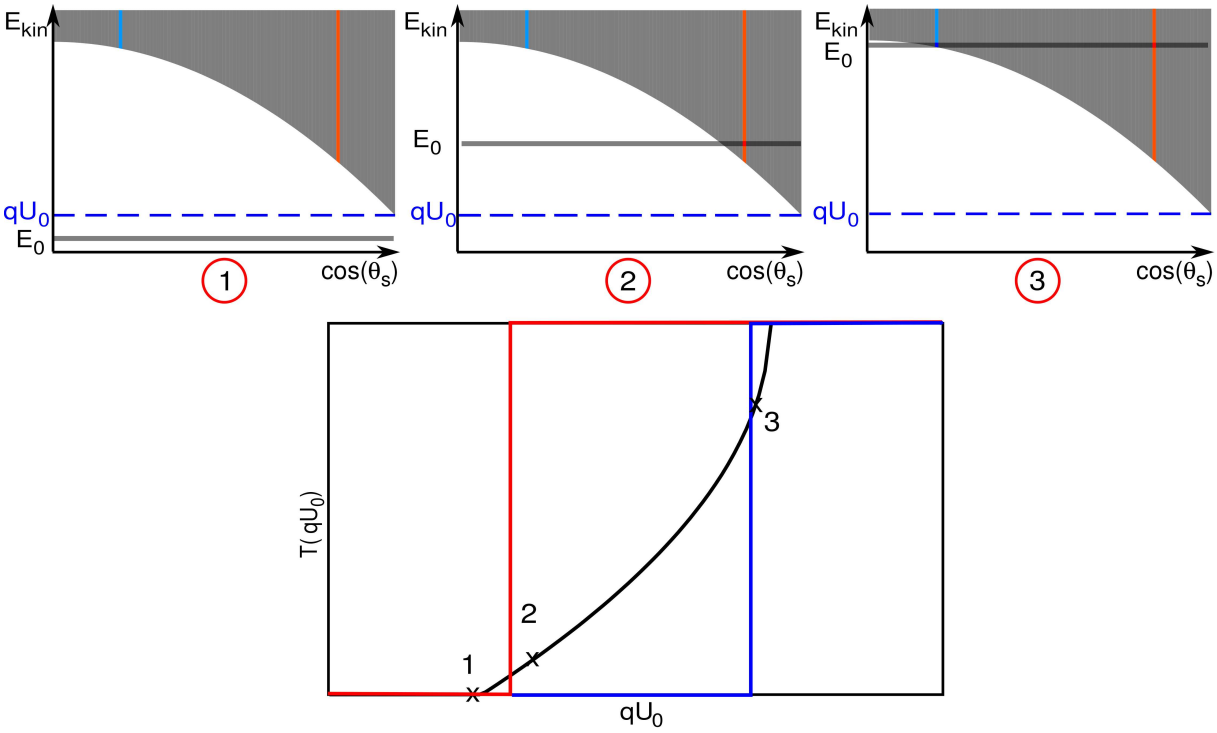

Figure 3.3.: Graphic representation of the integration of the product of the transmission condition and the source function of a mono-energetic electron source with well defined angle θ_s.

3.2. Design requirements for an electron source to investigate the properties of the main spectrometer

Different properties of the main spectrometer need to be investigated before analyzing the neutrino mass measurements. The requirements for an electron source and the characteristics of the main spectrometer that will be tested with them are listed in the following:

1. **Finite spot size and movability**
   Due to the size of the main spectrometer the potential and the magnetic field strength in the analyzing plane are not homogeneous, but exhibit a certain radial depression. Electro-magnetic design simulations show that the potential varies from the center of the spectrometer ($r = 0\,\mathrm{m}$, on-axis) to its borders ($r = 4.5\,\mathrm{m}$) by $\Delta U \approx 1.2\,\mathrm{V}$[1], the magnetic field strength increases by $\Delta B \approx 0.4\,\mathrm{G}$ (see figure 3.5(a)). Measuring an isotropic, mono-energetic source covering the whole flux tube would yield a broadening of the ideal transmission function from $\Delta E = 0.93\,\mathrm{eV}$ at $E = 18.6\,\mathrm{keV}$ to $\Delta E \approx 2\,\mathrm{eV}$ as can be seen in figure 3.5(b). To reduce the impact of the field depressions, the electron detector at the end of the KATRIN main spectrometer is segmented into 148 pieces of equal area (see also figure 2.8). The radial segmentation is adapted to the shape of the potential depression, thus each pixel covers a similar range of potential change taken from simulations. To be able to take full advantage of this segmentation, the mean and spread of the transmission functions for each pixel have to be measured precisely. Hence, a point-

[1] These values were obtained with one specific system configuration and depends on the eventual setting chosen, *e.g.*, for potentials applied to the wire electrode system.

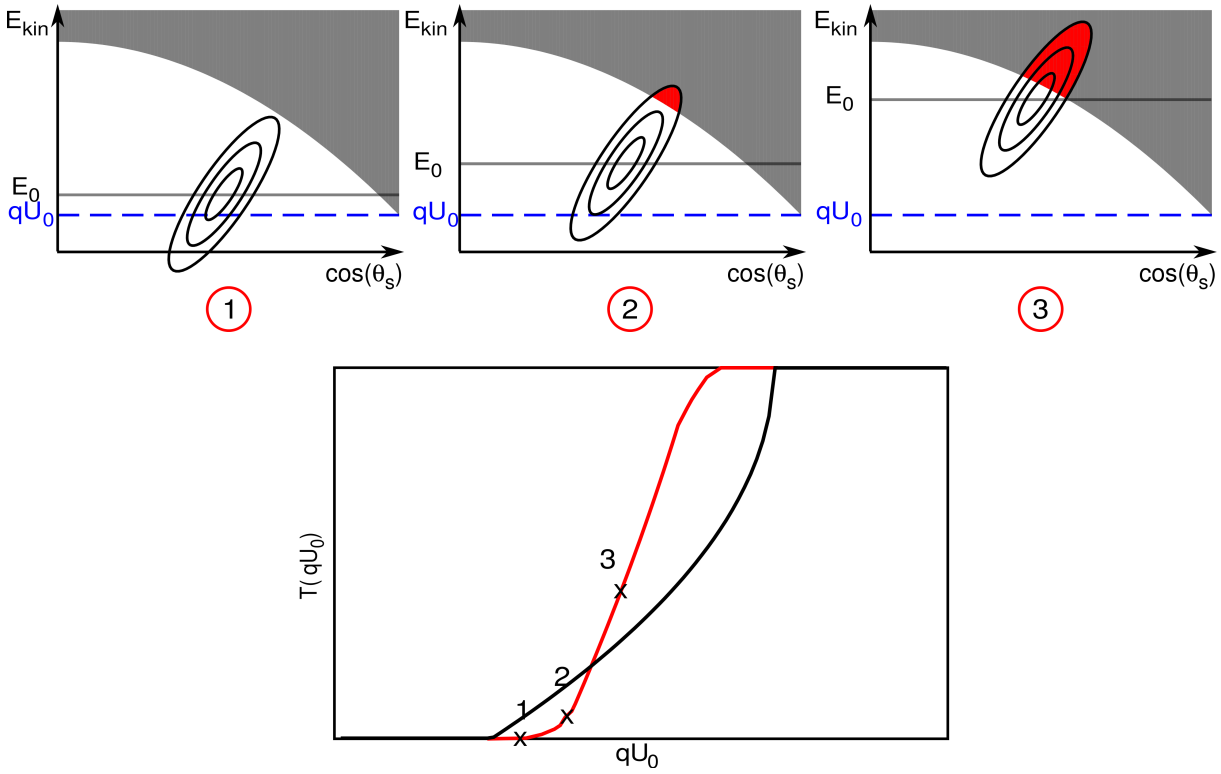

Figure 3.4.: Graphic representation of the integration of the product of the transmission condition and the source function of an electron source with correlated energy E_{kin} and angle θ_{s}. The elliptical shape describes the emission distribution of the example electron source. Steps 1 to 3 illustrate the transmission function for different values of E_{kin}.

like mono-energetic electron source that is movable to cover the whole flux tube of 191 Tcm^2 is needed to address each pixel individually.

2. **Limited energy spread**
   The measured transmission function $T(qU_0)$ is an integration of the product of the transmission condition and the source function (see section 3.1). Measuring a broadened transmission function thus can either result from field depressions across the area covered by the detector pixel, or be attributed to an energy spread at the source. Hence, it is important that the electron source used to investigate the transmission function of each detector pixel has an energy spread smaller than the ideal width of the transmission function. This implies a spread of $\delta E < 0.93\,\mathrm{eV}$ at $E_{\mathrm{tot}} = 18.6\,\mathrm{keV}$, thus a relative width of $\delta E/E_{\mathrm{tot}} \approx 10^{-5}$ for the KATRIN main spectrometer.

3. **Angular selectivity**
   The discussion of the transmission function $T(qU_0)$ of the KATRIN main spectrometer in section 2.2 has shown that the width ΔE of the transmission function is caused by the angular spread of the source electrons. Using now an electron source with a fixed and well-defined angle θ_{s} and small energy spread σ_E allows to disentangle different contributions to the total width of the transmission functions. Figure 3.6 shows the ideal transmission function of the KATRIN experiment for an isotropic mono-energetic source (black line) together with transmission functions for mono-energetic sources with fixed angles and for electron sources with fixed angle

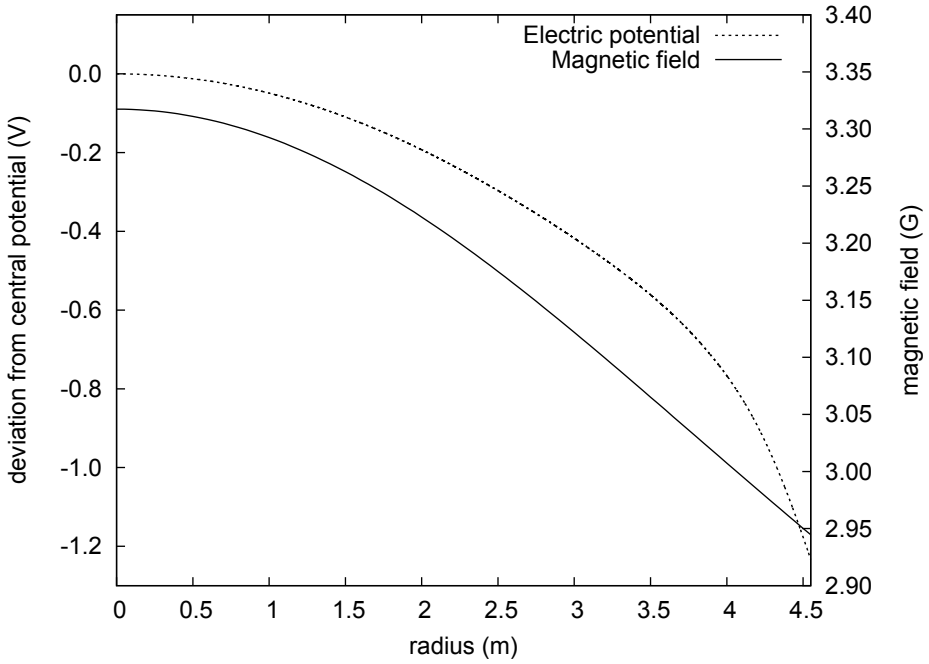

(a) Potential depression and depression of magnetic field in the KATRIN main spectrometer analyzing plane. The potential varies by $\Delta E = 1.2$ V, the magnetic field strength decreases by $\Delta B = 0.4$ G over the complete flux tube.

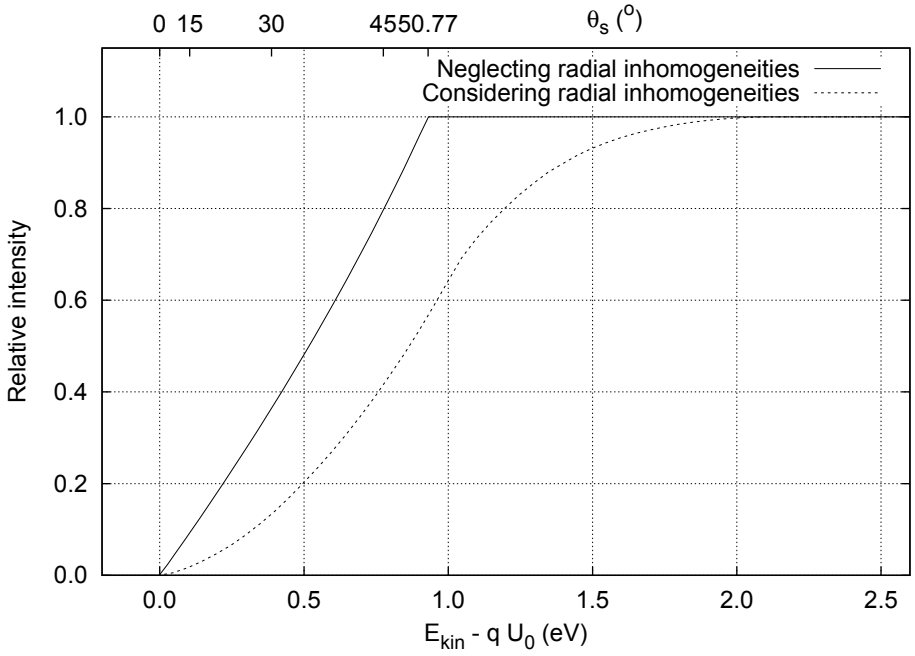

(b) Broadening of the ideal KATRIN main spectrometer transmission function for an isotropic mono-energetic electron source due to the depressions in potential and magnetic field strength in the analyzing plane.

Figure 3.5.: Potential depression and depression of magnetic field in the KATRIN main spectrometer analyzing plane and their influence on the transmission function.

and energy spread. Using a fixed angle to test the transmission functions allows to disentangle different features of the experiment. Simulations have shown that elec-

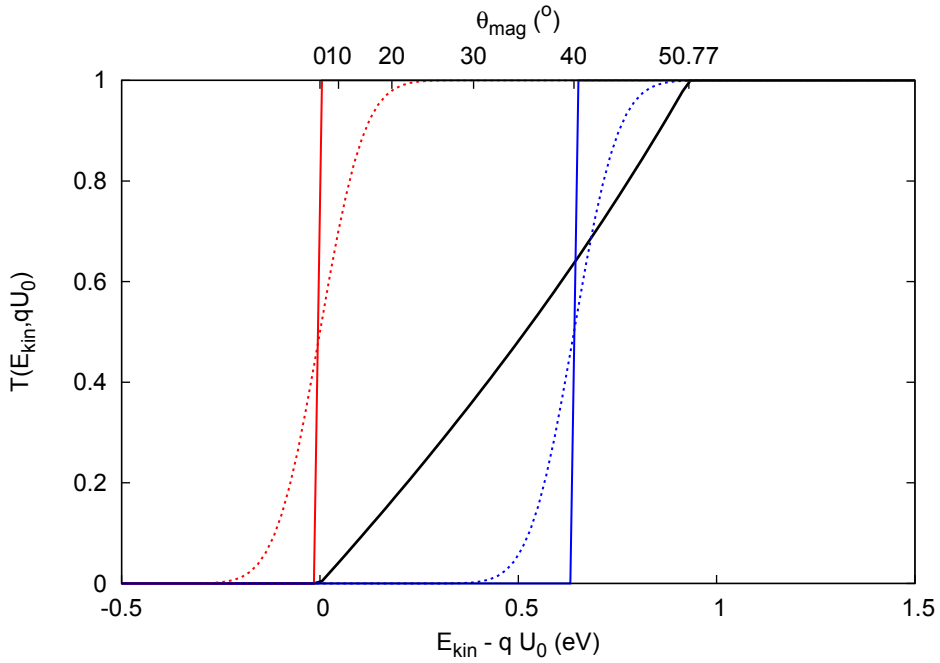

Figure 3.6.: Transmission functions at the KATRIN experiment for a mono-energetic isotropic electron source (black line), mono-energetic electron source with angular selectivity (solid red line for $\theta_s = 0\,°$ and solid blue line for $\theta_s = 40\,°$) and for electron sources with angular selectivity and an energy spread σ (dashed red and blue lines).

trons passing through the spectrometer at large starting radii with large starting angles θ_{mag} are most sensitive to misalignments of the electrode setup[Val09a].

4. **Pulsed mode**
   Using an electron source with a well-defined angle, it is possible to investigate deviations from the ideal setup by comparing the measured time of flight for a setting to the simulated time of flight or by comparing the time of flight distributions for electrons emitted from different starting positions on a circle in a plane perpendicular to the beam line.
5. **Adjustable intensity**
   The intensity should be adjustable to allow for single-electron emission for time of flight studies as well as high-intensity electron beams for transmission function measurements with high statistics and for some background tests.

A detailed discussion of these points can also be found in [Val09a, Hei10] and [Bec13].

Different electron sources have been developed, built and operated at the KATRIN experiment. They are used for varying applications. At the pre-spectrometer a quasi mono-energetic isotropic electron source on the basis of photo-emission with a spot-like emission that can be moved over the whole flux tube is in use for transmission function test measurements [Hab09, Hug08]. In the scope of the present thesis an electron source for inspections of the main spectrometer properties with a new method to select the emission angle has been developed.

3.3. The parallel plate electron source

Based on the function principle of the pre-spectrometer electron source, a mechanism to produce electrons with well defined angles has been developed. In this section a short description of the pre-spectrometer electron source and the first prototype for an angular-selective electron source will be given.

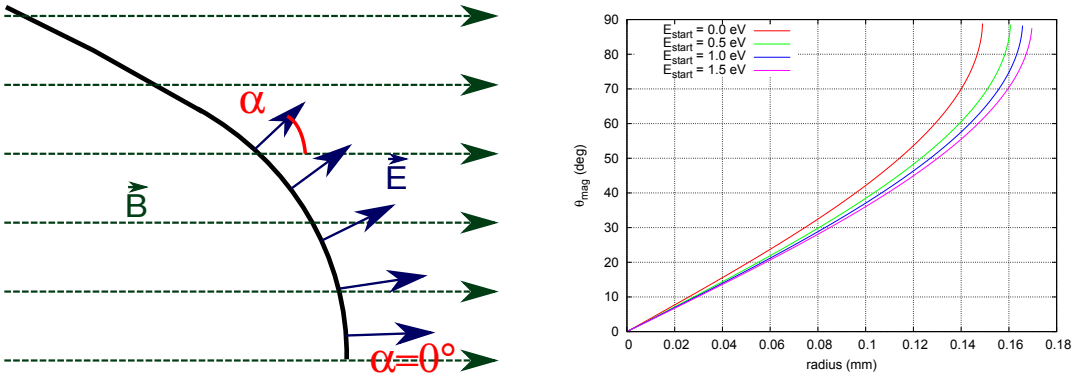

(a) Emission points on the electron source tip. Blue arrows indicate the electric field at the tip, green ones the magnetic field.

(b) Relationship of the angle θ_{mag} reached in the magnet and the emission point (characterized by the coordinate r).

Figure 3.7.: Simulation of the pre-spectrometer electron source: Electrons are emitted on the electron source tip and immediately accelerated by the electric field. Subsequently the electrons are guided along the magnetic field lines. The angle α between electric and magnetic field at the emission point determines the starting angle θ_{s} of the electron with respect to the magnetic field and thus the angle θ_{mag} reached at the position of the magnet (compare also figure 3.10). Figures taken from [Hug08].

For the discussion of the angular selectivity the angle θ_{mag} inside the entrance magnet of the used spectrometer has been chosen as parameter to describe the source. In the case of symmetric magnetic fields as used in the stand-alone setups in Mainz and with the KATRIN pre-spectrometer, the field inside the entrance magnet is the maximum magnetic field resulting in an acceptance of θ_{mag} between $0\,^\circ$ and $90\,^\circ$.

In [Hug08] the angular emission of the pre-spectrometer electron source has been investigated in detail. It was found that the electron source, which is positioned outside the entrance magnet where the magnetic field strength is reduced by a factor of about 1/200, mimics quite well an isotropic source in the entrance magnet. The achieved angles θ_{mag} in the entrance magnet strongly depend on the applied fields: Electrons emitted via the photo-electric effect at the front of the electron source tip, close to the symmetry axis of the electron source tip, initially have a small angle with respect to the magnetic field and thus obtain only small angles θ_{mag} in the higher magnetic field of the entrance magnet. If electrons are emitted off-axis, thus further along the spherical arc of the electron source tip, the angle between magnetic and electric field increases and thus also the angle θ_{mag} achieved in the magnet (see also figure 3.7). To test the possibility of creating electrons with reduced angular spread, the emission positions on the tip have been restricted to small areas by illuminating only part of the tip using fibers (see figure 3.8(a)). The measured transmission functions (see figure 3.8(b)) show different width and shapes implying a successful implementation of basic (albeit limited) angular selectivity [Val09a, Val11].

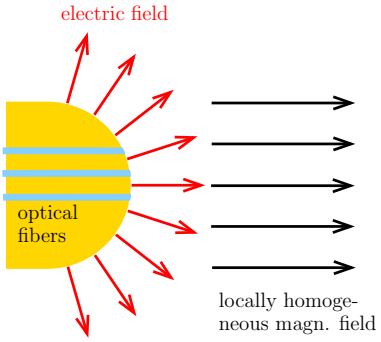

(a) Working principle of fiber electron source: Only parts of the tip are illuminated from the back side with fibers. Figure taken from [Val09a].

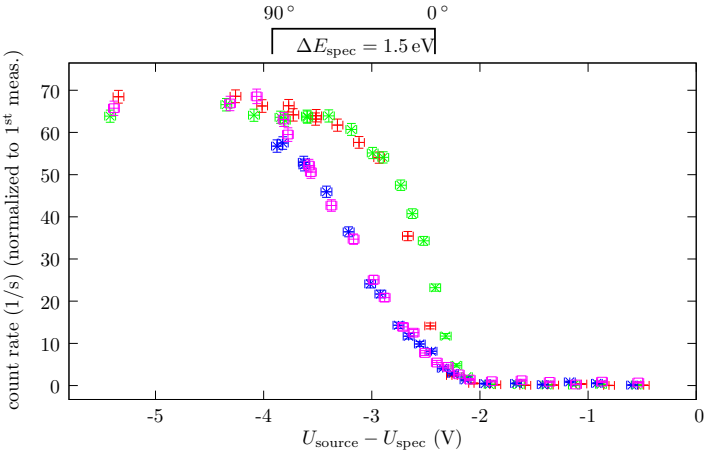

(b) First measurements with the fiber electron source: transmission functions for two fibers positioned at different radii in the spherical tip. Figure taken from [Val09a].

Figure 3.8.: The fiber electron source: working principle and first test measurements.

Detailed simulations have shown that the angular range addressed by the fibers overlaps as the emission spots still cover a significantly extended area [Hei10].

An photo-electron source with an energy spread of $\sigma = 0.21(\pm 0.02)\,\text{eV}$ for electrons with a total energy of $E = 18\,\text{keV}$ has been presented in [Val09b].

An improved electron source with adjustable angular emission and small energy spread was developed using the principle that the angle between electric and magnetic field at the emission point of the electron determines the ultimate angles θ_{mag} reached in the magnet. The angular spread has been drastically reduced by using a homogeneous electric field whose orientation with respect to the fixed magnetic field can be adjusted.

3.3.1. Basic principle

In the scope of this thesis a source of mono-energetic electrons with small spread and adjustable angles was designed. Its properties are strongly dependent on the applied electric and magnetic fields. Electrons are created on a planar electrode via the photoelectric effect and are accelerated with an electric potential difference according to

$$\vec{F} = q \cdot (\vec{E} + \vec{v} \times \vec{B}). \tag{3.4}$$

Due to the electrons' low initial energy ($v \approx 0$) the influence of the magnetic field is low at the start of the trajectory. Only after gaining energy and thus momentum, the electrons are guided along the magnetic field lines. The angle θ_{mag} in the entrance magnet between an electron's momentum and the magnetic field is determined by the early acceleration phase and can be regulated by the angle α between electric and magnetic field together with the electric field strength $E = \Delta U_{\text{plate}}/d$ in the beginning. A sketch illustrating the electron source principle is shown in figure 3.9.

The transversal energies reached in this setup alone are in the order of several 10 eV at the beginning for a total energy of $E = qU_{\text{egun}} = 18.6\,\text{keV}$ corresponding to angles of

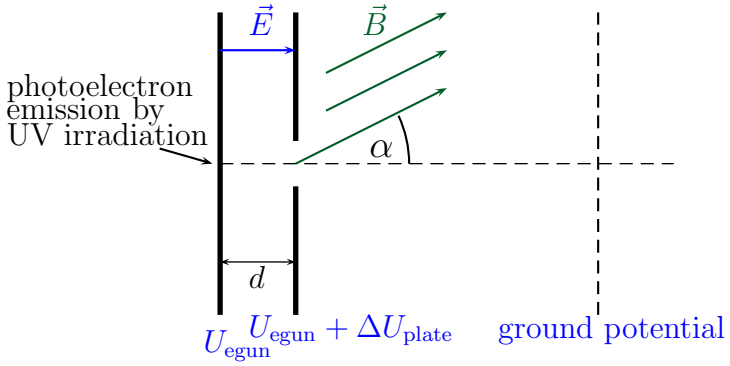

Figure 3.9.: Schematic principle of the angular-selective electron source: Electrons are emitted from the back plate on the negative potential U_{egun} and accelerated by the electric field between back and front plate due to the potential difference ΔU_{plate}. The gain in velocity allows the magnetic guidance according to $\vec{F_L} = q \cdot \vec{v} \times \vec{B}$ to take over, and subsequently the electrons move along the magnetic field lines in a cyclotron motion. When reaching the ground potential the electrons are accelerated to their maximum energy $E = qU_{\text{egun}}$. The fraction of energy in the cyclotron motion $E_\perp$ is determined by the potential difference ΔU_{plate} and the angle α between electric and magnetic field.

$\theta_s < 5\,°$. These angles are increased by guiding the electrons adiabatically into a stronger magnetic field. The angle then transforms according to equation (2.12). A schematic drawing illustrating the principle of the angular transformation is shown in figure 3.10.

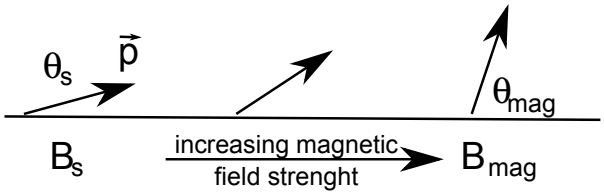

Figure 3.10.: Change of the angle θ between the electron momentum $\vec{p}$ and the magnetic field $\vec{B}$ if the electron moves from low magnetic field strength B_s to a region of high magnetic field strength B_{mag}. The angle θ_{mag} is determined by equation (2.12).

3.3.2. Simulations

The simulations have been conducted with the program package *elcd3_2* for the electric fields. *elcd3_2* was developed for rotational symmetric electrode setups and uses the boundary element method to calculate surface charges on electrode segments. Source points are constructed with which the electric field can be extracted. The program *el-traj* tracks electrons microscopically. The programs were written by F. Glück [Glu11e, Glu13] and maintained by S. Vöcking [Voe08].

The design simulations have been conducted with a simplified model using rotational symmetry and are described in detail in [Hei10]. They have been used to investigate the general acceleration procedure in the setup and to optimize the geometrical parameters, such as the starting radius r, the acceleration potential between the plates ΔU_{plate}, etc. The design is summarized in table 3.1.

Table 3.1.: Parameters for the electron source prototype setup used in Mainz.

plate diameter	$\varnothing_{\text{plate}}$	100 mm
aperture diameter	$\varnothing$	6 mm
distance between plates	d	10 mm
plate thickness	w	2 mm
maximum applicable voltage difference	ΔU_{plate}	4 kV
movement range for angle	α	0 ° to 18 °
electron emission from 3 fibers:		
central fiber 1	r_1	0.1 mm
outer fiber 2	r_2	0.9 mm
outer fiber 3	r_3	1.8 mm
fiber core diameter	$\varnothing_{\text{fiber}}$	15 μm
rotation point (center of front plate):		
distance to center of spectrometer	z_{egun}	2.638 m
distance to center of magnetic field	$\Delta z_{\text{egun-mag}}$	0.628 m
magnetic field strength at electron source	B_{egun}	20.8 mT
maximum magnetic field strength	B_{max}	6.014 T

The simulations have been conducted for a discrete set of angles α. They state that the setup should yield a source with adjustable $\theta_{\text{mag}} \in [0 : 90\,^\circ]$ with limited width σ_θ. The expected dependency of the angle θ_{mag} on the adjustable parameters tilt angle α and acceleration potential ΔU_{plate} for the settings stated in table 3.1 is shown in figure 3.11. As emission point fiber 2 ($r = 0.9\,\text{mm}$) has been chosen.

For settings with the tilt angle $\alpha = 4\,^\circ$ the simulations state that the maximum angle $\theta_{\text{mag}} = 90\,^\circ$ cannot be reached. For higher potential differences ΔU_{plate} low angles θ_{mag} cannot be achieved. $\theta_{\text{mag}} \approx 0\,^\circ$ can only be reached with low potential differences ΔU_{plate} and small angles α. $\theta_{\text{mag}} = 0\,^\circ$ can only be achieved if no energy is in the cyclotron component $E_\perp$. This is only possible if the electrons are emitted parallel to the magnetic field and thus for an tilt angle $\alpha = 0\,^\circ$ or if the electrons are emitted from the fiber with an angular spread, resulting in a few of them with momentum parallel to the magnetic field.

The simulations show that the spread of the angle θ_{mag} can be attributed to the size of the emission area, which therefore has been chosen to be sufficiently small, and to the passage of the electrons through the aperture. Due to the gyration around the magnetic field lines the electrons have different distances to the aperture and thus see at that point different effective potentials that accelerate or slow down the particles. Electrons with small angles θ_{mag} have only a small gyration radii and are therefore only marginally influenced by the aperture. Thus, the width of the angular distribution is minimal ($\Delta\theta_{\text{mag}} < 1\,^\circ$) for electron source settings producing $\theta_{\text{mag}} \approx 0\,^\circ$ and increases for larger angles to a maximum of $\Delta\theta_{\text{mag}} < 4\,^\circ$. The angular distributions are cut off at $\theta_{\text{mag}} = 90\,^\circ$. Hence, angular distributions at θ_{mag} up to $90\,^\circ$ show a decrease in width in the simulations.

3.3.3. Realization

The electron source has been designed and operated together with Hendrik Hein, details are also discussed in his diploma thesis [Hei10]. A short introduction has been published

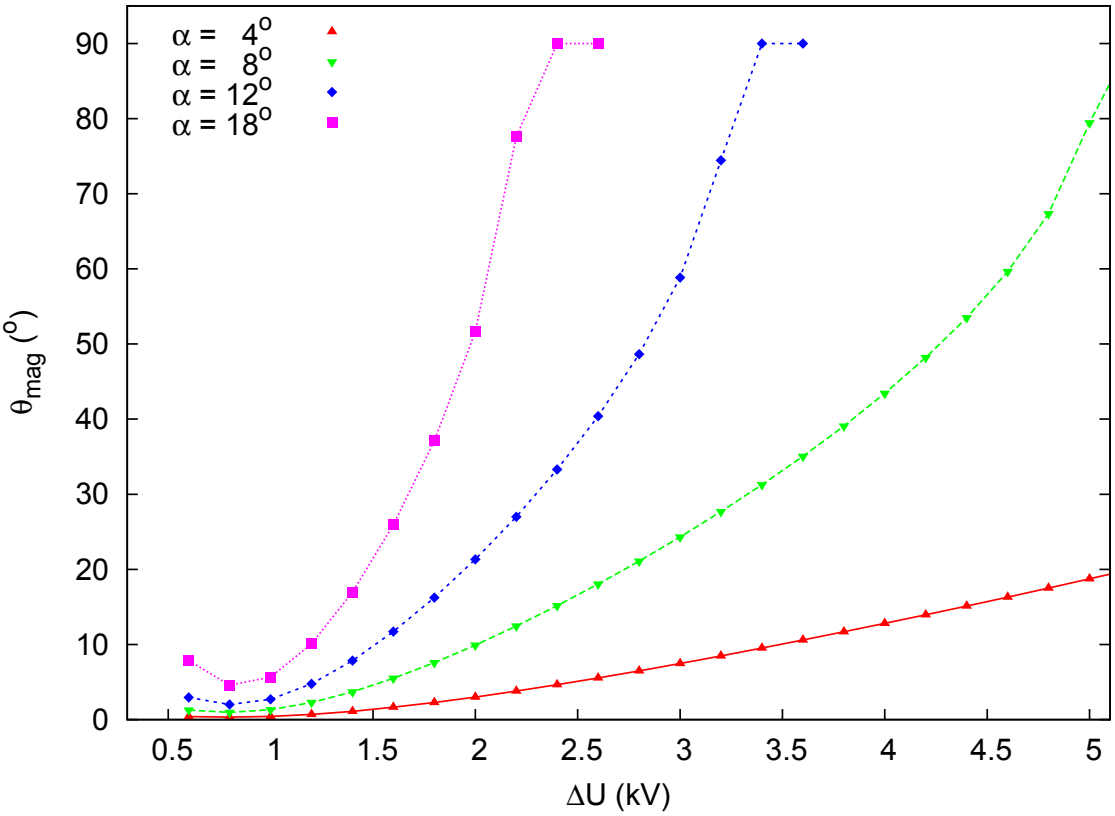

Figure 3.11.: Simulations of the angle θ_{mag} in the magnet achievable for different settings of the acceleration potential $\Delta U_{\mathrm{plate}}$ and the angle α between E- and B-field. The simulations have been conducted for $U_{\mathrm{egun}} = -18.6\,\mathrm{keV}$ and a fiber positioned at $r = 0.8\,\mathrm{mm}$ off-center. Contributions to the angular spread have been neglected.

in [Hug10] and a part of this work is currently being prepared for publication in [Bec13].

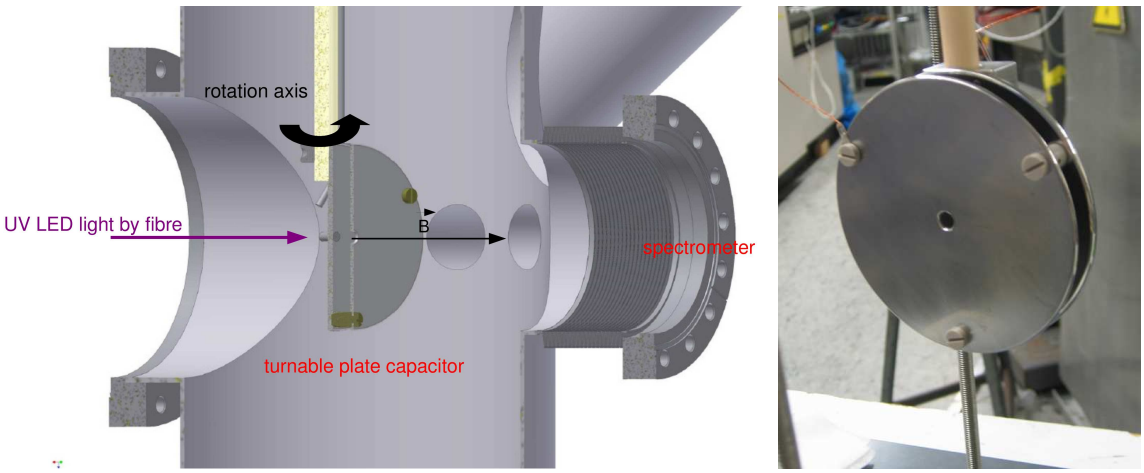

(a) Technical drawing

(b) The electron source before its implementation into the setup.

Figure 3.12.: The parallel plate electron source.

Electrons are created at the electron source via the photoelectric effect. UV light of

wavelengths around 265 nm[2] is guided with a fiber of type FEQ100-15000100 (15 μm core diameter/125 μm cladding/250 μm outer diameter) supplied by the company j-fiber GmbH Jena to an electrode on high voltage. The fibers are glued into a cylinder with three micro boreholes of diameter $\varnothing_{\text{micro}} = 300\,\mu\text{m}$ with fiber center positions $r_1 = 0.1\,\text{mm}$, $r_2 = 0.9\,\text{mm}$ and $r_3 = 1.8\,\text{mm}$ with *H2O* EPOXY at a moderate temperature[3]. The cylinder with the end of the fiber is coated with a polycrystalline silver layer of $35(\pm5)\,\frac{\mu\text{g}}{\text{cm}^2}$ density with an expected work function of $\Phi_{\text{Au}} = 4.00(\pm0.15)\,\text{eV}$[Eas70][4]. The cylinder is then laser welded into an electrode surface that will be the backplate of the parallel plate capacitor. The electrons are emitted from the surface with expected energies of

$$E_{\text{start}} = E_\gamma - \Phi_{\text{Au}} = \frac{hc}{\lambda} - \Phi_{\text{Ag}} \approx 0.68\,\text{eV}, \tag{3.5}$$

using the central wavelength of the diode of $\lambda = 265\,\text{nm}$. As the LED does not emit monochromatic light, the distribution with a FWHM of 0.27 eV needs to be taken into account for the energy calculation. The electrons are emitted somewhere in the polycrystalline material and therefore need to traverse the rest of the material in which they can lose some of their energy. Therefore, the energy distribution of the electrons cannot be given, only the fact that their energy is expected to be in the region below 1 eV. In addition, there is a thermal broadening of the order of $kT = 1/40\,\text{eV}$ as the density of occupied states does not end sharply at E_{Fermi} at $T > 0\,\text{K}$.

The two plates of the electron source are mechanically fixed together with PEEK screws that electrically insulate the plates while fixing their distance to $d = 10\,\text{mm}$. The plates are mounted onto a rotation feed through using an elbow so that the rotation is centered around the lens position.

A technical drawing can be found in figure 3.12(a), a picture of the assembled electron source in 3.12(b).

3.4. Experimental setup

3.4.1. The Mainz spectrometer

The properties of this electron source were tested at the Mainz spectrometer[5] (see figure 3.13) while it was still running at the Johannes-Gutenberg Universität Mainz. For these measurements the setup includes two superconducting coils supplying a magnetic field of $B_{\text{mag}} = 6\,\text{T}$ at the entrance and the exit of the spectrometer. Additional coils around the spectrometer were used for the compensation of the earth magnetic field, to shape the flux tube and to adjust the image of the source on the detector (earth field compensation coils, $I_1 = 15\,\text{A}$ and $I_2 = 40\,\text{A}$). The magnetic field strength in the center of the spectrometer can be adapted for fine tuning the resolution of the spectrometer by adjusting the currents in the air coil system. For these measurements a configuration with $I_{\text{LS4}} = -5\,\text{A}$, $I_{\text{LS2}} =$

[2] A UV-LED of type T9B26C with a central wavelength of 265 nm has been used as light source, for detailed information see also [Val09a].

[3] The glue was dried at about 50 °C for one day as the fibers can be damaged at higher temperatures

[4] The work function strongly depends on surface treatment, therefore the literature values can only be taken as indication of the expected energy.

[5] The former Mainz spectrometer is now used as monitor spectrometer for the KATRIN experiment.

8.8 A and $I_{\mathrm{LS1}} = I_{\mathrm{LS3}} = 19\,\mathrm{A}$ (see (iv) in figure 3.13) has been chosen. Simulations for this setup show a maximum magnetic field strength in the center of the superconducting magnets of $B_{\mathrm{max}} = 6.014\,\mathrm{T}$ and a minimal magnetic field strength in the center of the spectrometer of $B_{\mathrm{min}} = 18.94 \cdot 10^{-4}\,\mathrm{T}$, leading for an isotropic electron source with energies of 15 keV to an expected resolution of

$$\Delta E = \frac{B_{\mathrm{min}}}{B_{\mathrm{max}}} E_{\mathrm{tot}} = 4.72\,\mathrm{eV}. \tag{3.6}$$

This energy resolution is significantly worse than the typical energy resolution of $\Delta E = 0.9\,\mathrm{eV}$ used to operate the former Mainz spectrometer as a monitor spectrometer for KATRIN. The bad resolution was chosen on purpose to improve the identification of different angles from the electron source. As the electron source produces electrons with a narrow angular spread and a limited energy distribution, the measured width σ_{egun} of a transmission functions for one electron source setting is expected to be much smaller than the energy resolution

$$\sigma_{\mathrm{egun}} \ll \Delta E.$$

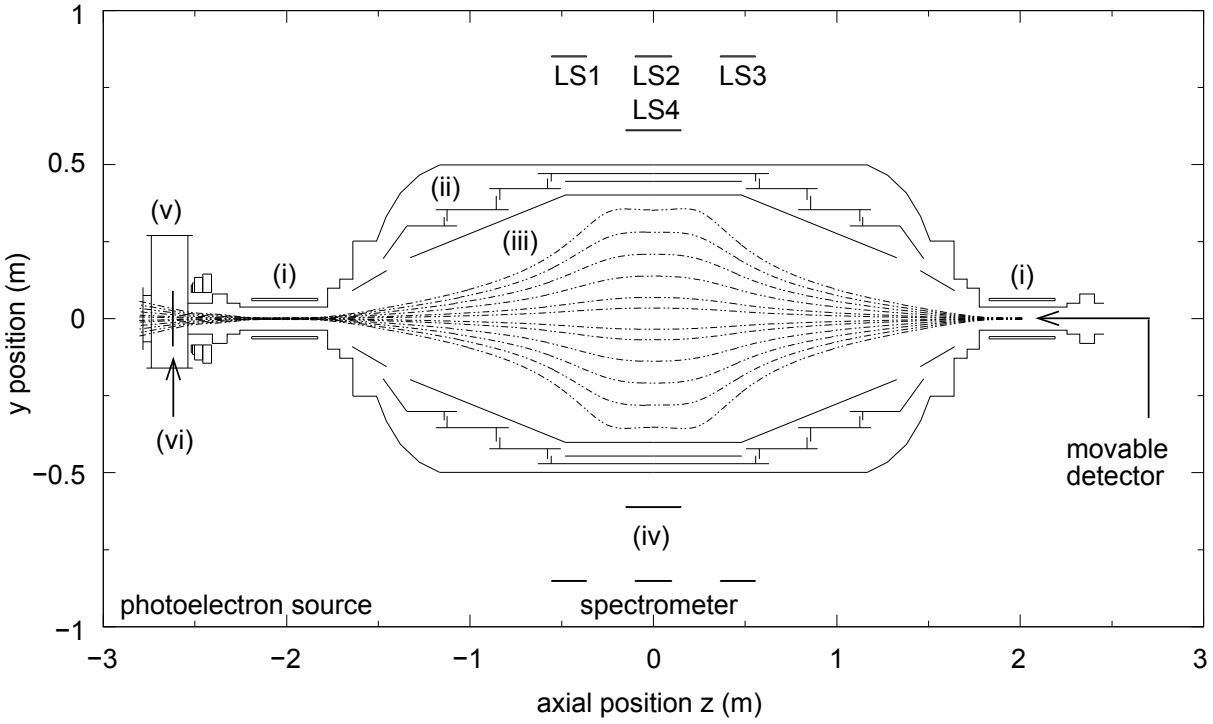

Figure 3.13.: Setup of the Mainz spectrometer: (i) superconducting solenoids, (ii) inner electrode system, (iii) wire electrode, (iv) air coil system, (v) ellipsometry vessel housing the electron source and (vi) position of electron source (figure adapted from [Val09a]).

The spectrometer vessel was set on ground potential. It encloses an inner full metal electrode system ((ii) in figure 3.13) to which an adjustable potential U_{spec} was applied for these measurements and a wire electrode system ((iii) in figure 3.13) that was set on a slightly more negative potential to reduce background. At the source side a vacuum vessel originally used for laser ellipsometry ((v) in figure 3.13) is connected via a shutter

to the spectrometer. It has its own pumping system thus allowing to insert different sources without venting the spectrometer. The parallel plate electron source was set up here. An unsegmented windowless silicon PIN diode has been used as electron counter. The detector setup and electronics as well as the data acquisition have been described in detail in reference [Zbo11]. The detector was positioned 0.469 mm from the center of the exit magnet in a magnetic field of 0.056 T. The data has been taken in 300 s periods and the counts were extracted by integrating the measured spectra in a fixed energy interval, cutting away the noise at low energy.

The pressure inside the spectrometer has been monitored to be constantly in the low 10^{-10} mbar region, in the source section values around $5 \cdot 10^{-9}$ mbar have been reached.

As the setup with the electron source at the entrance of the spectrometer is a Penning trap for electrons (electrostatic storage between the electron source and the analyzing plane of the spectrometer, magnetic storage in the 6 T magnet, for more information on Penning traps and how to avoid them see references [Val09a] and [Bec11]), a wire has been mounted off-axis into the center of the magnet to disrupt the path of the stored electrons (see figure 3.14).

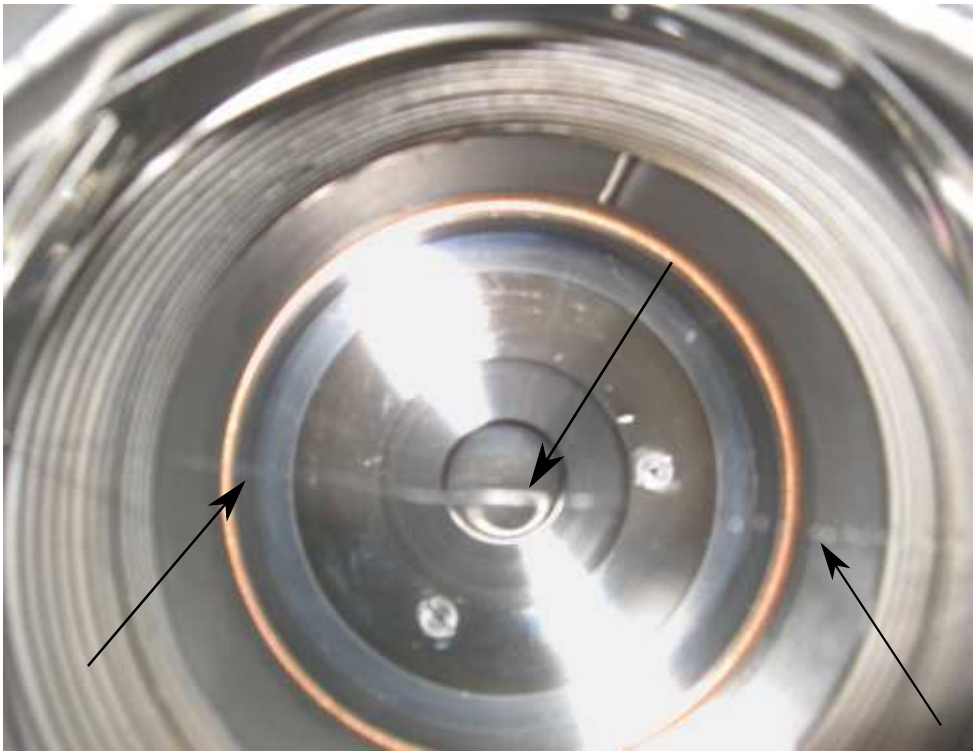

Figure 3.14.: Picture of the beam tube between electron source and spectrometer. The not focused horizontal line is the off-center wire to disrupt the path of trapped particles which will hit it due to their magnetron motion. In the background the shutter to the spectrometer is visible.

3.4.2. The electron source

The electron source has been installed in the ellipsometry chamber (see (v) in figure 3.13). The top flange has been replaced with a CF200-5×CF40 reducing flange (see figure 3.15). The rotation feed through for the electron source has been attached to the center CF40.

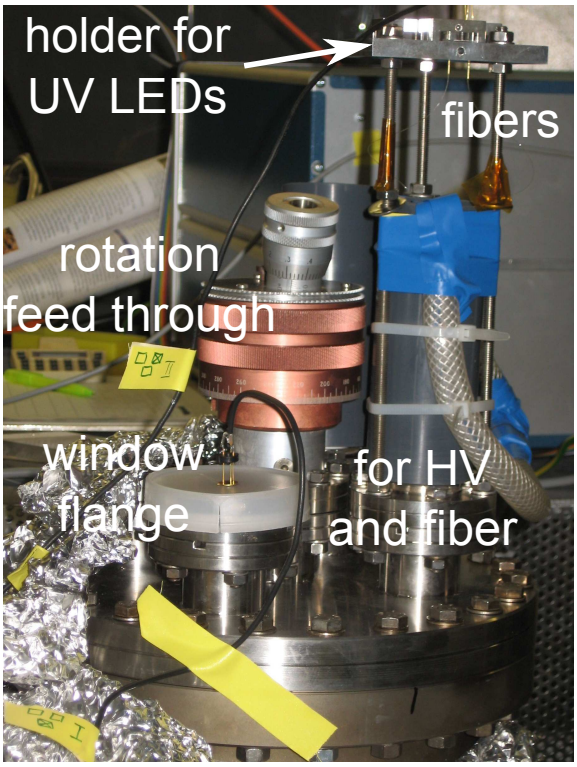

Figure 3.15.: Top view of electron source flange. At the center the rotation feed through is placed. Around it are 2 HV feed throughs, only the one leading to the backplate is visible. The feed through is also used for the optical fibers and is sealed with epoxy. The holder for the UV LEDs is visible on its top.

One CF40 has been used for the HV feed through for the front plate. A hollow HV feed through has been used for the back potential U_{egun} and to guide through the fibers. It has been closed with *H2O* EPOXY allowing for a minimal pressure in the chamber in the 10^{-9} mbar region. On top of the hollow HV feed through a holding structure for the UV-LEDs has been placed. The holder enables adjusting the LED positions to optimize the coupling of the light into the fiber. The remaining two flanges have been used for window flanges through which the setup could be monitored. For the measurements the windows have been covered. A picture of the electron source inside the ellipsometry chamber is shown in 3.16.

Instead of supplying the LED with a dc current, it was operated in pulsed mode with a duty cycle of 10^{-3} at 1 kHz (1 μs pulse length) repetition rate and output amplitude of 4.57 V supplied with an arbitrary function generator. This way the driving current can be increased to improve the output power. A resistor of 90 Ω has been added in series to protect the LED.

3.4.3. HV setup

Two high voltages sources are needed for the electron source: The potential U_{egun}[6] is applied to the backplate of the setup and determines the total energy $E_{\text{kin}} = qU_{\text{egun}}$ the electron will obtain. To generate a potential difference between the back- and the front

[6]High voltage supplied with FUG HCN 140M - 35 000, set point resolution $\pm 10^{-4}$.

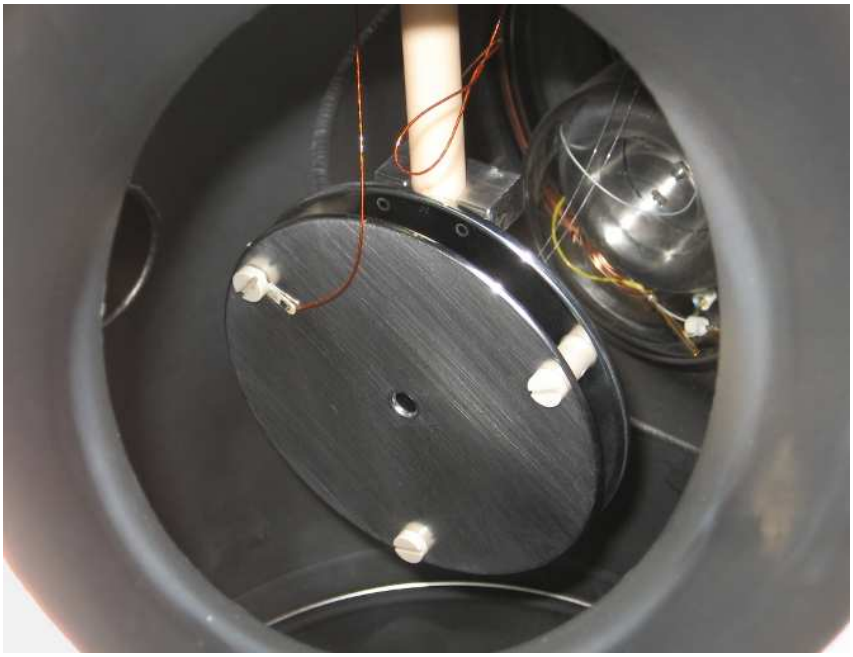

Figure 3.16.: The electron source implemented in the ellipsometry chamber in the setup as seen from a side flange. At the back of the parallel plates the fibers are visible. The Kapton wires are used to apply the potential to the electron source plates. The PEEK screws insulate the two plates from each other.

plate, an adjustable second positive potential ΔU_{plate}[7] is applied on top of U_{egun} to the front plate. This potential difference together with the angle between electron source and magnetic field determines the fraction of the total energy $E_{\perp}$ in the cyclotron motion.

The potential in the analyzing plane of the spectrometer U_{ana} determines whether an electron has sufficient longitudinal energy $E_{\parallel}$ to pass the MAC-E filter. It is controlled by the voltages applied to the spectrometer electrodes U_{spec} and wire electrode system $U_{\text{el}} = U_{\text{spec}} - \Delta U_{\text{wire}}$. For these measurements the wire electrode has been put on a slightly more negative potential to reduce the background. The spectrometer has also a potential depression due to the influence of the positive potential from the ground electrodes at entrance and exit of the spectrometer (compare potential depression of the main spectrometer shown in figure 3.5(a)). Its magnitude depends on all applied potentials. To determine the exact values the electric field in the setup has to be simulated. With the wire electrode on a $\Delta U_{\text{wires}} = -95.8\,\text{V}$ more negative potential than the main electrode system of the spectrometer at $U_{\text{spec}} = -15\,\text{kV}$ the potential in the center of the analyzing plane, through which the electron source's electrons pass, is $\Delta U_{\text{dep}} = 3.6\,\text{V}$ more positive than the potential of the wire electrode.

To measure the transmission functions in this setup the voltages applied to the spectrometer were varied. As the region of interest for these measurements is close to the voltage applied to the electron source U_{egun}, a high precision voltage supply ΔU_{EHS}[8] and a constant potential difference ΔU_{b} have been added to it for the spectrometer voltage $U_{\text{spec}} = U_{\text{egun}} + \Delta U_{\text{EHS}} + \Delta U_{\text{b}}$ [9].

[7] high voltage supply: ISEG NHQ 226 L, set point precision 100 mV
[8] High voltage supply ISEG EHS 8205p-K, 8 mV set point precision
[9] The constant potential difference ΔU_{b} has initially been implemented to set the spectrometer potential

The constant voltages supplied by battery sets have been controlled regularly and were $\Delta U_\mathrm{b} = 18.4(\pm 0.1)\,\mathrm{V}$ and $\Delta U_\mathrm{wire} = 95.6(\pm 0.1)\,\mathrm{V}$ at the time of the measurements presented below. The total high voltage setup can be seen in figure 3.17.

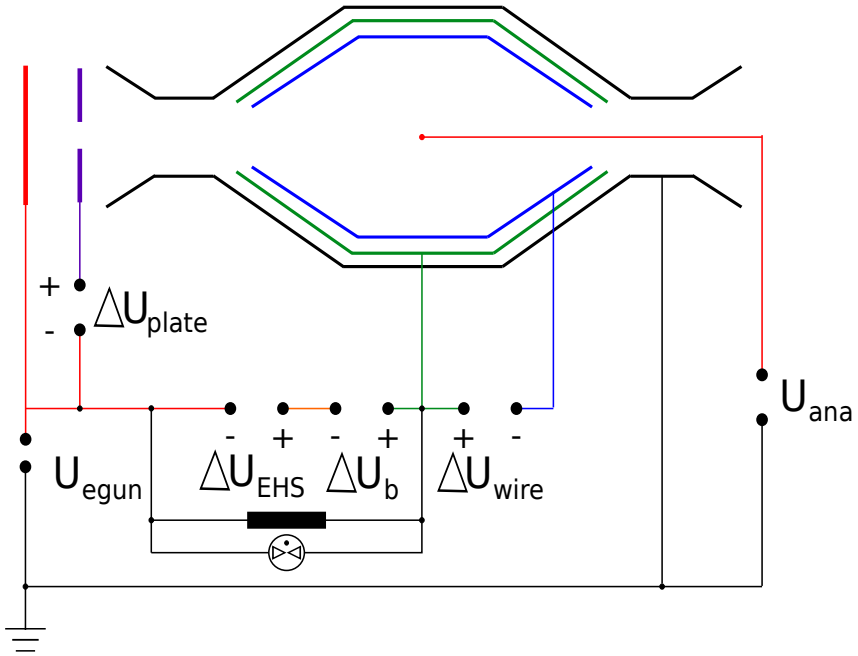

Figure 3.17.: High voltage supply for the experimental setup. A basic potential is applied as U_egun to the back plate of the electron source. The potential difference between the two plates of the electron source is achieved by adding the positive potential ΔU_plate to the electron source potential U_egun. U_egun is also applied to the spectrometer with the constant potential difference ΔU_b and the adjustable ΔU_EHS. To avoid discharges, a spark gap is built in for protection with a resistor put in parallel to avoid noise. The wire electrode is set on a more negative potential by applying ΔU_wire. As in the analyzing plane influences of the ground potential can be seen, the effective potential U_ana in the analyzing plane on the axis needs to be simulated.

The surplus energy δE is defined as

$$\delta E = q \cdot \delta U = q \cdot (U_\mathrm{egun} - U_\mathrm{ana}). \tag{3.7}$$

For retardation energies $q \cdot U_\mathrm{ana}$ larger than the electron source energy $q \cdot U_\mathrm{egun}$, thus $\delta E < 0\,\mathrm{eV}$, it is expected that the produced electrons cannot pass the filter. In the region $q \cdot U_\mathrm{ana} \leq q \cdot U_\mathrm{egun} \leq q \cdot U_\mathrm{ana} + \Delta E$ corresponding to $0\,\mathrm{eV} \leq \delta E \leq \Delta E$ electrons are expected to pass the spectrometer depending on their initial angle θ_s (see section 2.2). In

in blocking direction ($U_\mathrm{egun} > U_\mathrm{spec}$) as the voltage supply ΔU_EHS only provides positive potentials. It is important to acquire some points in blocking direction of the spectrometer for the transmission function and for the background estimation. As in the course of measurements the wire electrode has been set on a more negative potential, it was chosen to leave the battery set used for ΔU_b in the circuit, changing its connecting direction to decrease the offset supplied with ΔU_EHS.

terms of the applied potentials the surplus energy δE is

$$\begin{aligned} \delta E &= q \cdot \delta U \\ &= q \cdot (U_{\text{ana}} - U_{\text{egun}}) \qquad (3.8) \\ &= q \cdot (\Delta U_{\text{EHS}} + \Delta U_{\text{b}} - \Delta U_{\text{wire}} + \Delta U_{\text{dep}}) \\ &= q \cdot (\Delta U_{\text{EHS}} - 73.8(\pm 0.2)\,\text{V}). \qquad (3.9) \end{aligned}$$

The transmission functions presented in the following sections were not measured for surplus energies $\delta E \in [0 : \Delta E]$, but show an offset (see equations (3.14) to (3.16)). This offset could not be reproduced with the HV-components in a stand-alone setup, therefore it is attributed to some charging up effect in the field cage or at the connections to the spectrometer.

To secure the electronics against discharges spark gaps ($5 \times 90\,\text{V}$) have been included in the setup. A resistor ($500\,\text{k}\Omega$) is applied in parallel to attenuate noise on the potential.

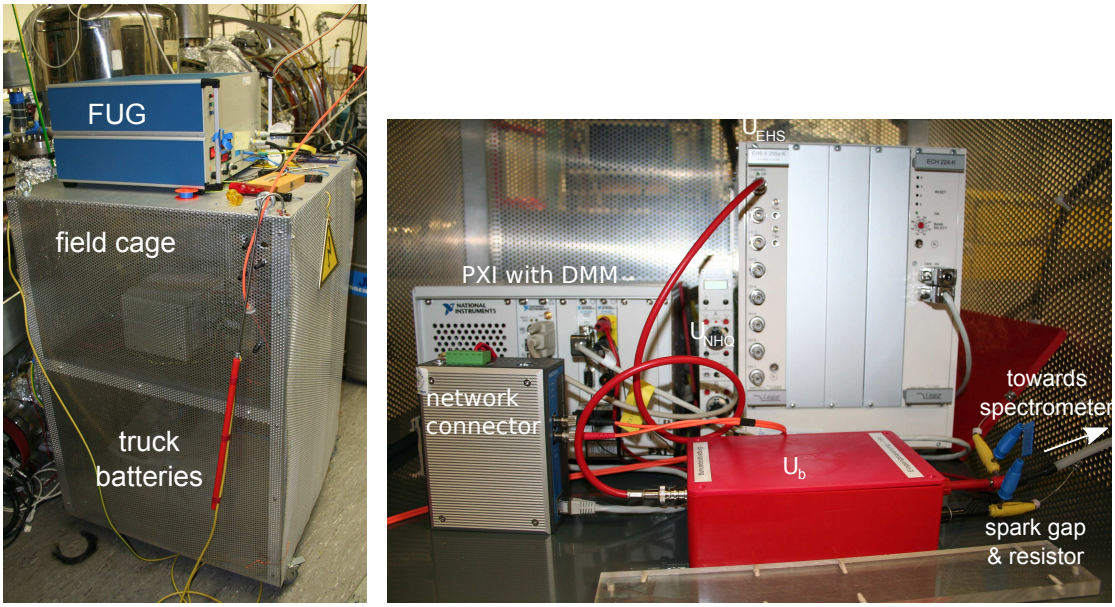

(a) Field cage with the high voltage supply for U_{egun} on top.

(b) Top shelf of field cage with the precision voltage supplies EHS and NHQ.

Figure 3.18.: Photographs of the high voltage setup in field cage. On the top shelf the voltage supplies EHS and NHQ as well as the PXI system with DMI voltage control, ADC with optical fiber, the battery set ΔU_{b} in the red box and the spark gaps with resistor are positioned. All components are encased by a field cage as they are all put to the elevated potential U_{egun} which is supplied from the outside by a FUG high voltage supply. On the bottom shelf truck battery packs are placed to provide stable supply voltages of $\pm 6\,\text{V}$, $\pm 12\,\text{V}$ and $\pm 24\,\text{V}$ for the HV components.

The HV setup has been designed this way to reduce the amount of voltages that need to be set and monitored precisely, here specifically the voltage difference ΔU_{EHS} (set point accuracy 8 mV) between electron source and spectrometer, monitored in combination with the battery set ΔU_b with the PXI DMM multimeter with 1 mV accuracy[10]. Pictures of the HV cage that has been used for the HV components are shown in figure 3.18.

[10]In the course of the experiment discharges damaged a slot of the PXI crate so that the transmission

To reduce the noise on the high voltage, choking coils and capacitances have been implemented. For the measurements a noise level of the order of 100 mV peak-to-peak has been achieved.

3.5. Measurements

Measurements have been conducted in April 2009 at the Mainz spectrometer by H. Hein, M. Beck and me with support by J. Bonn, M. Zbořil, S. Bauer, S. Rosendahl, S. Streubel and C. Weinheimer.

3.5.1. Settings

Measurements with the electron source were conducted with $U_{\mathrm{egun}} = -15\,\mathrm{kV}$ instead of the planned $U_{\mathrm{egun}} = -18\,\mathrm{kV}$ as higher voltages could not be applied due to discharges occurring at the electron source. The spectrometer voltage has been adjusted by changing U_{EHS}. Transmission functions have been measured for several sets of tilt angles α of the electron source plates and voltage differences between the plates $\Delta U_{\mathrm{plate}}$. Measurements have only been conducted with fiber 2 positioned at $r = 0.9\,\mathrm{mm}$ off-center as the fiber for the outer emission point broke during preparation and the intensity emitted from the central fiber was very low [11].

The potential difference between the plates of the electron source $\Delta U_{\mathrm{plate}}$ has been varied between $\Delta U_{\mathrm{plate}} = 1\,\mathrm{kV}$ and $\Delta U_{\mathrm{plate}} = 4\,\mathrm{kV}$ and the tilt angle between $\alpha = 0\,^\circ$ and $\alpha = 14\,^\circ$.

For these measurements, the width of the transmission function of the Mainz spectrometer for an isotropically emitting electron source has been set to $\Delta E = 4.72\,\mathrm{eV}$ (see equation (3.6)). As the electrons emitted with the electron source under investigation have a limited angular spread, the width σ of a transmission function measured for one electron source setting is expected to be much smaller than the total width ΔE. Examples for this are shown in figure 3.6 (theoretical graphics) and in 3.8(b) (measurements with an electron source prototype). The experimental settings are listed in table 3.2.

3.5.2. Measurement overview

θ_{mag} is the angle of the electrons' momentum $\vec{p}$ with respect to the magnetic field $\vec{B}$ at the position of the entrance magnet. It is used to characterize the angular emission properties of the electron source and corresponds to a surplus energy $\delta E = q\delta U$. For different tilt angles α the angular range of θ_{mag} was tested by determining the minimum angle $\theta_{\mathrm{mag}}^{\mathrm{min}}$ and maximum angle $\theta_{\mathrm{mag}}^{\mathrm{max}}$ achieved in the entrance magnet.

functions were not measured with the DMM. Only the applied potential could be noted down. While the DMM was still working, the settings of ΔU_{EHS} agreed with the values read from the DMM to the 20 mV range.

[11] The low intensity could not be improved with a better coupling of the UV light. Therefore, we assume the Ag layer was not homogeneous, but its thickness varied. A thicker layer would lead to a decrease in transmittance for electrons from this fiber and thus resulting in less photoelectrons. A thin layer would be passed by many photons without interactions and thus also result in lower photoelectron intensity.

Table 3.2.: Experimental parameters

parameter	value
U_{egun}	-15 kV
ΔU_{plate}	1 kV - 4 kV
α	0 ° - 14 °
fiber 2	0.9 mm
B_{max}	6.014 T
B_{min}	18.94 G
$\Delta E(15\,\text{keV})$	4.72 eV

Transmission functions were measured for several sets of parameters α and ΔU_{plate}.

Procedure to determine settings for the minimum angle $\theta_{\text{mag}}^{\text{min}}$

Simulations (see figure 3.11) imply that there is a minimum angle $\theta_{\text{mag}}^{\text{min}}$ for a fixed tilt angle α at a certain potential difference, which we then call $\Delta U_{\text{plate}}^{\text{min}}$. Changes in the applied potential difference around $\Delta U_{\text{plate}}^{\text{min}}$ result in an increase in θ_{mag} and thus the transmission function for this setting can be found at higher values of $\delta U = U_{\text{ana}} - U_{\text{egun}}$ (see equation (3.8)).

The minimum angle $\theta_{\text{mag}}^{\text{min}}(\Delta U_{\text{plate}}^{\text{min}})$ can now be determined by fixing δU to values close to the expected minimum and measuring the rate for varying acceleration potential differences ΔU_{plate}. As the analyzing potential U_{ana} and the starting energy E_{kin} are constant, the changes seen in the rate can be directly attributed to changes in the adjusted electron source angle θ_{mag}. Assuming a constant emission intensity, the transmitted rate should increase if the set angle θ_{mag} is lower. Thus a peak in the measurement denotes the value of ΔU_{plate} for which the smallest angle $\theta_{\text{mag}}^{\text{min}}(\Delta U_{\text{plate}})$ is achieved.

The position $\delta U(\Delta U_{\text{plate}})$ of the transmission function yielding the smalles value of $\theta_{\text{mag}}^{\text{min}}$ has been determined for the tilt angles $\alpha = 8\,°$ and $\alpha = 12\,°$ and is shown in figure 3.19. They correspond to the angle $\theta_{\text{mag}}^{\text{min}} = 0$.

Procedure to determine settings for the maximum angle $\theta_{\text{mag}}^{\text{max}}$

To experimentally determine the maximum angle $\theta_{\text{mag}}^{\text{max}}$ that can be achieved for a fixed tilt angle α, the spectrometer is set into transmission ($\delta U = 16.4\,\text{V}$ without offset correction, thus about 30 V above the positions of the transmission functions) and the maximum potential difference $\Delta U_{\text{plate}} = 4\,\text{kV}$ is applied to the parallel plates. If an electron rate is measurable, a transmission function can be found for this setting by varying δU. The resulting angle θ_{mag} does probably not or barely correspond to $\theta_{\text{mag}} = 90\,°$. If no rate is measurable, the electrons for this setting are reflected in the magnet ($\theta_{\text{mag}} > 90\,°$). To find a transmission function for which electrons still arrive at the detector, the potential difference ΔU_{plate} is reduced until a setting is found for which electrons can pass again. The angular distribution for electrons emitted for this setting includes some with $\theta_{\text{mag}} = 90\,°$.

In figure 3.20 the maximum applied potential differences ΔU_{plate} are shown with respect to the set tilt angle α. One can see that there is a minimum tilt angle for which the complete range of electron angles $\theta_{\text{mag}} \in [0\,° : 90\,°]$ is producible. It is positioned between

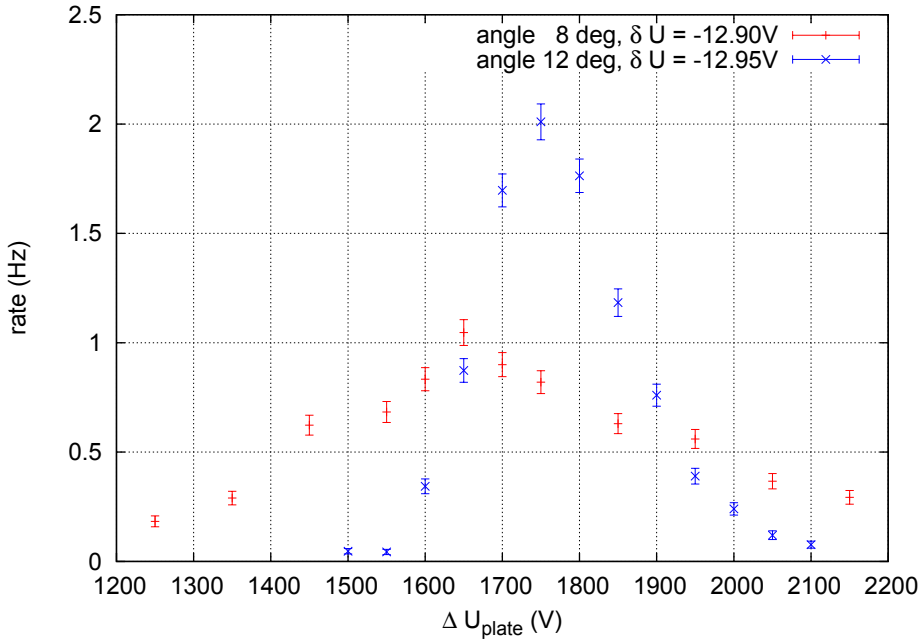

Figure 3.19.: Rate for a fixed setting of tilt angle α and surplus potential of δU. The maximum rate indicates the value $\Delta U_{\text{plate}}^{\text{min}}$ for which the minimum angle $\theta_{\text{mag}}^{\text{max}}$ can be achieved. Note that the surplus potential δU has an offset between $-13.474(\pm 0.009)\,\text{V}$ and $-13.118(\pm 0.008)\,\text{V}$ (see equations (3.14) to (3.16)) which has not been corrected here.

$\alpha = 8\,^\circ$ for which $\theta_{\text{mag}} < 90\,^\circ$ has been achieved with $\Delta U_{\text{plate}} = 4\,\text{kV}$ and $\alpha = 12\,^\circ$ for which the maximum angle $\theta_{\text{mag}} = 90\,^\circ$ is achieved for $\Delta U_{\text{plate}} = 3.5\,\text{kV}$.

Transmission functions

An overview of the parameter combinations of α and ΔU_{plate} covered with these measurements can be found in table 3.3. In figure 3.21 the measurements sorted by day are shown without background correction.

Table 3.3.: Measurement overview: combinations of ΔU_{plate} and α, the numbers 1, 2 and 3 indicate the day of measurement.

ΔU_{plate}	1.0 kV	1.75 kV	2.0 kV	3.0 kV	3.5 kV	4.0 kV
$\alpha = 0\,^\circ$			1			
$\alpha = 4\,^\circ$			2	2		2
$\alpha = 8\,^\circ$	2		2	2		2
$\alpha = 12\,^\circ$		3	3	3	3	
$\alpha = 14\,^\circ$			1		3.4 kV, 1	

On day one a transmission function for $\alpha = 0\,^\circ$ and $\Delta U_{\text{plate}} = 2\,\text{kV}$ has been measured. The angle has been increased to $\alpha = 14\,^\circ$ and a transmission function has been measured for $\Delta U_{\text{plate}} = 2\,\text{kV}$. Then the transmission function for the maximum angle $\theta_{\text{mag}}^{\text{max}}$ has been measured using the procedure stated in the previous section at 3.4 kV.

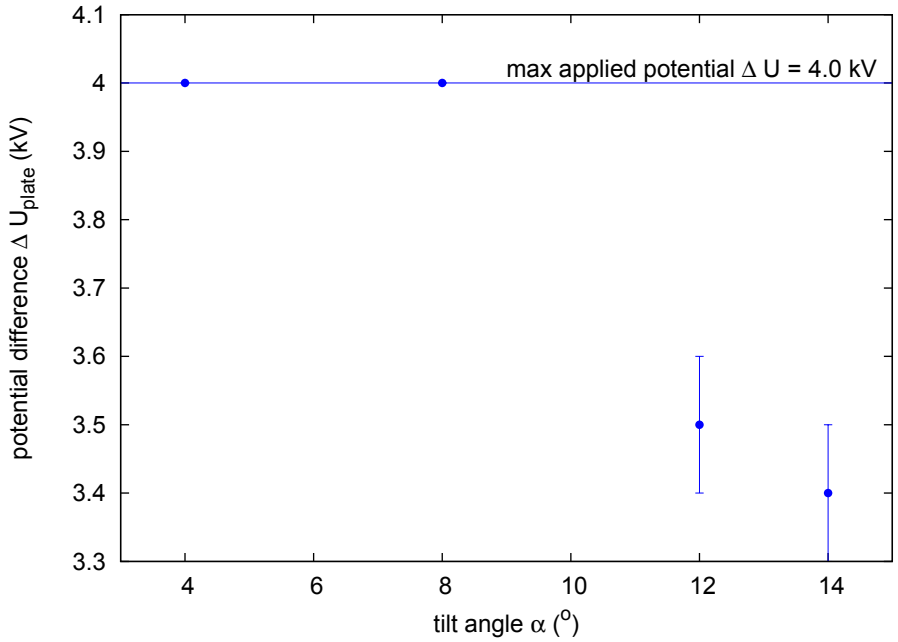

Figure 3.20.: Maximum potential difference ΔU_{plate} for which transmission functions can be measured at different tilt angles α. The line denotes the maximum potential difference ΔU_{plate} applicable to the electron source. For $\alpha = 12\,^\circ$ and $\alpha = 14\,^\circ$ no electrons have been detected above the noted values of ΔU_{plate}.

On the second day the transmission functions have been measured for $\alpha = 4\,^\circ$ and $8\,^\circ$ for the complete range of ΔU_{plate} between 1 kV and 4 kV without detecting a cut-off.

On day three the transmission functions for the tilt angle $\alpha = 12\,^\circ$ have been measured. For this tilt angle a minimal transmission function has been found at $\Delta U_{\text{plate}} = 1.75\,\text{kV}$ and a cut-off for potential differences higher than $\Delta U_{\text{plate}} = 3.5\,\text{kV}$.

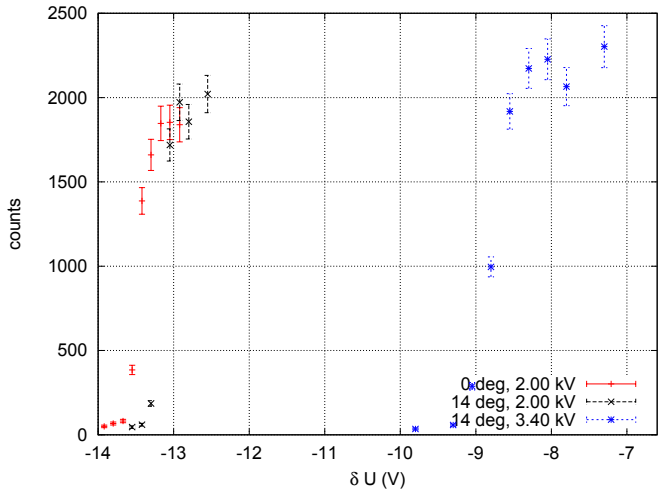

(a) Day one

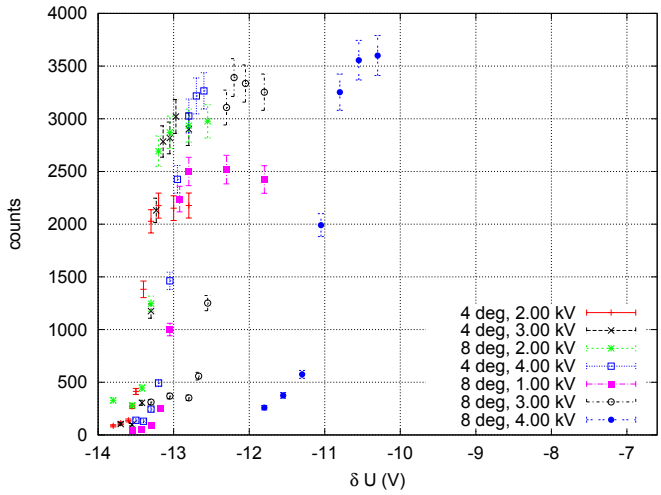

(b) Day two

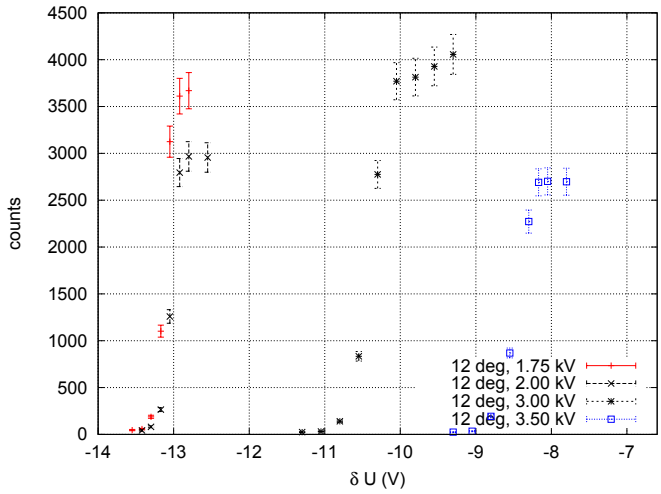

(c) Day three

Figure 3.21.: All transmission functions sorted by the measurement day. Note that δU has an offset between $-13.474(\pm 0.009)\,\mathrm{V}$ and $-13.118(\pm 0.008)\,\mathrm{V}$ (see equations (3.14) to (3.16)).

3.5.3. Problems

Different problems occurred during the measurements that have to be taken into account in the analysis:

HV fluctuations: As already mentioned in section 3.4.3, a residual high frequency fluctuation was measured on the high voltage. The peak-to-peak amplitude has been estimated to be of the order of 100 mV. The fluctuation has to be taken into account while analyzing the transmission functions.

Background problems: On the different measurement days the background level fluctuated by one order of magnitude, on day one and three the level was stable at about 0.1 Hz, but on day two problems persisted with the Penning trap between electron source and spectrometer, causing spikes in the measured rates on the detector. Whenever this occurred, the high voltages of the system had to be lowered to empty the trap. Still the measured background rates were one order of magnitude higher on this day compared to the other days. The charging up of the Penning trap can influence the work function of the photocathode due to ion bombardment. Therefore, the different measurement days have been considered separately for the offset determination (see equations 3.14 to 3.16).

Intensity fluctuations: During the measurements it became visible that the measured rates were not reproducible within the statistical error of the counts N. Several effects have been made out which influence the total intensity. The effects and the measures to account for them in the analysis are listed here:

- The layer thickness of the photocathode varies due to the deposition of further atoms. This leads to a drift in the work function Φ_{Au} due to the attachment of different atoms, which influences the electrons' energies. In addition the intensity of the emitted photoelectron current changes. For layers with a small thickness only few photoelectrons are emitted as the cross section for the reaction is low and many photons just pass through the layer. If the layer thickness is too high, electrons are produced inside the layer, but their emission is suppressed. Depending on the initial thickness one thus expects an increase in intensity until the best layer thickness is achieved, after which the intensity decreases again. During the measurement period described here, the pressure in the source section was about $5 \cdot 10^{-9}$ mbar. The attachment rate of a monolayer is of the order of 10^3 s. The change of the layer thickness is therefore a long term effect that needs to be taken into account if the rates in different measurements will be compared, but does not play a role for a stand alone transmission function.
- In the Penning trap between the electron source and the spectrometer charged ions are produced and are accelerated from the trap towards electrodes on potential. They may hit the photocathode surface resulting in a change in work function.
- The LED has been driven with a pulse generator. Instabilities of the generator would be visible in the intensity. The reproducibility of pulse characteristics has been tested to the per mill level, therefore this effect can be neglected.
- The warm-up behavior of the LED in its electrical circuit is not known. Rates measured at the end of a day and at the beginning of the next day with the same

setting showed a variation of about 20 %. Therefore, the absolute intensities cannot be compared.

- Changes of the coupling of the LED light into the optical fibers strongly influence the intensity. Although the LEDs have been fixed mechanically, slight changes of the positioning were possible during the measurement time due to mechanical vibrations of the setup induced by the pumps or due to accidental contact with the LED cables while turning the function generator on or off.
- The company delivering the LEDs stated that their lifetime is greatly reduced, if the LEDs are not stored under atmosphere [Seo08]. As the change in intensity is even higher if the coupling of the LEDs is changed, their positioning was fixed and they were left in the normal environment for the measurement time. Therefore, a change in intensity is expected due to degradation.
- The short term stability of the LEDs is not known.

Several of these problems can be be avoided or improvements are accessible for future measurements. For the analysis of the measurements presented here, the following approach has been chosen to take them into account:

- The fitted widths of the transmission functions have to be corrected for the HV fluctuation before they are used for further analysis.
- The absolute intensities cannot be compared. Instead only relative intensities are used. The transmission functions are normalized to their amplitude.
- Each day is analyzed separately for the offset of the potential scale to take into account the work function changes.
- An additional relative error of 5 % has been introduced to account for the short-term intensity variations of the LED.

3.6. Analysis and results

3.6.1. Transmission function fits

The transmission function for a MAC-E filter has been discussed in sections 2.2 and 3.1. In this section the expected contributions to the transmission functions and their expected shape will be studied before the fits are presented.

With the previously mentioned settings of the Mainz spectrometer the expected transmission function for an isotropic source has been calculated and is shown in figure 3.22. An ideal electron source emits electrons with a well defined angular emission and fixed energy. The expected transmission functions for $\theta_{\mathrm{mag}} = 0\,^\circ$ and for $\theta_{\mathrm{mag}} = 90\,^\circ$ are indicated in red and blue respectively in the same plot.

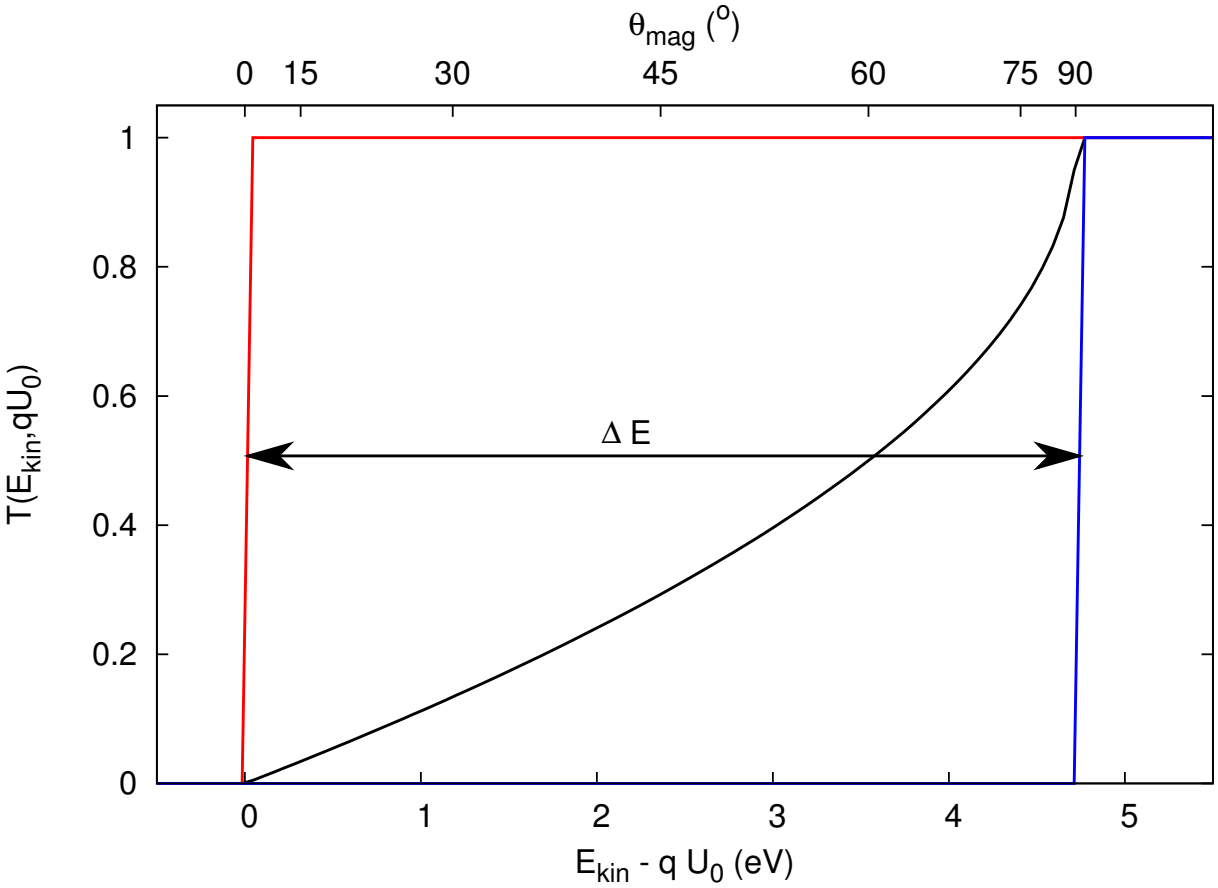

Figure 3.22.: Expected transmission functions for the settings of the Mainz spectrometer. The black line denotes the transmission function for a mono energetic, isotropic source. The red line is is the transmission function measured for a mono energetic electron source emitting electrons with $\theta_{\mathrm{mag}} = 0\,^\circ$ and the blue for electrons with $\theta_{\mathrm{mag}} = 90\,^\circ$.

Three different cases and their influence on the transmission function of an electron source with a sharp angle are discussed below:

- **HV fluctuations:**
  If a high frequency fluctuation with a mean deviation of σ_{HV} is present on the potential applied to the setup, the shape of the transmission functions will be smeared

out. The influence of this effect on the widths of the transmission functions should be the same regardless of the surplus energy δU and thus the angle θ_{mag}. Starting from an electron source emitting mono energetic electrons with well defined angles, the distance between the centers of the transmission functions measured for $\theta_{\mathrm{mag}} = 0\,^\circ$ and for $\theta_{\mathrm{mag}} = 90\,^\circ$ should cover the energy resolution ΔE, although the shape varies (see figure 3.23).

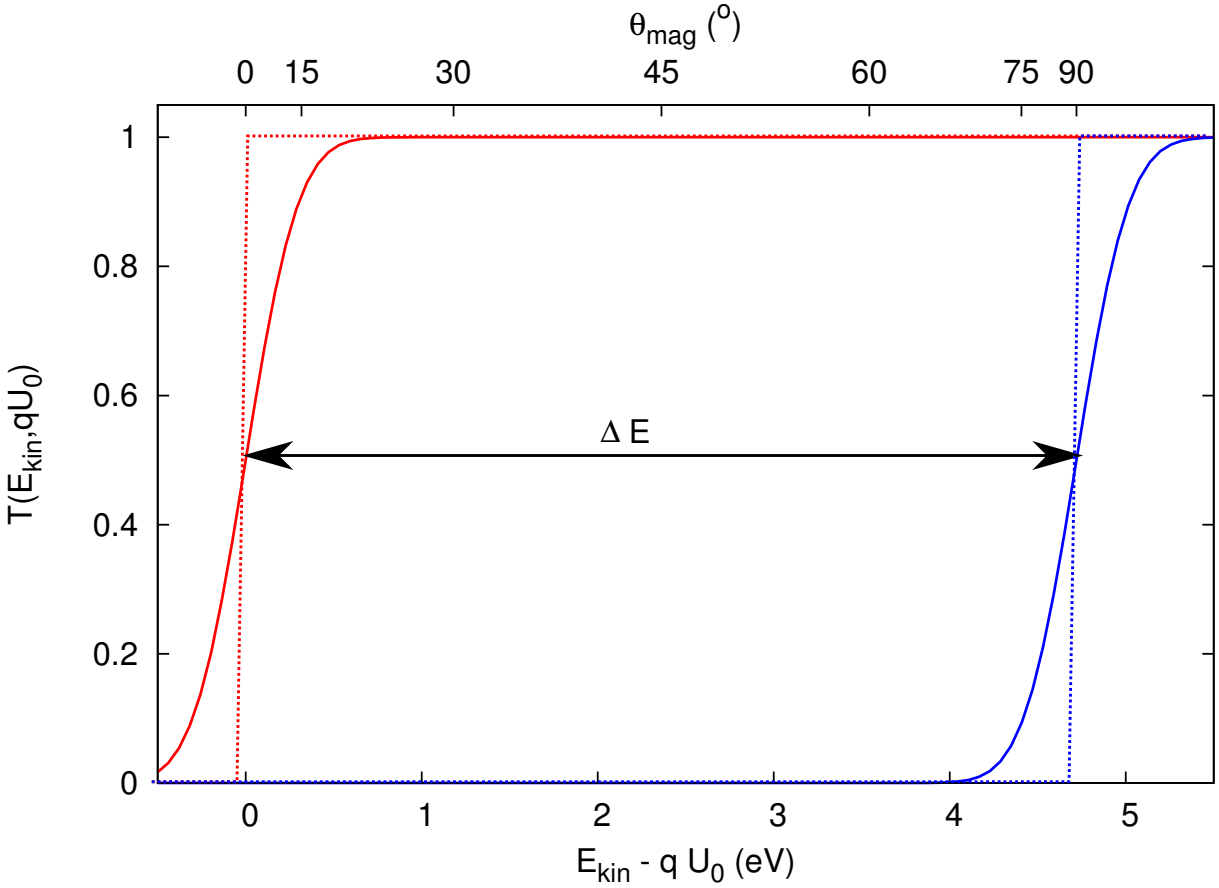

Figure 3.23.: Expected transmission functions for a setup with HV fluctuations measuring a mono energetic electron source emitting electrons with $\theta_{\mathrm{mag}} = 0\,^\circ$ (red) and with $\theta_{\mathrm{mag}} = 90\,^\circ$ (blue). The dashed lines denote the ideal transmission function of this source without fluctuations. The effect of HV fluctuations is not distinguishable from the effect arising from a spread on the electrons' energy.

- **Energy spread for electrons with defined angle θ_{mag}:**
  If the electron source produces electrons with well defined angles θ_{mag} and a Gaussian energy distribution, the transmission functions correspond to error functions (see figure 3.6). If the energy width is fixed, all transmission functions are broadened with the same factor. Their centers remain fixed and cover the energy resolution ΔE. The influence of a Gaussian energy spread is not distinguishable from a Gaussian fluctuation on the HV.
- **Angular spread for mono energetic electrons:**
  If the emitted mono energetic electrons have an angular spread, the transmission functions will change differently depending on the absolute angle (see figure 3.24). The transmission functions are cut off at the angles $\theta_{\mathrm{mag}} = 0\,^\circ$ and $\theta_{\mathrm{mag}} = 90\,^\circ$.

The produced angles are not any more correlated to the centers of the measured transmission functions. Instead the whole range of the transmission functions has to be considered: The minimal onset of the transmission functions at the low angle side corresponds to $\theta_{\mathrm{mag}} = 0\,°$, the end of the transmission functions at the high angle side of the spectrum to $\theta_{\mathrm{mag}} = 90\,°$. As the angular distributions are cut off, it is possible that the transmission functions measured close to the cutoff show much smaller width than the ones measured further away from the cutoff.

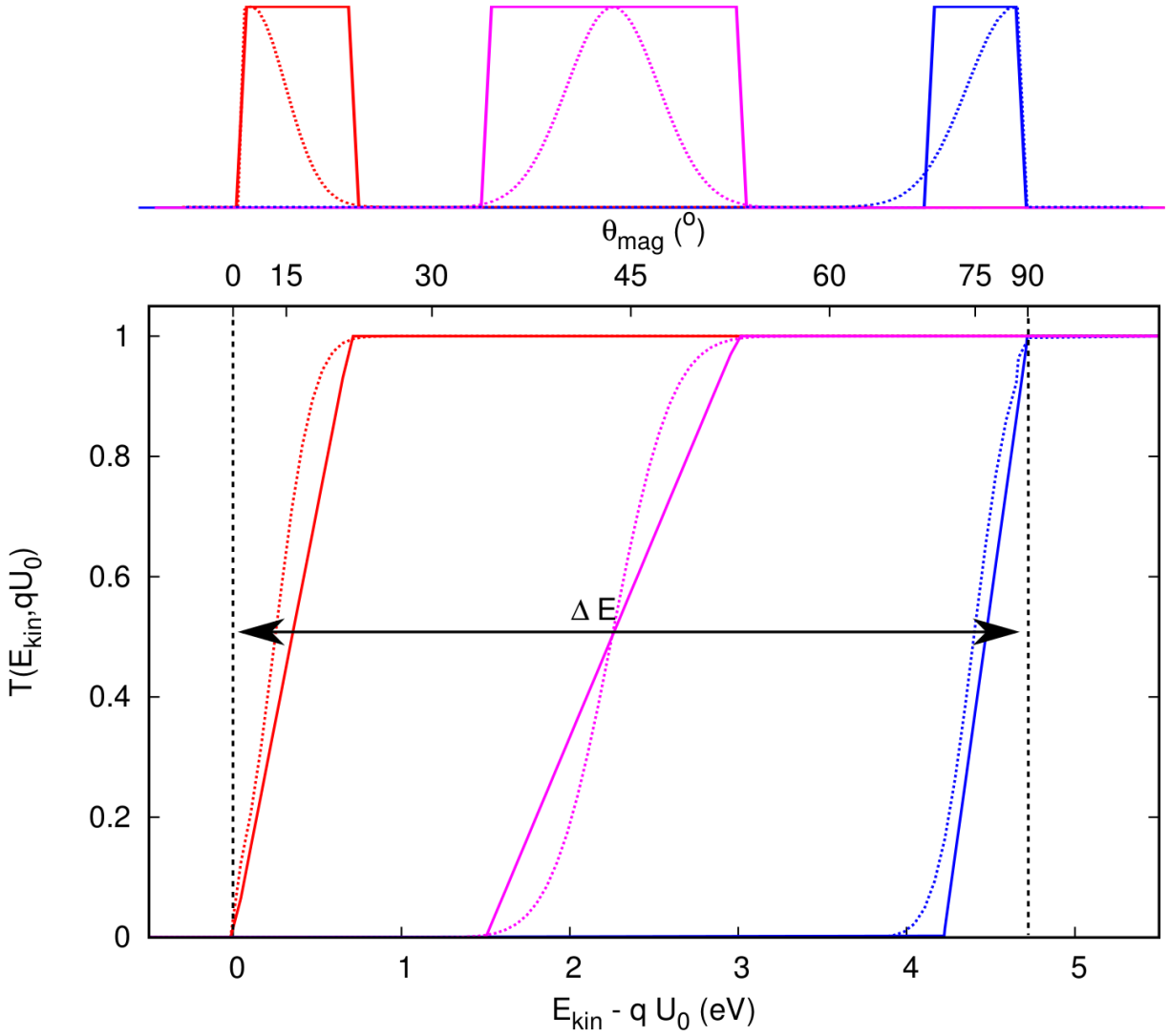

Figure 3.24.: Expected transmission functions for a mono energetic electron source emitting electrons with two kinds of angular spread (dotted lines: Gaussian, rectangular). At the borders of $\theta_{\mathrm{mag}} = 0\,°$ and $\theta_{\mathrm{mag}} = 90\,°$ the transmission function is cut off.

As stated in section 3.3.2 and 3.5.3, we expect all three changes to the ideal transmission function to be visible in our measurements.

Assuming Gaussian distributions for the HV fluctuation, the initial energy distribution and the angular spread, the measured curves should be an integration of the product of these three curves with the transmission condition (see section 3.1), that is, an error

function. Error functions of the form

$$f(\delta U) = d + c\left[1 + \mathrm{erf}\left(\frac{(\delta U - \delta U_0)}{\sqrt{2}\sigma}\right)\right] \tag{3.10}$$

have been fitted to the data with δU_0 denoting the center of the function[12], σ being the total Gaussian width, $2 \cdot c$ the total amplitude and d the constant background. The error function is defined as

$$\mathrm{erf}(x) = \frac{2}{\sqrt{\pi}} \int_0^x e^{-t^2} dt. \tag{3.11}$$

Example fits are shown together with their residuals in figure 3.25. All data sets with fits and their residuals can be found in the appendix, section A.1.

No structure is visible in the χ_r^2 distribution and the χ_r^2 scatter around one with the exception of one measurements taken during a noisy period ($\alpha = 8\,^\circ$ and $\Delta U_{\mathrm{plate}} = 4\,\mathrm{kV}$, the measurement had to be stopped in between due to background reasons). Thus we can assume that an error function describes the data reasonably well. The fit values of δU_0 and σ can be found in table 3.4, the χ_r^2 values in table A.1.

Still it was chosen to investigate whether the integration of the product of a rectangular angular distribution and the error function arising from HV fluctuations and energy spread would describe the data better. This approach has the advantage that the width of the angular distribution w_θ is included as additional fit parameter and can thus be extracted directly. The fit function has been defined as a discrete f. The fit itself yields χ^2 values that change only marginally in comparison the error function fit as the functions strongly resemble. Due to the decrease of the degrees of freedom, the χ_r^2 values for these fits are worse. The fit itself is problematic as the two implemented widths, w_θ for the width of the rectangular distribution and $\sigma = \sqrt{\sigma_{\mathrm{HV}}^2 + \sigma_E^2}$ as width of the error function, are directly correlated. Therefore, it was decided to stick to the error function fits.

[12]The center position δU_0 corresponds to an angle θ_{mag}, which does not lie in the center of the angular distribution as they are correlated via equation (2.15).

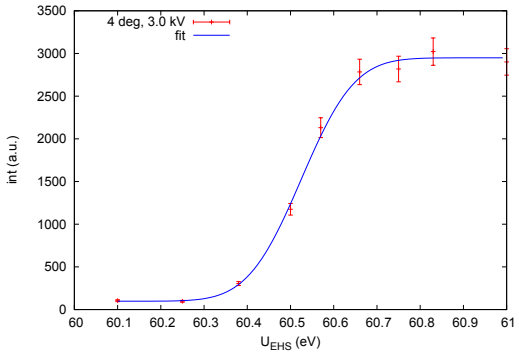

(a) fit: $\alpha = 4\,°$, $\Delta U_{\text{plate}} = 3.0\ kV$, $\chi_r^2 = 0.7$

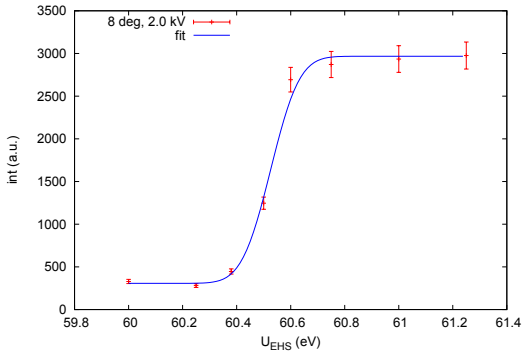

(b) fit: $\alpha = 8\,°$, $\Delta U_{\text{plate}} = 2.0\ kV$, $\chi_r^2 = 1.8$

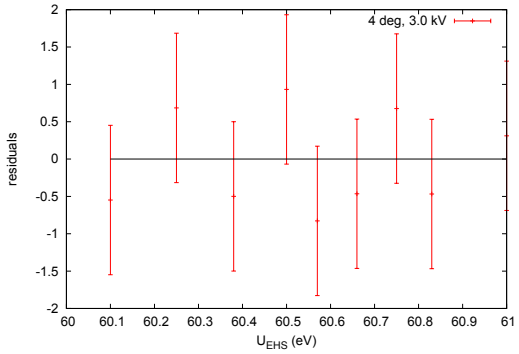

(c) residuals: $\alpha = 4\,°$, $\Delta U_{\text{plate}} = 3.0\ kV$, $\chi_r^2 = 0.7$

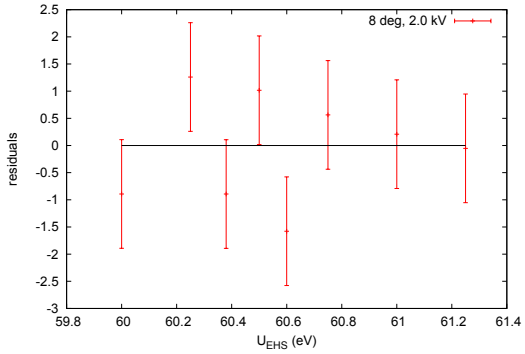

(d) res: $\alpha = 8\,°$, $\Delta U_{\text{plate}} = 2.0\ kV$, $\chi_r^2 = 1.8$

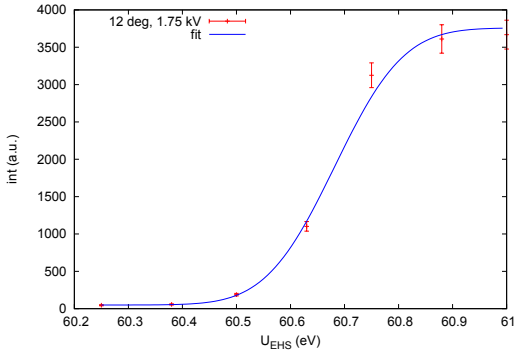

(e) fit: $\alpha = 12\,°$, $\Delta U_{\text{plate}} = 1.75\ kV$, $\chi_r = 1.7$

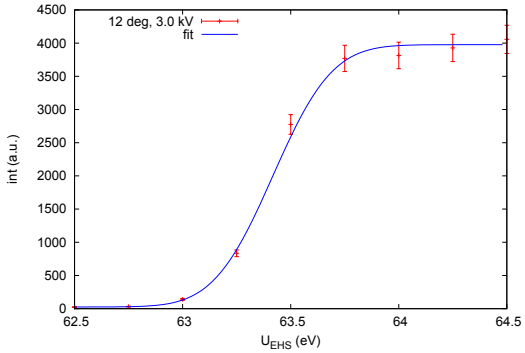

(f) fit: $\alpha = 12\,°$, $\Delta U_{\text{plate}} = 3.0\ kV$, $\chi_r = 0.9$

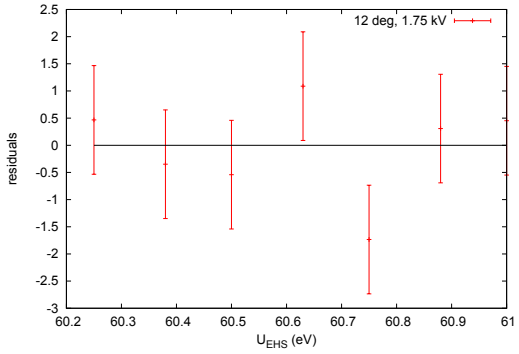

(g) res: $\alpha = 12\,°$, $\Delta U_{\text{plate}} = 1.75\ kV$, $\chi_r = 1.7$

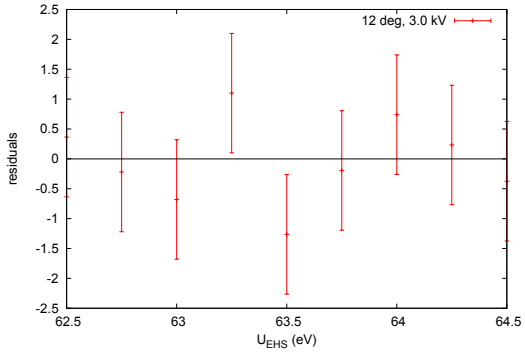

(h) residuals: $\alpha = 12\,°$, $\Delta U_{\text{plate}} = 3.0\ kV$, $\chi_r = 0.9$

Figure 3.25.: Example for error function fits for $\alpha = 4\,°$, $\Delta U_{\text{plate}} = 3.0\,\text{kV}$, $\chi_r^2 = 0.7$, for $\alpha = 8\,°$, $\Delta U_{\text{plate}} = 2.0\,\text{kV}$, $\chi_r^2 = 1.8$, for $\alpha = 12\,°$, $\Delta U_{\text{plate}} = 3.0\,\text{kV}$, $\chi_r = 0.9$ and for $\alpha = 12\,°$, $\Delta U_{\text{plate}} = 1.75\,\text{kV}$, $\chi_r = 1.7$. The fit parameters δU_0 and σ are listed in table 3.4.

3.6.2. The angular emission of the electron source

The analysis was now conducted with the fit parameter extracted from the error function fit. The total Gaussian width σ of the error function is composed of the contributing width:

$$\sigma^2 = \sigma_{\mathrm{HV}}^2 + \sigma_E^2 + \sigma_\theta^2, \tag{3.12}$$

with σ_{HV} stemming from the high frequency HV fluctuations, σ_E from the energy distribution and σ_θ from the angular distribution. The total intensity as well as the background level varied strongly over the days and can therefore not be compared. Plots of the fitted data, normalized to one at full transmission with the background subtracted are shown in figure 3.26.

Table 3.4.: Transmission function parameters for stand alone fits.

α (°)	$\Delta U_{\mathrm{plate}}(kV)$	δU_0 (V)	σ (V)	χ_r^2
0	2	-13.474 ± 0.008	0.087 ± 0.008	0.9
4	2	-13.417 ± 0.007	0.091 ± 0.006	1.9
4	3	-13.275 ± 0.007	0.097 ± 0.006	0.7
4	4	-13.027 ± 0.010	0.147 ± 0.009	0.7
8	1	-13.020 ± 0.008	0.110 ± 0.007	1.8
8	2	-13.274 ± 0.007	0.084 ± 0.008	1.8
8	3	-12.486 ± 0.014	0.126 ± 0.013	0.6
8	4	-11.052 ± 0.019	0.186 ± 0.017	3.3
12	1.75	-13.118 ± 0.008	0.100 ± 0.006	1.7
12	2	-13.030 ± 0.008	0.091 ± 0.006	0.5
12	3	-10.382 ± 0.014	0.216 ± 0.011	0.8
12	3.5	-8.449 ± 0.017	0.221 ± 0.012	1.3
14	2	-13.160 ± 0.015	0.097 ± 0.010	0.6
14	3.4	-8.775 ± 0.016	0.229 ± 0.014	0.6

The influence of HV fluctuations and of the energy distribution should be the same for all curves. Therefore, the minimal width $\sigma_{\mathrm{min}} = \sigma_{\mathrm{HV}+E} = \sqrt{\sigma_{\mathrm{HV}}^2 + \sigma_E^2} = 0.084 \pm 0.008\,\mathrm{V}$ measured for the electron source settings of $\alpha = 8\,^\circ$ and $\Delta U_{\mathrm{plate}} = 2\,\mathrm{kV}$ is an upper limit for the contribution of these effects.

The expected angular width σ_θ of transmission functions measured for $\theta_{\mathrm{mag}} = 0\,^\circ$ is according to simulations zero. Thus only $\sigma_{\mathrm{HV}+E}$ should contribute to the width of transmission functions close to the minimum angle $\theta_{\mathrm{mag}}^{\mathrm{min}}$. The width σ for transmission functions with $\theta_{\mathrm{mag}} \approx 0\,^\circ$ agree with each other within their errors, supporting this claim.

The fluctuation of the HV has been measured with an oscilloscope to have a maximum amplitude of about 100 mV peak-to-peak. The Gaussian width σ_{HV} is lower, but cannot be extracted anymore.

To determine the offset of the measurements, each day has been considered separately. The corrected position δU_{corr} is then calculated by

$$\delta U_{\mathrm{corr}} = \delta U + U_{\mathrm{off}}^i \tag{3.13}$$

with $i \in 1, 2, 3$ denoting the measurement day. The offset corresponds to the lowest U_0 for each day for which $\theta_{\text{mag}} = 0\,^\circ$ and are:

$$U_{\text{off}}^1 = -13.474(\pm 0.009)\,\text{V}, \tag{3.14}$$
$$U_{\text{off}}^2 = -13.417(\pm 0.008)\,\text{V and} \tag{3.15}$$
$$U_{\text{off}}^3 = -13.118(\pm 0.008)\,\text{V}. \tag{3.16}$$

The minimum angular width σ_θ can be extracted using equation (3.12). The offset corrected positions δU_{corr} and the angular widths $\sigma_\theta = \sqrt{\sigma^2 - \sigma_{\text{HV}+E}^2}$ are listed in table 3.5. Figure 3.26 shows the offset corrected transmission functions sorted by day and tilt angle α with the background subtracted (starting at 0 intensity) and the function at full transmission normalized to one.

Table 3.5.: Transmission function parameters after offset correction and correction for the fluctuations $\sigma_{\text{HV}+E} = 0.084 \pm 0.008\,\text{V}$.

α (°)	ΔU_{plate}(V)	$\delta U_{0,\text{corr}}$ (V)	σ_θ (V)
0	2	0.000 ± 0.012	0.022 ± 0.044
4	2	0.000 ± 0.010	0.034 ± 0.025
4	3	0.141 ± 0.010	0.049 ± 0.018
4	4	0.390 ± 0.013	0.120 ± 0.012
8	1	0.397 ± 0.011	0.071 ± 0.015
8	2	0.142 ± 0.010	0.000 ± 0.000
8	3	0.930 ± 0.016	0.094 ± 0.019
8	4	2.365 ± 0.020	0.166 ± 0.020
12	2	0.088 ± 0.011	0.035 ± 0.025
12	1.75	0.000 ± 0.011	0.055 ± 0.016
12	3	2.736 ± 0.016	0.199 ± 0.012
12	3.5	4.669 ± 0.019	0.204 ± 0.014
14	2	0.314 ± 0.017	0.047 ± 0.025
14	3.4	4.699 ± 0.018	0.213 ± 0.015

The centers of the transmission functions cover the range $\delta U_{0,\text{corr}} \in [0\,\text{V} : 4.699\,\text{V}]$ and thus $\theta_{\text{mag}} \in [0\,^\circ : 86\,^\circ]$. If the angular spread is taken into account by adding σ_θ, a range $q \cdot \Delta\delta U = 4.91\,\text{eV}$ larger than the resolution of the spectrometer with $\Delta E = 4.72\,\text{eV}$ is covered. As several parameters are only approximately implemented in this analysis, this is to be expected. It is for example not possible for us to consider any correlation between an initial energy spread of the source and the angular distribution. But due to the working principle of our source, an effect like this has to be expected: The photons emitted from the UV LED have an initial energy spread and the work function also has some broadening as due to temperature fluctuations, therefore the electrons are ejected from levels around the Fermi energy and the energy distribution of the electrons emitted via photoelectric effect is not mono-energetic. The width of the distribution is expected to be smaller than 1 eV, [Val09b] gives indications of $\sigma_E \approx 0.2\,\text{eV}$ for a stainless steel photocathode. The angle θ_{mag} reached in the magnet depends on the early acceleration process and starting angle with respect to the magnetic field as well as on the primary photo electron energy. Already a small momentum vector $\vec{p}$ changes here the energy

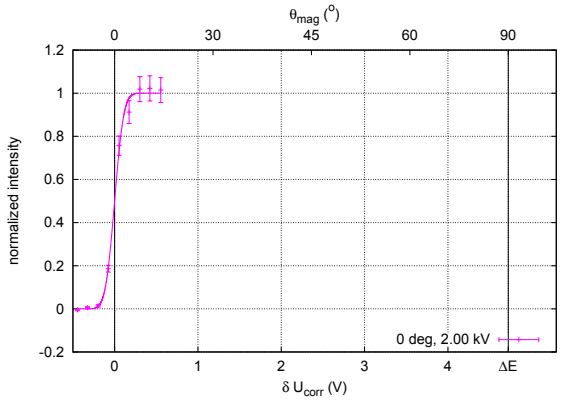

(a) 0 °, day one.

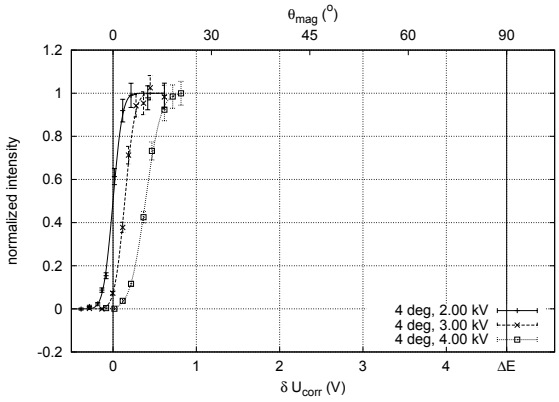

(b) 4 °, day two.

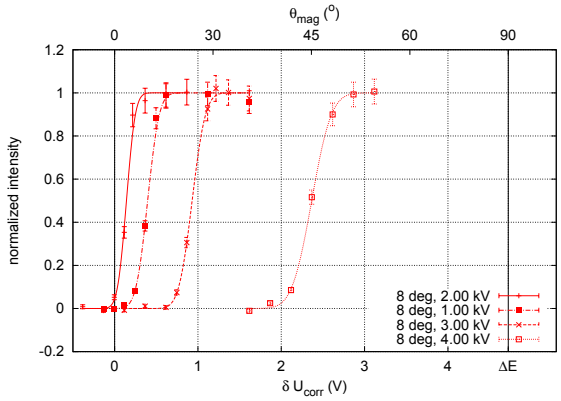

(c) 8 °, day two.

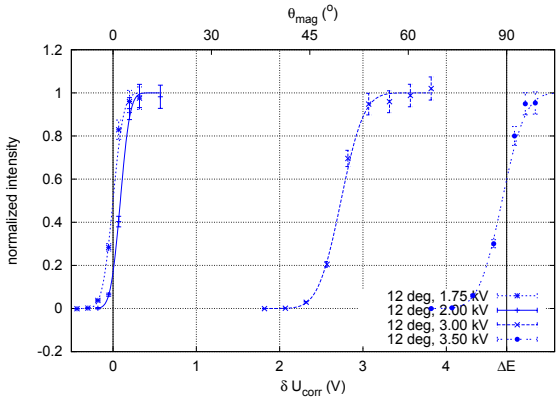

(d) 12 °, day three.

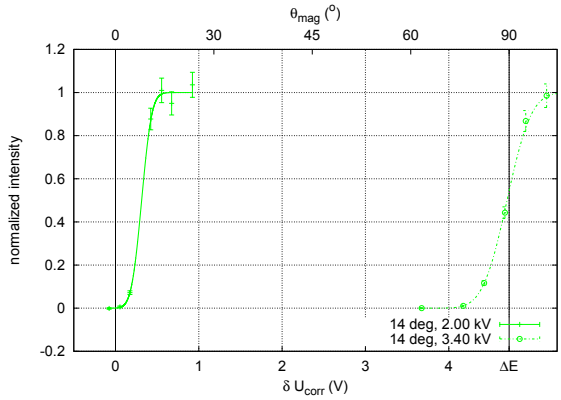

(e) 14 °, day one.

Figure 3.26.: All transmission functions, background subtracted and normalized to one using the parameters extracted from the fit functions, sorted by the electron source tilt angle α and measurement day. The upper scale denotes the angle θ_{mag} reached in the magnet.

distribution and thus the ultimate angle θ_{mag}. Thus we have to assume some correlation between the energy E_{kin} and the angle θ_{mag}.

The relation between the angle in the magnet θ_{mag} and the electron source parameters tilt angle α and potential difference $\Delta U_{\mathrm{plate}}$ is visible in figure 3.27. The errorbars denote the angular emission width σ_θ for the setting. The lines denote the results of the design

simulations for the electron source as already shown in figure 3.11.

The basic shape of the curves is similar for simulation and measurement. The minimum of the angle θ_{mag} is shifted towards higher values of $\Delta U_{\mathrm{plate}}$ for the measurements. Using electrons with a finite starting energy $E_{\mathrm{kin}} \neq 0\,\mathrm{eV}$ leads to a shift in this position. This effect will be investigated in detail in [Zac13].

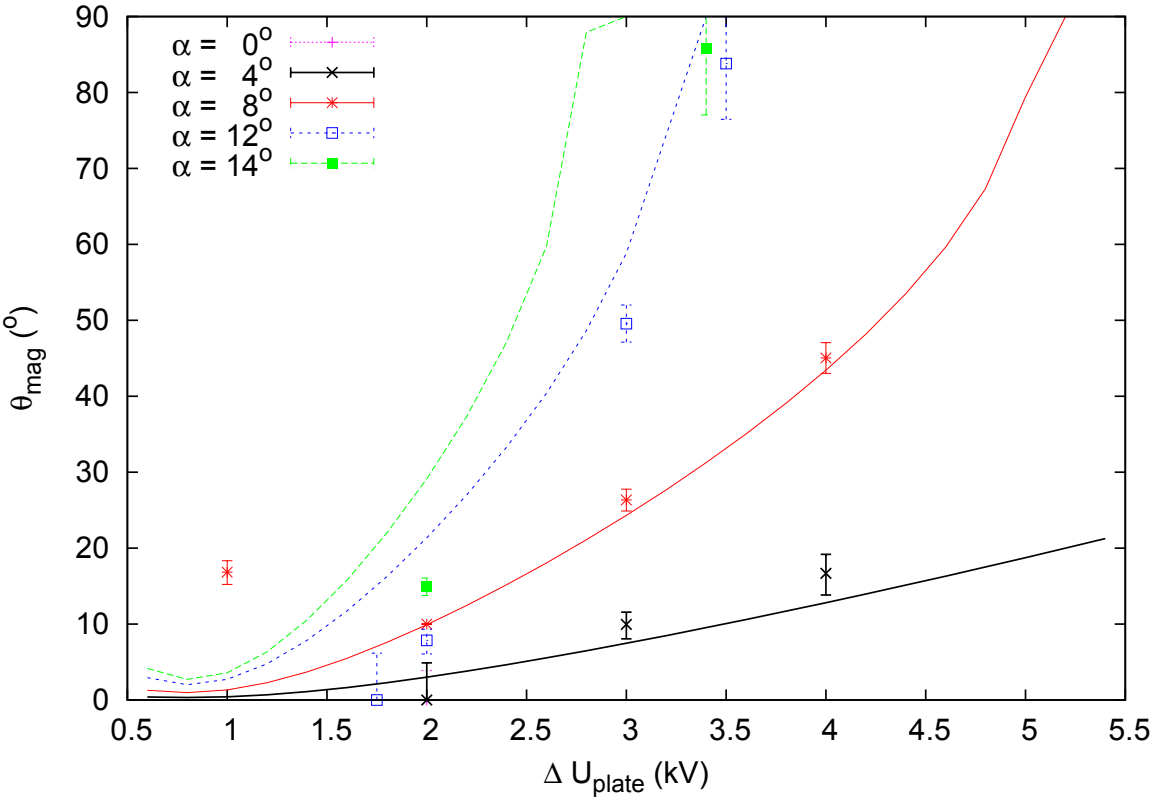

Figure 3.27.: Dependency of the angle in the magnet θ_{mag} on the parameter and $\Delta U_{\mathrm{plate}}$ of the electron source for different tilt angles α. The lines show the results of the design simulations for the electron source, the data points are the measured values.

In figure 3.28 the correlation between the angular width σ_θ and the angle θ_{mag}, calculated from the position of the transmission function, is shown. The angular spread is larger than estimated in the simulations. In this analysis it is between 2 ° to 8 ° for low angles, but increases to $\sigma_\theta \approx 13\,^\circ$ for angles close to 90 °. An increase of the angular spread was also seen in the simulations. It can be attributed to the path of these electrons through the aperture: Due to the large acceleration potential difference $\Delta U_{\mathrm{plate}}$, the field depression at the aperture is larger. As the tilt angle α is high, the electrons pass close to the edges through the aperture, where they see stray fields which cause acceleration or retardation and thus a spread in the absolute angular distribution. To avoid these effects, the next stage electron source has a larger aperture diameter [Zac13].

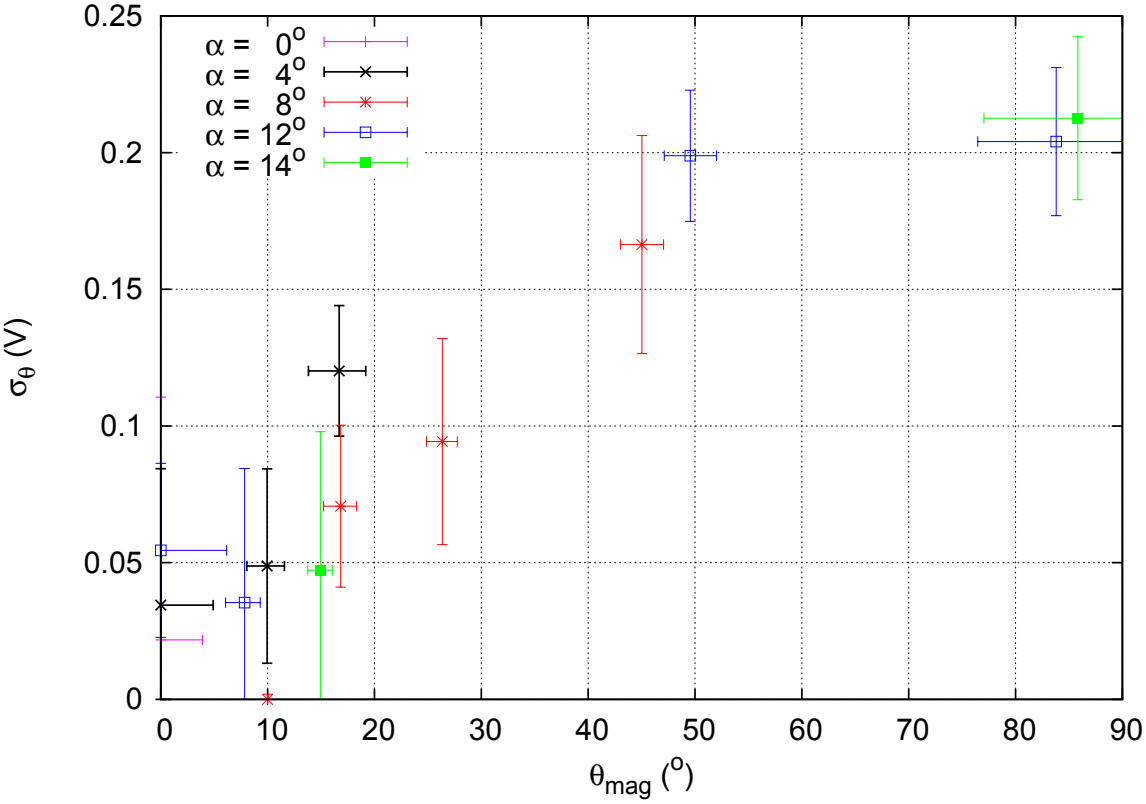

(a) Width σ_θ (V).

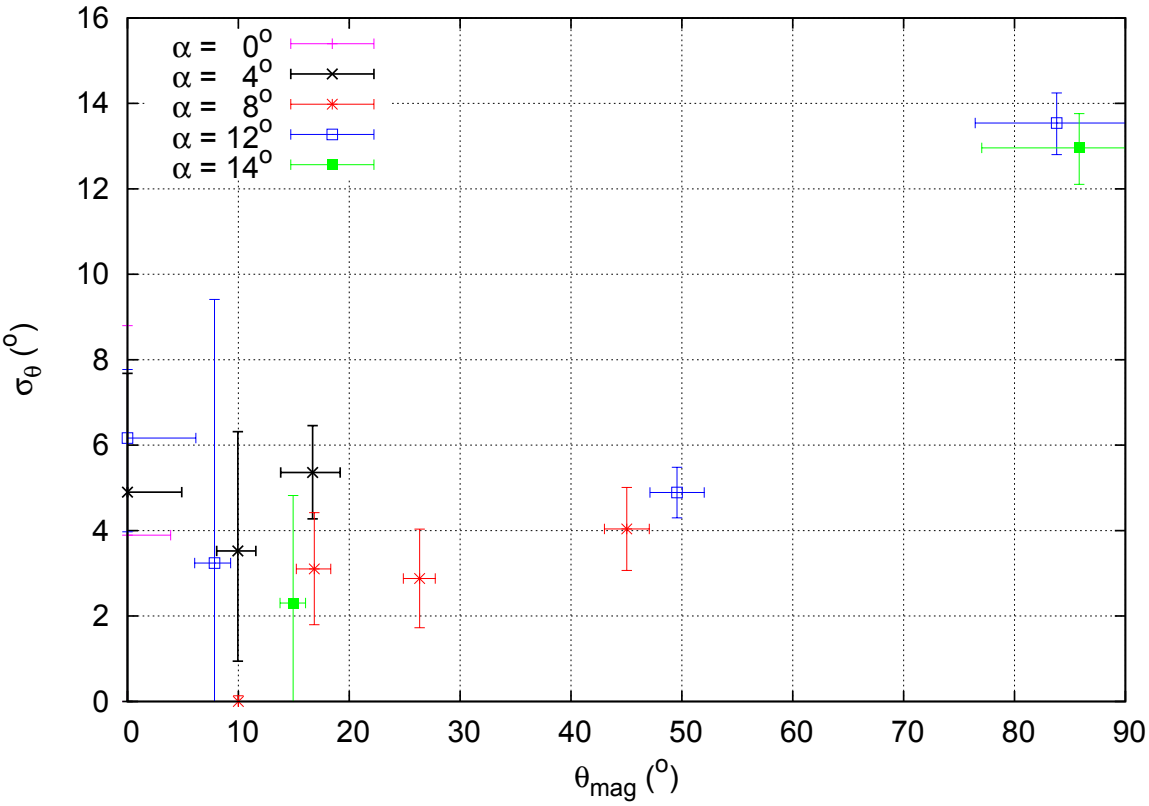

(b) Width σ_θ (°).

Figure 3.28.: Dependency of the width σ_θ of the angular emission on the angle θ_{mag}.

3.7. Conclusion and outlook

In this chapter the idea of an angular-selective electron source was presented. The working principle and thus the angular selectivity has been validated with measurements.

The concept of this electron source has been investigated with detailed design simulations using some assumptions to simplify the problem and reduce simulation times. The simulations for an ideal setup with an electron emission diameter of $\varnothing_{\text{fiber}} = 25\,\mu\text{m}$ promised an angular spread of $\Delta\theta_{\text{mag}} \approx \pm 0.35\,^\circ$ for $\theta_{\text{mag}} = 60\,^\circ$ and of $\Delta\theta_{\text{mag}} < \pm 4\,^\circ$ for $\theta_{\text{mag}} \approx 90\,^\circ$. Furthermore, the simulations predict that for angles $\alpha \leq 8\,^\circ$ and applied potentials $\Delta U_{\text{plate}} \leq 4\,\text{kV}$ the angle $\theta_{\text{mag}} = 90\,^\circ$ is not reached.

An electron source using the proposed principle has been constructed for test measurements and was implemented at the Mainz spectrometer. Measurements with this electron source have shown that the complete angular range of $\theta_{\text{mag}} \in [0\,^\circ : 90\,^\circ]$ is accessible by changing the two parameters of the electron source, the tilt angle α and the potential difference ΔU_{plate}. For certain parameter values it is even possible to fix one of the parameters and access the whole angular range through the other, see *e.g.* the measurements for $\alpha = 12\,^\circ$.

The dependency of the achieved angle θ_{mag} on the electron source parameters α and ΔU_{plate} has a similar shape in simulations and measurement. The position of ΔU_{plate} for the minimum angle $\theta_{\text{mag}}^{\text{min}}$ is shifted. First simulations investigating this effect attribute this difference to the missing starting energy in the simulations.

With $\sigma_\theta \in [2\,^\circ : 6\,^\circ]$ for the small angles and $\sigma_\theta \approx 13\,^\circ$ for angles θ_{mag} close to $90\,^\circ$, the Gaussian angular spread is larger than anticipated in the simulations. This has been attributed to an unknown starting energy distribution and details of the electro-magnetic setup not implemented in the simulations.

Although the analysis used for these measurements does not take any correlations between the energy spread σ_E and the angular spread σ_θ into account, the results show a consistent picture that can already be explained qualitatively. In order to investigate the energy spread of the electron source without being limited by its angular spread, measurements with a transmission function setting with very narrow width and ultra stable HV have been proposed. Any deviations from the ideal shape of the transmission function can then be attributed to the energy spread and can be used as input for further measurements and analysis.

These measurements serve as a proof-of-principle for the electron source design and will be published in [Bec13]. They have demonstrated the validity of the working principle and pointed out problematic components of the setup. In a next step, which is currently ongoing, several improvements are investigated [Win13, Zac13]. The improved design includes a laser setup and an improved preparation of the Ag layer to reduce the energy spread of the emitted electrons. The parallel plate setup is situated inside a ground field cage which is rotated together with the plates so that the electric field configuration is conserved. The electron source will be placed on a manipulator so that different positions on the flux tube can be accessed. As the magnetic field lines bend with increasing distance to the symmetry axis, the exact positioning of the electron source relative to the magnetic field lines has to be tracked. The electron source position is adjusted with motors and the exact positioning is read out with encoders. To improve the understanding of the measurements, simulations have been started with the simulation package KASSIOPEIA.

They are conducted with nearly realistic geometries.

The angular-selective electron source is an essential tool for the characterization measurements of the main spectrometer that are just now in preparation.

Investigation of the reflection properties of PTFE for Vacuum-UV light

4. The XENON experiment

The liquid noble gas experiment XENON100 aims to detect the recoil energy produced in a scattering of a WIMP from a nucleus. With an exposure of 224.6 livedays $\times$ 34 kg the XENON collaboration could establish an exclusion curve with minimum at $2 \cdot 10^{-45}\,\mathrm{cm}^2$ for masses of $55\,\mathrm{GeV/c}^2$ at 90 % confidence level [Apr12b].

In section 4.1 the experimental concept used for the XENON detector is presented. The setup of the XENON100 experiment is shown in section 4.2 and the results obtained with the detector up to date are explained in section 4.3. With a short presentation of the XENON1t experiment an outlook into the next stage of the XENON experiment is given in section 4.4.

4.1. Experimental concept

As the expected nuclear recoil rates are very low, the experiments are optimized to enhance the rate and suppress background reactions at the same time. The XENON collaboration uses liquid Xenon as target material for several reasons:

- With a high mass number of $A \sim 131$ the signal rate for spin independent interaction is enhanced at low threshold.
- Natural Xenon is composed by about the same number of odd and even isotopes. This allows to also set limits for spin-dependent WIMP interactions.
- The high atomic number $Z = 54$ enables self shielding.
- As impurities constantly emanate from the detector materials, continuous cleaning is inevitable to maintain a sub-ppm purity level. For noble gases the cleaning can be conducted with commercial getters.
- Xenon only has ^{136}Xe as long-living radioactive isotope. The double β-decay has a half-live of $2 \cdot 10^{21}$ y and is up to now a minor background process.
- Xenon is extracted from the air by means of distillation. Natural Krypton is still in the Xenon in concentrations of ppb. Therefore, the radioactive isotope ^{85}Kr contributes to the intrinsic background. Distillation columns have been designed remove Krypton to the ppt level, the column for XENON1twill be described in [Ros14].
- Xenon is an efficient scintillator producing $\sim 45 \cdot 10^3\,\gamma\mathrm{s/MeV}$ for relativistic electrons.
- As the scintillation light of $\lambda = 178\,\mathrm{nm}$ is emitted from an excited molecular state Xe_2^*, which does not have a stable ground state, when it dissociates, Xenon is transparent to its own scintillation light.
- As liquid Xenon has a density of 3 g/l, the detector is compact.

- With a boiling point of $T = 163.05\,\mathrm{K}$ at $p = 1\,\mathrm{atm}$, liquid Xenon is relatively easy to obtain and to handle.

The XENON experiment uses a dual phase **T**ime **P**rojection **C**hamber to detect low energy recoils. A schematic drawing of a TPC to detect recoils in noble gases can be found in figure 4.1. If a WIMP scatters from a nucleus in the liquid phase of the experiment,

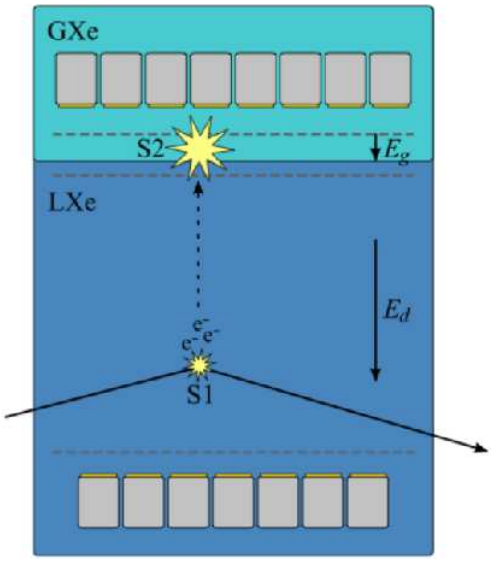

Figure 4.1.: Schematic drawing of a signal in a dual phase time projection chamber. The direct light from the scattering reaction gives the start signal S1. Electrons created in the event are drifted by the constant applied field E_d to the liquid-gas interface from which they are extracted with the field E_g. Due to the high field strength, proportional scintillation takes place, which also produces photons, then detected as the stop signal S2.

the nucleus moves through the medium, loosing the transfered recoil energy through further scattering reactions, ionizing and exciting atoms. The scintillation light is directly detected by two PMT arrays, located on top and bottom of the TPC, and forms the start signal S1. The electrons and ions produced in ionization events from the recoil are separated by a constant electric field E_d, which then drifts the electrons towards the top of the detector. There they are extracted into the gaseous Xenon phase by the additional anode field E_g. The field strength is close to the electrodes high enough to enable proportional scintillation. In the process photons are created which are then detected by the PMT arrays. This second signal S2 is used as stop signal. The z-position can be reconstructed by the drift time of the event. The PMTs have a size of $25\,\mathrm{mm} \times 25\,\mathrm{mm}$. The hit pattern of the S2 signal on the PMTs allows to reconstruct the x-y position of the event. For XENON100 the (x, y, z) position reconstruction is of the order of 3 mm for the xy- and 0.3 mm for the z-direction [Apr12a]. Using now the three-dimensional position information, fiducial volumes can be constructed to discriminate against radioactive decays from the chamber walls.

The ratio of the two signals S2 and S1 is characteristic for the type of recoil. Due to a higher ionization density in the nuclear recoil track, the separation of the charges by the applied field is suppressed and more recombination can take place in comparison to an electron recoil track, yielding a higher scintillation (S1) over charge (S2) ratio. This is used to discriminate between the recoil types and is used as additional measure to

suppress background events.

The XENON collaboration uses a multistage ansatz. Starting after an R&D phase, the first dark matter search was conducted with the XENON10 detector with a total mass of 15 kg and a fiducial mass of 5.4 kg from 2006 to 2007 (58.6 live days) [Ang08a, Ang08b, Ang09]. Starting in 2008 the XENON100 detector has been set up. 161 kg of XENON have been filled in total into the detector, with 62 kg making up the inner target. Depending on the fiducial cut within the analysis, the fiducial volume contains between 34 kg and 48 kg. Apart from maintenance periods, data taking has been continuous since 2011. The latest results from 225 live days with a fiducial mass of 34 kg has been published in [Apr12b] (see figure 1.6 for the published exclusion curve and 4.5 for exclusion curves including the projected XENON1t sensitivity). The XENON1t detector is now under construction. A total mass of about 3 t will be filled into the detector with 1 t in the active volume.

4.2. The XENON100 detector

The XENON100 experiment is located in the Laboratori Nationali del Gran Sasso Underground Laboratory in Italy. A rock burden of 3700 m water equivalent shields the detector from cosmic rays, reducing the flux of cosmic μs by 6 orders of magnitude.

The XENON100 detector uses 161 kg Xenon, 62 kg are located inside the target volume of the TPC, the rest is filled into the detector for self-shielding and veto purposes. The active volume is separated from the shield by a PTFE wall which is used to support the electrical field cage and to enhance the light collection efficiency by reflecting photons, keeping them constrained in the inner volume. A diving bell enables to surround the complete TPC volume with liquid Xenon while having a gaseous phase on top of the TPC. A technical drawing can be found in figure 4.2(a).

In total 242 PMTs are used in the detector. 80 PMTs with high quantum efficiency (QE) were chosen for the bottom array, aligned in a pattern with maximum coverage to enhance the detection of the S1 signal, as the S1 intensity is low. The passage of scintillation light to the top PMT array is suppressed due to total reflection at the liquid-gas boundary. In the top array 98 PMTs are placed in a circular shape. 2×32 PMTs are implemented in a circle at the top and the bottom of the detector, their view alternating between the top of the detector and the side. They are used as veto to discriminate against multi-scattering events.

Electric fields are applied in the XENON detector with grid electrodes. The hexagonal shape of the grid has been designed to optimize the light transition while maintaining a homogeneous field close to the electrodes. The cathode grid is implemented at the bottom of the TPC, with a shielding grid on ground potential between cathode and PMTs. A constant drift field of $E_d = 0.53\,\mathrm{kV/cm}$ is applied between the cathode mesh and a ground mesh at the top of the TPC in a distance of 30 cm. The liquid-gas interface is located between the ground mesh and the anode mesh. Here a potential of $U_a = 4.5\,\mathrm{kV}$ is applied to extract electrons from the liquid phase and accelerate them for proportional scintillation. To avoid discharges between the anode mesh and the PMTs another ground mesh is implemented between them. Homogeneity of the electric field for the whole detector volume is achieved with a field cage around the active volume. It consists of wires woven into a PTFE cage. They are connected with a resistor chain, resulting in

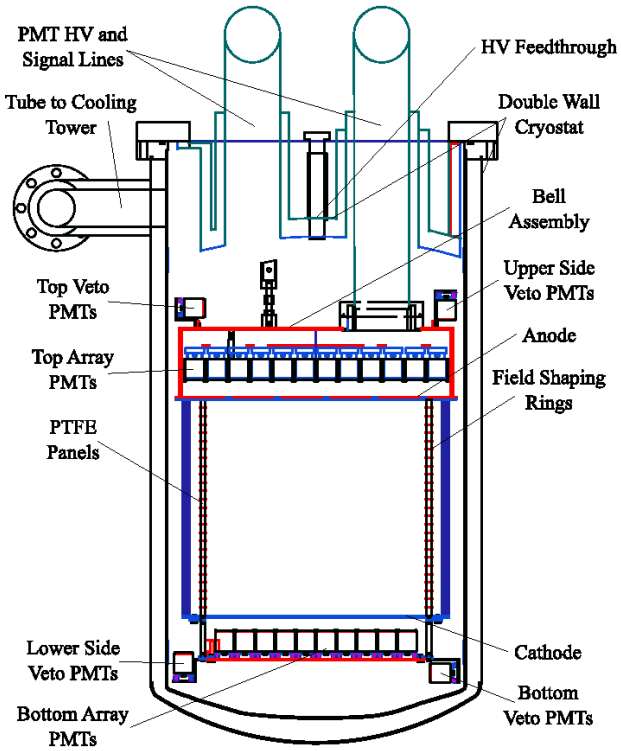

(a) Technical drawing of the XENON100 detector. Figure taken from [Apr12a].

(b) The TPC volume of the XENON100 detector during construction. On top and bottom the veto PMTs are visible. The PTFE walls with the woven field shaping wires restrict the inner detector volume.

Figure 4.2.: The XENON100 detector.

a constant potential gradient. PTFE has been chosen as support structure, as it is a dielectric material with a relative permittivity of $\epsilon_r \approx 2$. In addition it is known that PTFE powder reflects a high percentage of the incoming light - depending on the angle of incidence more than 80 % of the incident radiation for wavelength above 300 nm [Wei81]. As the scintillation light of Xenon has a wavelength of 178 nm, it is important to test, if the reflectivity changes with wavelength. In addition it is important to know the exact reflection pattern for the position reconstruction .

Electro-negative impurities as *e.g.* O_2 can absorb the electrons for the S2 signal during their drift to the top. As these impurities permanently enter the system due to outgassing of detector components, the Xenon needs to be continuously purified. This is done by extracting liquid Xenon from the bottom of the TPC into a buffer volume where it evaporates. The gaseous Xenon is then pumped through a hot getter, which extracts the electronegative elements by chemical reactions. It is then feed again into the system in the gaseous phase. The recirculation flow can be adjusted thus providing a tool to adjust the liquid level inside the detector. The level is monitored with level meters whose capacitances change according to the height of the liquid.

Materials for the XENON100 detector have been chosen on the basis of screening measurements and reflectivity [Apr11b]. The data has been used in MC simulations and compared with the measured background [Apr11a]. The good match between simulation and data emphasizes the good understanding of the detector.

As electron recoils and nuclear recoils have a different signature in the detector, an electron-recoil equivalent energy scale denoted with $\mathrm{keV_{ee}}$ and a nuclear-recoil equivalent energy scale denoted with $\mathrm{keV_{nr}}$ have been constructed. Although the detector is used in the search for nuclear recoil events, it is useful to implement the electron-recoil equivalent energy scale, as it can be used *e.g.* as a measure to identify background events from radioactive decays. The nuclear-recoil equivalent energy can be constructed from the measured S1 signals if the scintillation yield $L_{y,\mathrm{nr}}$ for nuclear recoils is known. As this quantity is difficult to measure, the relative scintillation efficiency for nuclear recoil $\mathcal{L}_{\mathrm{eff}}$ measured relative to the light yield L_y for electron recoils with energies of $E_{\mathrm{er}} = 122\,\mathrm{keV}$ from ^{57}Co is used. In addition, the quenching of the scintillation light due to the applied electric field has to be considered for electron-recoils S_{er} and for nuclear-recoils S_{nr}. The recoil energy E_{nr} is then

$$E_{\mathrm{nr}} = \frac{\mathrm{S1}}{L_y}\frac{1}{\mathcal{L}_{\mathrm{eff}}}\frac{S_{\mathrm{er}}}{S_{\mathrm{nr}}}. \tag{4.1}$$

To further suppress background from the environment, the detector is housed in a low radioactivity stainless steel vessel which is then placed into a passive shield cage consisting of the following layers: 5 cm of OFHC Copper, 20 cm of polyethylene (PTFE), 5 cm of low ^{210}Pb lead, 15 cm of regular lead, 25 cm of polyethylene from the bottom and 20 cm water/polyethylene on three sides and the top of the detector. With these actions the electromagnetic background has been reduced to $(5.3 \pm 0.6) \cdot 10^{-3}\,\mathrm{events/(keV_{ee} \cdot kg \cdot d)}$ in the region of interest. A detailed study of the electromagnetic background has been published in [Apr11a] and of the neutron background in [Apr13b].

For further details of the XENON100 detector see references [Pla12] and [Apr12a].

4.3. Results from the XENON100 experiment

Dedicated calibrations with γ sources[1] and with an AmBe neutron source have been conducted to to investigate the response of the detector to electron and nuclear recoils [Apr13a]. Figure 4.3 shows the events from these calibrations in the $\log_{10}(S2_b/S1)$ parameter space. With these events, data quality cuts have been derived and a WIMP search region has been defined. For an exposure of $7636.4\,\mathrm{kg \cdot d}$ a background of (1 ± 0.2) events has been expected. Two candidate events passed all cuts (see figure 4.4) which is consistent with the background expectation.

Using these results a profile likelihood analysis has been conducted. It states a probability of 26.4 % for the hypothesis of the background fluctuating to yield two events at these low energies. An exclusion limit for spin-independent WIMP-nucleon cross-section σ_χ has been derived[2] (see figure 1.6 and figure 4.5 including the projected limit of the XENON1t experiment). These results have been published in [Apr12b].

[1] The isotopes ^{137}Cs, ^{57}Co, ^{60}Co and ^{232}Th have been used to cover a broad energy range.

[2] The following assumptions have been used as input: isothermal WIMP halo with $\rho_\chi = 0.3\,\mathrm{GeV/cm^3}$, local circular velocity $v_0 = 220\,\mathrm{km/s}$ and Galactic escape velocity of $v_{esc} = 544\,\mathrm{km/s}$

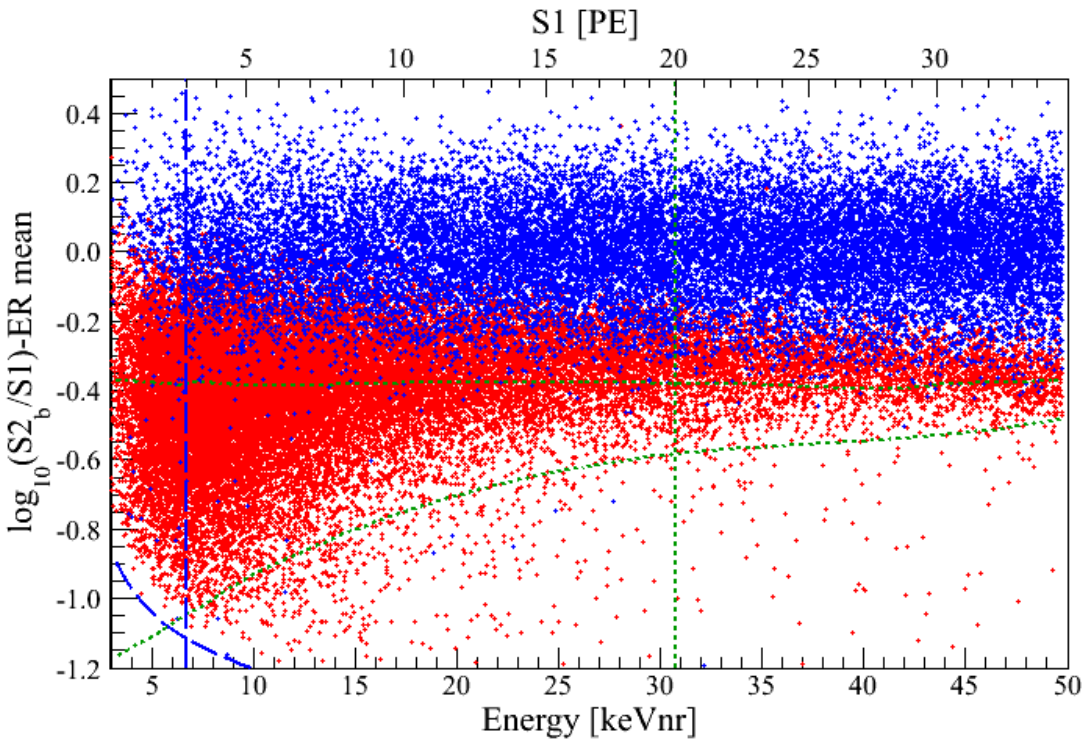

Figure 4.3.: Electron and nuclear recoil in $\log_{10}(S2_b/S1)$ parameter space. The energy scale has been derived from the S1 signal. The electron recoil mean has been subtracted as offset in the $\log_{10}(S2_b/S1)$ parameter space. The WIMP search region has been defined with these data, limited by the dashed blue lines denoting the low energy data cuts with $E > 6.6\,\mathrm{keV_{nr}}$ and $S2 > 150\,\mathrm{PE}$, the green dotted lines defining the region of interest for the WIMP search, limited from above by the 99.75 % electron recoil rejection, from below by the 97 % nuclear recoil acceptance and from the side by $E < 30.5\,\mathrm{keV_{nr}}$ (3-20 PE).

4.4. The XENON1t experiment

With the XENON1t experiment the XENON collaboration aims to improve the sensitivity for WIMP searches, aiming for a goal of $2 \cdot 10^{-45}\,\mathrm{cm}^2$, by increasing the total mass by a factor of 10 while reducing the total background by a factor of 100. One measure to achieve this is the installation of the XENON1t detector inside a huge water tank equipped with PMTs as active veto. A graph with exclusion curves including the projected sensitivity of the XENON1t experiment is shown in figure 4.5.

This quest poses several challenges which have already been resolved (*e.g.* see reference [Apr12c]) or are currently addressed. The construction of the next stage of the XENON experiment started this spring.

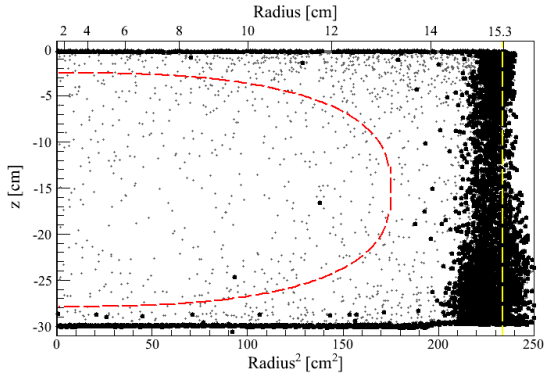

(a) Events passing the XENON100 cuts in a two-dimensional representation of the XENON100 detector. The red ellipse marks the fiducial volume. Gray points denote events above the 99.75 % electron recoil line, black circles events below (compare figure 4.3).

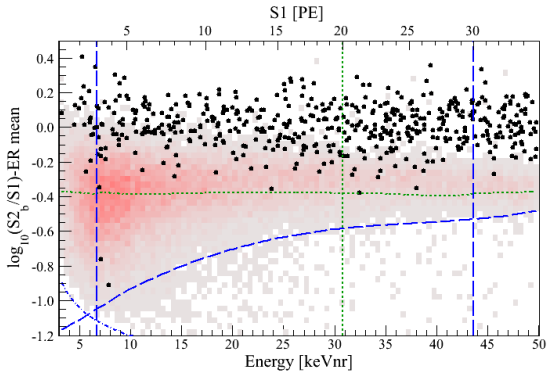

(b) Events passing the XENON100 cuts and lie in the fiducial volume in the $\log_{10}(S2_b/S1)$ plot. Only two events fall into the region of interest. The shaded events are from the calibration, already shown in figure 4.3.

Figure 4.4.: Events from the 225 d run of the XENON100 detector.

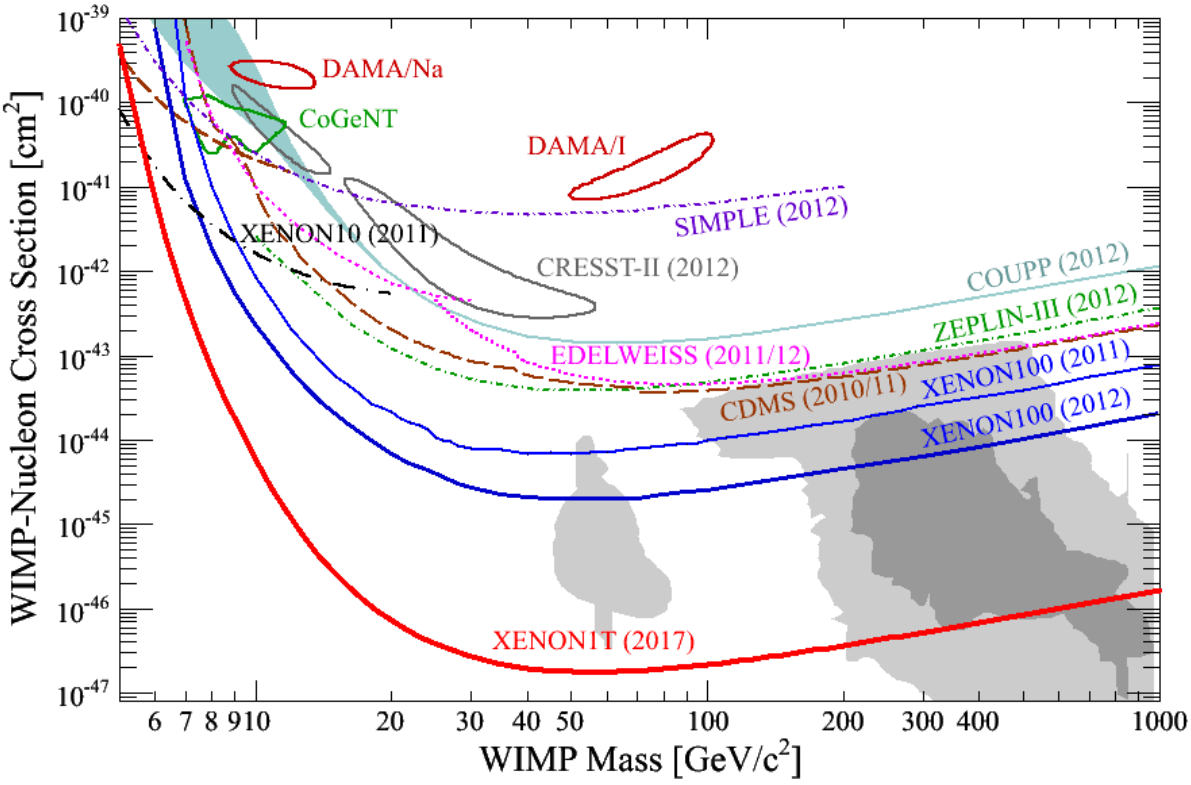

Figure 4.5.: Exclusion curves for the results of the analysis of the 225 d exposure of the XENON100 experiment (XENON100(2012)) including the projected limit of the XENON1t experiment. Also shown are limits from the following experiments EDELWEISS, CDMS, ZEPLIN, COUPP and SIMPLE. The Xenon100(2012) results are in conflict with the possible positive WIMP signals seen by DAMA, CoGeNT, CRESST-II and SuperCDMS (not shown) in the low mass region. Discussion on the different detector systematics leading to either a suppression of WIMP events or an overestimation of these are ongoing.

5. Measuring the reflectance of vacuum UV light from PTFE samples

For a complete simulation of the XENON100 experiment the detector properties need to be well known. One uncertainty in the GEANT4 model of the XENON100 detector is the reflectance of the polytetrafluoroethylene (PTFE) panels used in the detector as a holding structure for the field shaping wires. Apart from the wavelength, incident angle, temperature and atmosphere, the reflectance of PTFE also depends on the exact production process and the surface finish.

Pressed PTFE powder is known to be a good reflector in the wavelength region above 300 nm [Wei81] and studies have been conducted to determine the bidirectional reflection intensity distribution function for the XENON scintillation wavelength (178 nm) [Sil07, Sil10a, Sil10b]. The results of these studies have been implemented in the XENON100 Monte-Carlo-simulations. But it has been shown that the reflection properties of samples vary with their preparation procedures. Therefore, an experimental facility to determine the reflectance of the PTFE used in the XENON100 experiment as well as of the PTFE in consideration for the XENON1t experiment is needed. It was build in a joint effort of the group of Prof. Aprile at Columbia university and our group at WWU Münster. In addition to reflection measurements, it is also possible to test with this setup the quantum efficiency of different PMTs at low temperatures for vacuum UV light [Apr12d].

In this thesis the second version of the experimental setup has been developed and commissioned. As proof of principle first measurements of PTFE test samples have been performed and a Monte-Carlo-based analysis developed. These measurements have shown that the alignment procedure is very important for the measurements. The setup has been handed over to C. Levy Brown who conducted extensive, time-consuming alignment investigations and improved the results [Lev13]. The setup has also already been used by B. Choi to investigate the reflection properties of PTFE samples from the XENON100 detector [Cho12].

In the first section a short overview of the properties of PTFE will be given. Section 5.2 will then list some basics concerning reflection of light from surfaces. The experimental setup is described in section 5.3. As several stages of the experiment existed, the requirements are listed first, before the first setup is described in section 5.3.2 and the second in section 5.3.3. As a proof of principle a first set of measurements has been taken (see section 5.4 for a measurement overview) and analyzed. The analyzing procedure is described in section 5.5. The results of these measurements are presented in section 5.6. Concluding remarks are given in section 5.7.

5.1. Polytetrafluoroethylene (PTFE)

Polytetrafluoroethylene (abbreviated PTFE) in general is a label for plastics with the structure formula $(C_2F_4)_n$ (see figure 5.1). It is commonly known under the brand name *Teflon* by DuPont.

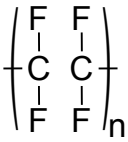

Figure 5.1.: Structure formula of PTFE.

PTFE is produced as powder. Then different methods as pressing, molding or extruding are used to extract a bulk material or to directly shape the material into the wished form. For industrial applications compounds are added to adapt some physical properties for specific applications.

PTFE is known to be nonreactive against many aggressive chemicals. Most environmental effects as *e.g.* humidity and UV radiation have no negative impact on the material. PTFE is a dielectric. Under mechanical stress PTFE is not stable, but has a tendency to cold flow. Some technical properties of PTFE can be found in [Hug13].

In the XENON experiment PTFE is used due to its dielectric properties and reflection characteristics as support structure for the field cage.

5.2. Reflectance

5.2.1. Definitions

"*Reflection* is the process by which electromagnetic flux[...], incident on a stationary[...] surface or medium, leaves that surface or medium from the incident side without change in frequency;[...] *reflectance* is the fraction of the incident flux that is reflected."

[Nic77]

The reflectance $\rho(\theta_i, \varphi_i, \theta_o, \varphi_o)$ from a sample seen in the direction described by the angles θ_o and φ_o depends on inclination of the incident ray, described by the angles θ_i and φ_i, and is defined as the ratio between the flux reflected in this direction $\frac{\Phi_o}{d\Omega}(\theta_i, \varphi_i, \theta_o, \varphi_o)$ (for a definition of the angles compare figure 5.2) and the total incident flux Φ_i:

$$\rho(\theta_i, \varphi_i, \theta_o, \varphi_o) = \frac{\frac{\Phi_o}{d\Omega}(\theta_i, \varphi_i, \theta_o, \varphi_o)}{\Phi_i}. \tag{5.1}$$

The total reflectance $\rho(\theta_i, \varphi_i)$ of a sample is thus the ratio of the total reflected flux in all directions

$$\Phi_o(\theta_i, \varphi_i) = \int_0^{2\pi} \int_0^{\pi} \frac{d\Phi_o}{d\Omega}(\theta_i, \varphi_i, \theta_o, \varphi_o) d\theta_o d\varphi_o \tag{5.2}$$

and the incident flux Φ_i:

$$\rho(\theta_i, \varphi_i) = \frac{\Phi_o(\theta_i, \varphi_i)}{\Phi_i} \tag{5.3}$$

and varies with the incident angles. With the assumption that the surface is isotropic, the angle φ_i can be defined independent of the surface. For this setup it has been chosen that φ_i is defined in reference to the plane encompassed by the incoming light ray $\vec{k}_i$ and the normal vector $\vec{n}$ of the surface. Therefore it is by definition always $\varphi_i = 180\,^\circ$ (see also figure 5.2) and the reflectance only depends on the angle θ_i:

$$\rho(\theta_i) = \frac{\Phi_o(\theta_i)}{\Phi_i}. \tag{5.4}$$

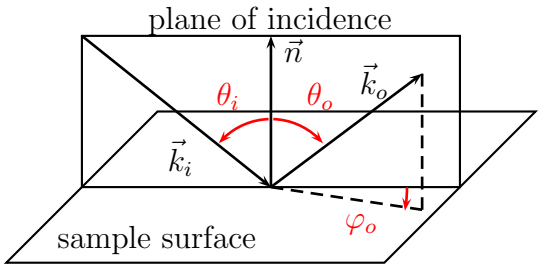

Figure 5.2.: Angles used to define the incident and outgoing light beam. The plane encompassing the incident light ray $\vec{k}_i$ and the normal vector $\vec{n}$ is used as reference to define the angle φ. For this analysis the incident angle φ_i is chosen to be $\varphi_i = 180\,^\circ$.

The reflectance $\rho_{\lambda;\vec{x}}(\theta_i)$ is a property of a sample. It does not only depend on the material the sample consists of, but also on the processing of the material as well as the surface treatment. The reflectance can vary locally on a sample due to inhomogeneities of the material or the surface finish. In addition the reflectance can depend on the wavelength λ of the incident light.

In this experimental setup a monochromatic light source will be used, therefore only the spectral reflectance will be considered. Wavelength changing processes as *e.g.* fluorescence will be neglected in the analysis. The incoming light beam and the reflected light will be measured with a photomultiplier in counting mode. Therefore, the reflectance can be shaped into the following form:

$$\rho(\theta_i) = \frac{\Phi_o(\theta_i)}{\Phi_i} = \frac{\dot{N}_o(\theta_i, \varphi_i) \cdot E_\gamma}{\dot{N}_i \cdot E_\gamma} = \frac{\dot{N}_o(\theta_i)}{\dot{N}_i}. \tag{5.5}$$

As a prove of principle measurements of one position on a sample will be conducted. The local variation of reflectance needs to be tested separately. In addition we assume that the sample is isotropic and the reflectance thus does not depend on the sample alignment.

5.2.2. Reflections

For most materials the reflection of light can be described with two types of reflection: specular and diffuse.

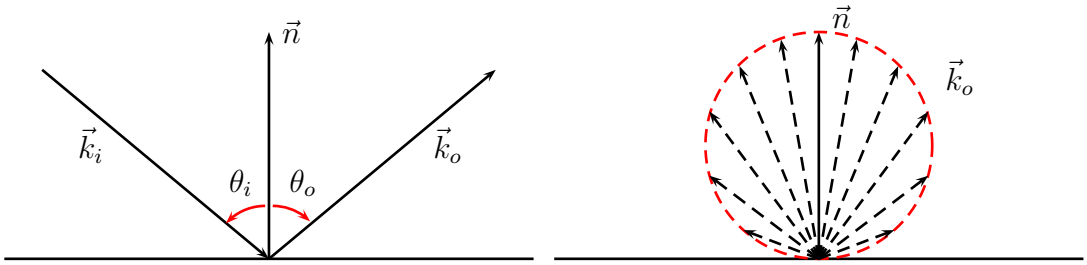

(a) Specular reflection

(b) Diffuse reflection

Figure 5.3.: Schematic of different reflection types in the plane $\varphi_o = 0\,°$.

Specular reflection is well known from mirror-like surfaces where incident and reflected ray lie in a plane with the surface normal ($\varphi_o = 0\,°$) and the angle between the surface normal and the exiting ray θ_o is equal to the angle of incidence θ_i (see also figure 5.3(a))

$$\theta_o = \theta_i. \tag{5.6}$$

The reflected intensity from a diffusely reflecting surface can be described with the following relation:

$$\frac{dI(\theta_o)}{d\Omega} = I_0 \cdot \cos\theta_o. \tag{5.7}$$

The intensity seen in a solid angle element $d\Omega$ is the initial intensity reduced by the cosine of the viewing angle θ_o.

In order to simulate the reflection from a rough surface, the surface can be characterized as an array of micro-surfaces. Their alignment distribution is then a measure of the roughness of the total surface (see also figure 5.4(a)) and can be characterized by the angle α. Surface roughness of an ideal specular reflector results in a broadening of a beam spot and thus the blurring of a picture. If a surface is very rough, light with high exit angles θ_o will be blocked by the surface itself resulting in a cutoff for these angles (see figure 5.4(b)).

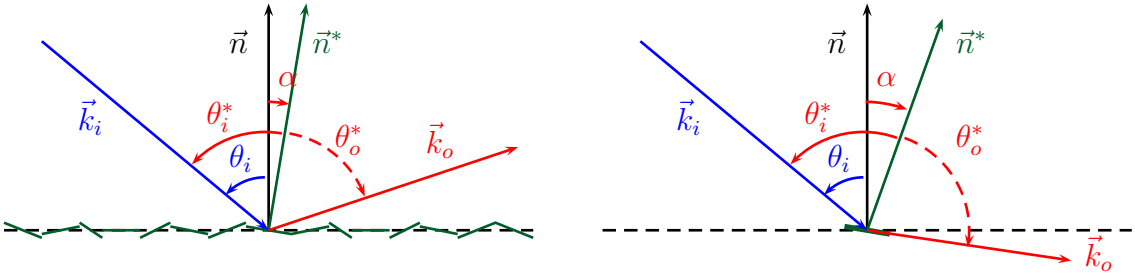

(a) Surface roughness presented by micro-surfaces. The reflected light $\vec{k}_o$ has to be calculated with respect to the local surface normal $\vec{n}^*$, not the average surface normal $\vec{n}$.

(b) Geometrical cutoff due to surface roughness. The theoretical path of the reflected ray $\vec{k}_o$ passes through the material.

Figure 5.4.: Micro-surfaces: Surface roughness and geometrical cutoff.

5.3. Experimental setup

For a total measurement of the reflectance of a surface, the reflected intensity into the whole hemisphere above the sample needs to be measured. As also the angular distribution of the reflected light and thus the flux $\Phi_o(\theta_i, \varphi_i, \theta_o, \varphi_o)$ is of interest, a position dependent detection is needed.

As a continuous angular resolved measurement covering the full solid angle of a hemisphere of 2π is quite difficult, a combinatorial approach in which the experimental data sets for discrete angles are matched with Monte-Carlo-simulations was chosen for this experiment. Therefore, the reflected light was only measured for specific sets of θ_i, φ_o and θ_o. Modeled data sets were then fitted to the measurements and a total result was derived from the fit.

5.3.1. Requirements and general implementation

Geometry

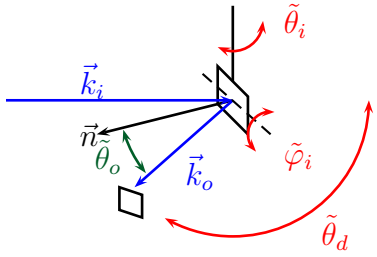

Figure 5.5.: Movement of components in the setup with the corresponding angles in red. The sample can rotated with respect to the incident light beam introducing the angle $\tilde{\theta}_i$. Tilting the sample results in a change of the angle $\tilde{\varphi}_i$. The detector can be rotated around the sample thus changing the angle $\tilde{\theta}_d$ that is defined with respect to the incoming light vector $\vec{k}_i$.

To measure the reflected flux $\Phi(\theta_i, \varphi_i, \theta_o, \varphi_o)$ for several sets of θ_i, φ_o and θ_o three movements are needed. As the designated light source with a vacuum monochromator (see also page 74) is heavy and large, the incoming light beam was chosen to be fixed. Instead the sample can be rotated in reference to it thus changing the angle $\tilde{\theta}_i$ (see figure 5.5). The detector can be rotated around the point on which the beam is focused thus changing the angle $\tilde{\theta}_o$. To introduce the additional angle $\tilde{\varphi}$ different concepts have been used in the separate stages of the setup[1]. In the second stage (see also section 5.3.3 and figure 5.5) the sample is rotated by the angle $\tilde{\varphi}_i$ out of the plane spanned by the incoming light vector $\vec{k}_i$ and the vector pointing towards the detector $\vec{k}_o$. The reflection measurements shown in sections 5.4, 5.5 and 5.6 have been conducted with the second setup. The relationship between the experimental angles $\tilde{\theta}_i$, $\tilde{\theta}_d$, $\tilde{\theta}_o$ and $\tilde{\varphi}_i$ (see figure 5.5 and 5.6(a)) and the angles θ_i, θ_o and φ_o relative to the surface normal used in the reflection models (see

[1]In the first stage (see also section 5.3.2) the detector was moved on a circular arc out of the plane spanned by the incoming light beam and the normal vector of the surface thus introducing $\tilde{\varphi}_o$.

section 5.2.2 and figure 5.6(b)) is given in equation (5.9) through (5.11) (the deviation of these relationships can be found in appendix B):

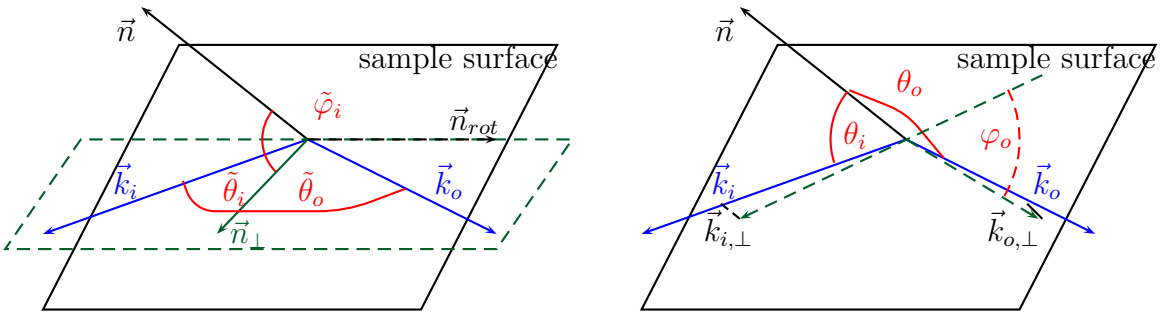

(a) Experimental angles with the sample inclination fixed as used in the second setup of 2011.

(b) Angles in reference to the surface normal $\vec{n}$ used for the models.

Figure 5.6.: The different sets of angles used to define the incident and outgoing light beam in the frame of the setup and with respect to the surface normal.

$$\tilde{\theta}_o = \tilde{\theta}_d + \tilde{\theta}_i - 180\,^\circ \tag{5.8}$$

$$\cos\theta_i = \cos\tilde{\theta}_i \cos\tilde{\varphi}_i \tag{5.9}$$

$$\cos\theta_o = \cos\tilde{\theta}_o \cos\tilde{\varphi}_i \tag{5.10}$$

$$\cos\varphi_o = \frac{\cos\tilde{\theta}_i \cos\tilde{\theta}_o \cos^2\tilde{\varphi}_i - \cos\left(\tilde{\theta}_i + \tilde{\theta}_o\right)}{\sqrt{\left(1-\cos^2\tilde{\theta}_i \cos^2\tilde{\varphi}_i\right)\left(1-\cos^2\tilde{\theta}_o \cos^2\tilde{\varphi}_i\right)}}. \tag{5.11}$$

Light source

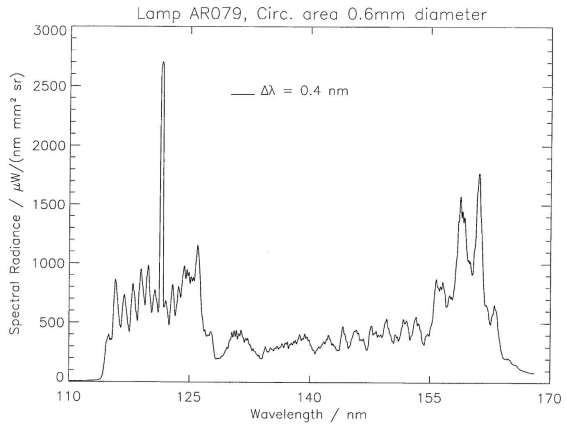

(a) Emission in the range 110 nm to 170 nm

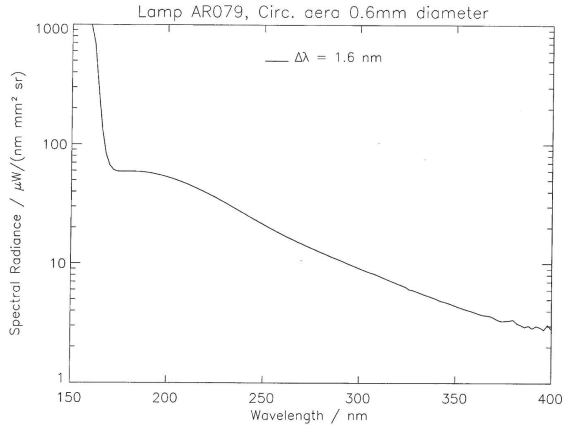

(b) Emission in the range 150 nm to 400 nm

Figure 5.7.: Emission spectrum deuterium light source taken from [McP632]

At the time of the construction of the experiment, different noble gases were under discussion for the next generation of liquid noble gas detectors. Therefore, a tunable light

source has been chosen for this experiment. A McPherson Model 632 Deuterium light source provides spectral lines in the range of 110 nm to 170 nm and continuous emission from 170 nm to 400 nm (see also figure 5.7) . The wavelength is selected with a McPherson Model 218 vacuum monochromator (see figure 5.8) using a 1200 grooves/mm grating with a blaze wavelength of 150 nm.

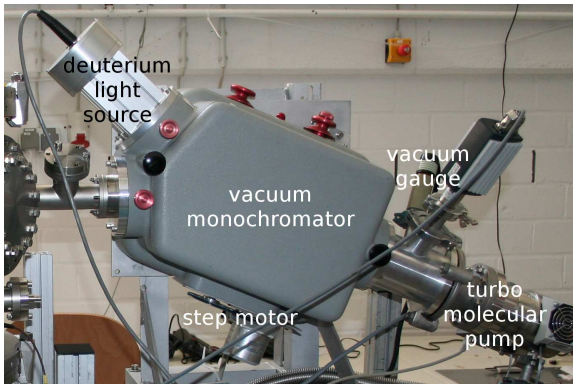

(a) McPherson vacuum monochromator and deuterium lamp.

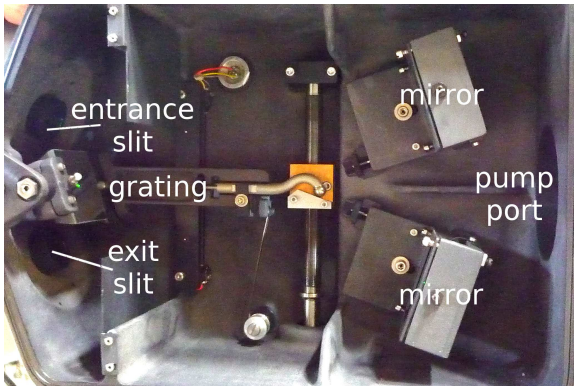

(b) Inside view of McPherson vacuum monochromator.

Figure 5.8.: McPherson vacuum monochromator and deuterium lamp.

Resolution and light intensity depends on the slit size used in the experiments. The vacuum monochromator has a rectangular opening with changeable slits with maximum height height $h_{\text{slit}} = 2\,\text{mm}$ and maximum width $w_{\text{slit}} = 20\,\text{mm}$. The resolution is affected by the height of the slit as the grating inside the vacuum monochromator diffracts the light continuously according to its wavelengths in this direction. The direction is fixed by the alignment of the ruling of the grating. The height slit opening therefore extracts a part from the continuous spectrum. The reciprocal linear dispersion is given for the grating to be 26.5 Å/mm [McP218], thus the resolution for these measurements with a slit height of $h_{\text{slit}} = 2\,\text{mm}$ is 5.3 nm. Calibrations and tests of the vacuum monochromator can be found in reference [Apr09, Spr11].

Vacuum

The Xenon scintillation light is with 178 nm well into the vacuum UV light range. In this range the absorption cross section σ of oxygen with $10^{-19}\,\text{cm}^2$ [Mainz] dominates and

reduces the mean free path $l = (\sigma n)^{-1}$ at normal pressure for this wavelength to

$$l = \frac{V_0}{\sigma N_A} = \frac{22.4 \cdot 10^3\,\mathrm{cm}^3}{10^{-19}\,\mathrm{cm}^2 \cdot 6.02 \cdot 10^{23}} \approx 3.7\,\mathrm{cm}, \tag{5.12}$$

with V_0 the molar norm volume and N_A the Avogadro constant. To increase the mean free path to be about 1 m, the total optical path length, the particle density has to be reduced to be below $10^{17}\,\mathrm{cm}^{-3}$ corresponding to a pressure in the low mbar range.

The vacuum monochromator has greased feed through for the movement of the grating to select the wavelength (see als figure 5.8). To avoid absorption of the grease on the sample surface or the PMT, these were built into a second vacuum chamber separated from the vacuum monochromator by a UV-transmitting MgF_2 window (transmittance $\approx 80\,\%$ at 178 nm [Hea66]). Only CF seals were used to close the scattering chamber. The vacuum monochromator uses O-ring seals, hence the minimum achievable pressure is limited to the low $1e^{-5}$ mbar region. The MgF_2 window is build into a CF-flange. A groove for O-ring sealing is placed on its outside to seal the connection to the vacuum monochromator (see also figure 5.9) enabling a completely evacuated light path.

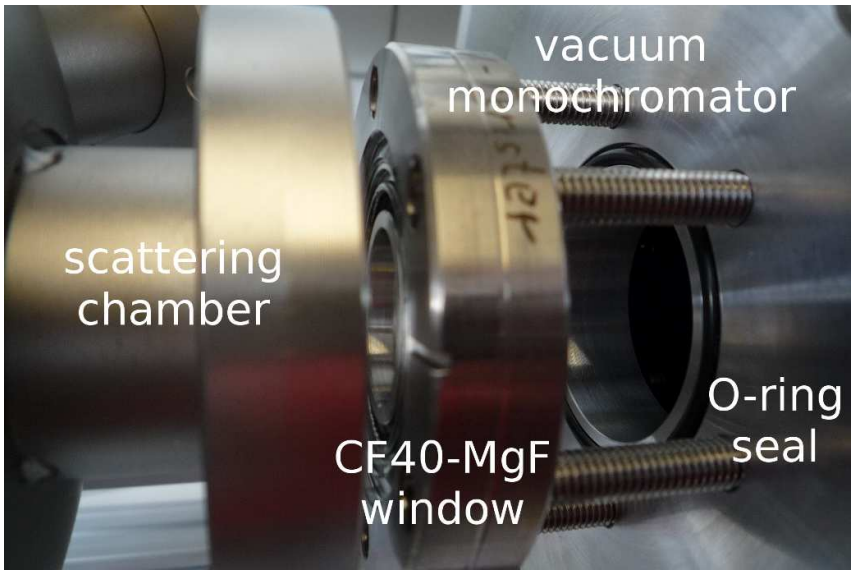

Figure 5.9.: Connection between vacuum monochromator and scattering chamber via MgF_2 window. The screws for the CF connection are bolted into the O-ring flange of the vacuum monochromator.

To avoid absorption of residual gas as *e.g.* water on the cooled PMT surface (about -100 °C to decrease noise and to mimic the conditions in liquid Xenon), the pressure in the scattering chamber needs to be reduced well below the saturation vapor pressure of $2 \cdot 10^{-5}$ mbar for water [Wut]. In addition a colder surface can be introduced, doubling as cryo pump to remove residual gas by absorption and avoiding absorption on the PMT surface.

Sample

The preparation of the sample is important for the reflectivity. Therefore, any surface treatment needs to be specified and reproducible.

The sample needs to be positioned accurately, the point of incidence of the light beam on the sample needs to be the center of rotation of the sample itself as well as the center of rotation for the detector. It is important to note for the construction, that the center of rotation for the sample is on its surface.

The size of the sample is important for the evaluation of the measurement. Only an effective length of $l_{\mathrm{s,eff}} = l_{\mathrm{s}} \cdot \cos\theta_i$ is in the light path. Hence at large incident angles θ_i part of the light beam passes the sample. To determine the total reflectance, the incoming intensity has then to be adapted for these angles.

As light is not always scattered from the PTFE surface, but also penetrates into it (see figure 5.10) there should be no material at the backside of the sample. Scattering from the backside could distort the result of the measurement.

Figure 5.10.: Light transmittance through a PTFE sample: a laser pointer (right) with the wavelength 532 nm shining vertically on a PTFE sample of 5 mm thickness. The light penetrates into the sample and also leaves through the side walls.

Detector

PMTs of the type 1"-square Hamamatsu R8520-AL as used in the XENON100 experiment and the successor model R8520-406 have been implemented in this setup. One PMT and its holding structure can be seen in figure 5.11.

The detector electronics have been changed for the different setup iterations (see sections 5.3.2 and 5.3.3). As the dark rate of the PMT is with about 20 Hz relatively high at room temperature, it is cooled down to about -100 °C (liquid Xenon temperature) where the dark rate is reduced below 1 Hz. Therefore, a copper case connected to a cooling device was used for the placement of the PMT. As several PMTs should be tested for the quantum efficiency measurements, exchanging the PMTs should be relatively easy. Hence the case consists of an upper and a lower part between which the PMTs are screwed to realize the best thermal contact. Copper braids leading to a cooling device are connected to both parts (see also figure 5.12). The lateral placement of the PMT inside the case is done by spacers (see also figure 5.11). The PMT is in direct contact with the cooling device. Therefore, it has to be operated with positive high voltage applied to the last dynode. In the negative mode the voltage would be applied to the photocathode and therefore also to the shell of the PMT.

With a 25.4 mm × 25.4 mm (1 In × 1 In) window, the sensitive area of the PMTs is large.

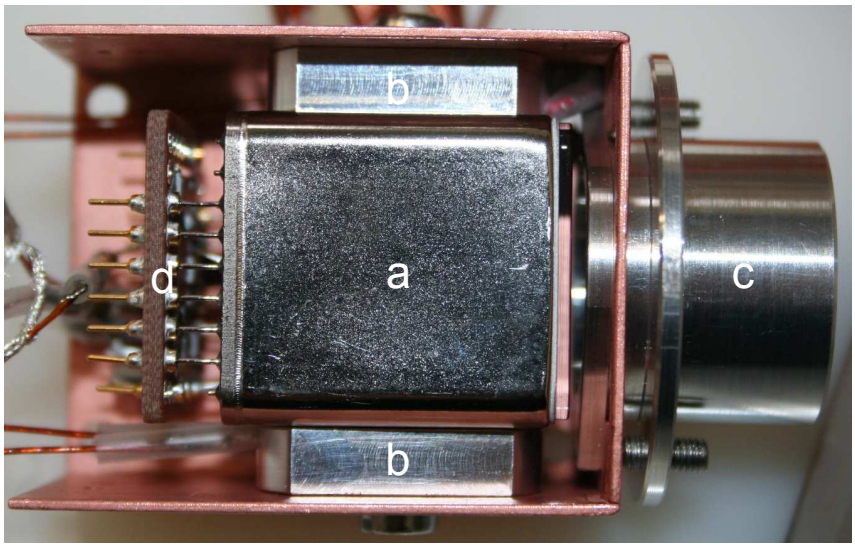

Figure 5.11.: PMT positioned in copper case. a) PMT, b) spacer, c) detector aperture and d) PMT base with resistor chain and cable connections to HV and signal readout.

To reduce the solid angle seen with the PMT, an exchangeable aperture (in the following called detector aperture) is attached to the case as can be seen in figures 5.11 and 5.12.

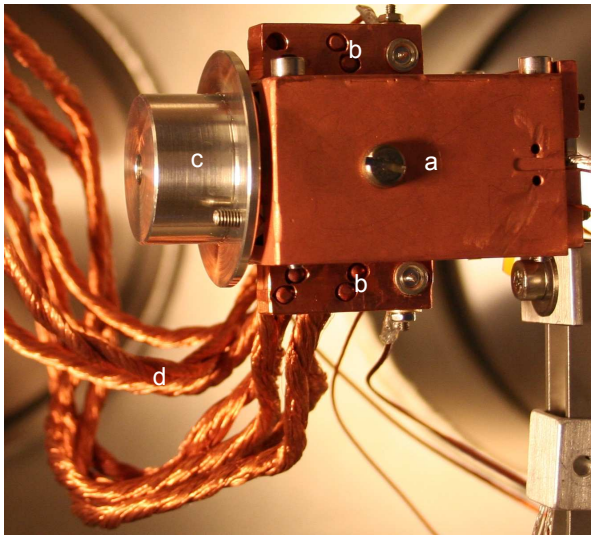

Figure 5.12.: Closed copper case with braids to connect to cooling facility. a) copper case, b) connectors for copper braids, c) detector aperture and d) cooling braids.

Cooling

For the cooling of detector and sample a pulse tube refrigerator (PTR) Iwatani PDC 08 with a cooling power of 5 W at 77 K has been implemented.

5.3.2. First implementation 2009

The design and setup of a chamber for reflection and quantum efficiency measurements was started in 2009. The setup was built at WWU Münster and shipped to Columbia

university in Fall 2009.

Overview

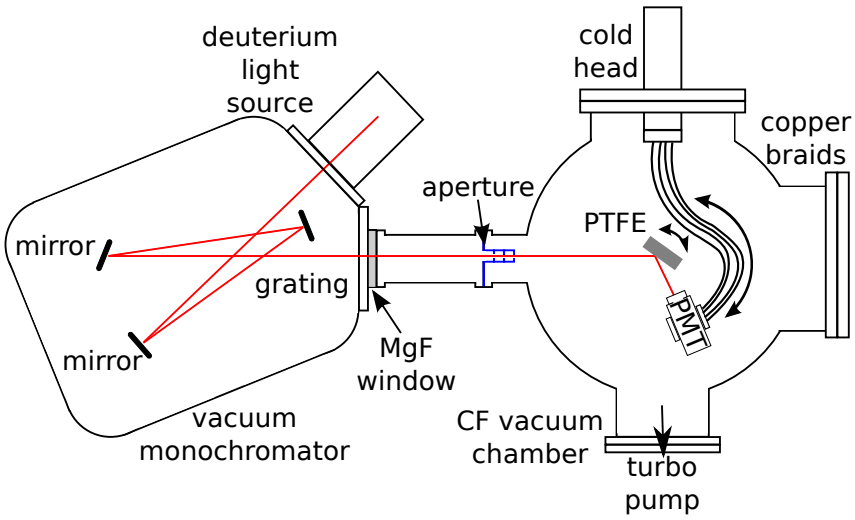

Figure 5.13.: Schematic drawing of the setup. The red line indicates the light path from the source to the sample from which it is reflected to the detector. On the left the light source with deuterium lamp and vacuum monochromator is visible. It is separated from the scattering chamber on the right by a UV-transmitting MgF_2 window. A cold head enables the cooling of the PMT. The PTFE sample is rotated around the point of incident of the light. The PMT is rotated around the sample.

In figure 5.13 a schematic drawing of the setup with its main components is shown. All movements with their corresponding angles (see section 5.3.1) are illustrated in figure 5.14.

The complete setup is shown in picture 5.15, with figure 5.15(a) displaying the technical drawing while 5.15(b) shows the realization of the setup at Columbia university.

The light source has been described on page 74. To achieve a collimated light beam, an aperture has been build into the scattering chamber at a distance of 110 mm to the exit slit of the vacuum monochromator. The aperture consisted of three stages screwed together, each with a minimum opening of 7 mm, thus reducing the stray light component in the beam. The opening angle of the beam was $\alpha = 0.9\,°$. The beam spot on the PTFE piece at a distance of $d_{\text{slit}} = 255\,\text{mm}$ to the exit slit had a diameter of $d = h_{\text{slit}} + 2 \cdot d_{\text{slit-PTFE}} \cdot \tan\alpha = 10\,\text{mm}$.

As scattering chamber a sphere of 230 mm diameter with two CF160 flanges, two CF100 flanges, one CF63 flange and three CF40 flanges has been used. The two CF100 flanges were placed on opposing sites with one CF40 perpendicular to them. This CF40 was used for the MgF_2 window and the connection to the vacuum monochromator. On the CF100 flanges the rotation feed throughs for the PMT and for the PTFE were placed. The rotation feed through for the PMT sat on a three-dimensional movement table thus allowing for the adjustment of the PMT position and two-dimensional measurements of the beam spot[2]. The rotation feed through of the PTFE sample was a CF40 feed

[2]Due to spacial limitaions it was not possible to use the third movement to measure the beam spot at

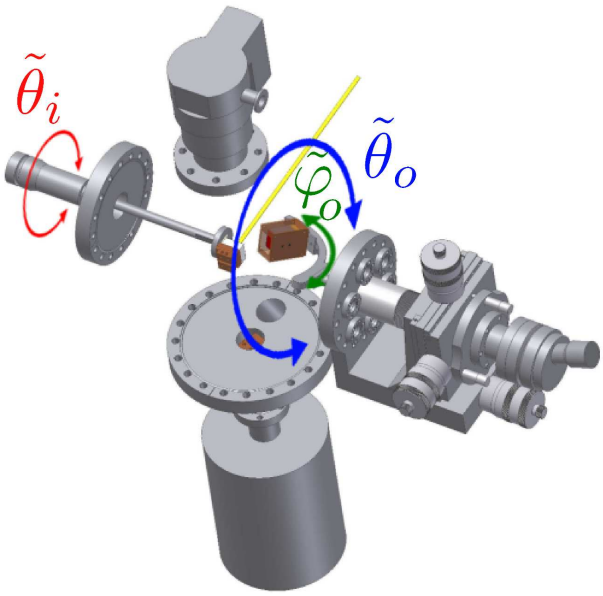

Figure 5.14.: Movement of the components and the corresponding angles for first setup. View from bottom. Note that in this drawing a LN_2-dewar is used instead of a PTR.

through and therefore was mounted on an adapter flange CF40-CF100. To allow easier experimental access, the sphere was mounted in a way that the CF100 flanges with the rotation feed throughs showed to the sides (see figure 5.15). The turbo molecular pump was mounted on the CF63 flange with the pump being in an upright position. Opposing to it a CF160-2CF40 adapter was on top of the chamber with the PTR and the vacuum gauge attached to it. The second CF160 was on the opposite site of the CF40 flange for the light. It was used to access the chamber. The last two CF40 flanges are used for a multipin electrical feed through and to purge the setup. For the QE measurements a cryo pump and an RGA have been connected to the last CF40 flange.

To be able to test the influence of sample thickness on the reflectance, the holding structure was designed to allow for an adjustable placement of the sample. The sample itself was screwed onto a copper holder. To avoid reflections of light transmitted through the sample from the copper a hole was placed in its center. To cool the sample, copper braids from the PTR were connected to the copper holder. The sample was thermally insulated from the rotation feed through by round ceramic pieces that were inserted into grooves in copper holder and the round end of the rotation feed through. The sample could be positioned along these groves and was fixed on the round plate with a screw. The surface of the sample had to be adjusted to be directly in the middle of the round end of the feed through. The holding structure can be seen in figure 5.16(a).

The detector was mounted on a rotational feed through on the opposite side of the PTFE feed through. It was placed on an arc segment. The outermost position of the arc put the detector in the plane of the incoming light beam. Moving the detector on the arc changed the angle $\tilde{\varphi}_o$ (see figure 5.14). The lateral positioning of the detector was done with a 3d movement table.

For the reflection measurements a PMT was used. An aperture with an opening diameter of 5 mm was placed in front of the PMT case at a distance of 25 mm to the scattering

different distances to the aperture.

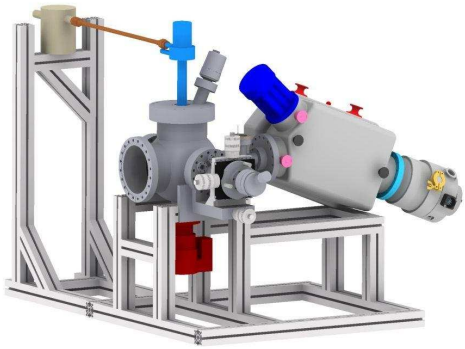

(a) Technical drawing of the first setup.

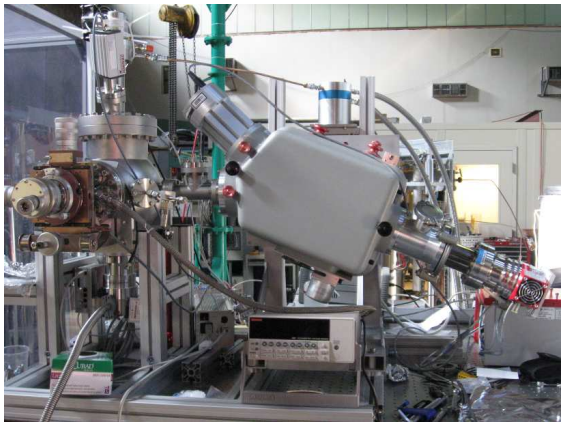

(b) Picture of the setup as it was built up at Columbia university

Figure 5.15.: Technical drawing of the complete setup and its realization at Nevis, Columbia university.

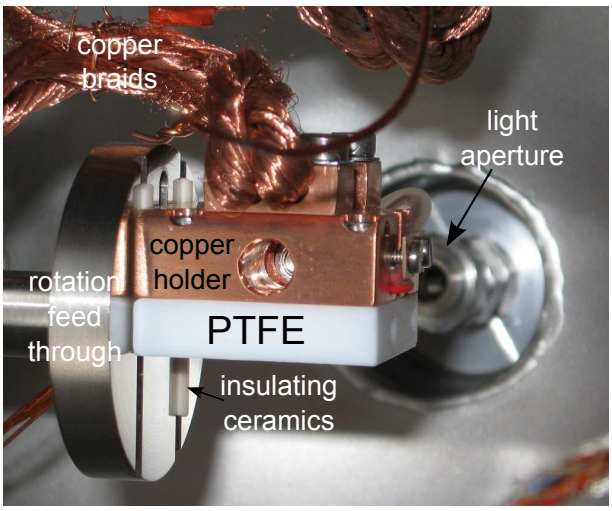

(a) PTFE holder

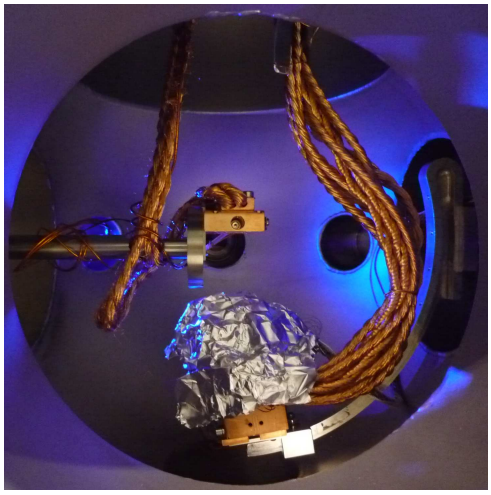

(b) View inside the setup.

Figure 5.16.: Components inside the setup

center. To be able to measure also the absolute light intensity for the gain measurements, a NIST calibrated PIN diode was implemented.

The vacuum monochromator was pumped with a Pfeiffer HiCube 80 Eco pumping station to pressures of the order $1e^{-5}$ mbar. The scattering chamber was pumped with a Pfeiffer TMU 071P and a Pfeiffer MVP 040-2 diaphragm as baking pump achieving pressures in the low $1e^{-6}$ mbar or high 10^{-7} mbar region, depending on the conditions inside the chamber. To avoid contaminations of the chamber while opening to change something inside, the system was flushed with liquid Nitrogen off-gas. In addition the system was backed for 2-3 days at low temperatures before measurements. While backing the temperatures were not allowed to exceed 50 °C to avoid damage to the PMTs.

Sample and PMT were cooled by a Iwatani PDC08 PTR with a cooling power of 5 W at 77 K. To enable movement of the PTFE sample and the PMT, the connection to the cold head was done with copper threads as can be seen in picture 5.16(b).

Several PT100s have been implemented inside the setup to monitor the temperature of the PMT and the sample. The temperature was adjusted by resistive heating with a Zener diode, the applied current is regulated via a PID control. The sensors were positioned on top of the copper holding at PTFE sample and for the PMT one outside the case at the contact point of the copper braids where also the heating diodes are positioned and one in the spacers for the lateral positioning of the PMT. As the later was at the maximum distance to the heating diode and cold contact, it was used for the PID control. The temperature and pressure monitoring as well as the PID control have been programmed in LabView by R. Jöhren.

For the reflection measurements the PMT was used in counting mode. Therefore, a standard base (see [Pla12] for more info on the PMTs) with different resistances between the dynodes was used. 850 V were applied to the PMT. Its signal was then processed by a LeCroy 12 Channel PMT Amplifier and fed to an Ortec 450 Research Amplifier. The result was converted into a digital signal with a Philips 706 discriminator and counted with a scaler.

For the quantum efficiency measurements the amount of charge induced at the photocathode by the light and thus the current read from the first dynode for a minimal voltage applied between photocathode and dynode to allow charge collection but no signal amplification was of interest. Therefore, a potential difference was applied between photocathode and first dynode of the PMT. The current detected at the first dynode was then read directly with a Keithley 6485 picoammeter. The current meter was also used to measure the response of the calibrated PIN diode used as reference.

Reflectance measurements and problems with the setup

After commissioning the setup at Columbia university measurements have been conducted by B. Choi [Cho12]. A reflectance measurement of an arbitrary PTFE sample is shown in figure 5.17. With the help of this example the disadvantages of this setup will be discussed.

- The general background level in the setup was high ($> 10^2$ Hz) due to light leaks and reflections off the chamber walls. It was reduced by installing non-reflecting lining paper which on the other hand worsened the pressure due to outgassing. Still with this light intensity the diffuse reflections cannot be distinguished from the background, only the specular peak for large incident angles is visible (see figure 5.17).
- Due to soldering of the components inside the chamber and the need to regularly open the chamber, the ultimate pressure reached was in the high 10^{-7} mbar, low 10^{-6} mbar range.
- The beam size was with 10 mm diameter at the sample position very large. For the experiments this results in a reflectance from a large spot of the PTFE sample, thus a convolution of reflections with different exit angles θ_o from different positions. For larger angles of incidence the effective area of the PTFE sample was smaller than the beam size. Thus only part of the initial beam was reflected, part transmitted (see also 80 ° measurement in figure 5.17).
- The opening angle of the detector was large due to its close vicinity to the sample as well as the large aperture diameter.

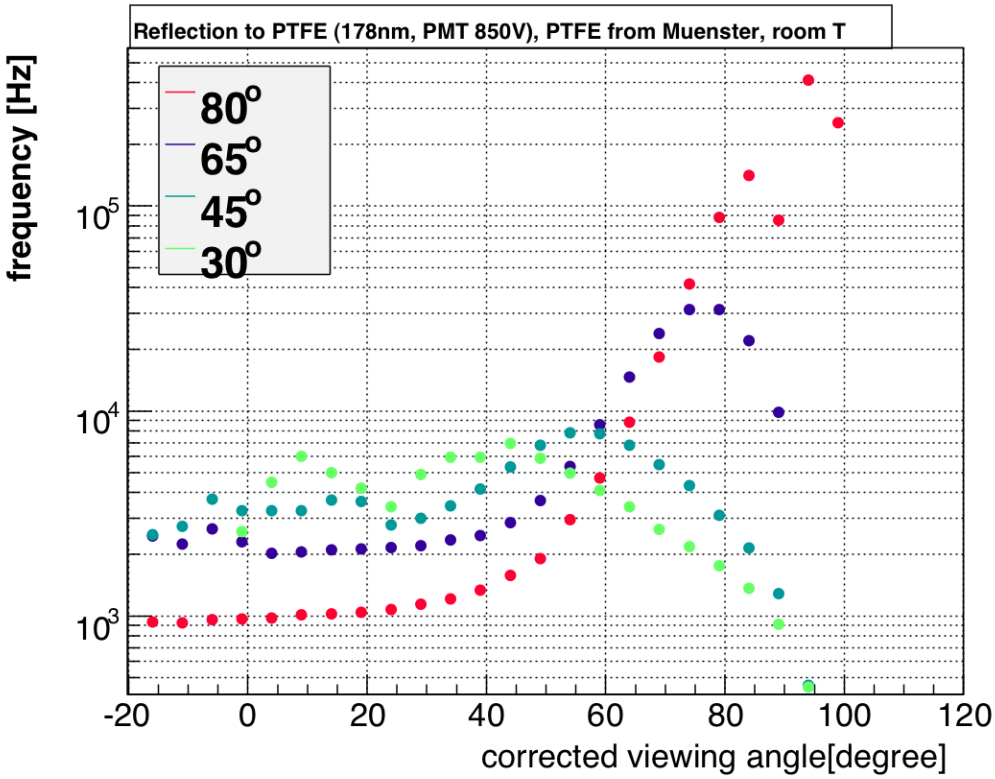

Figure 5.17.: Measurements with the first setup. Figure taken from [Cho10].

- The light source could not be measured completely in lateral dimensions as the space inside the chamber was limited and the holding structure scratched the chamber surfaces. The exact alignment of the PTFE sample could not be tested as it was build only on a rotational feed through.
- The sample together with the copper threads for cooling and the cables for the temperature control and readout took much space. It was difficult to ensure that none of the cables moved into the light path during the rotation of the sample.
- Noise problems occurred at the detector as the signal lines scrapped the inner walls of the vacuum vessel during rotation. The limited space also made working inside the chamber difficult with the consequence that several times connections broke.
- Opening the chamber to change the angle $\tilde{\varphi}_o$ proved to be not feasible as with each opening the experimental conditions inside the chamber changed. In addition warming up the components inside the chamber before opening and cooling down again took several hours. As the connections were quite unstable there was the possibility to break something with each movement.

Quantum efficiency measurements

Hamamatsu improved the PMT used in the XENON100 experiment (R8520-06-Al) to have a higher sensitivity at 178 nm (R8520-406). To test the behavior of the quantum efficiency of these PMTs with respect to their temperature, measurements have been

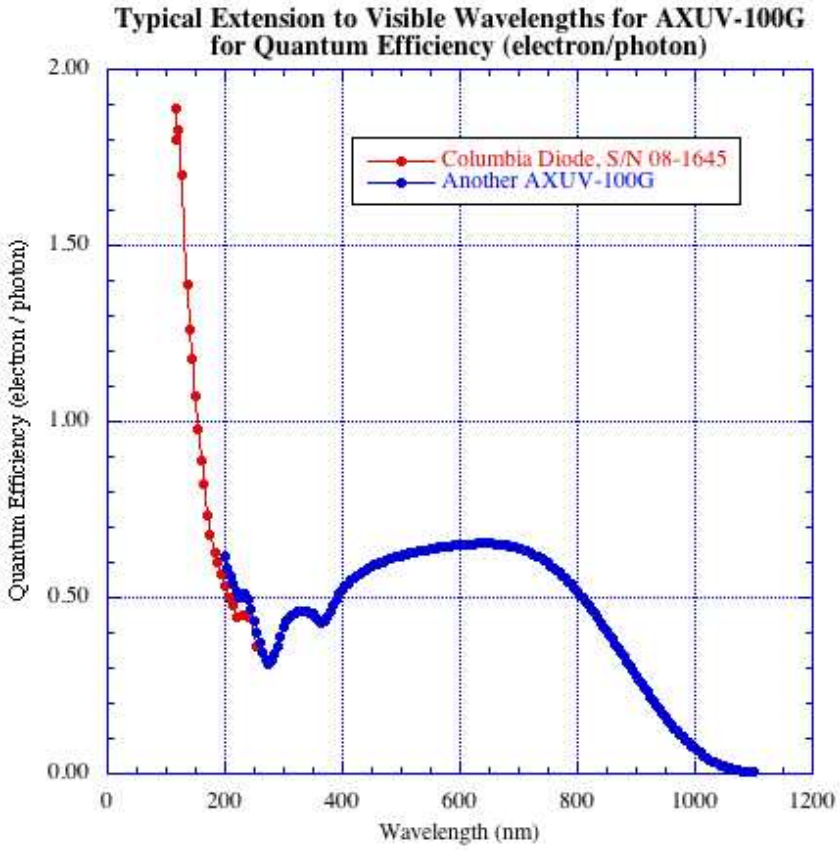

Figure 5.18.: Quantum efficiency of the Columbia diode measured by NIST. Figure taken from [Cho10].

conducted. These are described in detail in reference [Apr12d] and [Cho12]. Here only a short description of the setup will be given.

To measure the QE of a detector, the light intensity needs to be known. Therefore, it is measured with a detector with known QE, here a NIST calibrated silicon photodiode, of type AXUV-100G with an effective area 10 mm × 10 mm. The QE curve is shown in figure 5.18.

The quantum efficiency of a PMT is the number of electrons extracted per incident photon. As HV applied to the dynode array influences the amount of electrons extracted from the photocathode due to the applied larger electric fields, the circuit diagram for the PMT has been redesigned for these measurements. As photoelectrons created at the photocathode would recombine, a small negative potential $U_{\mathrm{pc}} < 100\,\mathrm{V}$ has been applied to it. The incident current on the first dynode will be measured. The current level depends on he incident light intensity, wavelength and the detector properties. For this setup it was in the pA region. The low current requires a thorough reduction of all electronic noise sources.

As the photocathode, that is connected to the PMT case is placed on a potential, the PMT needs to be isolated from its holding case. This has been done by wrapping it into a layer of Teflon tape. As this insulated the PMT thermally, a temperature sensor has been directly placed onto the PMT, held into place by the tape, allowing to read the real temperature at the PMT.

The ratios of the QE of the PMT and the diode are directly correlated with the ratio of the measured currents at a specific wavelength.

$$\frac{\mathrm{QE}_{\mathrm{PMT}}}{\mathrm{QE}_{\mathrm{diode}}} = \frac{I_{\mathrm{PMT}}}{I_{\mathrm{diode}}} \tag{5.13}$$

As the QE of the diode is known, the QE of the PMT can be calculated.

The measurements (see figure 5.19) have shown that the QE of the new PMTs increases by about 5 % to 10 % when decreasing the temperatures to values between 160 K and 170 K [Apr12d]. This effect has been attributed to the decreasing energy loss in the lattice.

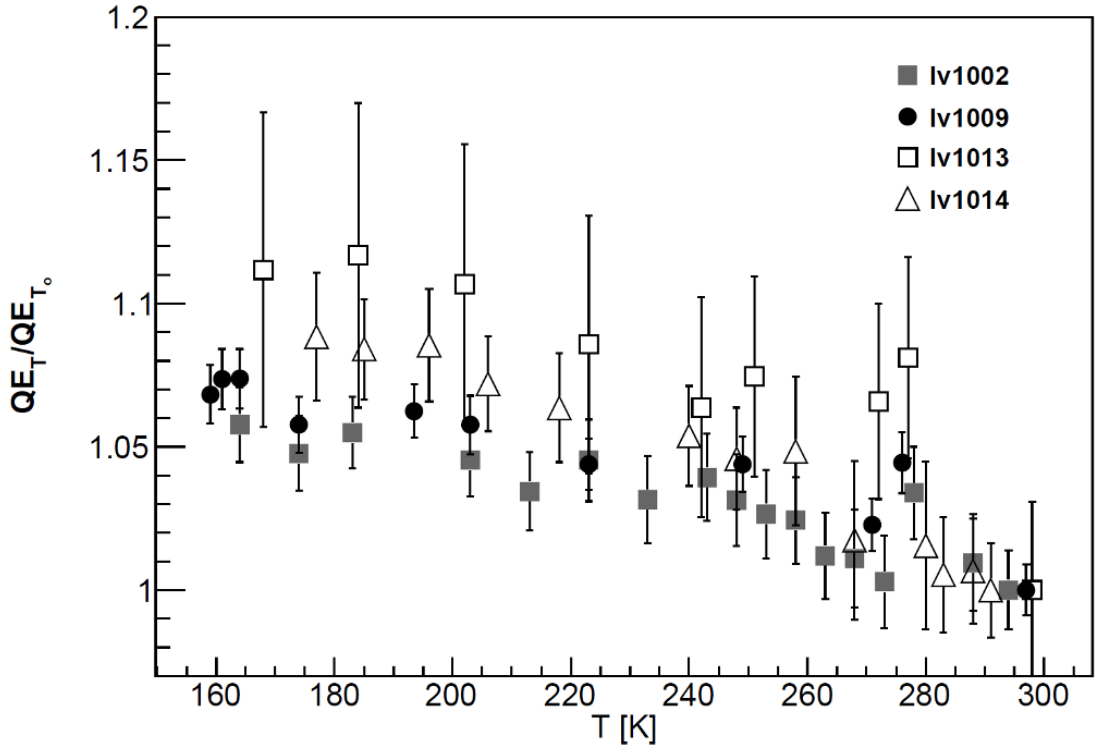

Figure 5.19.: Temperature dependence of the quantum efficiency for four high QE Hamamatsu R8520-406 PMTs [Apr12d].

5.3.3. Changes for the second setup 2011

Changes

As several problems were noted with the old setup (see page 82), the concept of the measurement was revisited and several changes were implemented upon recommissioning of the setup. A picture of the improved total setup can be seen in figure 5.20.

- The light source section from deuterium lamp and vacuum monochromator to the MgF_2 window has been left unchanged.
- To improve the light intensity a lens has been mounted into the light path, focusing the light beam onto the sample. To restrict the dimensions of the beam and to reduce its opening angle, a collimator has been mounted into the setup with its ultimate aperture close to the sample. The aperture is a cap that can be exchanged depending on the intensity and beam size requirements of the measurement.

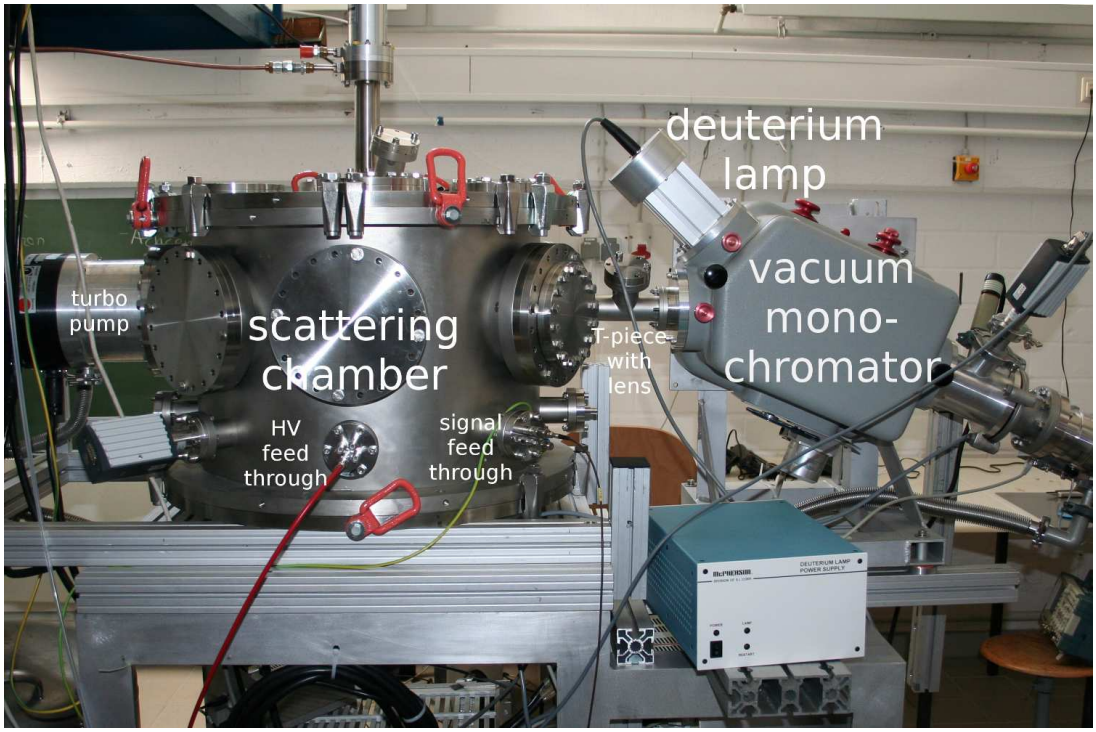

(a) Side view

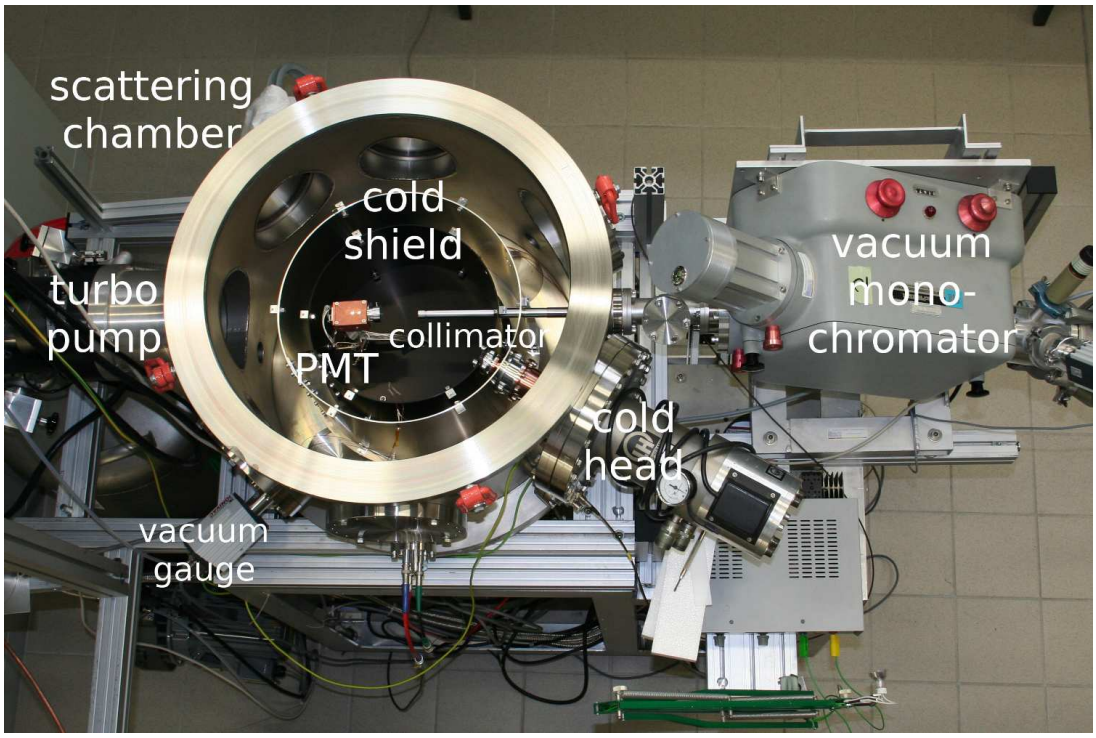

(b) Top view

Figure 5.20.: Improved total setup in 2011.

- A larger vacuum vessel is used for the scattering chamber thus increasing the space available for working on the setup as well as the cabling.
- The vacuum was improved by using a pump with larger pumping speed. In addition a two stage Aluminum cold shield was introduced, surrounding the complete area

with sample and PMT. It is on the one hand used as cryo pump, on the other hand the nearly closed structure helped reducing the background from stray light. In addition the inner cold shield was anodized[3] and dyed black to avoid reflections.

- To improve the solid angle seen by the PMT an easy exchangeable aperture in front of the detector case was introduced. It offers the option to widen/reduce the covered solid angle for different tests. The cabling has been done where possible with plug-and-socket connections. This enables an easy removel of the complete detector structure from the chamber. The case with PMT and base can then be opened on a dedicated workplace outside the vacuum chamber. This improved not only the time needed to change things at the detector, but also the signal quality. The mounting structure for the PMT included space through which the cables can be guided.
- The movement for the angle $\tilde{\theta}_i$ is done as before by rotating the PTFE sample. The detector is rotated around the sample changing the angle $\tilde{\theta}_o$. The third angle will be changed at the sample. In the design stage the sample was supposed to be rotated around an additional rotation axis via a linear feed through. Due to time constrains and technical details this has not been implemented up to now. Instead the rotation feed through for the PTFE sample can hold in total four samples. They are aligned with the angles $\tilde{\varphi}_i = 0\,°, 3\,°, 12\,°$ and $20\,°$ to the incident beam. To access a specific sample a linear feed through is used to move the holder. The PTFE holder is mounted on a 3d lateral movement table with rotational feed through, thus allowing to determine the exact position of the sample with reference to the beam.

Specifications

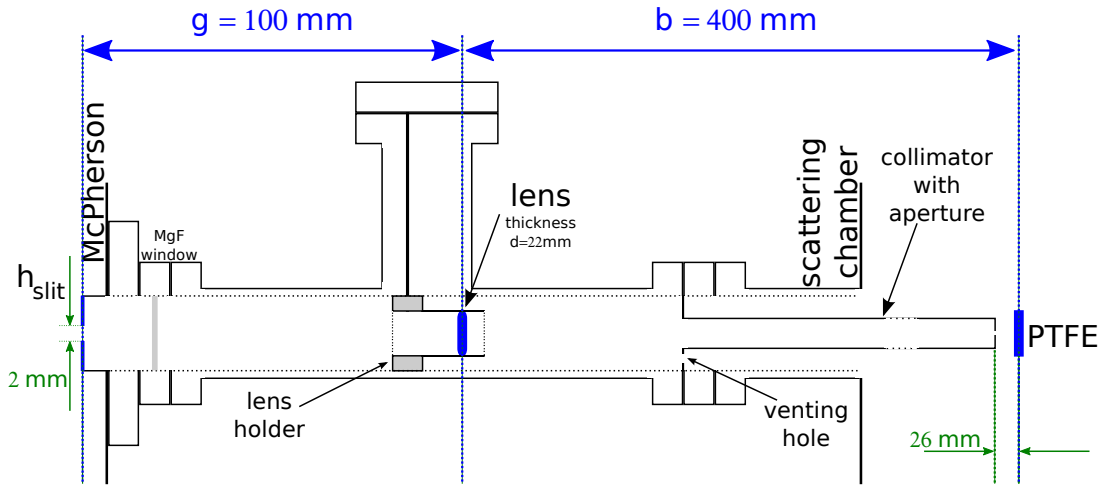

Figure 5.21.: Lens and collimator

To improve the light intensity an uncoated quartz lens[4] has been mounted into a T-piece connecting the vacuum monochromator with the scattering chamber at a object distance of $g \approx 100\,\text{mm}$ to the exit slit of the vacuum monochromator. It has been adjusted to

[3] oxide layer thickness about $15\,\mu\text{m}$

[4] Edmund optics Ltd, NT48-297, LENS DCX-UV 25×100 UNCTD, focal length 100 mm at $\lambda = 589\,\text{nm}$ and 80 mm at $\lambda = 178\,\text{nm}$

get a focused beam point on the PTFE piece at the image distance of $b = 400\,\text{mm}$ to the exit slit.

To reduce the beam size, a collimator has been included into the setup. It consists of a tube with an inner diameter of 14 mm, length 302 mm, welded into a two face CF40 flange, width 15 mm, with a ventilation slit of 5 mm diameter on the bottom, well outside the beam spot, and is mounted between T-piece and chamber at a distance of 168.5 mm (see also figure 5.21 and 5.22). The aperture is designed as an exchangeable cap. For the data presented in sections 5.4, 5.5 and 5.6 an aperture with a diameter of 1.5 mm at a distance of 474 mm to the exit slit corresponding to 26 mm distance to the sample has been used. This part of the setup is also discussed in [Spr11].

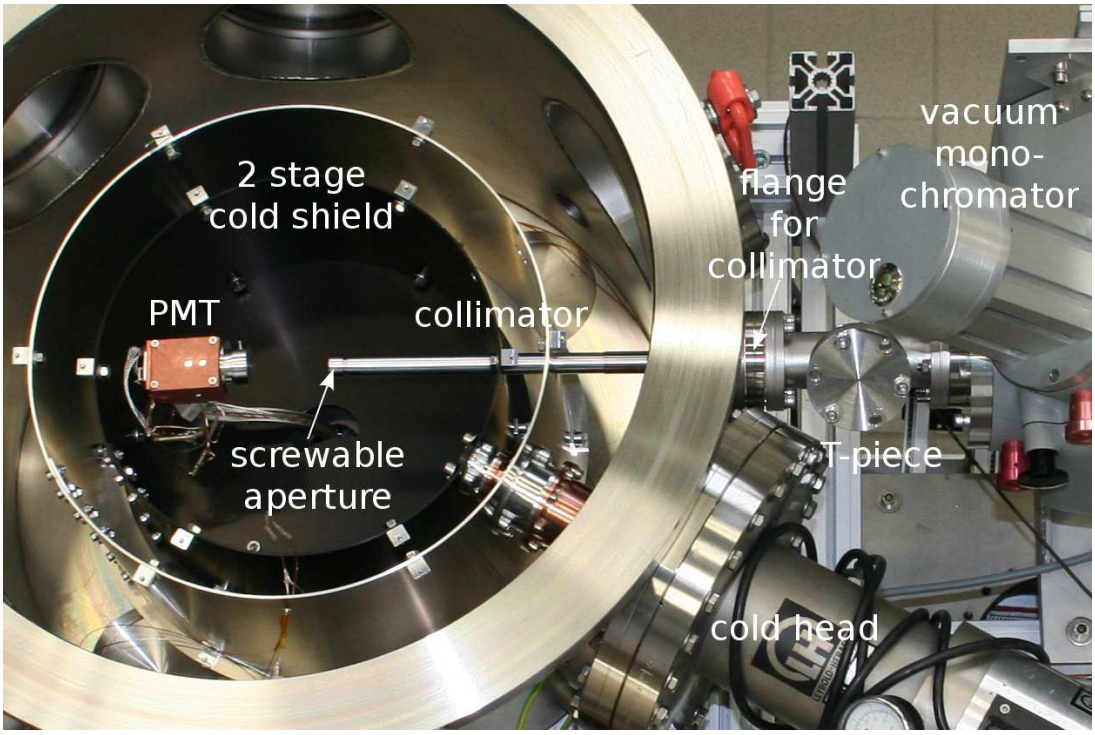

Figure 5.22.: Picture of collimator build into the setup.

A measurement of the beam spot in the plane of the PMT (41 mm from the focusing point) yielded an ellipsoidal beam spot (see also figure 5.23). Fitting simulated beam profiles with an initial Gaussian beam to these data gives FWHM of $\approx 0.8\,\text{mm}$ for the small axis and $\approx 1.4\,\text{mm}$ for the larger one. As can be seen from the beam profile pictures in figures 5.24(a) and 5.24(b) the profiles are asymmetric. For the vertical beam profile a very small second spot has been detected. This has been attributed to alignment errors. Considering the total intensity only 1.5 % go into this peak. For this first proof of principle this is negligible and the alignment has not been corrected. Assuming no focal point between the aperture and the sample the beam spot has a FWHM of about 0.7 mm respectively 0.9 mm on the PTFE.

As a major change the vacuum chamber for sample and PMT has been replaced by a larger one with more flanges (see picture 5.25). It has an outer diameter of 630 mm, an inner diameter of 520 mm and a height of about 400 mm. Two rows of flanges are set into the cylindrical part of the chamber. Eight CF40 flanges are evenly distributed in a bottom array, the top array consists of seven CF160 flanges and one CF40. The CF40

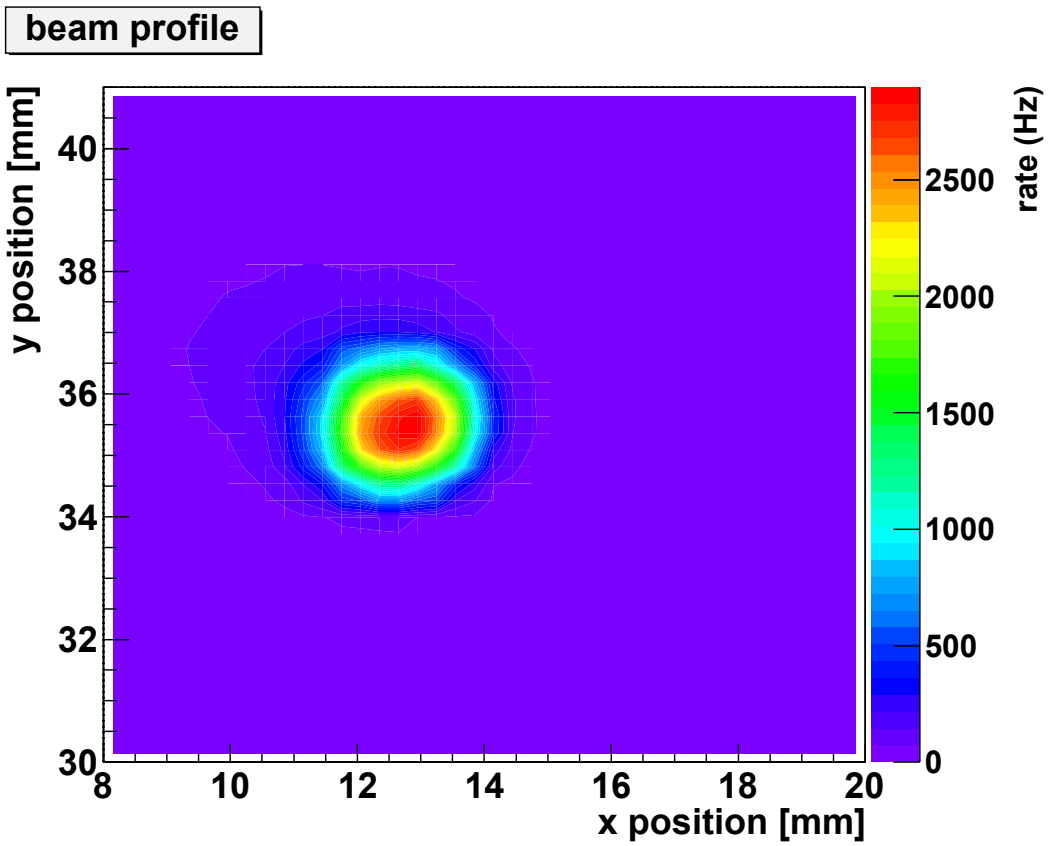

Figure 5.23.: Beam profile for $\lambda = 158.5(\pm 2.4)$ nm and a collimator aperture diameter of 1 mm

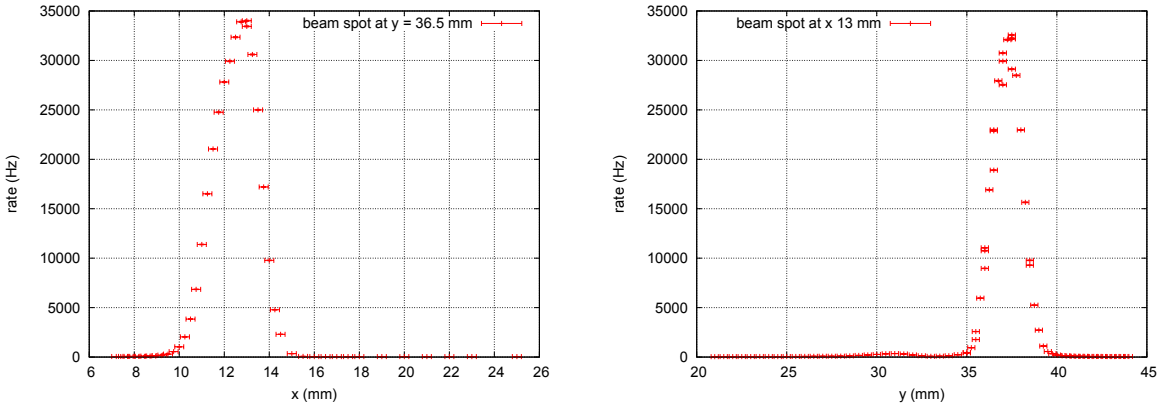

(a) Beam spot profile in horizontal direction.

(b) Beam spot profile in vertical direction.

Figure 5.24.: Beam spot profiles in horizontal and vertical direction for $\lambda = 178.3(\pm 2.3)$ nm and a collimator aperture of 1.5 mm diameter.

is aligned with a CF40 flange from the bottom array. The two adjoining CF160 flanges are placed close to the CF40 and thus do not follow the even distribution of the bottom flanges. The last five CF160 flanges are again evenly distributed, placed directly on top of CF40 flanges from the bottom array (see also figure 5.25.

The top and bottom of the chamber are closed of by O-ring seals[5]. Five flanges are placed on the top and the bottom flanges each, a CF160 in the center with four CF100

[5] 2 viton O-rings with a thickness of 8 mm and an inner diameter of 565 mm are in use.

symmetrically around it. The center flanges are used for the rotational feed through for the PTFE (top) and the PMT (bottom) as they thus have the same center of rotation.

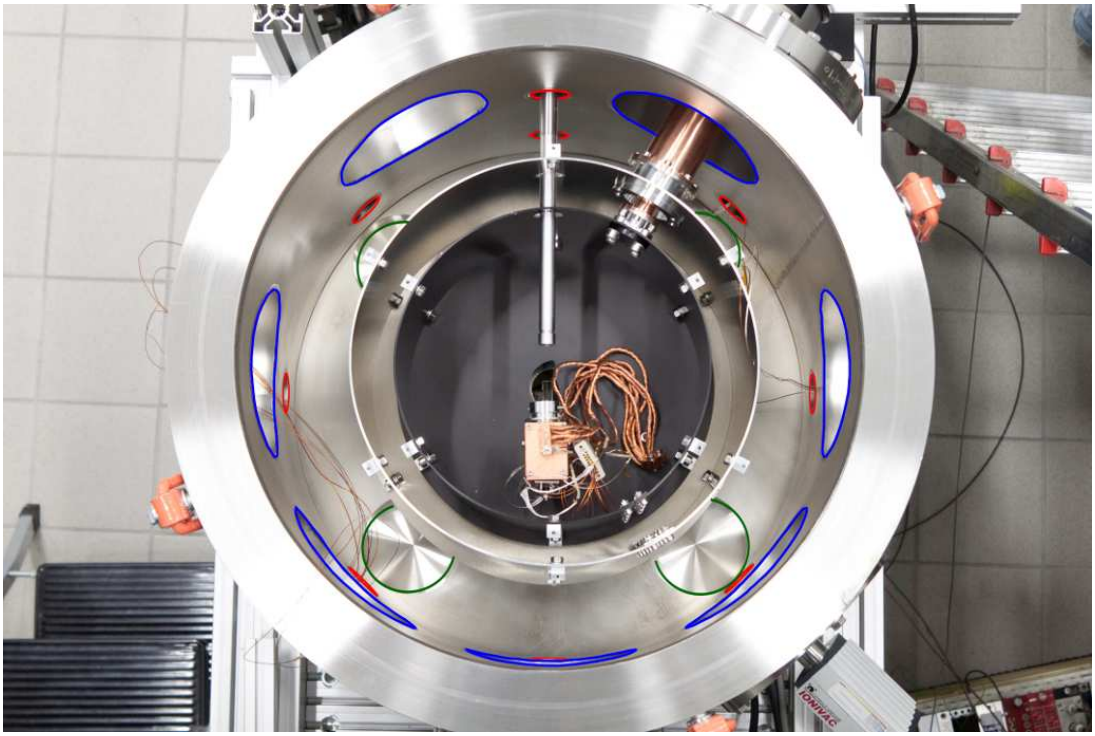

Figure 5.25.: Top view of the scattering chamber with the cold shield already installed. The red circles indicate the CF40 flanges. Eight of them are equidistant distributed. The blue circles indicate the CF160 flanges. Five of them are positioned above CF40 flanges. The bottom and top flange each have four CF100 flanges grouped around a centered CF160 flange (not visible in this picture). The inner cold shield has been anodized and dyed black.

The CF40 flange in the top array of the cylinder is used for the light path. A T-piece, in which the lens to focus the light beam is placed, is connected to it and ends in the MgF_2 window which is on the other side O-ring sealed to the vacuum monochromator (see also figure 5.9). On the opposing side the CF160 flange is used for the turbo molecular pump. The three CF160 flanges on the right side of the CF40 flange are used to access the inner part of the setup if the top flange is closed. On the other side of the CF40 the cold head is placed. As it is welded on a CF200, only the position close to the CF40 offers enough space to accomondate the cold head. On the bottom CF40 flanges feed throughs for the PMT high voltage, the PMT signal and the PT100 signals are mounted.

As a larger chamber is used and the vacuum should be improved, a Leybold Turbovac 340M (340 l/s, on a CF160 flange) is used. The prevacuum is pumped with a Leybold Scrollvac SC 5 D (5.4 m^3/h). The turbo molecular pump has a magnetical bearing and thus works without grease that could evaporate and cover the sample surface. The backing pump is also dry thus avoiding all contamination risks. It is also used to back the turbo molecular pump Pfeiffer TMU 071P used at the vacuum monochromator. To avoid long running times of the backing pump, a buffer volume with a two set point vacuum gauge, an electronically controlled pneumatic valve and an electronic unit have been added to the setup (see also figure 5.26). The lower set point of the vacuum gauge has been set to a pressure (0.01 mbar) close to the minimum pressure reachable with the Scrollvac, the

higher to the maximum inlet pressure of the Turbovac (0.09 mbar). If the pressure falls between these values, the Scrollvac will be turned on. The pneumatic valve will be opened two minutes after the backing pump is started to avoid a rise in pressure as the backing pump is vented each time it is turned off.

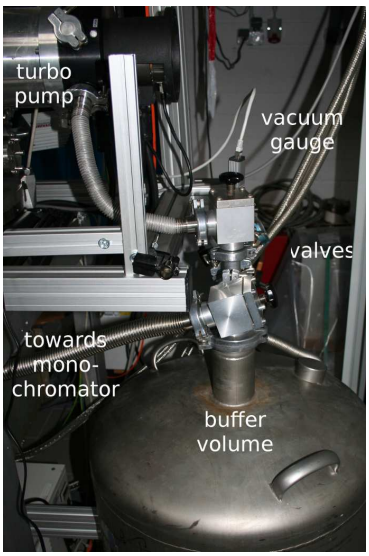

Figure 5.26.: Buffer volume with valves and pumping lines to the turbo molecular pumps.

A cold head of type Leybold RPK 1500 E is used to cool a two stage cold shield. Its first stage can supply at a temperature of 80 K a power of 12 W, the second stage supplies 2 W at 20 K. The helium lines of the cold head are connected to a compressor which needs to be supplied with cooling water. The cold shield was designed with the above mentioned

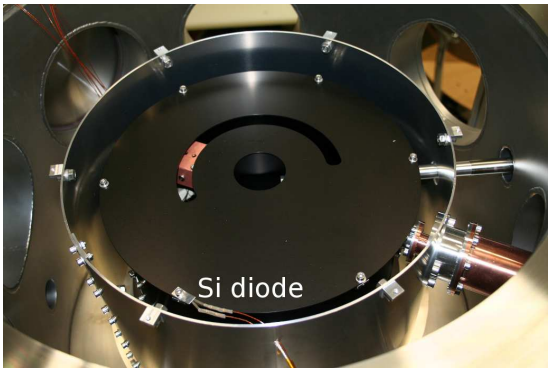

(a) Top view with closed inner cold shield. The open half circle has been included to enable the feed through of copper braids for a separate cooling of the PMT.

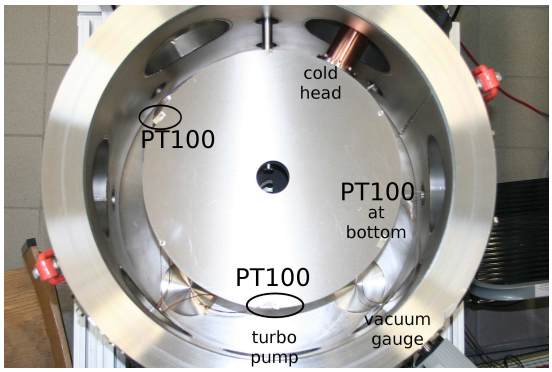

(b) Outer cold shield with the positions of the PT100s marked.

Figure 5.27.: Two stage cold shield with temperature sensors.

power values in mind (see reference [Spr11]). For the calculations cylinders with covers on both ends were assumed for the cold shield shape and the heat loss due to radiation respectively heat conductance has been calculated for equidistant spacing with the only contact between the cold shields being the Teflon rods mechanically supporting the inner cold shield. As the emission and transmission coefficients of the material as well as the

absolute temperature in the lab were not known, a conservative design with a spacing of 80 mm between vacuum vessel and outer cold shield and 40 mm between outer and inner cold shield has been chosen. A picture of the open cold shield can bee seen in figure 5.25, the closed inner shield is shown in 5.27(a) and the closed outer shield can be seen in figure 5.27(b).

Three platinum temperature dependent resistors PT100 of type C have been installed at the outer cold shield for temperature reading. One is fixed to the bottom of the outer cold shield under a screw close to the cold head, one at the top close to the turbo molecular pump and another one at the top close to the light feed through (see also figure 5.27(b)). Two additional PT100s have been installed in the PMT case. A Silicon diode[6] has been attached to the inner cold shield (see also figure 5.27(a)) with the cabling feed through a small hole in the outer shield.

Due to some offset behavior of the PT100 readout when turning on the pumps, only relative temperatures with large errors values can be given. The temperature at the outer cold shields was decreased by about 170 K from room temperature thus being at about 120 K. The temperature on the inner cold shield has been measured with a Silicon diode to decrease to about 80 K, while the temperature at the second stage of the cold head was measured with an internal sensor at the cold head to reach 24 K. The intended temperature values have not been reached. The difference between design and reached temperature can be attributed to several points. The calculations assumed fully closed cylinders for both cold stages. This is not true as several holes have been introduced to place the PMT and the PTFE sample, to allow separate cooling of the PMT, for feed throughs and to let the light into the inner cold shield (see also figure 5.27). Hence, even the inner cold shield gets radiation impact from the warm surrounding surfaces. In addition spacial restrictions at the cold head reduced the available space for the connectors to the cold shield. Here the distances between the cold shields is reduced below the design values. The components inside the inner volume of the cold shields are also cooled due to heat radiation. Although having no direct contact to either shield the temperature at the PMT is reduced by about 120 K.

Still the cold shield improved several aspects of the experiment:

- The vacuum inside the scattering chamber has been improved to be below $3 \cdot 10^{-8}$ mbar at the measuring point outside the cold shields[7].
- The total background due to light leaking into the chamber and due to reflected light from the walls has been reduced.

The sample holder is mounted from the top on a 3d movement table with a rotation feed through. The holder itself is build to accommodate 4 different PTFE samples of dimensions 12 mm × 6.5 mm × 5 mm. They are positioned to face the light beam with the angles $\tilde{\varphi}_i = 0\,^\circ$, $\tilde{\varphi}_i = 3\,^\circ$, $\tilde{\varphi}_i = 12\,^\circ$ and $\tilde{\varphi}_i = 20\,^\circ$. A picture of the sample holder is shown in figure 5.28.

By moving the measurement table in y-direction, different samples are moved to face the beam. As the table has a range of 25 mm, only three pieces can be moved into the

[6] LakeShore DT-471-SD, measurement current for the read out 10 μA

[7] The vacuum inside the inner cold shield is expected to be even better. The pressure values could not be determined more accurately as the gauge had to be turned off during the measurement as it produced too much light even with the cold shields protecting the PMT.

investigation position[8]. At $y = 3\,\text{mm}$ the center of the 12 ° sample faces the beam spot, at $y = 12\,\text{mm}$ the 3 ° sample and at $y = 21\,\text{mm}$ the sample facing the light beam can be investigated. This positioning has been checked by monitoring optical light transmitted through the light path on the sample via a window flange and some holes in the cold shields from the side with an accuracy of 0.1 mm. During experiments the window flange is covered with a light tight cap.

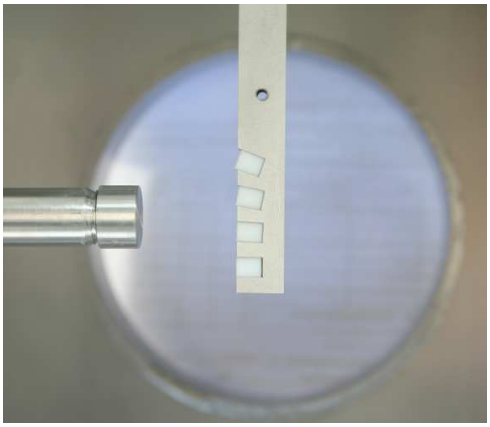

Figure 5.28.: Sample holder mounted inside the chamber. On the left the beam collimator is visible.

The PMT is mounted from the bottom on a 3d movement table with rotational feed through. A check has been conducted to make certain that the rotational center of the PMT movement is in the center of the large vacuum chamber with a positioning accuracy of $\pm 1\,\text{mm}$.

The PMT[9] high voltage is supplied via an ISEG NHQ 224M high voltage supply. Its signal is fed into an ORTEC timing filter amplifier[10] to amplify and shape the signal. Then a CAEN Mod. N979 fast amplifier is used to increase the amplitude by a factor of 10. The resulting signal is fed into an ORTEC Model 406A single channel analyzer[11] whose output can then be counted in a counter. As manual counter a CAEN MOD. N1145 has been used. For automated measurements the signal is fed into the counter of a NI6008 USB ADC. The angular movement of the PMT has been automated with a step motor that is controlled via a LabView program. A 96-teeth gear wheel is mounted on the PMT rotation feed through, the motor gear wheel has 24 teeth. Thus one step of the motor corresponds to 0.45 °.

[8] Initially it was planned to use a different feed through with a range to access all samples, but it proved to be unstable.
[9] Serial number LV1094
[10] Settings: coarse gain: 20, fine gain: 2, integrating: 50 ns, differentiating: 20
[11] threshold 0.6 V

5.4. Measurements

In this section a short overview of the measurements and their problems will be given.

5.4.1. Alignment

The alignment of the system is very important for the measurements. Deviations from the ideal geometry lead to structures in the data that can easily be misinterpreted to be caused by a different effect.

For these measurements the rotation center of the PMT has been adjusted to be in the center of the chamber by determining the distance of the PMT to the chamber walls. The positioning had an accuracy of 1 mm. The position of the PMT in the plane perpendicular to the beam axis has been chosen to be in the maximum of the 2d beam profile.

To align the sample holder laterally, a measurement with the PMT facing the beam spot was conducted. The sample was aligned parallel to the beam and moved to a position where it does not cover the beam any more ($x = 15\,\mathrm{mm}$). Then the intensity of the beam was measured while the sample was rotated (see figure 5.29).

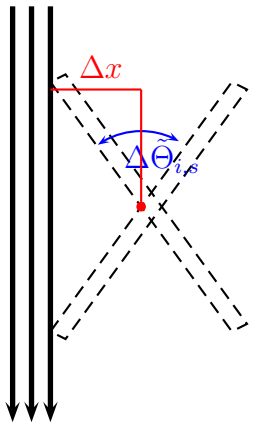

(a) Schematic drawing of PTFE positioning measurement. The maximum rate is measured at the PMT, if the PTFE does not block the beam. The distance of the center of rotation in this measurement to the position it needs to be in for the reflectivity measurement is given by $\Delta x = \frac{l_{\mathrm{PTFE}}}{2} \sin \frac{\Delta\tilde{\Theta}_{i,s}}{2}$

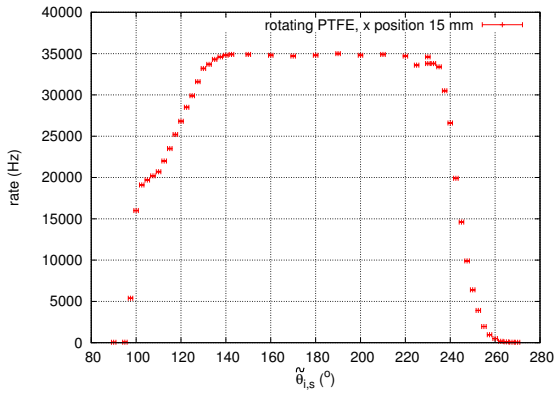

(b) Measurement to determine the PTFE positioning for the sample at $x = 15$ mm. Between the angles $\tilde{\theta}_{i,s}$ =140°and $\tilde{\theta}_{i,s}$ =230°the PTFE does not block the beam. Thus the sample needs to be moved to $x = x - \Delta x = 15\,\mathrm{mm} - 6\,\mathrm{mm} \cdot \sin\frac{90^\circ}{2} = 10.75$ mm. The center of the plateau corresponds to the sample being aligned parallel to the beam ($\tilde{\theta}_{i,s} = \tilde{\theta}_i + 95^\circ$).

Figure 5.29.: Determining the sample positioning.

The alignment of the rotation centers relative to each other has been checked by checking the position of the specular peaks. As the peaks turned out to be relatively broad, the precision of this alignment is not known.

Problems

Several problems related to the geometrical alignment of the setup have been noted during the measurements and while analyzing the data:

- **distances:** The distances between the components, specifically between PMT and sample couldn't be measured directly in the setup, as the access was restricted by the cold shields when everything was implemented. The distances were instead derived from the measured distance between collimator and PMT in combination with the assumption that the sample was positioned at the center of the chamber. The simulations use the distance between sample and PMT. Changes of this distance directly influences analyzed reflectance as the solid angle seen by the PMT changes and therefore also the simulated reflected intensity.
  For these measurements the distance of the sample to the PMT, d_{det}, has been extracted to be

$$d_{\text{det}} = 30(\pm 2)\,\text{mm}. \tag{5.14}$$

  The simulations have been conducted with $d_{\text{det}} = 30\,\text{mm}$. The solid angle and thus the seen intensity can change within the stated error by about 20 %.

- **center of rotation:** The alignment of the centers of rotation have been done with respect to the outside geometry and with limited precision. This can lead to different rotation centers for the sample rotation and for the PMT movement. In the measurements this can be indicated by specular peaks whose positions are shifted with respect to the expected positions. The size of the shift should change with the angle of incidence, it should be most prominent for large angles of incidence.
  If the center of the rotation of the PMT is positioned *behind* the center of rotation of the sample[12], reflected light from the sample will be blocked at high viewing angles θ_o, resulting in a cutoff of the reflected light distribution (see also figure 5.30). The cutoff should also be more prominent for larger angles of incidence. As the PMT with aperture will in the case of mismatching rotation centers not look directly onto the sample, the solid angle and thus the light intensity changed.

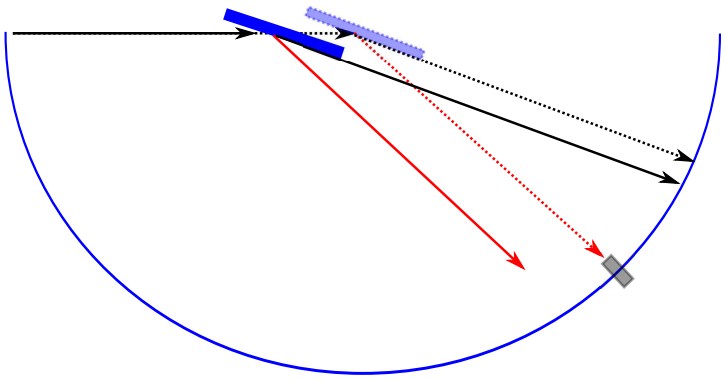

Figure 5.30.: Mismatched rotation centers: The dotted lines denote the ideal position of the sample with the specular reflected ray (red) and a light ray indicating the maximum reflection angle. The solid lines denote a sample shifted relative to the ideal position. The resulting spectra should show the specular peak at a shifted angle and exhibit a cutoff. Please note that the size of the shift is greatly exaggerated.

Due to the above-mentioned points, rather large, systematic effects are possible. They can be reduced by improving the alignment procedure. As the focus of this thesis has been the setup and commissioning of the experiment, the setup has after these measurements been

[12]Behind denotes here further away from the collimator.

handed over to the next phd student, C. Levy Brown, who conducted extensive, time-consuming measurements for a correct alignment of all components with which results with improved systematics could be obtained [Lev13].

5.4.2. Procedure for reflectivity measurements

A measurement to determine the reflectivity of a sample consists of several data sets taken for different $\tilde{\theta}_d$, $\tilde{\theta}_i$ and $\tilde{\varphi}_i$. The change of the angle $\tilde{\theta}_d$ is automated, therefore one data subset is taken for fixed angles $\tilde{\theta}_i$ and $\tilde{\varphi}_i$.

As the intensity can change *e.g.* due to degradation of the Mg_2F window in the run of irradiation with VUV light, the total light intensity is monitored before and after taking a measurement set[13]. For this the PTFE sample is removed from the beam to the position $x = 15\,\text{mm}$ and aligned parallel to the beam with the sample scale showing $\tilde{\theta}_{i,s} = 185\,°$ corresponding to $\tilde{\theta}_i = 90\,°$. The PMT rate is measured in steps of $0.9\,°$ at the positions between $\tilde{\theta}_{d,s} = 23.5\,°$ and $\tilde{\theta}_{d,s} = -140\,°$ on the PMT scale[14]. An example beam spot measurement can be seen in figure 5.31.

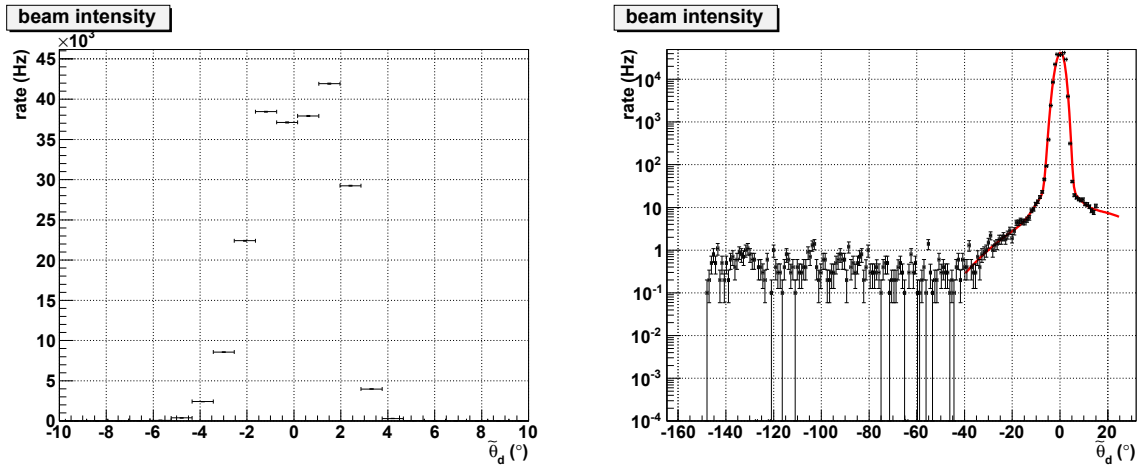

(a) Beam spot

(b) Beam spot, logarithmic

Figure 5.31.: Total beam intensity. A clearly focused beam is visible between $\tilde{\theta}_d = -4\,°$ and $4\,°$. Looking at the beam spot in logarithmic scale, unfocused parts due to misalignments becomes visible.

Setting the sample holder on the position $x = 10.75\,\text{mm}$ and adjusting the y position of the holder that the beam hits a PTFE sample, a data set with the PMT being moved from $\tilde{\theta}_{d,s} = 10\,°$ to $\tilde{\theta}_{d,s} = -140\,°$ is taken for the PTFE angles of $\tilde{\theta}_{i,s} = 175\,°/\tilde{\theta}_i = 80\,°$ to $\tilde{\theta}_{i,s} = 95\,°/\tilde{\theta}_i = 0\,°$ in steps of $10\,°$ and additionally for $\tilde{\theta}_{i,s} = 140\,°/\tilde{\theta}_i = 45\,°$. Such a set of measurements is shown in figure 5.32. This is repeated for different y-positions of the PTFE sample holder to measure the reflected intensity for different $\tilde{\varphi}_i$.

[13] The dependence of the light intensity on the turn on as well as the running time has been investigated in [Spr11] and was considered for the measurements.

[14] At the position of $\tilde{\theta}_{d,s} = 8.5\,°$ on the PMT scale the PMT is facing the beam spot. This corresponds to the angle $\tilde{\theta}_d = 0\,°$.

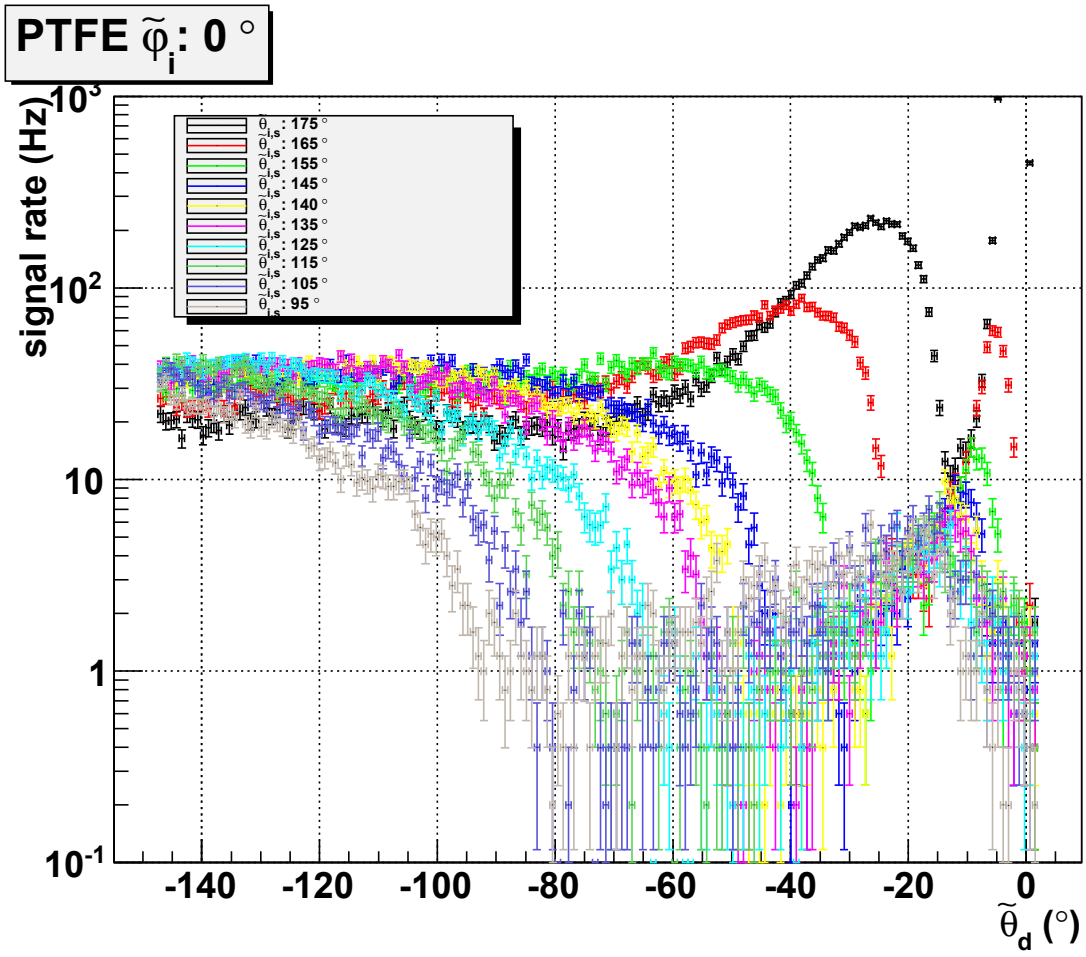

Figure 5.32.: Example for a set of measurements with $\tilde{\varphi}_i = 0\,°$. No background corrections applied.

5.4.3. Measurement overview

Two different PTFE samples have been investigated. For the both a complete measurement set for the angles $\tilde{\varphi}_i = 0\,°$, $3\,°$ and $12\,°$ has been performed for the wavelength $\lambda = 178.3(\pm 2.3)$ nm.

To test the wavelength dependence of the reflectivity, measurements for $\tilde{\varphi}_i = 0\,°$ and all $\tilde{\theta}_i$ have been taken with the first PTFE sample for $\lambda = 165.5(\pm 2.4)$ nm and $198.7(\pm 2.2)$ nm. In addition measurement points for $\tilde{\varphi}_i = 0\,°$, $\tilde{\theta}_i = 10\,°$ and $\tilde{\theta}_{d,s} = -130.4\,°$ and for $\tilde{\varphi}_i = 12\,°$, $\tilde{\theta}_i = 50\,°$ and $\tilde{\theta}_{d,s} = -120\,°$ have been taken for wavelength between $163.5(\pm 2.4)$ nm and $299.3(\pm 1.9)$ nm. A list of all measurements can be found in table 5.1.

Table 5.1.: Measurement overview

Sample	λ (nm)	$\tilde{\varphi}_i$	$\tilde{\theta}_i$	$\dot{\theta}_{d,s}$
1	178.3($\pm$2.3)	0 °	0 ° to 80 ° (10 ° steps) + 45 °	-130 ° to 10 ° (0.9 ° steps)
1	178.3($\pm$2.3)	3 °	0 ° to 80 ° (10 ° steps) + 45 °	-130 ° to 10 ° (0.9 ° steps)
1	178.3($\pm$2.3)	12 °	0 ° to 80 ° (10 ° steps) + 45 °	-130 ° to 10 ° (0.9 ° steps)
2	178.3($\pm$2.3)	0 °	0 ° to 80 ° (10 ° steps) + 45 °	-130 ° to 10 ° (0.9 ° steps)
2	178.3($\pm$2.3)	3 °	0 ° to 80 ° (10 ° steps) + 45 °	-130 ° to 10 ° (0.9 ° steps)
2	178.3($\pm$2.3)	12 °	0 ° to 80 ° (10 ° steps) + 45 °	-130 ° to 10 ° (0.9 ° steps)
1	165.5($\pm$2.4)	0 °	0 ° to 80 ° (10 ° steps) + 45 °	-130 ° to 10 ° (0.9 ° steps)
1	198.7($\pm$2.2)	0 °	0 ° to 80 ° (10 ° steps) + 45 °	-130 ° to 10 ° (0.9 ° steps)

5.5. Analysis

5.5.1. Analysis principle

To be able to extract the reflectance $\rho(\theta_i)$ (see eq. 5.5) from the measurements, one has to consider several things:

- The experimental data sets have been measured with the angle $\tilde{\theta}_{d,s}$ shown on the rotation feed through of the PMT. To correct the angle for an offset to the angle $\tilde{\theta}_d$ (see figure 5.5) the beam profile has been measured and fitted. The middle of the profile has been determined and the offset used to correct all data sets of this run.
- The initial light beam shows some tails that can pass the PTFE sample when tilted for reflection measurements. Therefore, the beam profile measurement has been subtracted from the reflected data sets. As soon as the resulting rate droops below zero (the light is blocked by the sample), it is set to zero. An example is shown in figure 5.33.
- The beam or reflection profiles are measured with a detector with an aperture of $d_{\mathrm{ap}} = 3\,\mathrm{mm}$ positioned at a distance of $z_1 = 30\,\mathrm{mm}$ to the rotation center in the angular range between $\tilde{\theta}_d = -140\,^\circ$ and $\tilde{\theta}_d = 0\,^\circ$ with a step size of $\Delta\tilde{\theta}_d = 0.9\,^\circ$. Hence, they are discrete convolutions of the real spectra with the detector aperture. In order to obtain the relevant rates $\dot{N}_i$ respectively $\dot{N}_o(\theta_i)$, Monte-Carlo-simulations on the basis of different assumptions of the initial beam respectively the reflection process have been conducted and were fitted to the data. The measured rate $\dot{N}$ is then obtained as the product of the input rates $\dot{N}_{\mathrm{MC}}$ of the simulations and the fit parameter for the amplitude. The simulation and fit programs are described in the next sections and examples for the analysis are shown. For the fits a Minuit adaptation of H. Barth has been used.

5.5.2. Total intensity

To determine the reflectance with equation (5.5), the incoming rate $\dot{N}_i$ is needed. As the measured beam profile is a convolution of the initial beam profile and the discrete detector positions, a Monte-Carlo-simulation of the beam profile has been set up. The detector positions are implemented in the simulations characterized by the parameters r, z_0, z_1 and α, with r being the aperture radius of the detector, z_0 the distance between

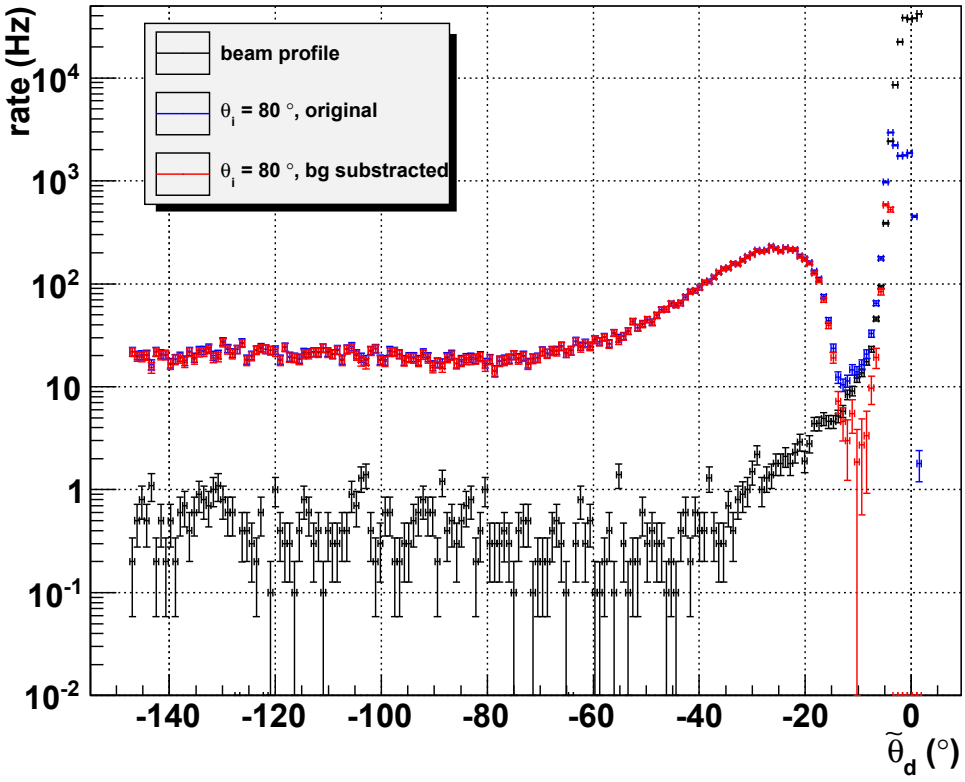

Figure 5.33.: Example measurement showing the 80 ° reflection with background. One can clearly see the contribution of the original beam passing the sample at $\tilde{\theta}_d > -13\,°$. An excess of light can still be found for the background subtracted sample at angles above $-10\,°$. This can be attributed to light being emitted from the side of the sample (see also figure 5.10).

the rotation point and the collimator aperture, z_1 the distance between the rotation point and the position of the detector aperture and α the rotation angle by which the detector is rotated from the z-axis (see also figure 5.34). To simulate the beam, light rays are crated at the collimator aperture ($z = 0\,\mathrm{mm}$, $r_{\mathrm{app}} = 1.5\,\mathrm{mm}$) following a to be specified distribution, *e.g.* homogeneous or Gaussian, with their velocity vector pointing with a cosine distribution in forward directions restricted by a maximum opening angle. The exact opening angle is unknown as the alignment of the lens system is not exact. Therefore the fits have been conducted for several opening angles. For each light ray each detector position is tested whether it can detect the light, by propagating the light to the position z_0, rotating the ray into a coordinate system rotated by the angle α around the x-axis, propagating it to the position of the detector aperture and testing whether the ray arrives within the detector aperture radius r: $r_\gamma = \sqrt{x'_\gamma(z_1)^2 + y'_\gamma(z_1)^2} < r$. If a ray can be detected in a certain detector position, the number of counts for this position is increased by one.

The simulated data points are included in a fit program in C via a header file. To get a continuous function from the discrete points, a linear interpolation is used.

The output of the simulated beam spot fails to describe the data. The simulated beam profiles are symmetric in contrast to the measured which show asymmetric slopes. Sim-

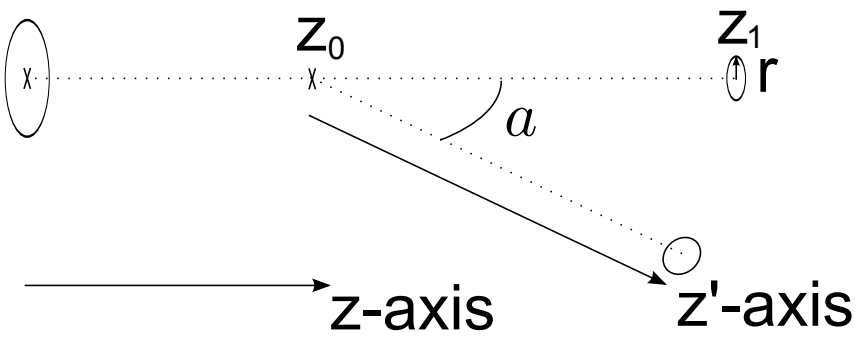

Figure 5.34.: Illustration of the detector implementation for the beam spot simulation.

ulated beam profiles with comparable slopes do show a flat plateau in the middle, while the measured beam profile shows some structure on top of the plateau (see figure 5.35). The deviation of the measured beam profile from the simulated shape can be attributed to some misalignments in the lens system. To be able to fine tune the position of the lens, the holding structure of the lens was designed to be movable. This turned out to be problematic as the structure could thus tilt inside the beam tube. The holding structure and its alignment will be improved.

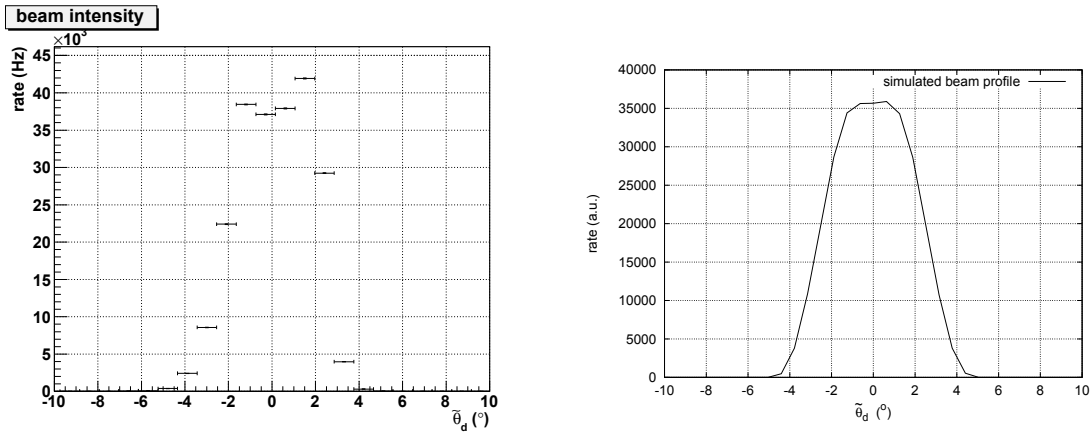

(a) Measurement.

(b) Monte-Carlo-simulation.

Figure 5.35.: Beam spot with Monte-Carlo-simulation.

As these test measurements are a proof of principle and no highly precision measurements, the incoming rate has been estimated. The general shape of the beam profile indicates that the initial beam spot size is smaller than the detector aperture, as an approximate plateau with steep slopes leading to it were measured. The length of the plateau corresponds to the aperture size of the detector. Thus the rate measured at one point of the plateau corresponds to the complete initial rate $\dot{N}_i$ which can then be used for further evaluation. As the plateau includes some fluctuations, the initial rate times the detection efficiency is

$$\dot{N}_i = 3.885(\pm 0.21) \cdot 10^4\,\mathrm{Hz}. \tag{5.15}$$

5.5.3. Reflected data sets

To determine the rate $\dot{N}_o(\theta_i)$ needed for equation (5.5) from the reflected data set, simulations for all settings of $\tilde{\theta}_i$ and $\tilde{\varphi}_i$ employed in the experiment have to be conducted.

Data sets for diffuse and specular reflection are simulated solitary to allow determining their amplitude separately without making assumptions on their ratio.

The program has been constructed to simulate the whole reflection process, its output describing the intensity seen by the detector. Therefore simulations of the whole hemisphere in which light is reflected are possible (see figure 5.36).

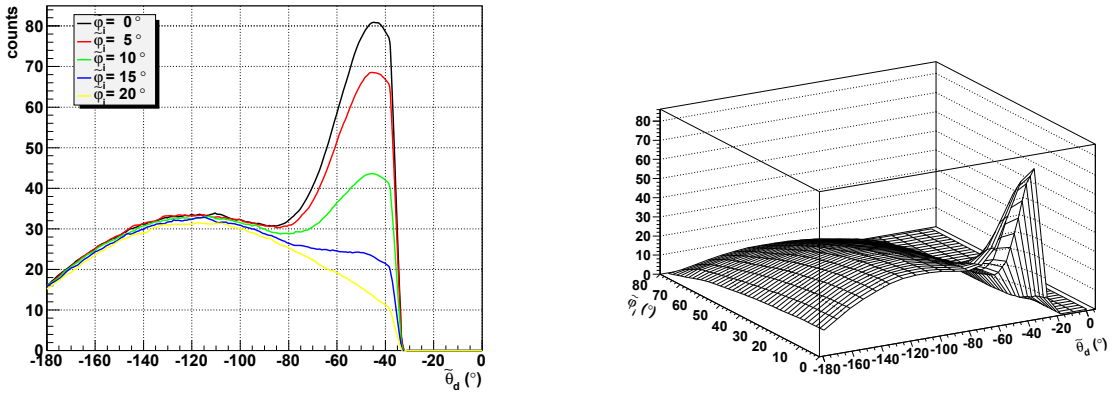

(a) Simulated intensity profiles in 2d.

(b) Simulated intensity profiles in 3d.

Figure 5.36.: Simulation of diffuse and specular intensity profile for different tilt angles $\tilde{\varphi}_i$ and an incident angle of $\tilde{\theta}_i = 70\,°$.

The output of the Monte-Carlo-simulation needs to be comparable to the data sets, therefore the angles $\tilde{\varphi}_i$ and $\tilde{\theta}_i$ that can be adjusted in the setup have been implemented as input parameters. The range and step size of the detector angle $\tilde{\theta}_o$ is the same for all data sets and therefore fixed in the simulation. As the reflection process as described in section 5.2.2 depend on the system angles θ_i, θ_o and φ_o, the experimental angles $\tilde{\theta}_i$, $\tilde{\theta}_d$ and $\tilde{\varphi}_i$ are converted using equations (5.8) to (5.11). Assuming the surface shows a certain roughness, the reflection process is influenced by it, as *e.g.* the specular peak broadens. The roughness can be characterized by the angle α, which is the deviation of the micro-surface normal vector $\vec{n}'$ from the overall surface normal vector $\vec{n}$ (see also figure 5.4(a)). In this simulations a Gaussian distribution of α is assumed with the width σ being an input parameter. In addition the rate $\dot{N}_{\mathrm{MC}}$ in the simulation can be adapted, changing the statistics and the computation time.

The simulation program uses a coordinate system with the overall surface normal vector aligned with the z-axis. In a first step the detector angles $\theta_{o,\mathrm{det}}$ and $\varphi_{o,\mathrm{det}}$ are computed from the input angles $\tilde{\theta}_i$ and $\tilde{\varphi}_i$ following the equations (5.9) to (5.11). The resulting normal vector pointing in the direction of the detector positions is then

$$\vec{n}_{\mathrm{det}} = \begin{pmatrix} \cos\varphi_{o,\mathrm{det}} \sin\theta_{o,\mathrm{det}} \\ \sin\varphi_{o,\mathrm{det}} \sin\theta_{o,\mathrm{det}} \\ \cos\theta_{o,\mathrm{det}} \end{pmatrix}. \tag{5.16}$$

The incoming light beam $\vec{k}_i$ is assumed to be spot like and can therefore be simply characterized with the angle θ_i. For each light ray a new surface normal $\vec{n}'$ is created following a random Gaussian distribution with the width σ around the overall surface normal $\vec{n}$. With the random numbers r_1 and r_2 between $[0:1)$ the x and y coordinates

of $\vec{n}'$ are

$$n'_x = 2\sqrt{-\ln 1 - r_1}\cos(2\pi r_2)\sigma \tag{5.17}$$

$$n'_y = 2\sqrt{-\ln 1 - r_1}\sin(2\pi r_2)\sigma. \tag{5.18}$$

In spherical coordinates this normal vector can also be described as

$$\vec{n}' = \begin{pmatrix} \cos\varphi' \sin\alpha \\ \sin\varphi' \sin\alpha \\ \cos\alpha \end{pmatrix}. \tag{5.19}$$

Hence, the z coordinate can be computed from n'_x and n'_y as

$$n'_z = \cos\alpha = \cos\left(\arcsin\sqrt{n'^2_x + n'^2_y}\right). \tag{5.20}$$

The reflected ray $\vec{k}_o$ needs to be constructed in reference to the new normal vector $\vec{n}'$. Therefore, a new coordinate system is introduced with the z^*-axis pointing into the direction of $\vec{n}'$. A vector is converted into a stared-vector in the new system by rotation with the angle α around the normalized rotation axis $\vec{a}$ (see also figure 5.37(a)). The vector $\vec{a}$ is perpendicular to both vectors $\vec{n}$ and $\vec{n}'$ and thus can be constructed as the cross product of the two vectors normalized by the sinus of the angle α between them:

$$\vec{a} = \frac{\vec{n} \times \vec{n}'}{\sin\alpha}. \tag{5.21}$$

A rotation matrix $R_{\vec{a}}(\alpha)$ for the rotation with angle α around the normalized vector $\vec{a}$ can be found in equation (B.1).

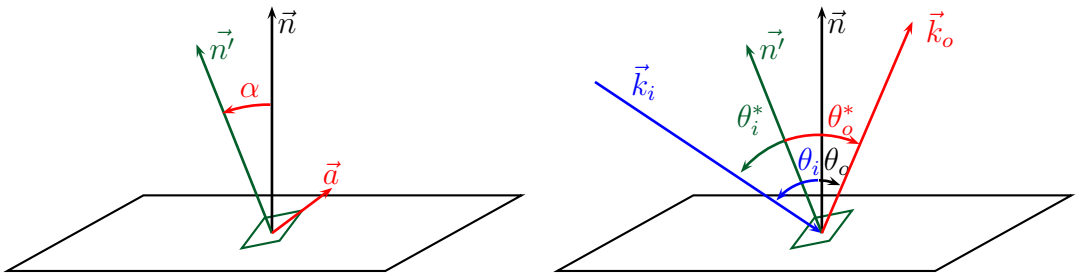

(a) Rotation from $\vec{n}$ to $\vec{n}'$

(b) Construction of the outgoing light vector from the micro-surface normal vector $\vec{n}'$.

Figure 5.37.: Illustration of the geometry steps in the simulation.

The diffuse reflection is independent of the incoming light vector. The distribution of the reflected light is given by equation (5.7). The angle θ^*_{diff} can be created from the random number $3_3 \in [0:1[$ via the relation: $\theta^*_{\text{diff}} = \arcsin\sqrt{r_3}$ (the deviation of this distribution is shown in appendix B.3).. For a 3-dimensional distribution the azimuthal angle φ^*_{diff} is created uniformly in $[0:2\pi)$ resulting in

$$\vec{k}^*_o = \begin{pmatrix} \cos\varphi^*_{\text{diff}} \sin\theta^*_{\text{diff}} \\ \sin\varphi^*_{\text{diff}} \sin\theta^*_{\text{diff}} \\ \cos\theta^*_{\text{diff}} \end{pmatrix}. \tag{5.22}$$

The specular reflection depends on the incident light ray. Hence, the vector $\vec{k}_i$ is then transformed into the new coordinate system:

$$\vec{k}_i^* = R_{\vec{a}}(\alpha) \cdot \vec{k}_i. \tag{5.23}$$

With the normal vector $\vec{n}'^*$ defining the z^*-direction, the reflected ray is

$$\vec{k}_o^* = \begin{pmatrix} -(\vec{k}_i^*)_x \\ -(\vec{k}_i^*)_y \\ (\vec{k}_i^*)_z \end{pmatrix} \tag{5.24}$$

The outgoing light vector $\vec{k}_o$ in the original coordinate system is obtained with a rotation around the axis $\vec{a}$ by the angle $-\alpha$

$$\vec{k}_o = R_{\vec{a}}(-\alpha) \cdot \vec{k}_o^*. \tag{5.25}$$

In order to take into account the geometrical cutoff blocking the light vectors that would pass into the surface (see section 5.3.1 and figure 5.4(b)), the angle θ_o between the overall surface normal $\vec{n}$ and the reflected ray $\vec{k}_o$ is tested. If it is bigger than 90 ° ($\cos\theta_o = \vec{\omega}_o \cdot \vec{n} < 0$), the ray will be rejected and cannot be detected in any detector position. Comparison between the simulation output and data (see figure 5.38) indicate that the geometrical cutoff needs to be applied for smaller angles θ_o. This can be attributed to the micro-surfaces having a length $l > 0\,\text{mm}$. If they are misaligned, a part rises out of the surface, thus blocking more light. Therefore, the blocking angle θ_o^{co} has been included as a changeable parameter.

In a final step the detection with the PMT has to be calculated. The opening angle ν_{det} of the detector aperture is given by the distance of the detector to the scattering center d_{det} and the radius of the detector aperture r_{app}

$$\nu_{\text{det}} = \arctan\frac{r_{\text{app}}}{d_{\text{det}}} = \arctan\frac{1.5\,\text{mm}}{30\,\text{mm}} \approx 0.05\,\text{rad}. \tag{5.26}$$

For each reflected light ray $\vec{k}_o$ the angle $\nu_{\text{light,det}}$ it encloses with each detector position characterized by the normal vector $\vec{n}_{\text{det}}$ is computed

$$\nu_{\text{light,det}} = \arccos(\vec{k}_o \cdot \vec{n}_{\text{det}}). \tag{5.27}$$

If this angle is smaller than the opening angle ν_{det}, the counter for this detector position is increased. A visualization of the detector implementation can be found in figure 5.39.

The output of the program is a tabular file with each line comprising the detector angle $\tilde{\theta}_d$, the rate N_{θ_f} for this position and the detector angle relative to the surface normal θ_o.

To optimize the matching between the data sets and the simulated data the following parameters have been varied in the simulation:

- the distribution of the micro-surfaces and
- the cutoff angle θ_o^{co}.

Specular and diffuse reflection are simulated separately, their ratio is determined by the fit.

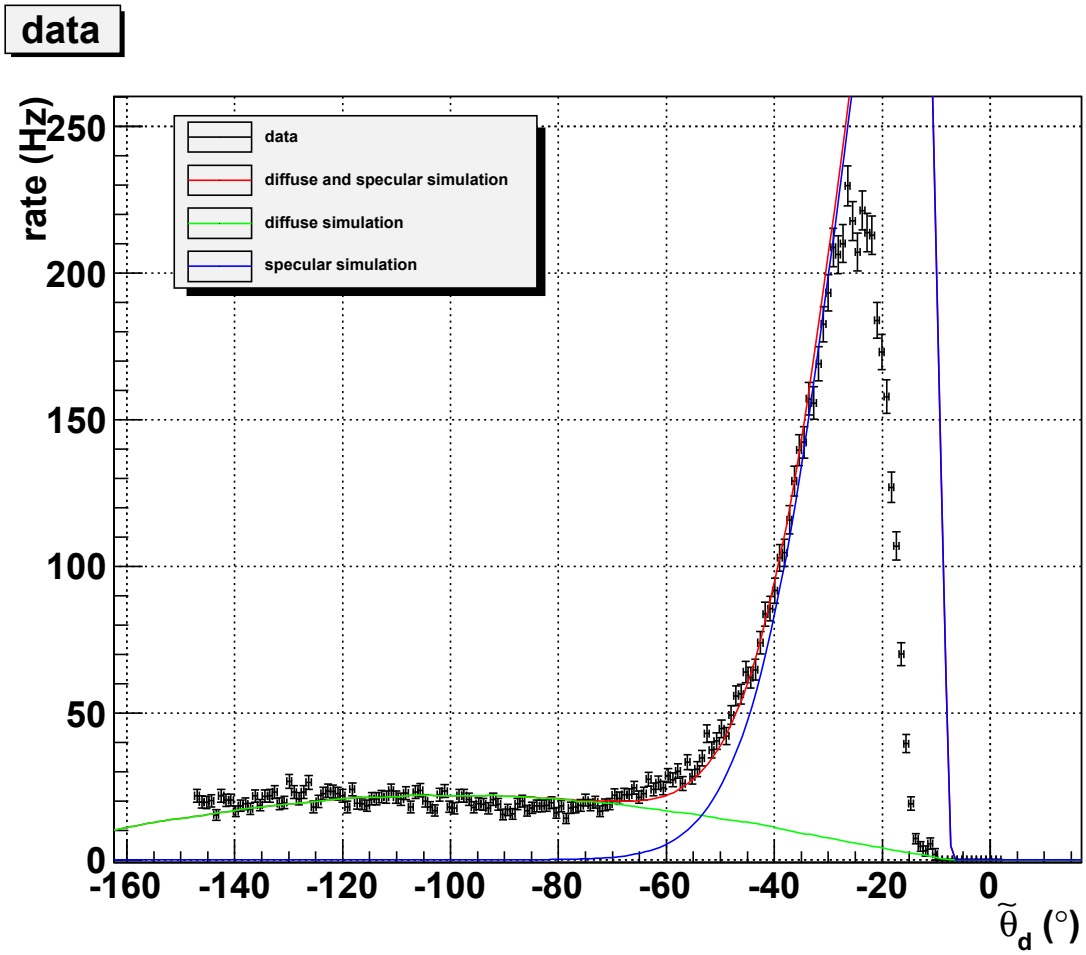

Figure 5.38.: Example of simulation with cutoff angle $\theta_o^{\text{co}} = 90\,^\circ$ and data for $\tilde{\theta}_i = 80\,^\circ$. The mismatch between data and simulation at high reflectance angles $\tilde{\theta}_d$ is clearly visible.

For the fits a Minuit adaptation of H. Barth has been used. The fit program uses a linear interpolation routine to be able to fit the discrete simulations to the data continuously. As the amplitude of the diffuse reflection should not change with angle of incidence, the data for all $\tilde{\theta}_i$ and $\tilde{\varphi}_i$ need to be fitted at the same time in a common fit using only one fit parameter a_{diff} for describing the diffuse reflection. Therefore, the complete simulated data set is included in header files and the measured data set is compiled into one file with the angle $\tilde{\theta}_d$ modified according to table 5.2. The amplitude of the specular peak is expected to decrease when viewing it from outside the plane encompassed by the normal vector $\vec{n}$ and the incident light ray $\vec{k}_i$ ($\tilde{\varphi}_i \neq 0\,^\circ$, see figure 5.36). This effect is already taken into account in the simulation as the complete reflection process is simulated, not only the rays relevant for the used detector angles. Therefore, the simulated specular data needs to be fitted to the experimental data for all $\tilde{\varphi}_i$ with the same amplitude $a_{\text{spec}}(\tilde{\theta}_i)$.

The fit function is defined section wise for each $\tilde{\theta}_i$ and $\tilde{\varphi}_i$ separately using the diffuse data from simulation for the given $\tilde{\theta}_i$ and $\tilde{\varphi}_i$ with the common amplitude a_{diff} and the specular data from the simulation for the given $\tilde{\theta}_i$ and $\tilde{\varphi}_i$ with the amplitude $a_{\text{spec}}(\tilde{\theta}_i)$

$$f_{\tilde{\theta}_i,\tilde{\varphi}_i}(\tilde{\theta}_{d,\text{mod}})|_{x<\tilde{\theta}_{d,\text{mod}}<x+200\,^\circ} = a_{\text{diff}} \cdot d^{\text{lin in}}_{\tilde{\theta}_i,\tilde{\varphi}_i}(\tilde{\theta}_d) + a_{\text{spec}}(\tilde{\theta}_i) \cdot s^{\text{lin in}}_{\tilde{\theta}_i,\tilde{\varphi}_i}(\tilde{\theta}_d), \tag{5.28}$$

with $d^{\text{lin in}}_{\tilde{\theta}_i,\tilde{\varphi}_i}(\tilde{\theta}_d)$ the linear interpolation of the diffuse simulated data set and $s^{\text{lin in}}_{\tilde{\theta}_i,\tilde{\varphi}_i}(\tilde{\theta}_d)$ the

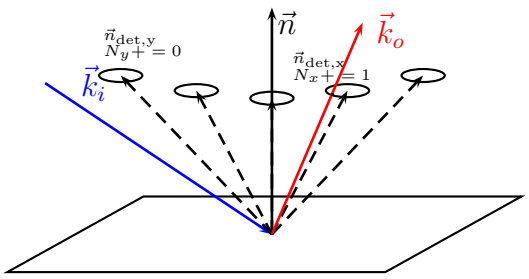

Figure 5.39.: Light detection in the detector positions.

Table 5.2.: Modification of detector angle for complete fit

$\tilde{\varphi}_i$	$\tilde{\theta}_i$	$\tilde{\theta}_{d,\mathrm{mod}}$	$\tilde{\varphi}_i$	$\tilde{\theta}_i$	$\tilde{\theta}_{d,\mathrm{mod}}$	$\tilde{\varphi}_i$	$\tilde{\theta}_i$	$\tilde{\theta}_{d,\mathrm{mod}}$
0 °	0 °	$\tilde{\theta}_d + 0\,°$	3 °	0 °	$\tilde{\theta}_d + 2000\,°$	12 °	0 °	$\tilde{\theta}_d + 4000\,°$
0 °	10 °	$\tilde{\theta}_d + 200\,°$	3 °	10 °	$\tilde{\theta}_d + 2200\,°$	12 °	10 °	$\tilde{\theta}_d + 4200\,°$
0 °	20 °	$\tilde{\theta}_d + 400\,°$	3 °	20 °	$\tilde{\theta}_d + 2400\,°$	12 °	20 °	$\tilde{\theta}_d + 4400\,°$
0 °	30 °	$\tilde{\theta}_d + 600\,°$	3 °	30 °	$\tilde{\theta}_d + 2600\,°$	12 °	30 °	$\tilde{\theta}_d + 4600\,°$
0 °	40 °	$\tilde{\theta}_d + 800\,°$	3 °	40 °	$\tilde{\theta}_d + 2800\,°$	12 °	40 °	$\tilde{\theta}_d + 4800\,°$
0 °	45 °	$\tilde{\theta}_d + 1000\,°$	3 °	45 °	$\tilde{\theta}_d + 3000\,°$	12 °	45 °	$\tilde{\theta}_d + 5000\,°$
0 °	50 °	$\tilde{\theta}_d + 1200\,°$	3 °	50 °	$\tilde{\theta}_d + 3200\,°$	12 °	50 °	$\tilde{\theta}_d + 5200\,°$
0 °	60 °	$\tilde{\theta}_d + 1400\,°$	3 °	60 °	$\tilde{\theta}_d + 3400\,°$	12 °	60 °	$\tilde{\theta}_d + 5400\,°$
0 °	70 °	$\tilde{\theta}_d + 1600\,°$	3 °	70 °	$\tilde{\theta}_d + 3600\,°$	12 °	70 °	$\tilde{\theta}_d + 5600\,°$
0 °	80 °	$\tilde{\theta}_d + 1800\,°$	3 °	80 °	$\tilde{\theta}_d + 3800\,°$	12 °	80 °	$\tilde{\theta}_d + 5800\,°$

linear interpolation of the specular simulated data set for the angles $\tilde{\varphi}_i$ and $\tilde{\theta}_i$ at the position $\tilde{\theta}_d$.

Looking at the experimental data (see figure 5.40) one can see that the diffuse amplitude is roughly the same for all $\tilde{\theta}_i$ but for $\tilde{\theta}_i = 80\,°$. This is attributed to the reduced incoming intensity due to light passing the sample. The effective length of the sample blocking the light path is reduced to $l_{\mathrm{eff}}(80\,°) = l_{\mathrm{sample}} \cdot \cos\tilde{\theta}_i \approx 2\,\mathrm{mm}$. Therefore, a factor $r_{\mathrm{red}}(80\,\mathrm{deg}) < 1$ is introduced into the fit. As the reduction of the reflected intensity does not only apply to the diffuse reflection, but also to the specular peak, the factor is multiplied to both factors for all data with $\tilde{\theta}_i = 80\,°$.

Initial values for the fit parameters are stored into a file labeled start.pun. The parameter names and their function are listed in table 5.3.

The fits are conducted for one simulated data set and the χ^2_r are determined. As the distribution of the micro-surfaces as well as the geometrical cutoff angle θ_o^{co} are fixed for one data set, fits for each simulation have to be conducted separately. The resulting χ^2_r were compared and the best simulation model determined.

During the fit process it turned out that the two input parameters of the simulation, the distribution of the micro-surfaces and the geometrical cutoff angle θ_o^{co}, needed to be adjusted at the same time.

The distribution of the micro-surfaces has been assumed to be Gaussian around the normal vector $\vec{n}$ with a changeable width σ (see equations (5.17), (5.18) and (5.20) in the previous section). Table 5.4 gives an overview of the χ^2_r results of some fits with different widths

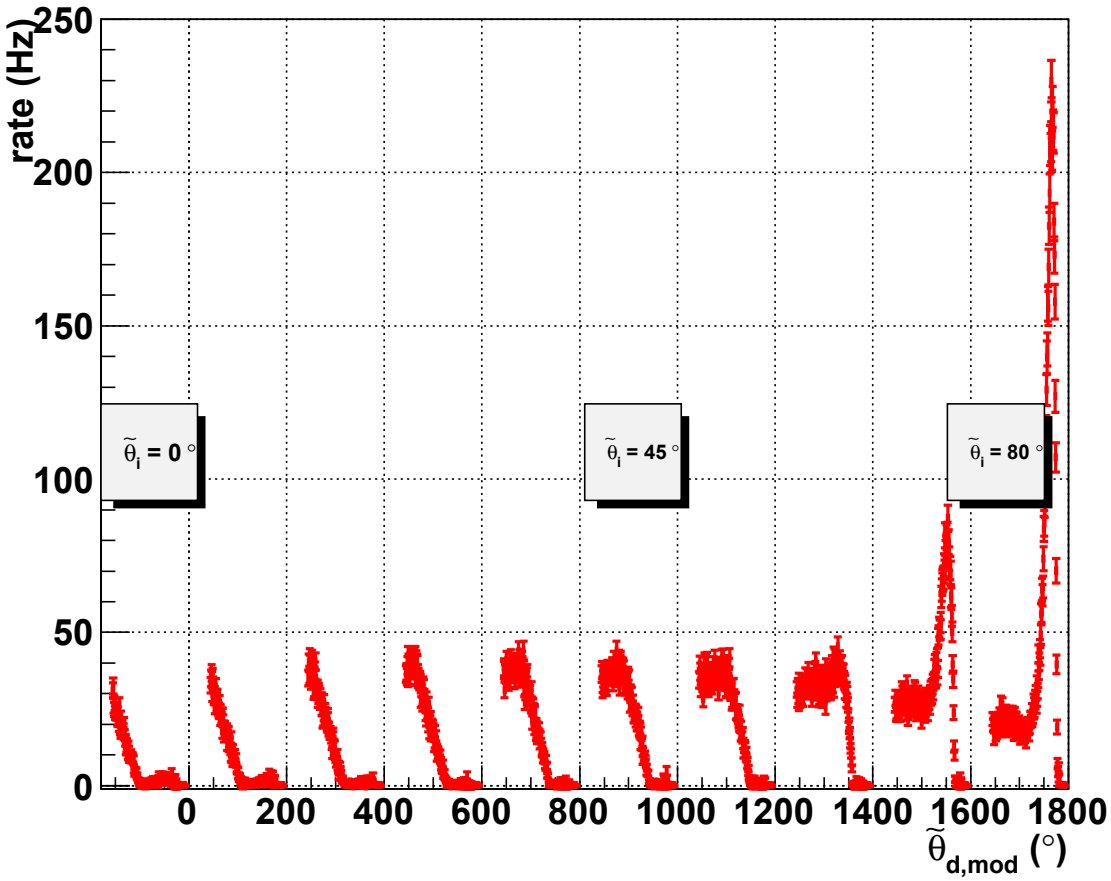

Figure 5.40.: Experimental data set for $\tilde{\varphi}_i = 0\,^\circ$ plotted against $\tilde{\theta}_{d,\mathrm{mod}}$. The amplitude for the diffuse reflection, as can be estimated by eye, is the same for each data subset at small angles $\tilde{\theta}_{d,\mathrm{mod}}$. Comparing the diffuse amplitude for $\tilde{\theta}_i = 80\,^\circ$, it is lower. This can be attributed to parts of the incoming light not being reflected, but passing the sample as it does not completely block the light path (see also figure 5.33).

σ and different cutoff angles θ_o^{co} for sample 1.

Example fits for cutoff angles of $\theta_i^{\mathrm{co}} = 0\,^\circ$ and $\theta_i^{\mathrm{co}} = 5\,^\circ$ are shown for $\tilde{\theta}_i = 80\,^\circ$ in figure 5.41. It is visible that the model is not describing this data set well, in fact the major contribution to the overall χ_r^2 value arises from the mismatch for $\tilde{\theta}_i = 80\,^\circ$. A possible improvement is a change from the hard cutoff angle to a smeared, broader cutoff distribution, which will be tested in the future.

After obtaining the best fit, equation (5.5) can then be evaluated with the fit parameters. The reflected rate for a certain incoming angle $\tilde{\theta}_i$ is the simulated rate $\dot{N}_{\mathrm{sim}}$ times the fit amplitude for diffuse reflection plus the fit amplitude for specular reflection for this angle

$$\dot{N}_o(\tilde{\theta}_i) = \dot{N}_{\mathrm{MC}} \cdot a_{\mathrm{diff}} + \dot{N}_{\mathrm{MC}} \cdot a_{\mathrm{spec}}(\tilde{\theta}_i). \tag{5.29}$$

After determining the total rate $\dot{N}_0$ and the reflected rate $\dot{N}_{\mathrm{ref}}(\tilde{\theta}_i)$ the total reflectance

Table 5.3.: Fit parameter and their function

nr	parameter	function
1	a_{diff}	diffuse amplitude scaling factor, only one parameter for whole fit
2	$a_{\text{spec}}(0\,^\circ)$	specular amplitude scaling factor for $\tilde{\theta}_i = 0\,^\circ$
3	$a_{\text{spec}}(10\,^\circ)$	specular amplitude scaling factor for $\tilde{\theta}_i = 10\,^\circ$
4	$a_{\text{spec}}(20\,^\circ)$	specular amplitude scaling factor for $\tilde{\theta}_i = 20\,^\circ$
5	$a_{\text{spec}}(30\,^\circ)$	specular amplitude scaling factor for $\tilde{\theta}_i = 30\,^\circ$
6	$a_{\text{spec}}(40\,^\circ)$	specular amplitude scaling factor for $\tilde{\theta}_i = 40\,^\circ$
7	$a_{\text{spec}}(45\,^\circ)$	specular amplitude scaling factor for $\tilde{\theta}_i = 45\,^\circ$
8	$a_{\text{spec}}(50\,^\circ)$	specular amplitude scaling factor for $\tilde{\theta}_i = 50\,^\circ$
9	$a_{\text{spec}}(60\,^\circ)$	specular amplitude scaling factor for $\tilde{\theta}_i = 60\,^\circ$
10	$a_{\text{spec}}(70\,^\circ)$	specular amplitude scaling factor for $\tilde{\theta}_i = 70\,^\circ$
11	$a_{\text{spec}}(80\,^\circ)$	specular amplitude scaling factor for $\tilde{\theta}_i = 80\,^\circ$
12	$r_{\text{red}}(80\,\text{deg})$	Reduction of incoming intensity as a percentage of the incoming beam does not hit the sample for $\tilde{\varphi}_i = 80\,^\circ$

Table 5.4.: List of χ^2_r-fit results for simulations with changing cutoff angle θ_o^{co} and changing Gaussian distribution width σ fitted to the data set of sample 1.

	$\theta_o^{\text{co}} = 84\,^\circ$	$\theta_o^{\text{co}} = 83\,^\circ$	$\theta_o^{\text{co}} = 82\,^\circ$	$\theta_o^{\text{co}} = 81\,^\circ$
# rays	10^5	10^5	10^5	10^5
$\sigma = 4.00\,^\circ$	5.6	5.2	5.3	5.8
$\sigma = 4.50\,^\circ$	5.0	4.7	4.7	5.1
$\sigma = 5.00\,^\circ$	4.6	4.3	4.5	4.9
$\sigma = 5.50\,^\circ$	4.6	4.3	4.5	4.8
$\sigma = 5.75\,^\circ$	4.6	4.2	4.4	5.0
$\sigma = 6.00\,^\circ$	4.6	4.4	4.6	5.1
$\sigma = 6.25\,^\circ$	4.6	4.5	4.7	5.2
$\sigma = 6.50\,^\circ$	4.8	4.5	4.8	5.5
$\sigma = 7.00\,^\circ$	5.1	4.9	5.2	5.8

$\rho(\tilde{\theta}_i)$ can be calculated

$$\rho(\tilde{\theta}_i) = \frac{\dot{N}_o(\tilde{\theta}_i)}{\dot{N}_0}.$$

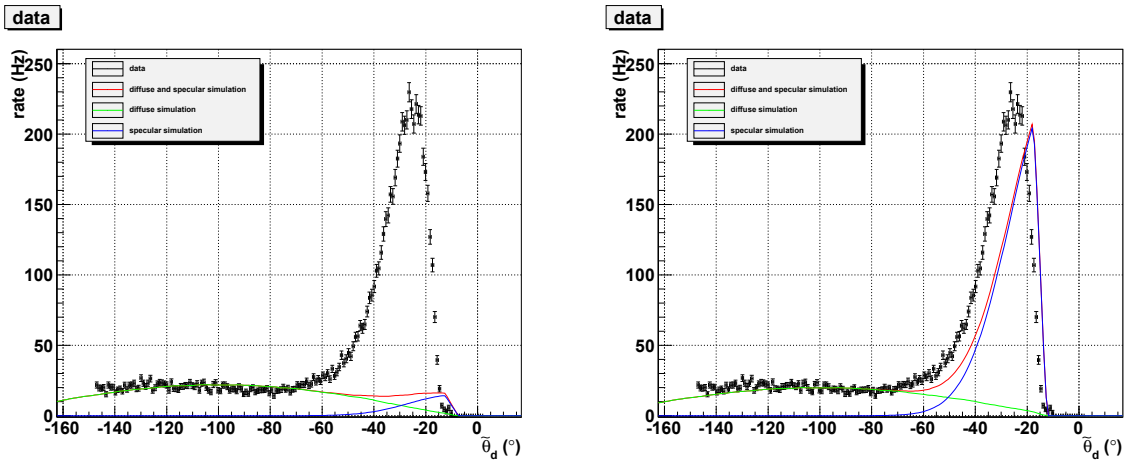

(a) Cutoff angle $\theta_i^{\mathrm{co}} = 0\ ^\circ$.

(b) Cutoff angle $\theta_i^{\mathrm{co}} = 5\ ^\circ$.

Figure 5.41.: Example for fits with different cutoff angles θ_i^{co}.

5.6. Results

In a first run of this experimental setup two different PTFE samples have been investigated. The first sample was milled out off commercially available PTFE. It has been cleaned in with alcohol. No additional surface treatment has been conducted.

The second sample has been produced from the same material. Its surface has been treated. The idea was to shape the surface by using the cold flow property of PTFE. The sample has been pressed with $2\,\mathrm{t}/(6.5\,\mathrm{mm} \times 5\,\mathrm{mm})$ for a period of 2 h. To guarantee that it still fits into the holding structure, a mold of the same dimensions as the holding structure in the experiment was prepared.

The analysis of the data taken for both samples follows the steps described in the previous section. Table 5.5 show the parameters used in the simulations to achieve the best fit.

Table 5.5.: Simulation parameters for the best fits achieved for the analysis of the two samples.

	sample 1	sample 2
θ_i^{co}	83 °	82 °
σ	5.75 °	4.0 °
χ_r^2	4.23	6.13

The fitted data is shown for sample 1 in figure 5.42, 5.43 and 5.44, for sample 2 in 5.45, 5.46 and 5.47. The fit parameters are listed in table 5.6 for sample 1 and in 5.7 for sample 2.

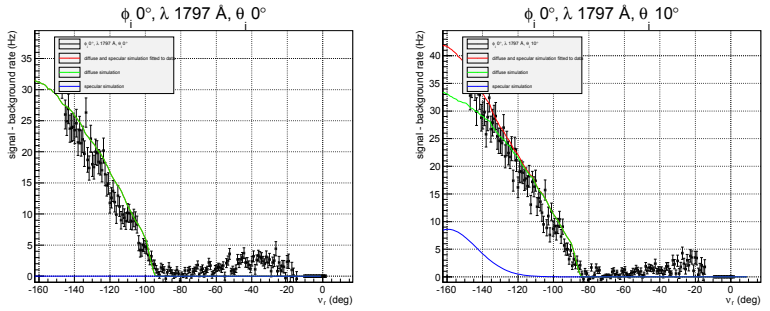

(a) $\tilde{\varphi}_i = 0\ ^\circ\ \tilde{\theta}_i = 0\ ^\circ$ (b) $\tilde{\varphi}_i = 0\ ^\circ\ \tilde{\theta}_i = 10\ ^\circ$

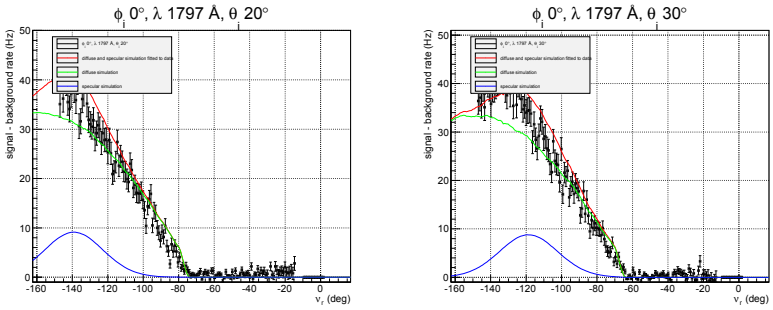

(c) $\tilde{\varphi}_i = 0\ ^\circ\ \tilde{\theta}_i = 20\ ^\circ$ (d) $\tilde{\varphi}_i = 0\ ^\circ\ \tilde{\theta}_i = 30\ ^\circ$

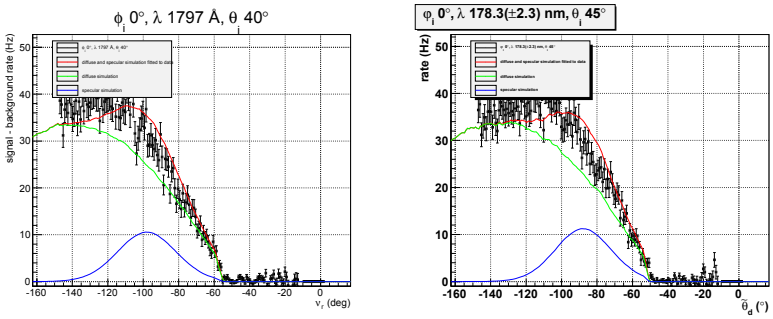

(e) $\tilde{\varphi}_i = 0\ ^\circ\ \tilde{\theta}_i = 40\ ^\circ$ (f) $\tilde{\varphi}_i = 0\ ^\circ\ \tilde{\theta}_i = 45\ ^\circ$

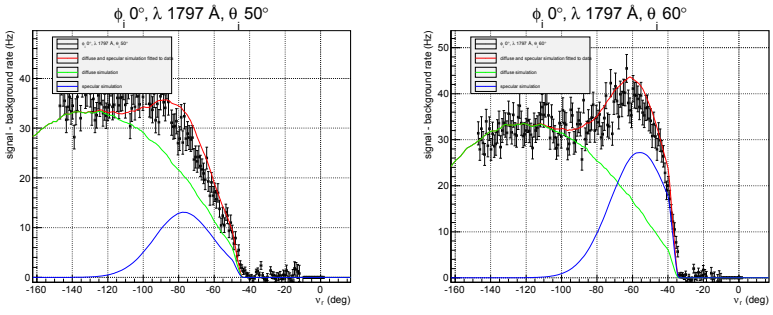

(g) $\tilde{\varphi}_i = 0\ ^\circ\ \tilde{\theta}_i = 50\ ^\circ$ (h) $\tilde{\varphi}_i = 0\ ^\circ\ \tilde{\theta}_i = 60\ ^\circ$

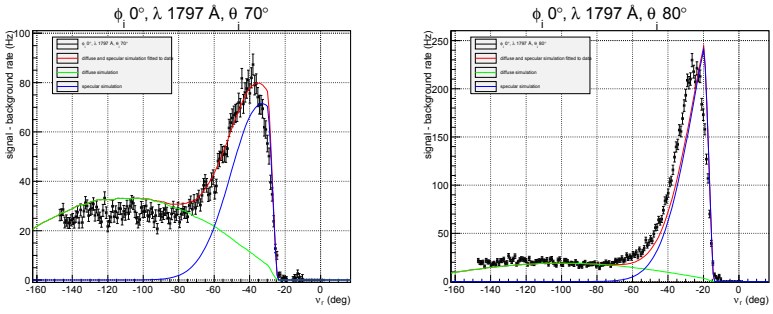

(i) $\tilde{\varphi}_i = 0\ ^\circ\ \tilde{\theta}_i = 70\ ^\circ$ (j) $\tilde{\varphi}_i = 0\ ^\circ\ \tilde{\theta}_i = 80\ ^\circ$

Figure 5.42.: Fit to data set of first sample, plots for $\tilde{\varphi}_i = 0\,^\circ$.

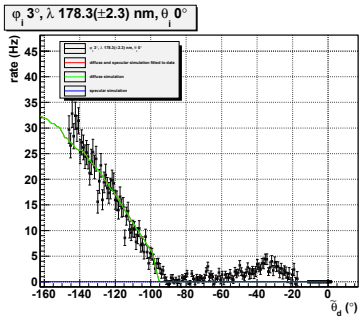

(a) $\tilde{\varphi}_i = 3\ ^\circ\ \tilde{\theta}_i = 0\ ^\circ$

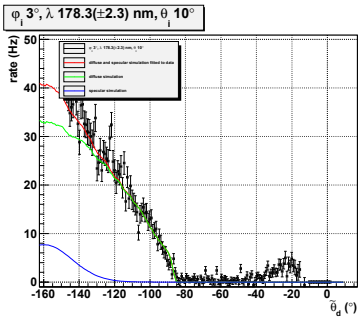

(b) $\tilde{\varphi}_i = 3\ ^\circ\ \tilde{\theta}_i = 10\ ^\circ$

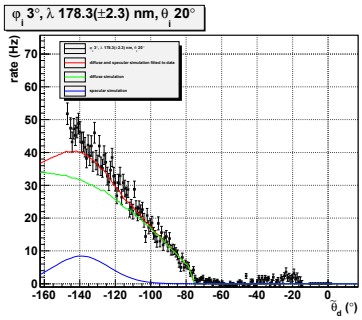

(c) $\tilde{\varphi}_i = 3\ ^\circ\ \tilde{\theta}_i = 20\ ^\circ$

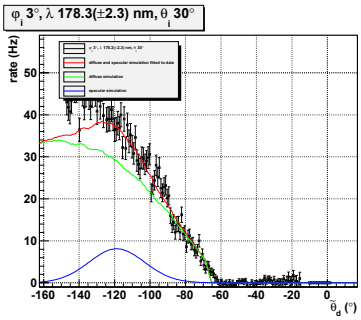

(d) $\tilde{\varphi}_i = 3\ ^\circ\ \tilde{\theta}_i = 30\ ^\circ$

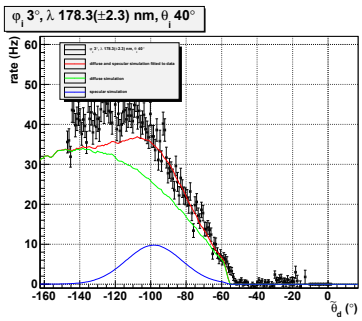

(e) $\tilde{\varphi}_i = 3\ ^\circ\ \tilde{\theta}_i = 40\ ^\circ$

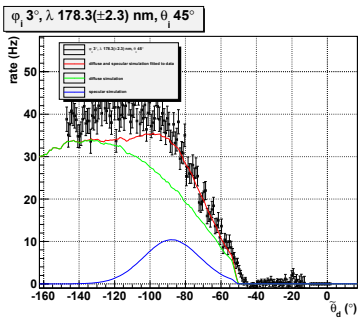

(f) $\tilde{\varphi}_i = 3\ ^\circ\ \tilde{\theta}_i = 45\ ^\circ$

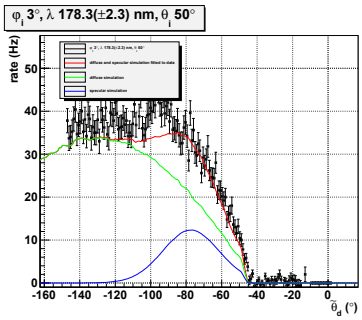

(g) $\tilde{\varphi}_i = 3\ ^\circ\ \tilde{\theta}_i = 50\ ^\circ$

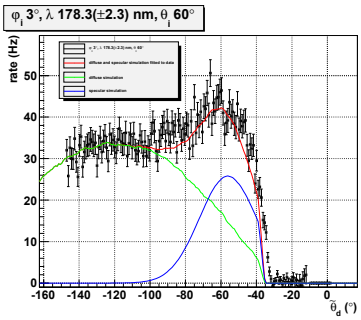

(h) $\tilde{\varphi}_i = 3\ ^\circ\ \tilde{\theta}_i = 60\ ^\circ$

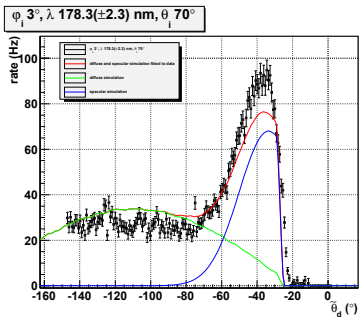

(i) $\tilde{\varphi}_i = 3\ ^\circ\ \tilde{\theta}_i = 70\ ^\circ$

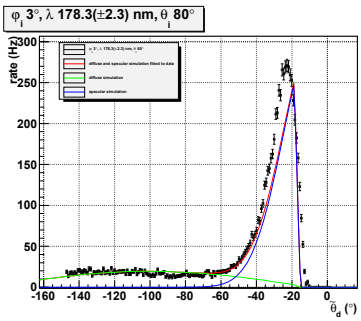

(j) $\tilde{\varphi}_i = 3\ ^\circ\ \tilde{\theta}_i = 80\ ^\circ$

Figure 5.43.: Fit to data set of first sample, plots for $\tilde{\varphi}_i = 3\,^\circ$.

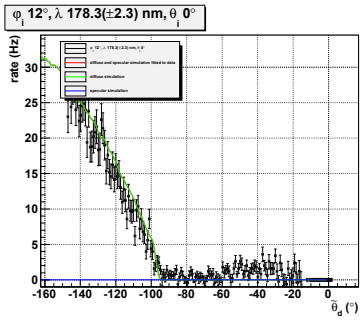

(a) $\tilde{\varphi}_i = 12\ ^\circ\ \tilde{\theta}_i = 0\ ^\circ$

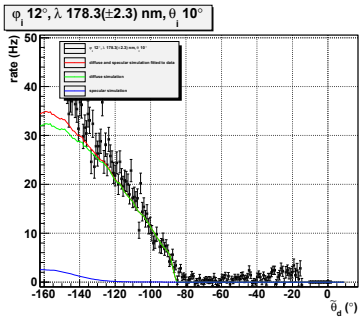

(b) $\tilde{\varphi}_i = 12\ ^\circ\ \tilde{\theta}_i = 10\ ^\circ$

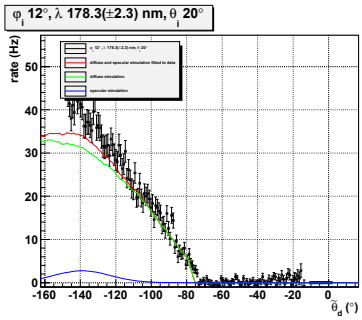

(c) $\tilde{\varphi}_i = 12\ ^\circ\ \tilde{\theta}_i = 20\ ^\circ$

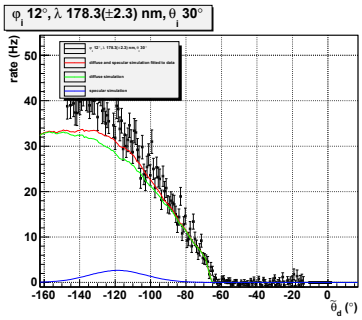

(d) $\tilde{\varphi}_i = 12\ ^\circ\ \tilde{\theta}_i = 30\ ^\circ$

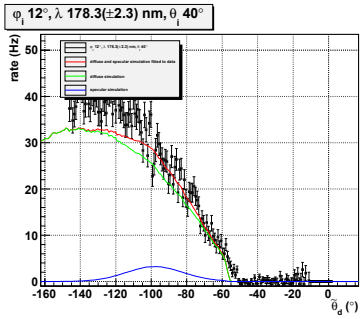

(e) $\tilde{\varphi}_i = 12\ ^\circ\ \tilde{\theta}_i = 40\ ^\circ$

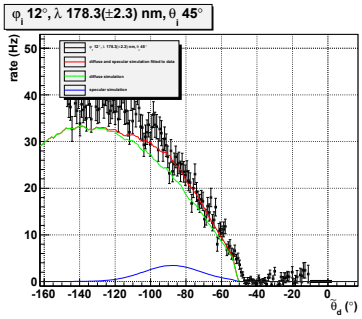

(f) $\tilde{\varphi}_i = 12\ ^\circ\ \tilde{\theta}_i = 45\ ^\circ$

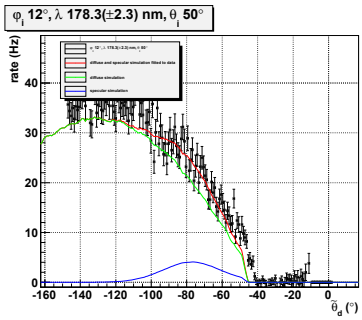

(g) $\tilde{\varphi}_i = 12\ ^\circ\ \tilde{\theta}_i = 50\ ^\circ$

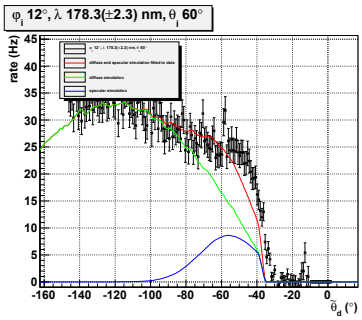

(h) $\tilde{\varphi}_i = 12\ ^\circ\ \tilde{\theta}_i = 60\ ^\circ$

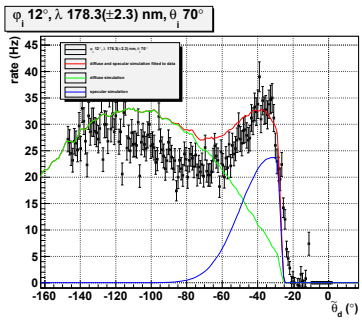

(i) $\tilde{\varphi}_i = 12\ ^\circ\ \tilde{\theta}_i = 70\ ^\circ$

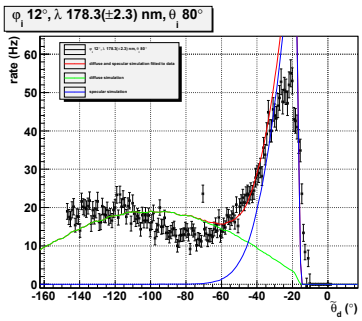

(j) $\tilde{\varphi}_i = 12\ ^\circ\ \tilde{\theta}_i = 80\ ^\circ$

Figure 5.44.: Fit to data set of first sample, plots for $\tilde{\varphi}_i = 12\,^\circ$.

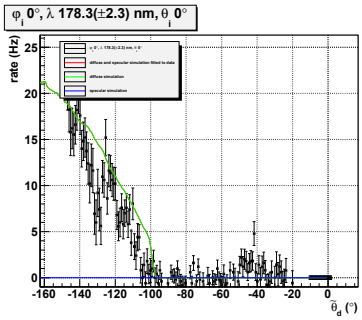

(a) $\tilde{\varphi}_i = 0\ ^\circ\ \tilde{\theta}_i = 0\ ^\circ$

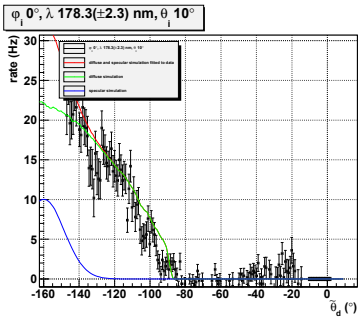

(b) $\tilde{\varphi}_i = 0\ ^\circ\ \tilde{\theta}_i = 10\ ^\circ$

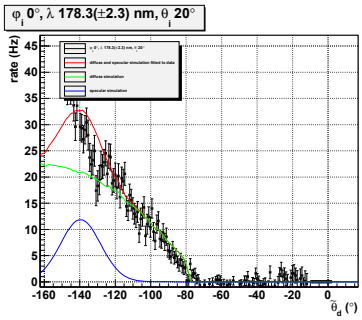

(c) $\tilde{\varphi}_i = 0\ ^\circ\ \tilde{\theta}_i = 20\ ^\circ$

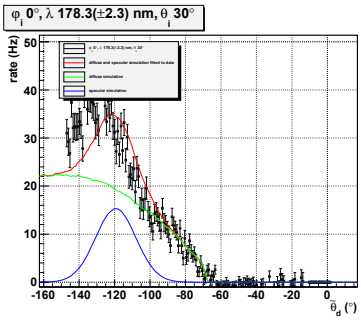

(d) $\tilde{\varphi}_i = 0\ ^\circ\ \tilde{\theta}_i = 30\ ^\circ$

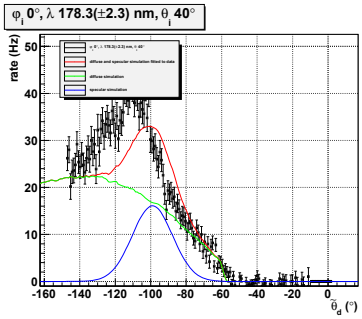

(e) $\tilde{\varphi}_i = 0\ ^\circ\ \tilde{\theta}_i = 40\ ^\circ$

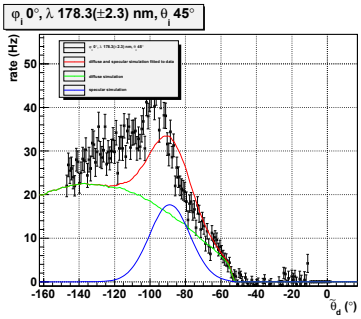

(f) $\tilde{\varphi}_i = 0\ ^\circ\ \tilde{\theta}_i = 45\ ^\circ$

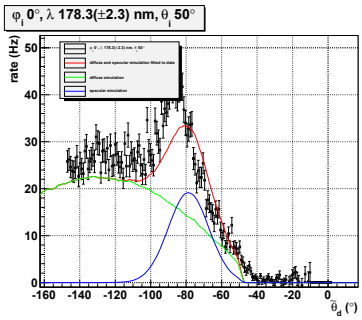

(g) $\tilde{\varphi}_i = 0\ ^\circ\ \tilde{\theta}_i = 50\ ^\circ$

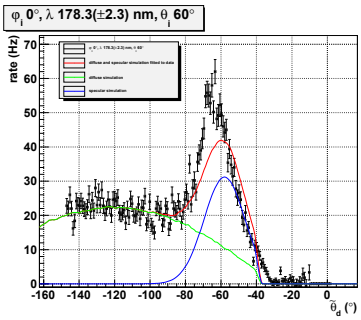

(h) $\tilde{\varphi}_i = 0\ ^\circ\ \tilde{\theta}_i = 60\ ^\circ$

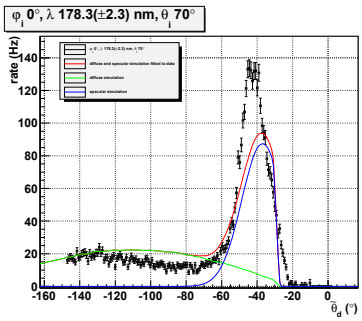

(i) $\tilde{\varphi}_i = 0\ ^\circ\ \tilde{\theta}_i = 70\ ^\circ$

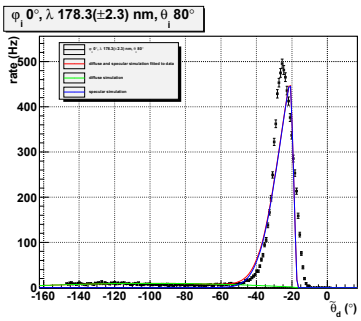

(j) $\tilde{\varphi}_i = 0\ ^\circ\ \tilde{\theta}_i = 80\ ^\circ$

Figure 5.45.: Fit to data set of second sample, plots for $\tilde{\varphi}_i = 0\,^\circ$.

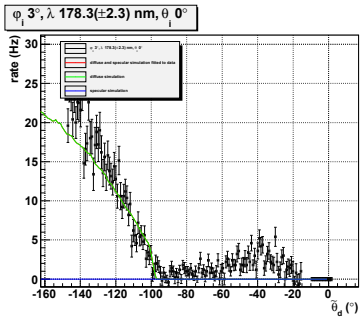

(a) $\tilde{\varphi}_i = 3\ ^\circ\ \tilde{\theta}_i = 0\ ^\circ$

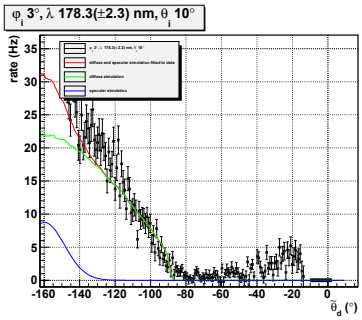

(b) $\tilde{\varphi}_i = 3\ ^\circ\ \tilde{\theta}_i = 10\ ^\circ$

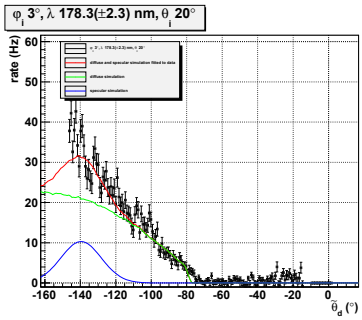

(c) $\tilde{\varphi}_i = 3\ ^\circ\ \tilde{\theta}_i = 20\ ^\circ$

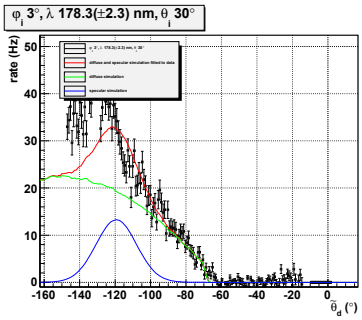

(d) $\tilde{\varphi}_i = 3\ ^\circ\ \tilde{\theta}_i = 30\ ^\circ$

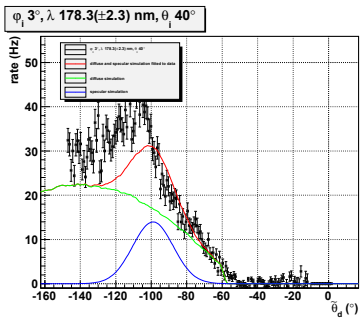

(e) $\tilde{\varphi}_i = 3\ ^\circ\ \tilde{\theta}_i = 40\ ^\circ$

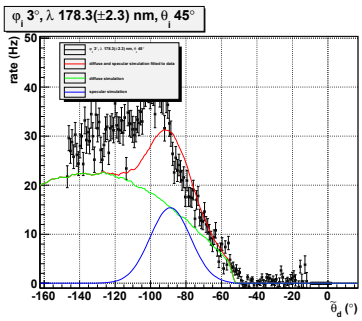

(f) $\tilde{\varphi}_i = 3\ ^\circ\ \tilde{\theta}_i = 45\ ^\circ$

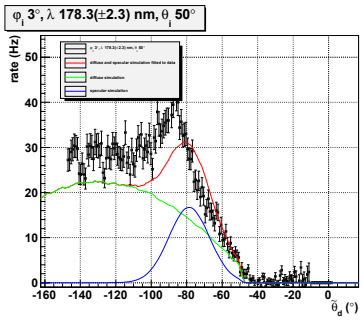

(g) $\tilde{\varphi}_i = 3\ ^\circ\ \tilde{\theta}_i = 50\ ^\circ$

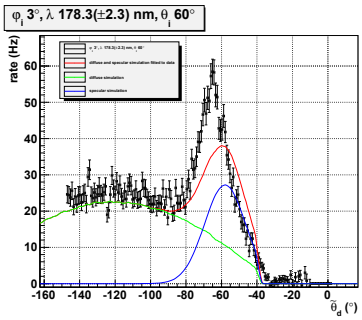

(h) $\tilde{\varphi}_i = 3\ ^\circ\ \tilde{\theta}_i = 60\ ^\circ$

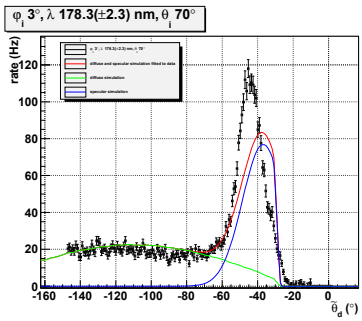

(i) $\tilde{\varphi}_i = 3\ ^\circ\ \tilde{\theta}_i = 70\ ^\circ$

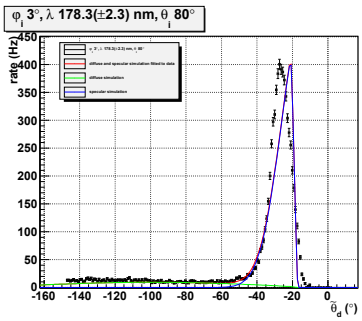

(j) $\tilde{\varphi}_i = 3\ ^\circ\ \tilde{\theta}_i = 80\ ^\circ$

Figure 5.46.: Fit to data set of second sample, plots for $\tilde{\varphi}_i = 3^\circ$.

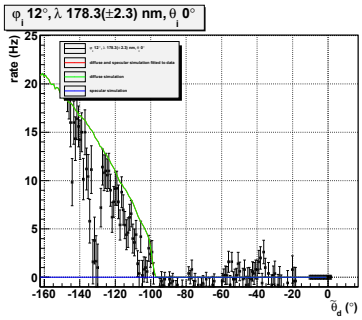

(a) $\tilde{\varphi}_i = 12\ ^\circ\ \tilde{\theta}_i = 0\ ^\circ$

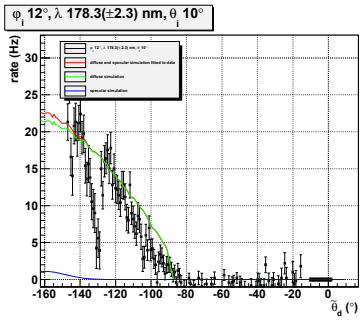

(b) $\tilde{\varphi}_i = 12\ ^\circ\ \tilde{\theta}_i = 10\ ^\circ$

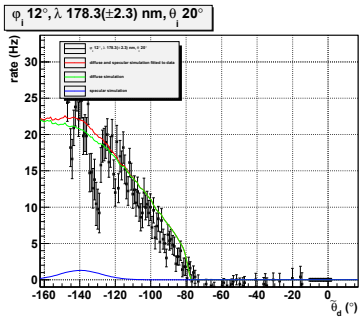

(c) $\tilde{\varphi}_i = 12\ ^\circ\ \tilde{\theta}_i = 20\ ^\circ$

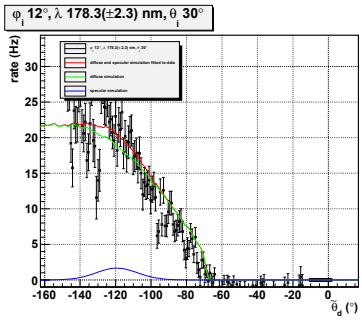

(d) $\tilde{\varphi}_i = 12\ ^\circ\ \tilde{\theta}_i = 30\ ^\circ$

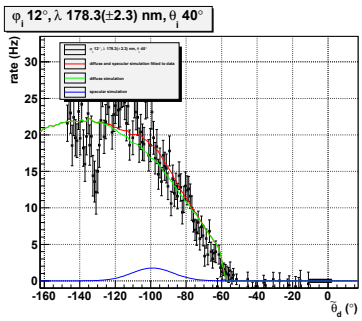

(e) $\tilde{\varphi}_i = 12\ ^\circ\ \tilde{\theta}_i = 40\ ^\circ$

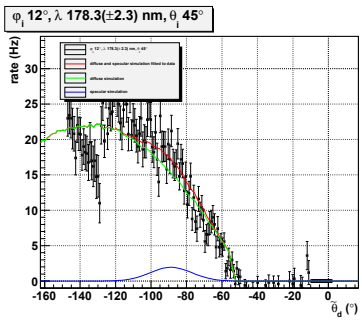

(f) $\tilde{\varphi}_i = 12\ ^\circ\ \tilde{\theta}_i = 45\ ^\circ$

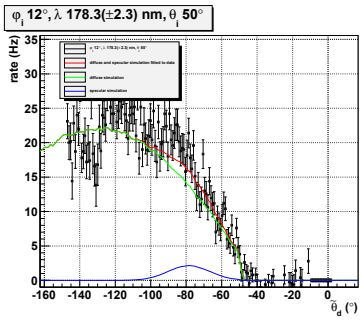

(g) $\tilde{\varphi}_i = 12\ ^\circ\ \tilde{\theta}_i = 50\ ^\circ$

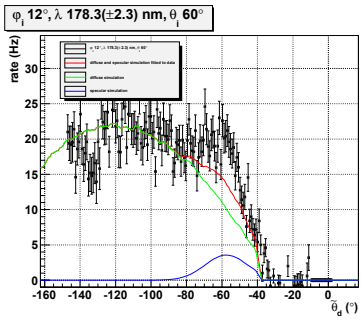

(h) $\tilde{\varphi}_i = 12\ ^\circ\ \tilde{\theta}_i = 60\ ^\circ$

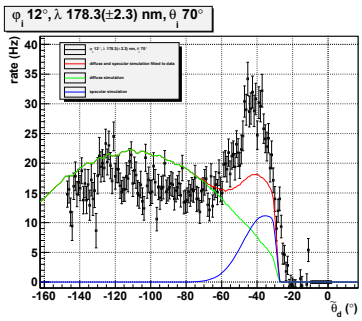

(i) $\tilde{\varphi}_i = 12\ ^\circ\ \tilde{\theta}_i = 70\ ^\circ$

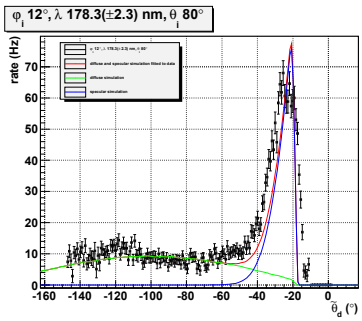

(j) $\tilde{\varphi}_i = 12\ ^\circ\ \tilde{\theta}_i = 80\ ^\circ$

Figure 5.47.: Fit to data set of second sample, plots for $\tilde{\varphi}_i = 12\,^\circ$.

Table 5.6.: Fit parameters for sample 1 data, fitting the Monte-Carlo-simulation with 100000 rays, cutoff angle $\theta_o^{\mathrm{co}} = 83\,^\circ$ and a micro-surface distribution with $\sigma = 5.5\,^\circ$.

parameter	value
a_{diff}	$1.369(\pm 0.004) \cdot 10^{-3}$
$a_{\mathrm{spec}}(10\,^\circ)$	$5.5(\pm 0.6) \cdot 10^{-5}$
$a_{\mathrm{spec}}(20\,^\circ)$	$5.57(\pm 0.25) \cdot 10^{-5}$
$a_{\mathrm{spec}}(30\,^\circ)$	$4.92(\pm 0.19) \cdot 10^{-5}$
$a_{\mathrm{spec}}(40\,^\circ)$	$5.21(\pm 0.16) \cdot 10^{-5}$
$a_{\mathrm{spec}}(45\,^\circ)$	$5.07(\pm 0.14) \cdot 10^{-5}$
$a_{\mathrm{spec}}(50\,^\circ)$	$5.40(\pm 0.13) \cdot 10^{-5}$
$a_{\mathrm{spec}}(60\,^\circ)$	$8.69(\pm 0.11) \cdot 10^{-5}$
$a_{\mathrm{spec}}(70\,^\circ)$	$15.10(\pm 0.11) \cdot 10^{-5}$
$a_{\mathrm{spec}}(80\,^\circ)$	$53.3(\pm 0.5) \cdot 10^{-5}$
$r_{\mathrm{red}}(80\,\mathrm{deg})$	$0.570(\pm 0.004)$

Table 5.7.: Fit parameters for sample 2 data, fitting the Monte-Carlo-simulation with 10000000 rays, cutoff angle $\theta_o^{\mathrm{co}} = 82\,^\circ$ and a micro-surface distribution with $\sigma = 4.0\,^\circ$.

parameter	value
a_{diff}	$9.07(\pm 0.03) \cdot 10^{-4}$
$a_{\mathrm{spec}}(10\,^\circ)$	$3.1(\pm 0.5) \cdot 10^{-5}$
$a_{\mathrm{spec}}(20\,^\circ)$	$3.53(\pm 0.14) \cdot 10^{-5}$
$a_{\mathrm{spec}}(30\,^\circ)$	$4.21(\pm 0.12) \cdot 10^{-5}$
$a_{\mathrm{spec}}(40\,^\circ)$	$3.93(\pm 0.10) \cdot 10^{-5}$
$a_{\mathrm{spec}}(45\,^\circ)$	$3.97(\pm 0.09) \cdot 10^{-5}$
$a_{\mathrm{spec}}(50\,^\circ)$	$3.92(\pm 0.08) \cdot 10^{-5}$
$a_{\mathrm{spec}}(60\,^\circ)$	$4.96(\pm 0.07) \cdot 10^{-5}$
$a_{\mathrm{spec}}(70\,^\circ)$	$9.33(\pm 0.07) \cdot 10^{-5}$
$a_{\mathrm{spec}}(80\,^\circ)$	$69.4(\pm 0.8) \cdot 10^{-5}$
$r_{\mathrm{red}}(80\,\mathrm{deg})$	$0.420(\pm 0.005)$

Looking at the data sets and fits one can already see by eye that the peaks of the specular reflection from the second sample are more defined for the second sample. They are already clearly visible at smaller incident angles $\tilde{\theta}_i$ and have a smaller broadening.

Several mismatches in the simulated data can be seen that will be improved in a next step. Generally the cutoff seems to be to steep in the simulation. This leads to problems for the measurements with $\tilde{\theta}_i = 80\,^\circ$. An improvement would be to introduce a smearing.

The simulation does not consider the extended beam spot size. After the alignment problem of the incoming beam is solved, the fit results for the incoming beam can be used as input parameter for the reflection simulations.

The reduced incoming intensity can also be seen for $\tilde{\theta}_i = 70\,^\circ$, the fit with the overall diffuse intensity clearly overestimates the measured diffuse intensity for $\tilde{\theta}_i = 70\,^\circ$.

The fit to the sample 2 data shows that the specular peaks measured do not coincide with the specular peaks of the simulation. There was a break between the two measurements, therefore it is possible that some misalignment occurred in the mean time. In addition the

complete sample holder was removed to change the sample, thus introducing an additional source for errors in alignment.

The data set for sample 2 with incident angle $\tilde{\varphi}_i = 12\,^\circ$ shows a reduced rate for $-150\,^\circ < \tilde{\theta}_d < -130\,^\circ$. This seems to be an artifact of the measurement. A possible explanation could be that the surface of the sample used for the $\tilde{\varphi}_i = 12\,^\circ$ slot had some anomalies. The artifact has little influence on the fit, therefore the data set has been included completely.

Using equation (5.29) together one can determine the reflectance $\rho(\theta_i)$ with equation (5.5) (see table 5.8 and figure 5.48). The initial rate for sample 1 is $\dot{N}(1) = 3.885(\pm 0.21)\cdot 10^4\,\mathrm{Hz}$ and for sample 2 $\dot{N}(2) = 3.24(\pm 0.19)\cdot 10^4\,\mathrm{Hz}$. The maximum intensity is reflected for grazing angles.

Table 5.8.: Reflectance $\rho(\theta_i)$ in % for both samples

	sample 1	sample 2
diffuse	35.2 ± 1.9	28.0 ± 1.7
10	1.41 ± 0.17	0.95 ± 0.16
20	1.43 ± 0.11	1.09 ± 0.08
30	1.27 ± 0.09	1.3 ± 0.09
40	1.34 ± 0.09	1.21 ± 0.08
45	1.31 ± 0.08	1.23 ± 0.08
50	1.39 ± 0.09	1.21 ± 0.08
60	2.24 ± 0.13	1.53 ± 0.10
70	3.89 ± 0.22	2.88 ± 0.17
80	13.71 ± 0.75	21.4 ± 1.3

Comparing the results for both samples the surface treatment does not seem to influence the total reflectance very much, but differences are clearly visible in the shape of the reflection curves. For sample 2 the micro-surface distribution is smaller and the cutoff angle θ_o^{co} differs which can be attributed to a smoothing of the surface. As this does not affect the diffuse reflectance, one can conclude that the diffuse reflectance is a process taking place in the bulk material due to reflections from subsurfaces in the bulk material. This has already been observed and described by L. Wolff (see [Wol94]).

This analysis is well suited to compare different sample surfaces and interpret the results with respect to the surface treatment. Results with this analysis cannot be directly implemented for simulations of the XENON experiment as they only describe the case of reflections in vacuum. The alternative approach described in section 5.6.1 characterizes the reflection with models using the refractive index of the medium in which the reflection takes place as input parameter. The result can be directly used for the XENON experiment.

Comparing the measured reflectance to the results presented in [Sil10b] for pressed polished PTFE in vacuum (see figure 5.49), one can see that the diffuse lobe from our sample is much lower than the one from Silva's sample. The intensity of the specular lobe is comparable. For the incidence angle $\tilde{\theta}_i = 80\,^\circ$ the specular reflectance is enhanced. This can be attributed to the coherent reflection process described in [Sil10b] as specular spike.

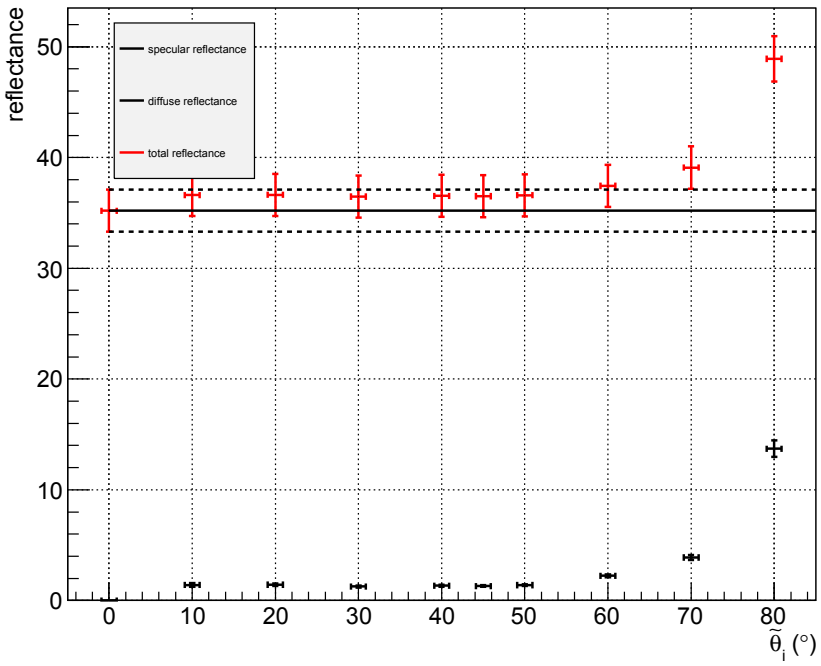

(a) Sample 1

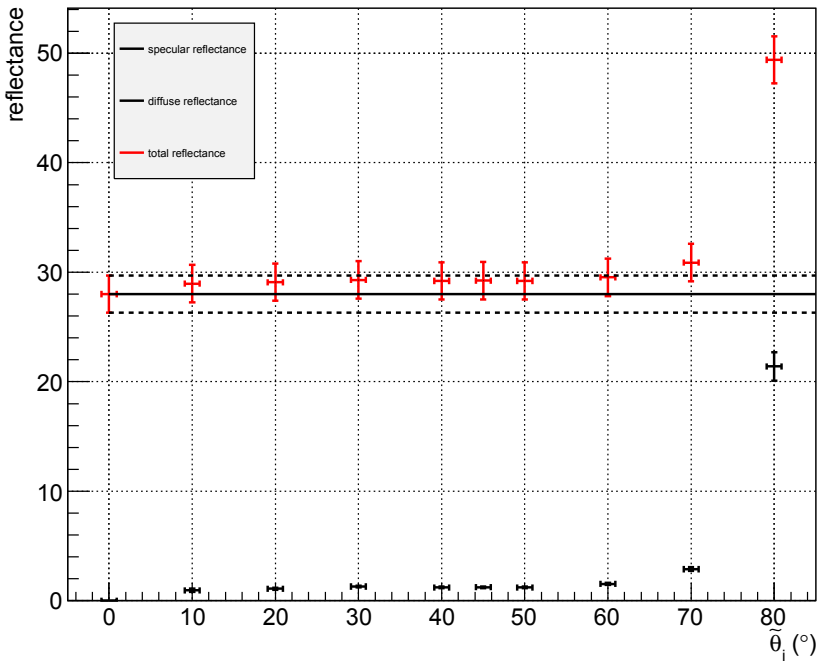

(b) Sample 2

Figure 5.48.: Reflectance for both samples. Please note that the systematic error due to possible misalignments has not been included in this graph.

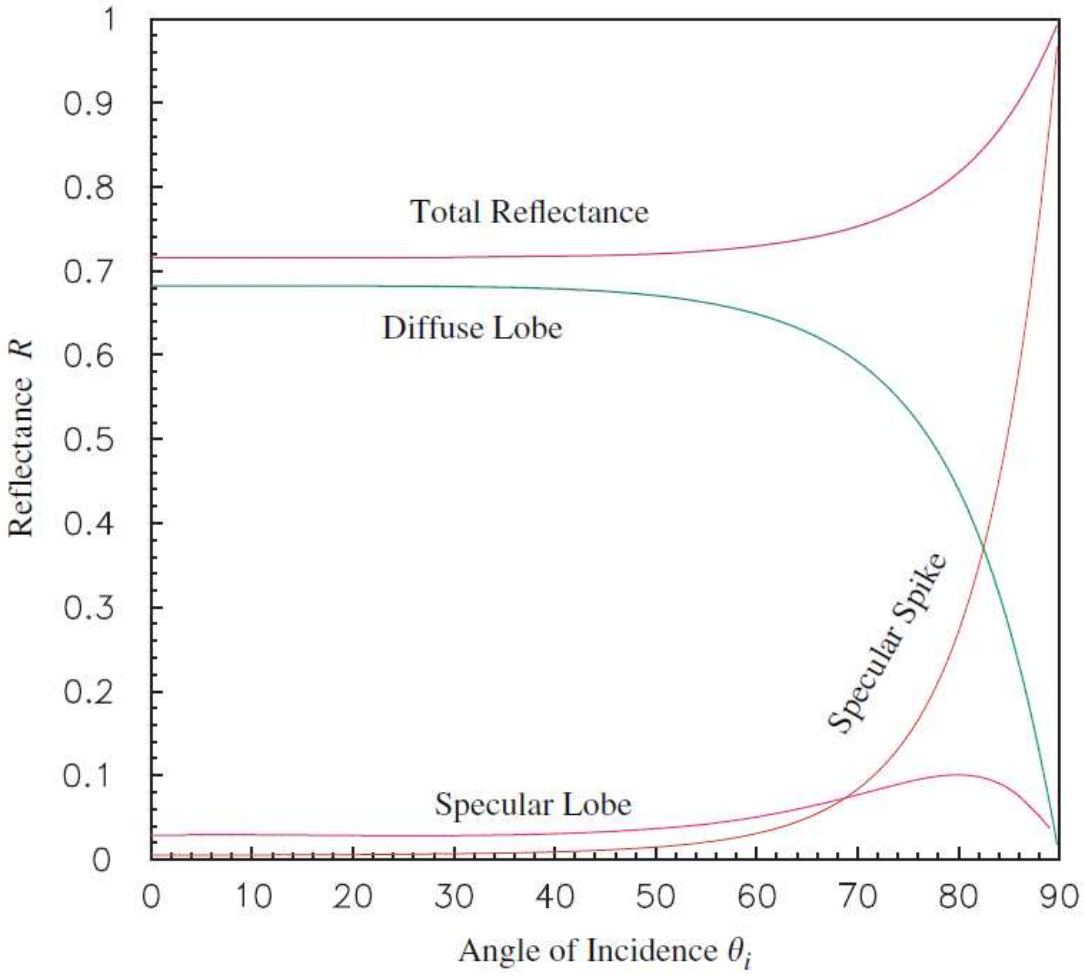

Figure 5.49.: The reflectance of pressed polished PTFE as a function of the angle of incidence θ_i for light of $\lambda = 178\ nm$ in vacuum. Figure taken from [Sil10b].

5.6.1. Possible alternative Analysis

Comparable measurements for different samples and their analysis have been described in [Sil10b]. In contrast to fitting Monte-Carlo-simulated data to the data, Silva *et al.* used a model bidirectional reflectance intensity distribution function (BRIDF) B with the refraction index of PTFE n_{PTFE}, the amplitude of the diffuse reflection ρ_L, the parameter γ to characterize the roughness of the surface and the parameter K for the intensity and its drop-off of the specular peak as free parameters to fit their data. The model has the advantage that it includes the refractive index of the medium in which the reflection takes place. It can therefore directly be used to simulate reflections in the relevant medium, here liquid Xenon with a refractive index of $n_0 = 1.69$ [Sol04].

The model BRIDF B of Silva *et al.* is assumed to be a sum of the BRIDF B_d for diffuse reflection, the BRIDF B_s for specular reflection and the BRIDF B_c for the coherent specular spike for correlated reflection. The diffuse component B_d is attributed to be due to internal scattering from substructures in the dielectric medium and therefore follows the Lambertian law. To take into account multiple scattering processes, it is modified using the power coefficient R for unpolarized light given by the Fresnel equations in the form[15]

$$F(\theta_i, n_{\mathrm{PTFE}}/n_0) = F(\theta_i, \theta_t) = R = \frac{1}{2}|r_\perp^2 + r_\parallel^2| = \frac{1}{2}\frac{\sin^2\theta_i - \theta_t}{\sin^2\theta_i + \theta_t}\left[1 + \frac{\cos^2\theta_i + \theta_t}{\cos^2\theta_i - \theta_t}\right].$$

The diffuse component has then the form (see reference [Wol94])

$$B_d = \frac{\rho_L}{\pi}\cos\theta_r[1 - F(\theta_i, n_{\mathrm{PTFE}}/n_0)][1 - F(\theta_t, n_0/n_{\mathrm{PTFE}})]. \tag{5.30}$$

The specular lobe is due to specular reflection, the width of the lobe can be attributed to surface roughness. It can be described geometrically. The specular spike is an enhancement of the lobe if the light is coherently reflected. The two specular reflection types are correlated, thus their amplitudes are fitted with the same factor (the specular spike with C, the specular lobe with $(1-C)$) that also describes the angular dependence of the intensity of the total specular reflection [Tor67]. The shape of this factor depends on the surface type. In contrast to the dependency stated in literature after the Beckmann-Spizzichino model with conductor boundary conditions $C = exp\left(-(4\pi/\lambda\sigma_h(\cos\theta_i + \cos\theta_o))^2\right)$ Silva *et al.* use their empirically found relation

$$C = exp\left(-K/2(\cos\theta_i + \cos\theta_o)\right). \tag{5.31}$$

To model the micro-surface distribution, they use the Trowbridge-Reitz function for ellipsoidal micro-surfaces:

$$P_{TR}(\alpha;\gamma) = \frac{\gamma^2}{\pi\cos^4\alpha(\gamma^2 + \tan^2\alpha)^2}. \tag{5.32}$$

To take into account the geometrical blocking of light by micro-surfaces, the factor

$$G(\theta_i, \theta_o, \varphi_o) \simeq H(\theta_i' - \pi/2)H(\theta_r' - \pi/2)\frac{2}{1 + \sqrt{1 + \gamma^2\tan^2\theta_i}}\frac{2}{1 + \sqrt{1 + \gamma^2\tan^2\theta_r}} \tag{5.33}$$

[15] using Snell's law $n_{\mathrm{PTFE}}\sin\theta_t = n_0\sin\theta_i$ and the principle of reversibility

is introduced into the equation with H the Heaviside step function.

The specular BRIDF B_s is then given by

$$B_s = \frac{(1-C)FPG}{4\cos\theta_i}, \tag{5.34}$$

the factor $1/4\cos\theta_i$ taking into account the solid angle covered by the micro-surface in relation to the one by the overall surface normal. The coherent reflection is described by

$$B_c = CFG. \tag{5.35}$$

5.6.2. Microscope measurements

Investigating the surfaces with an optical microscope shows that the first sample without surface preparation has scratches in all directions (see figure 5.50(a)). The microscope picture from sample 2 shows a better surface with fewer scratches. Several are still visible (see figure 5.50(b)) pointing to the assumption that only the scratches with low depth have been 'healed' while the deeper scratches are still in place.

This assumption is supported by an AFM measurement of ample 2. The overall surface appears quite smooth (see figure 5.51(a)), but while scanning the profiles several indents with depths larger than $1\,\mu$m were still visible (see figure 5.51). As the investigation of PTFE samples in the AFM proved difficult due their cold floating properties and the structure of the surface treated sample 2 also already tested the limits of this microscope sample 1 has not been examined with an AFM.

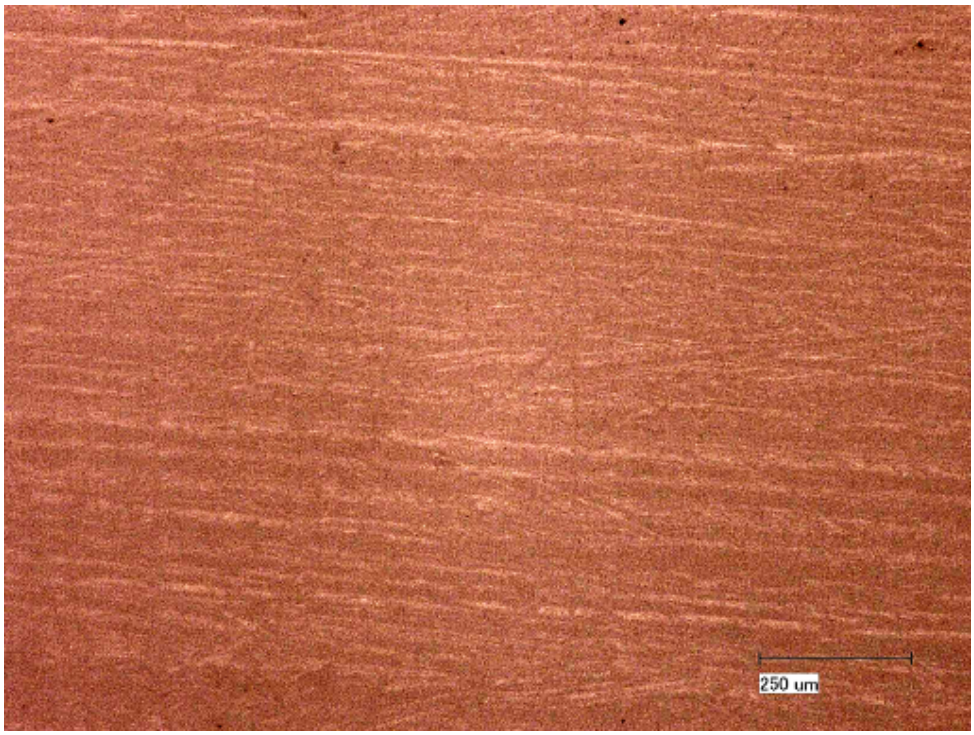

(a) Sample 1

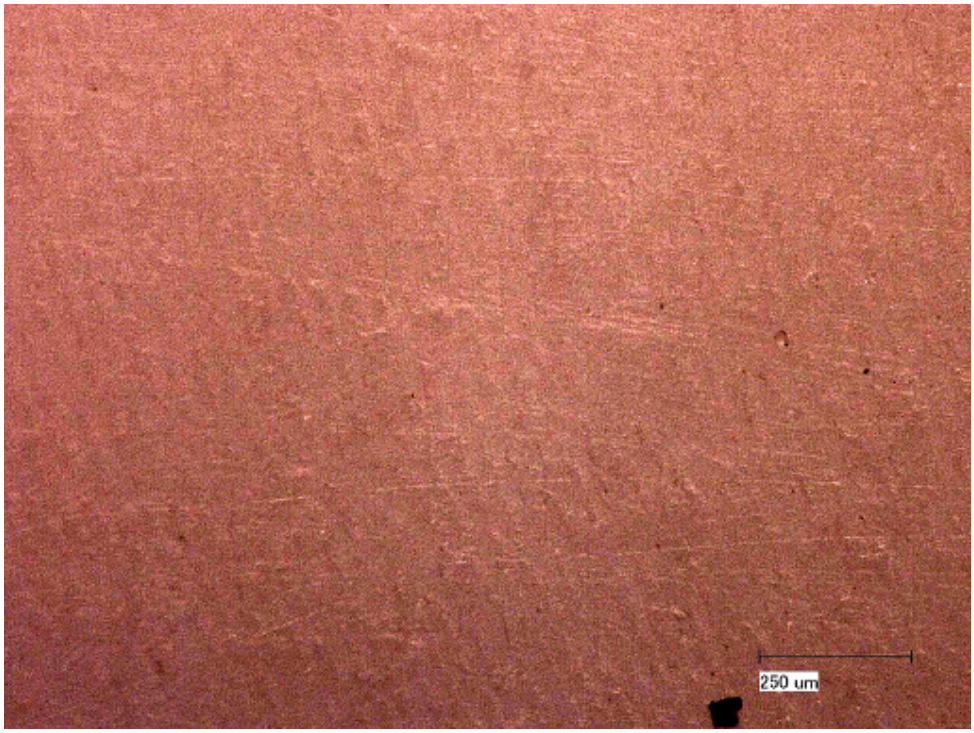

(b) Sample 2

Figure 5.50.: Microscope measurements.

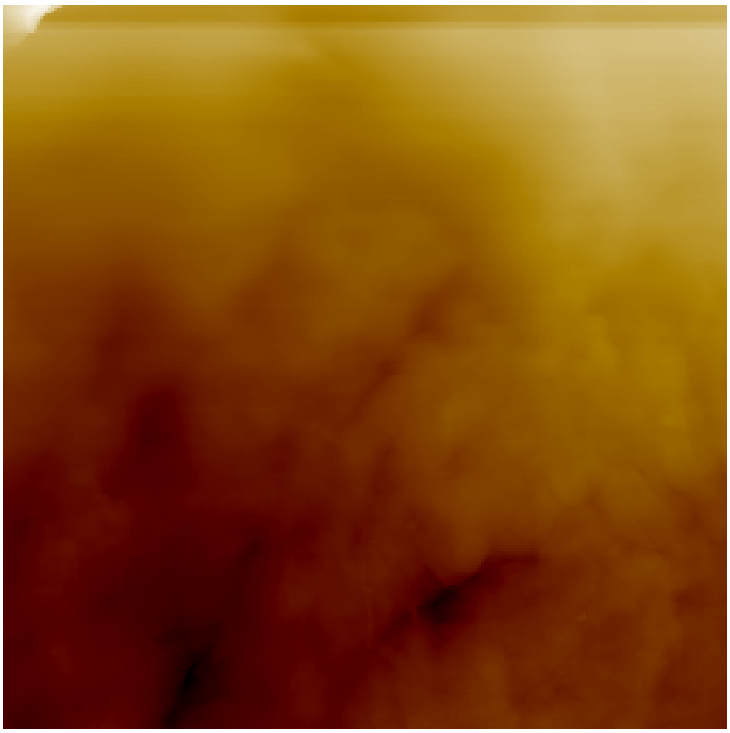

(a) 2d profile of one AFM measurement of sample 2. The shown section corresponds to a 40 $\mu m \times 40\ \mu m$ square on the sample. The sample has been scanned in horizontal lines starting at the top. The bottom appears darker due to the cold flow of the sample during investigation with applied pressure. Irregularities in the surface structure are visible at the bottom.

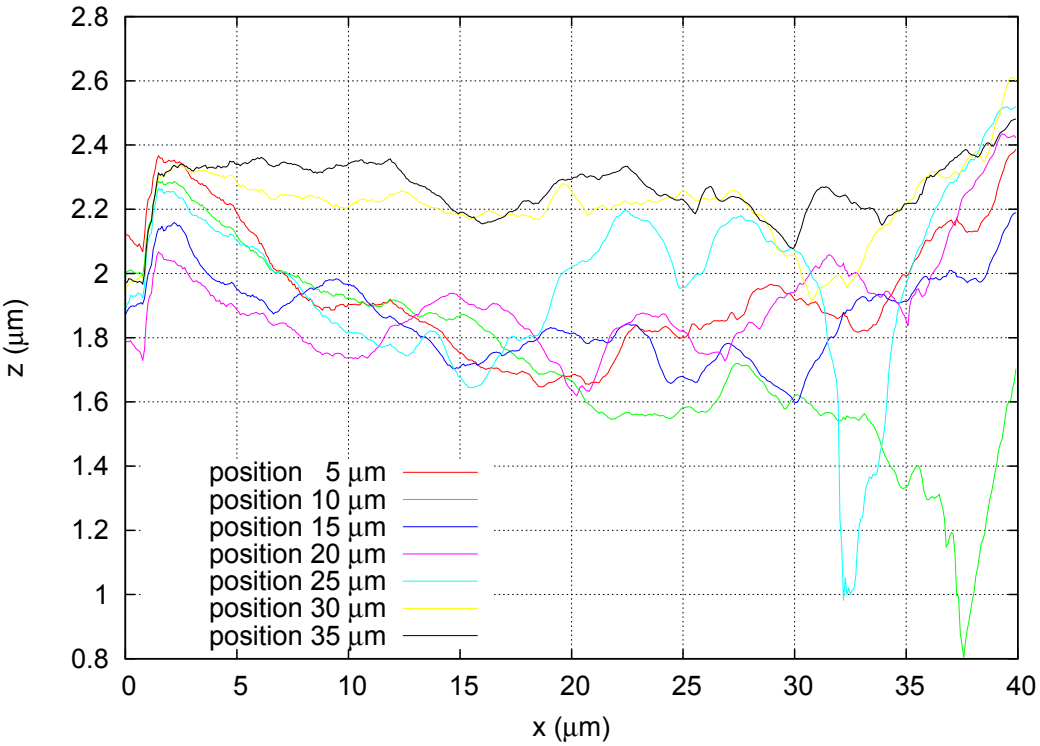

(b) AFM profiles taken in the above shown sample square with distance of 5 μm. The profile lines run in the above sample from top to bottom.

Figure 5.51.: AFM measurement of sample 2.

5.6.3. Wavelength dependence of reflectance

Only little information is available on the wavelength dependence of the reflectance from PTFE. Silva *et al.* showed in [Sil10a] that the reflectance increases drastically from 178 nm to 250 nm (see also figure 5.52). For the Teflon of type Spectralon it is known that the reflectivity decreases rapidly below 180 nm [Wes09].

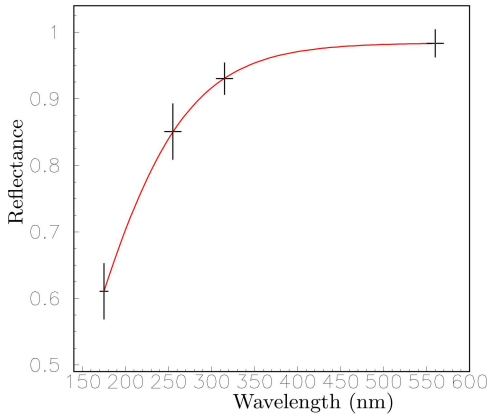

Figure 5.52.: Measurement of the wavelength reflectance taken from [Sil10a].

A point of general interest is now whether the reflectance of PTFE decreases smoothly as indicated in [Sil10a] or shows a more drastic behavior. Therefore, measurements have been taken for the wavelength of 165.5(±2.4) nm and 198.7(±2.2) nm with $\phi_i = 0\,^\circ$ for sample 1 (see figure 5.55 and 5.56). They have been fitted with the best fit Monte-Carlo-simulation model found before for sample 1[16].

The measurements are not easy to compare as several experimental difficulties have to be considered:

- The rate for the direct beam measurement at $\lambda = 165.5(\pm 2.4)$ nm was high. It is possible that dead time effects occured at the data acquisition (compare figure 5.7 for an indication of the size of the intensity change). Due to modifications at the setup, this measurement could not be repeated in this form. If the rate had been too high, the incoming intensity is underestimated in this analysis. To take this into account, the reflectance values for 165.5 nm should therefore be multiplied with an unknown factor f and cannot directly be compared to the measurements at the other wavelength.
- The vacuum monochromator exhibits a reciprocal linear dispersion. As the slits have been opened to their maximum to increase the light intensity, a wavelength range of 5.3 nm is measured instead of monochromatic radiation.
- The focal length of the lens depends on the wavelength, at $\lambda = 589$ nm it is specified to 100 mm. With the data supplied by the manufacturer it is possible to extract the focal length for the other wavelength (see table 5.9). With the current setup it is not possible to adjust the lens system during vacuum operation. Therefore the beam is not focused for measurements at $\lambda \neq 178$ nm.

The fit results for both wavelength show that the ratio between specular and diffuse reflectance behaves completely different for them (see figure 5.53 and 5.54). For $\lambda =$

[16] $\chi_r(198.7(\pm 2.2)\,\text{nm}) = 10.3$ and $\chi_r(165.5(\pm 2.4)\,\text{nm}) = 1.9$.

Table 5.9.: Wavelength dependence of the focal length of the used lens.

λ (nm)	f (mm)
589	100
200	83
178	78
165	72

165.5($\pm$2.4) nm the diffuse reflection is negligible while the specular reflection dominates at high angles. In contrast to that the measurement at $\lambda = 198.7(\pm 2.2)$ nm is dominated by the diffuse component.

The results are shown together with the measurement for $\lambda = 178.3$ nm in figure 5.57. Large differences are visible between the three measurements.

The measurements for 178.3($\pm$2.3) nm and 198.7($\pm$2.2) nm indicate a change of the reflectance by a factor of two between these wavelength. This is more than expected from Silva *et al.*. The measurement for 165.6($\pm$2.4) nm shows a very small reflectance[17] indicating a steep drop off of the reflectance in this wavelength region.

Although we cannot state the change of reflectance quantitatively, the result of these measurements show that the reflectance decreases drastically in this wavelength region. The measurements will be repeated with a proper alignment of the setup and better control of systematic effects.

[17]Due to dead time effects it is even possible that this value is overestimated.

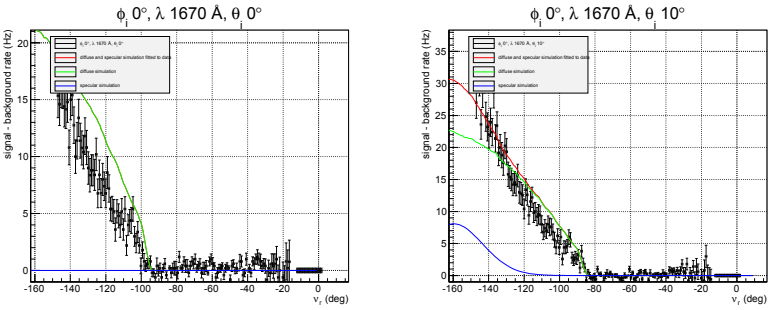

(a) $\tilde{\varphi}_i = 0\ ^\circ\ \tilde{\theta}_i = 0\ ^\circ$

(b) $\tilde{\varphi}_i = 0\ ^\circ\ \tilde{\theta}_i = 10\ ^\circ$

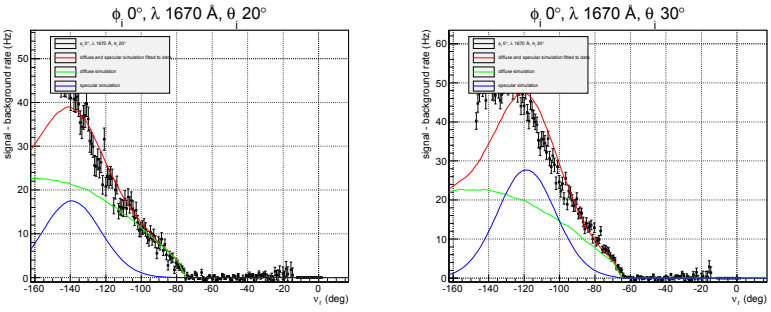

(c) $\tilde{\varphi}_i = 0\ ^\circ\ \tilde{\theta}_i = 20\ ^\circ$

(d) $\tilde{\varphi}_i = 0\ ^\circ\ \tilde{\theta}_i = 30\ ^\circ$

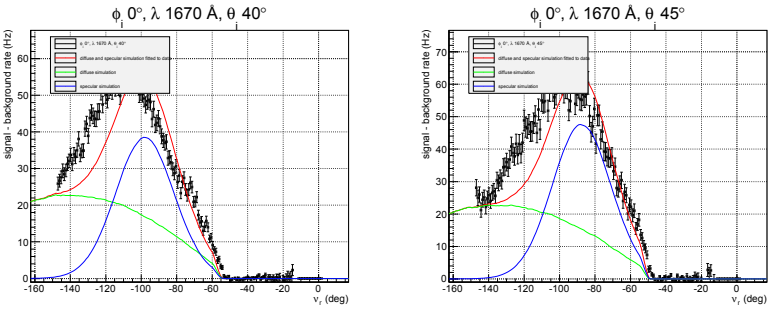

(e) $\tilde{\varphi}_i = 0\ ^\circ\ \tilde{\theta}_i = 40\ ^\circ$

(f) $\tilde{\varphi}_i = 0\ ^\circ\ \tilde{\theta}_i = 45\ ^\circ$

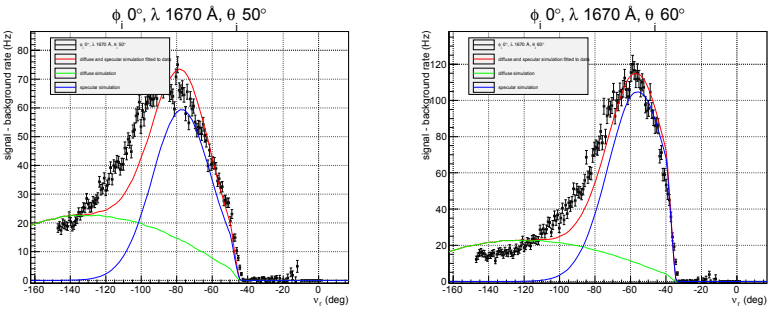

(g) $\tilde{\varphi}_i = 0\ ^\circ\ \tilde{\theta}_i = 50\ ^\circ$

(h) $\tilde{\varphi}_i = 0\ ^\circ\ \tilde{\theta}_i = 60\ ^\circ$

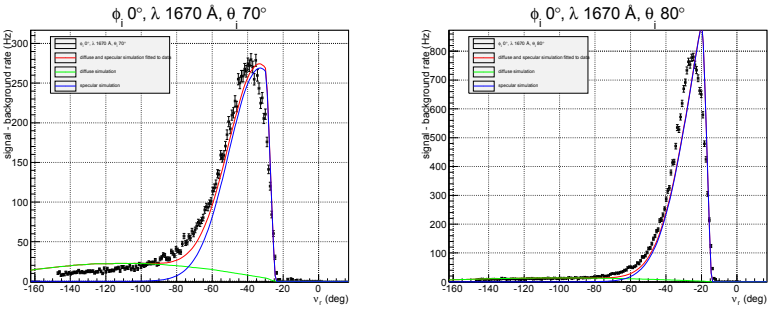

(i) $\tilde{\varphi}_i = 0\ ^\circ\ \tilde{\theta}_i = 70\ ^\circ$

(j) $\tilde{\varphi}_i = 0\ ^\circ\ \tilde{\theta}_i = 80\ ^\circ$

Figure 5.53.: Fit to data set of second sample for $\lambda = 165.5(\pm 2.4)\,\mathrm{nm}$.

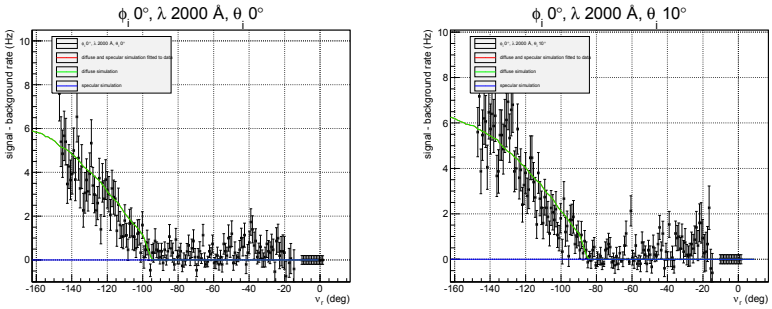

(a) $\tilde{\varphi}_i = 0\ ^\circ\ \tilde{\theta}_i = 0\ ^\circ$

(b) $\tilde{\varphi}_i = 0\ ^\circ\ \tilde{\theta}_i = 10\ ^\circ$

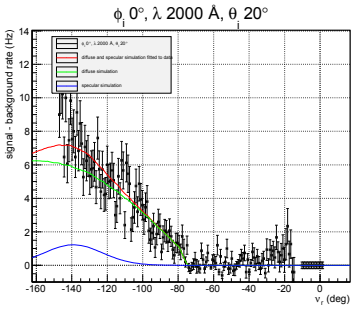

(c) $\tilde{\varphi}_i = 0\ ^\circ\ \tilde{\theta}_i = 20\ ^\circ$

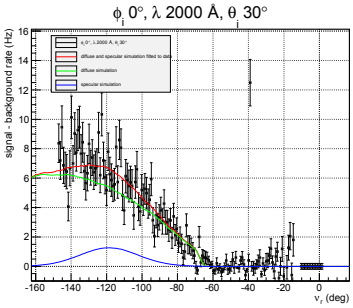

(d) $\tilde{\varphi}_i = 0\ ^\circ\ \tilde{\theta}_i = 30\ ^\circ$

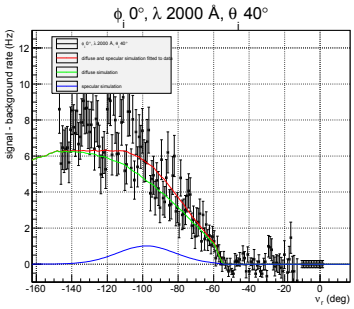

(e) $\tilde{\varphi}_i = 0\ ^\circ\ \tilde{\theta}_i = 40\ ^\circ$

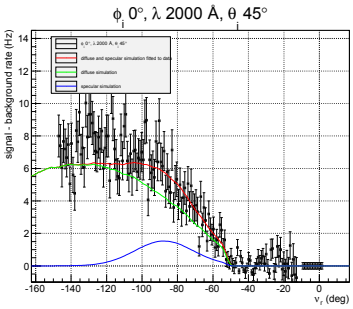

(f) $\tilde{\varphi}_i = 0\ ^\circ\ \tilde{\theta}_i = 45\ ^\circ$

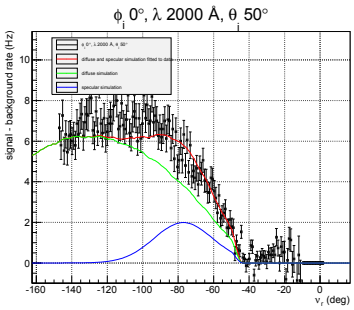

(g) $\tilde{\varphi}_i = 0\ ^\circ\ \tilde{\theta}_i = 50\ ^\circ$

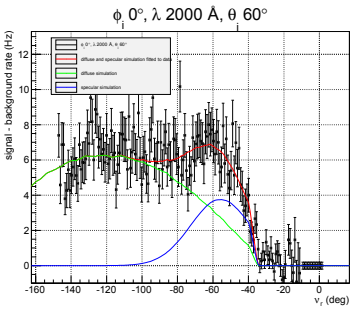

(h) $\tilde{\varphi}_i = 0\ ^\circ\ \tilde{\theta}_i = 60\ ^\circ$

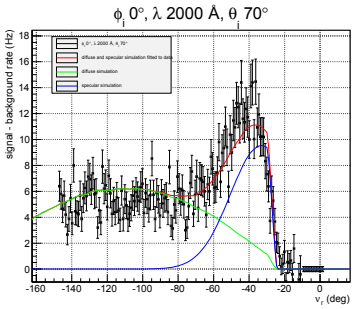

(i) $\tilde{\varphi}_i = 0\ ^\circ\ \tilde{\theta}_i = 70\ ^\circ$

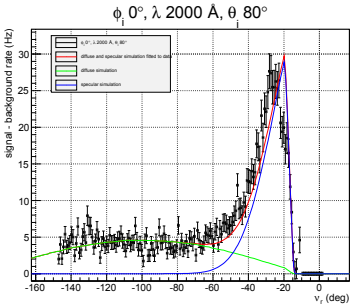

(j) $\tilde{\varphi}_i = 0\ ^\circ\ \tilde{\theta}_i = 80\ ^\circ$

Figure 5.54.: Fit to data set of second sample for $\lambda = 198.7(\pm 2.2)\,\mathrm{nm}$.

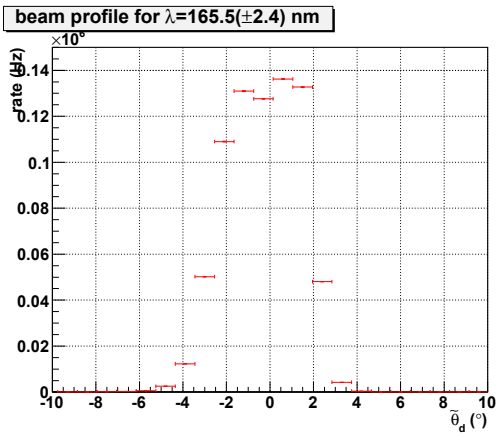

(a) Beam profile for $\lambda = 165.5(\pm 2.4)$ nm.

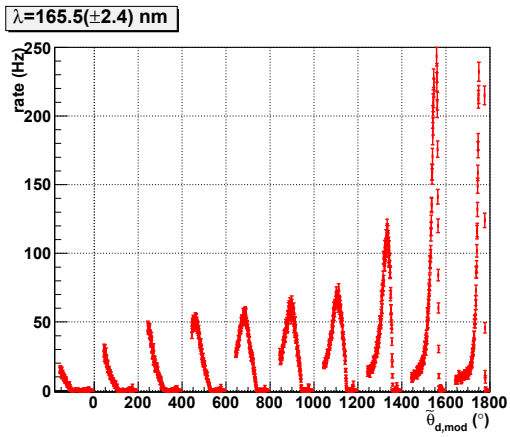

(b) Reflected beam profile for $\lambda = 165.5(\pm 2.4)$ nm and $\tilde{\varphi}_i = 0$ °.

Figure 5.55.: Measurements for $\lambda = 165.5(\pm 2.4)$ nm.

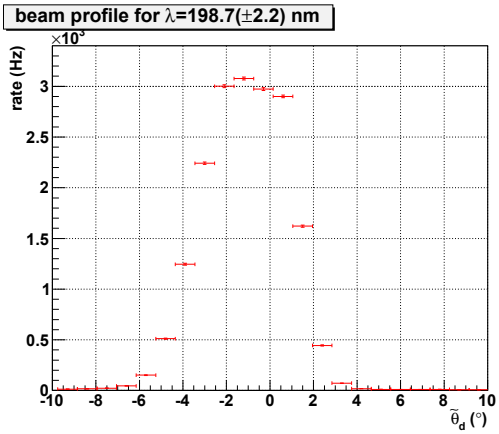

(a) Beam profile for $\lambda = 198.7(\pm 2.2)$ nm.

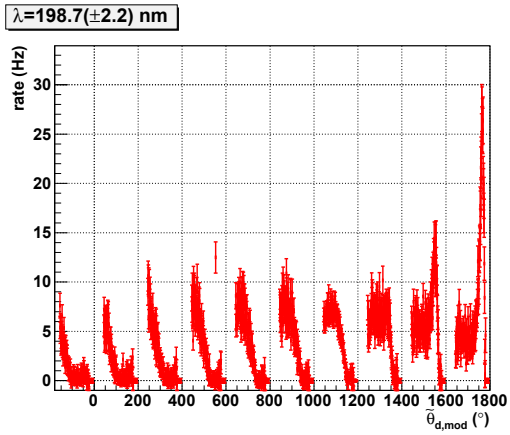

(b) Reflected beam profile for $\lambda = 198.7(\pm 2.2)$ nm and $\tilde{\varphi}_i = 0$ °.

Figure 5.56.: Measurements for $\lambda = 198.7(\pm 2.2)$ nm.

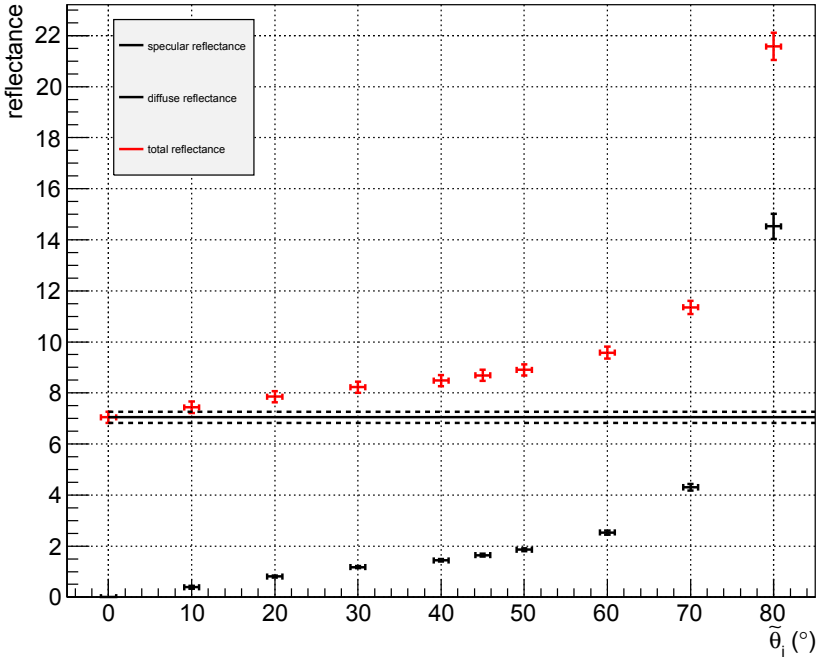

(a) Reflectance for $\lambda = 165.6(\pm 2.4)\ nm$.

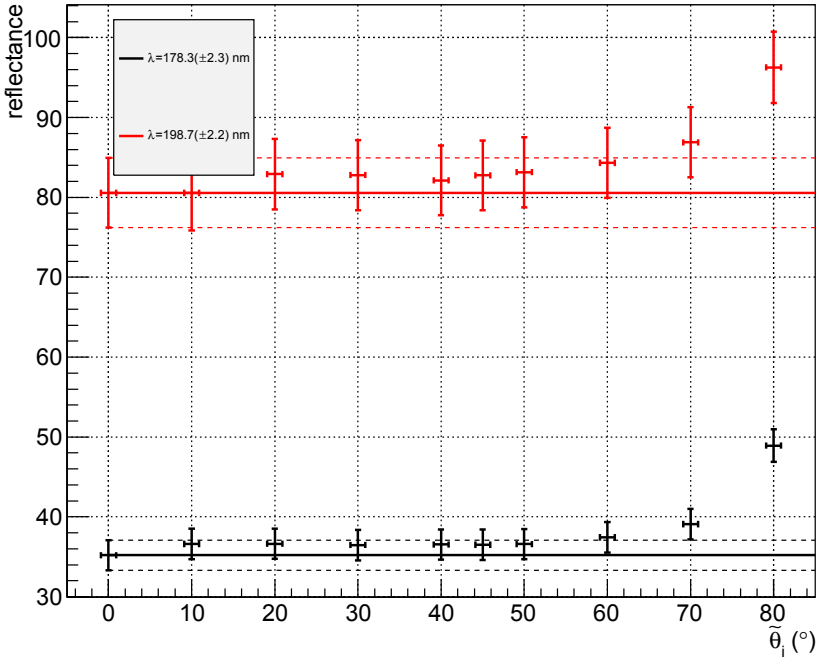

(b) Reflectance for $\lambda = 178.3(\pm 2.3)\ nm$ and $\lambda = 198.7(\pm 2.2)\ nm$.

Figure 5.57.: Reflectance for $\lambda = 165.5(\pm 2.4)\,\text{nm}$, $\lambda = 178.3(\pm 2.3)\,\text{nm}$ and $\lambda = 198.7(\pm 2.2)\,\text{nm}$. Please note that the systematic error due to possible misalignments has not been included in this graph. In addition dead time effects may have played a role in the measurement for $\lambda = 165.5(\pm 2.4)\,\text{nm}$ which would lead to a correction factor f for the total reflectance at this wavelength.

5.7. Summary and outlook

An experimental setup to measure the reflectivity of PTFE samples in the VUV has been designed, build and commissioned. First measurements have been presented with a method to analyze them. As result a maximum reflectance at grazing angles of $\rho(\tilde{\theta}_i = 80\,^\circ) \approx 50\,\%$ was measured with a diffuse lobe of $\approx 35\,\%$. This is lower than values measured by Silva *et al.* [Sil10a] and thus also lower than the values used in the XENON100 detector simulations, but these values have been measured for a random bad PTFE sample with a bad alignment.With better samples and a good alignment procedure, an average reflectivity of $73(\pm 7)\,\%$ has been determined by C. Levy Brown [Lev13]. For samples from the XENON100 experiment B. Choi determined the reflectivity with better aligned measurements to be between $\approx 61\,\%$ and $\approx 72\,\%$.

In addition a test of the wavelength dependence of the reflectance from a PTFE sample has been conducted which shows a decrease for decreasing wavelength. The setup also offers the possibility to investigate other topics as the shown with the quantum efficiency measurements published in reference [Apr12d]. As many of the components in this setup can be easily modified, as *e.g.* the wavelength, or replaced, as *e.g.* the sample holder, it promises the possibility to address various other open questions.

The analysis presented here for the reflection data is model independent and can therefore be used to directly compare different samples. It can be used for the XENON1t experiment to investigate the optical properties of the materials that are under discussion for the experiment. Samples from different providers with different production processes will be tested. Special emphasize will be directed to the question how the surface treatment influences the reflectance and which surface treatment should be used for the XENON1t experiment. Here the amount of material needed for the experiment needs to be kept in mind, the surface preparation process needs to be reproducible for large areas.

These measurements have been conducted in vacuum, therefore the result cannot be directly applied to the simulation of the experiment. In a next modification of this setup, that is tested at the moment, a small chamber for liquid Xenon in which the sample is situated, is inserted in place of the simple sample holder. The chamber is transparent and non refractive for vacuum UV light. The PMT holder and light source are kept in place. This modification promises model independent measurements of the reflectance from PTFE inside liquid Xenon. These improvements are conducted by C. Levy-Brown and will be presented in her thesis [Lev13].

In the mean time several improvements can be made for this stage of the setup and the presented analysis:

Experimental improvements Several problems and unknown effects have been mentioned in the description of the experimental setup. Here some points that should be investigated or improved are listed:

- The beam alignment proved to be problematic. The measurement accuracy depends on the exact knowledge of the incoming intensity as well as the profile. Special focus should be put to the lens system as the alignment proved to be difficult.
- To improve the accuracy of the angular scale, a specular reflector could be mounted on the sample holder for calibration.

- The measurements have shown that the angle $\tilde{\varphi}_i$ gives only a little additional information for the fit. It has been easily described with the simulation program. Therefore, the implementation of the original planned sample holder with the possibility to continuously change the angle $\tilde{\varphi}_i$ should be discussed with the expenses clearly in mind. Investigating the angle $\tilde{\varphi}_i$ could help to expose directional effects of *e.g.* the surface preparation process which otherwise could be missed.
- A new sample holder should leave the area behind the sample clear to avoid undesirable reflections.
- The inner surface of the cold shield has been eloxadized to reduce the stray light. It is not known whether the eloxadization also prevents the reflection of VUV light, but can be easily tested with the setup. In case the material is not 'black' for VUV light, the surface should be covered with a different paint as *e.g.* the surface coating MLS-85SB from AZ Technology, Inc.
- To avoid contaminations of the components inside the setup, it should be considered to flush the chamber with clean gas when opening it.

Improvements for the analysis There are several starting points for improvements of the Monte-Carlo-simulations and the fit.

- In the Monte-Carlo-simulation the beam spot size has not been taken into account. The fit corrects this with a larger micro-surface distribution.
- The model describing the reflection has several shortfalls. Up to now there are no connections between the different specular amplitudes.
- The geometrical cutoff is too harsh (see also figure 5.38), here the inclusion of a convolution would make sense.

6. Conclusion and outlook

Although the Standard Model of particle physics successfully describes nearly all observations, the quest for physics beyond the Standard Model is ongoing. In this thesis experimental work has been conducted in support of the calibration of two experiments investigating beyond Standard Model physics.

An angular-selective electron source for the KATRIN experiment

Neutrinos have been proven to have properties not in accordance with the Standard Model, the observation of neutrino oscillation has proven that the weak eigenstates are a superposition of the mass eigenstates, whose mass differs from each other. Oscillation experiments can determine the size of the mass differences, but have no information about the absolute mass scale. The KATRIN experiment aims to determine the mass of the electron anti-neutrino m_{ν_e} by measuring the spectral shape of the ^{3}H β-decay to a limit of 0.2 eV with 90 % confidence level. To achieve this, a high resolution spectrometer using magnetic adiabatic collimation with electrostatic filter has been constructed in which the electrons energies are analyzed by parallelizing the electrons momenta and applying an electrostatic potential as high pass filter. The maximum of the electric retarding potential is applied at the position of the minimum of the magnetic field strength, the so-called analyzing plane. As the potential is inhomogeneous over the radius of the flux tube of 5 m in the analyzing plane, the electron detector used as counter for the electrons passing the high pass filter, is segmented. This allows to analyze electrons passing different sections of the spectrometer separately and to take into account the effect of the inhomogeneities.

To calibrate the detector pixels as well as to investigate the exact properties of the spectrometer, an electron source with the following properties is needed:

- finite spot size and movability,
- limited energy spread,
- angular selectivity,
- pulsed emission and
- adjustable intensity.

Electron sources with finite spot size, limited energy spread, pulsed emission and adjustable intensity have been reported in [Val09a, Val09b] and [Val11]. On the basis of these a novel concept for an angular-selective electron source has been developed and tested in this thesis.

Low energy electrons are emitted via the photo-electric effect from an Ag photocathode using a UV LED. They are accelerated in a combination of homogeneous, non-parallel

electric and magnetic fields. The electrons' angles θ with respect to the magnetic field can be adjusted by changing the electric acceleration field strength or by changing the angle between the electric and the magnetic field. The electrons are guided adiabatically into the entrance magnet. Due to the increase in field strength, the angle θ increases. The angle θ_{mag} inside the entrance magnet has been used to characterize the angular-selectivity of the electron source.

A prototype of the angular-selective electron source has been constructed and was successfully tested at the Mainz spectrometer. The measurements have proven the working principle of the electron source and it has been shown that the angular emission is adjustable. The complete range of electrons accepted in the spectrometer with angles between $\theta_{\mathrm{mag}} \in [0\,^\circ : 90\,^\circ]$ is accessible by fixing one parameter of the electron source and adjusting the other. The angular spread has been determined to be below $\Delta\theta_{\mathrm{mag}} < 15\,^\circ$, for small angles θ_{mag} it is $\Delta\theta_{\mathrm{mag}} \in [2\,^\circ : 6\,^\circ]$.

These successful proof-of-principle measurements indicate several points where problems persist. The Penning trap for electrons between the electron source on negative potential and the analyzing plane of the spectrometer has caused problems in the measurement. Discharges have been circumvented by installing a wire after the model of [Bec11]. The whole electron source setup has been revisited in simulations and has been refined with regards to the experience gained in the Mainz measurement phase. The energy spread has been improved by implementing a laser system with fixed wavelength and narrow spread and by improving the application of the photo-cathode material. Improved simulations have shown that the angular spread can be reduced by using a larger aperture and implementing the electron source setup in a movable ground field cage. The setup has been constructed and tested [Zac13]. It has now been installed at the KATRIN experiment for test measurements of the KATRIN main spectrometer [Win13].

Investigation of the reflection properties of PTFE for Vacuum-UV light

Astrophysical observations on different scales require the introduction of an unknown type of matter that has up to now only been seen through its gravitational properties. The observations point to non-baryonic matter not coupling to the strong and the electromagnetic force. Interaction cross sections of the weak scale are still allowed and at the time of the structure formation the particles should be cold. The WIMP is the most favored particle by experimental physicists as it can be detected with modern detectors.

The XENON experiment uses a dual phase TPC in the search for WIMP particles by detecting the energy deposited in a scattering reaction with a nucleus. The energy transfer becomes visible as the nucleus moves through the medium, loosing its energy through ionization and excitation. The scintillation light is detected as start signal S1 with PMTs. An electric fields separates the created charges, drifting the electrons to the liquid-gas interface, where they are extracted and amplified. The light visible from the amplification process is detected by the PMTs as stop signal S2. To enhance the light collection in the top and bottom PMT arrays, the side of the TPC is covered with PTFE which is known to be a good reflector in the wavelength region above 300 nm. As dielectric material, the PTFE is also used to support the field cage required to ensure the homogeneity of the

electric field.

As the exact values for the reflectivity of PTFE is not known for VUV light and is expected to change with the sample preparation process, a setup to investigate it has been designed, build and tested. Measurements of the reflectivity from samples from the XENON100 detector will be used as input for detector simulations. For the XENON1t detector different sample batches and different surface treatment methods will be tested before choosing the material for implementation.

For a determination of the angular dependent reflection of light, the incoming intensity needs to be known as reference. The position dependent intensity of the reflected light needs to be measured in dependence of the incident angle on the investigated surface. As it is difficult to cover the hemisphere above the sample for a position dependent measurement, a movable detector has been implemented in the setup measuring the reflected intensity for discrete positions. A MC simulation has been written, simulating the light reflection in case of diffuse or specular reflectance for surfaces with micro-surfacefollowing a to be specified distribution in dependence of the incoming angle θ_i and the outgoing angles θ_o and φ_o. The output is then fitted to the measured data, allowing to extract the total reflected intensity as function of the incoming angle θ_i.

Due to the absorption of VUV light in air, the experiment needs to be in vacuum. A commercial deuterium lamp and a vacuum monochromator to select the wavelength are used to create the light beam. The beam is focused with a lens and collimated with an exchangeable aperture. The sample and detector are located in a second vacuum chamber separated from the light source by a VUV transmitting MgF window. The sample is implemented on a rotation feed through allowing to change the angle of incidence. A PMT is used as detector and is implemented on a rotation feed through with three dimensional lateral movement. The measurement has been partially automated.

First results have been obtained for two PTFE samples of different surface preparation at a wavelength of 178 nm. A reflectance of 35 % to 49 % depending on the angle of incidence has been determined for the first sample and of 28 % to 49 % for the second. The pattern of diffuse and specular reflectance changes in a way that can be explained with the surface preparation process. This conclusion is supported by additional microscope measurements. In addition measurements have been conducted for one sample at different wavelength. It shows that the reflectance drops off for wavelength below 200 nm.

The presented first results show that the setup is working nicely. Measurements with samples from the XENON100 experiment using this setup have been conducted and are presented in [Cho12].

Improvements of the calibration of sample position, incident angle and detector angle are investigated by C. Levy-Brown and will be presented in [Lev13]. In addition the effect a different index of refraction will be investigated by using liquid Xenon as medium. For this an improved sample holder with an optical transparent, non-refractive Quartz cylinder is being implemented in this setup. The sample will be positioned in the cylinder which is then filled with liquid Xenon. The complete small sample chamber is attached to a rotation-able flange on top of the chamber. The light source and detector are used as before [Lev13].

The chamber can serve different purposes. The flexibility of the setup allows to investigate different effects, as *e.g.* the quantum efficiency measurements published in [Apr12d]. More measurements are planed and will be shown in future theses.

A. Electron source

A.1. Single errorfunction fits with residuals

Table A.1.: Transmission function parameters for stand alone fits.

α (°)	$\Delta U_{\text{plate}}(kV)$	δU_0 (V)	σ (V)	χ^2	χ^2_r
0	2	-13.474 ± 0.008	0.087 ± 0.008	4.4	0.9
4	2	-13.417 ± 0.007	0.091 ± 0.006	13.2	1.9
4	3	-13.275 ± 0.007	0.097 ± 0.006	3.6	0.7
4	4	-13.027 ± 0.010	0.147 ± 0.009	3.7	0.7
8	1	-13.020 ± 0.008	0.110 ± 0.007	9.0	1.8
8	2	-13.274 ± 0.007	0.084 ± 0.008	7.1	1.8
8	3	-12.486 ± 0.014	0.126 ± 0.013	3.1	0.6
8	4	-11.052 ± 0.019	0.186 ± 0.017	9.9	3.3
12	1.75	-13.118 ± 0.008	0.100 ± 0.006	5.1	1.7
12	2	-13.030 ± 0.008	0.091 ± 0.006	1.0	0.5
12	3	-10.382 ± 0.014	0.216 ± 0.011	4.2	0.8
12	3.5	-8.449 ± 0.017	0.221 ± 0.012	5.2	1.3
14	2	-13.160 ± 0.015	0.097 ± 0.010	1.8	0.6
14	3.4	-8.775 ± 0.016	0.229 ± 0.014	2.9	0.6

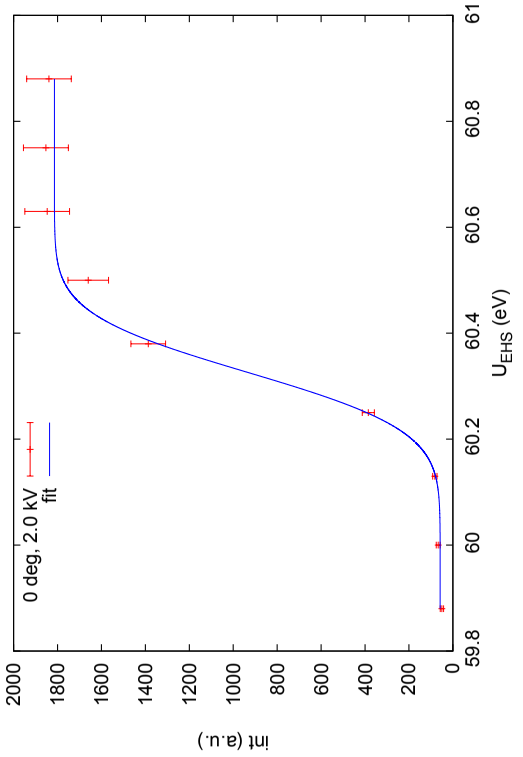

(a) fit: $\alpha = 0\ °$, $\Delta U_{\text{plate}} = 2.0\ kV$

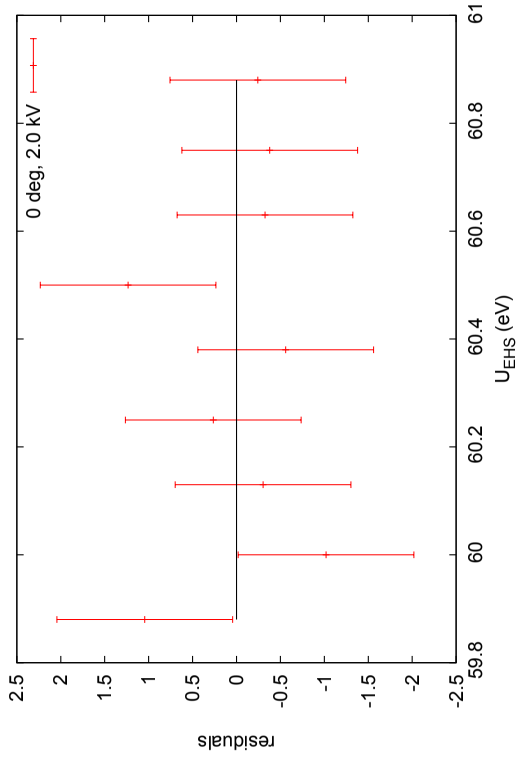

(b) res: $\alpha = 0\ °$, $\Delta U_{\text{plate}} = 2.0\ kV$

Figure A.1.: $\alpha = 0\,°$, $\Delta U_{\text{plate}} = 2\,\text{kV}$, $\chi_r^2 = 0.9$

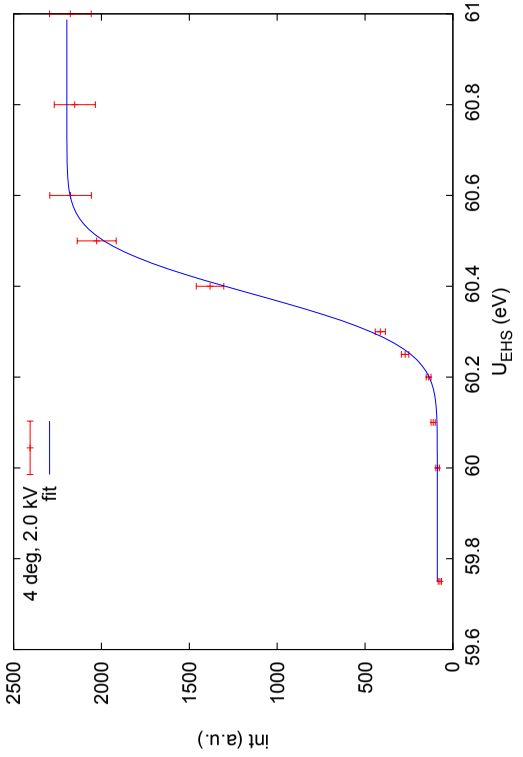

(a) fit: $\alpha = 4\ °$, $\Delta U_{\text{plate}} = 2.0\ kV$

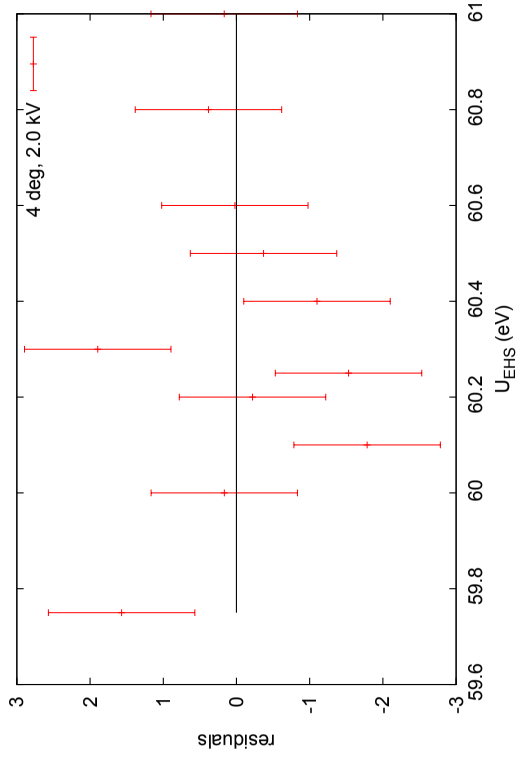

(b) res: $\alpha = 4\ °$, $\Delta U_{\text{plate}} = 2.0\ kV$

Figure A.2.: $\alpha = 4\,°$, $\Delta U_{\text{plate}} = 2\,\text{kV}$, $\chi_r^2 = 1.9$

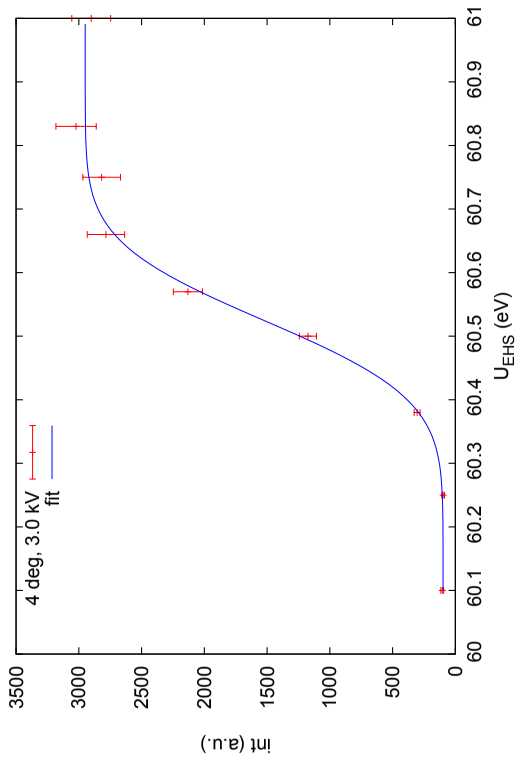

(a) fit: $\alpha = 4\ °$, $\Delta U_{\text{plate}} = 3.0\ kV$

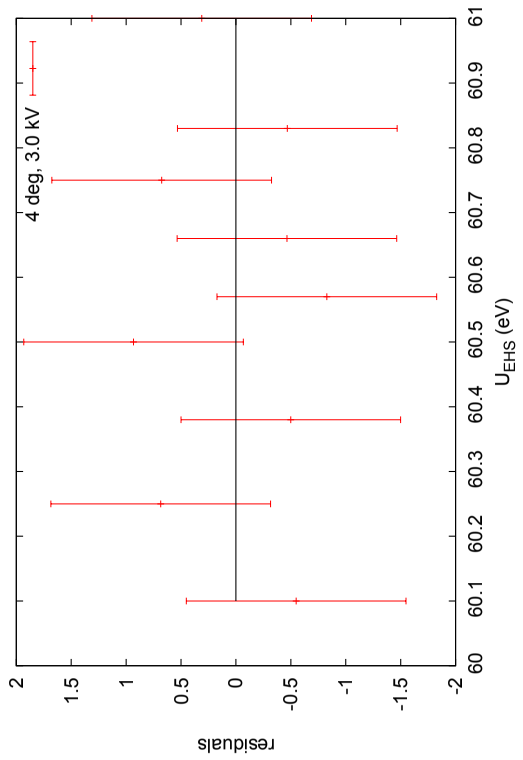

(b) res: $\alpha = 4\ °$, $\Delta U_{\text{plate}} = 3.0\ kV$

Figure A.3.: $\alpha = 4\,°$, $\Delta U_{\text{plate}} = 3\,\text{kV}$, $\chi_r^2 = 0.7$

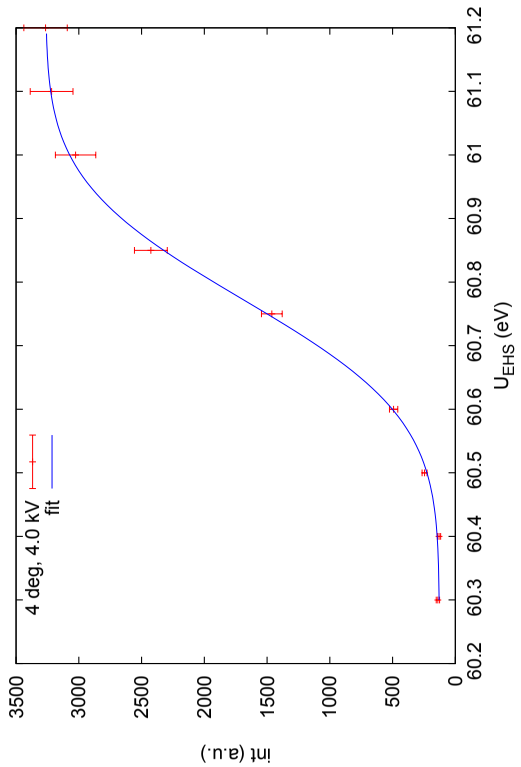

(a) fit: $\alpha = 4\ °$, $\Delta U_{\text{plate}} = 4.0\ kV$

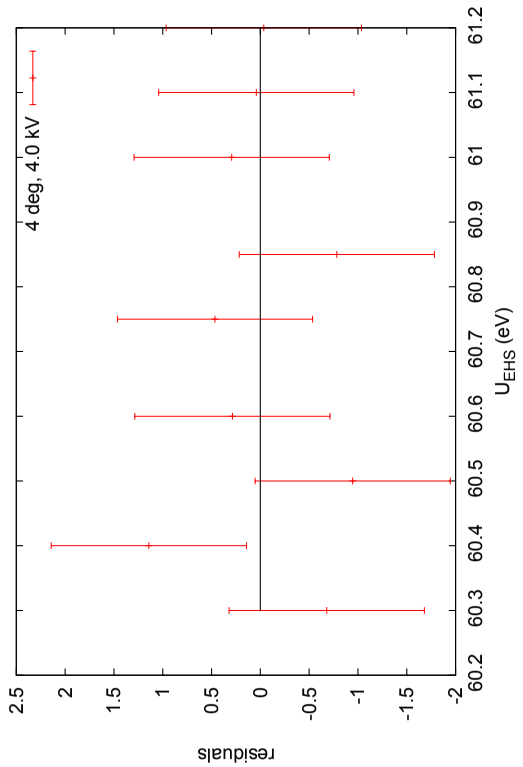

(b) res: $\alpha = 4\ °$, $\Delta U_{\text{plate}} = 4.0\ kV$

Figure A.4.: $\alpha = 4\,°$, $\Delta U_{\text{plate}} = 4\,\text{kV}$, $\chi_r^2 = 0.7$

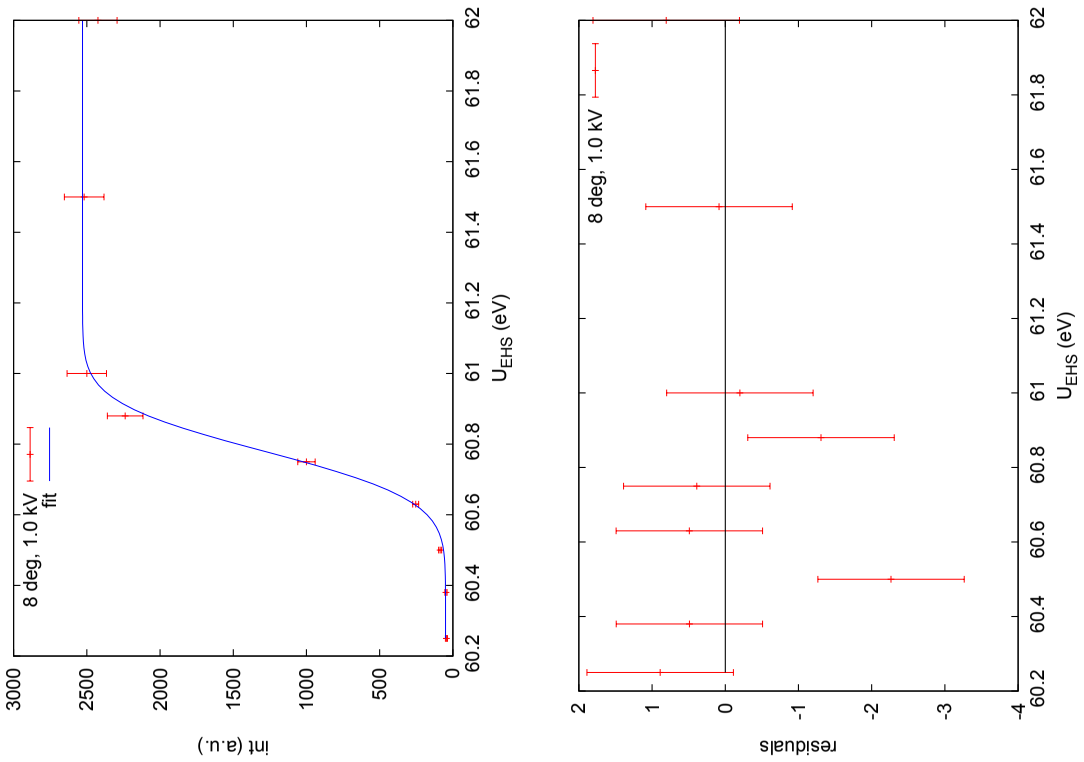

(a) fit: $\alpha = 8\ °$, $\Delta U_{\text{plate}} = 1.0\ kV$ (b) res: $\alpha = 8\ °$, $\Delta U_{\text{plate}} = 1.0\ kV$

Figure A.5.: $\alpha = 8\,°$, $\Delta U_{\text{plate}} = 1\,\text{kV}$, $\chi_r^2 = 1.8$

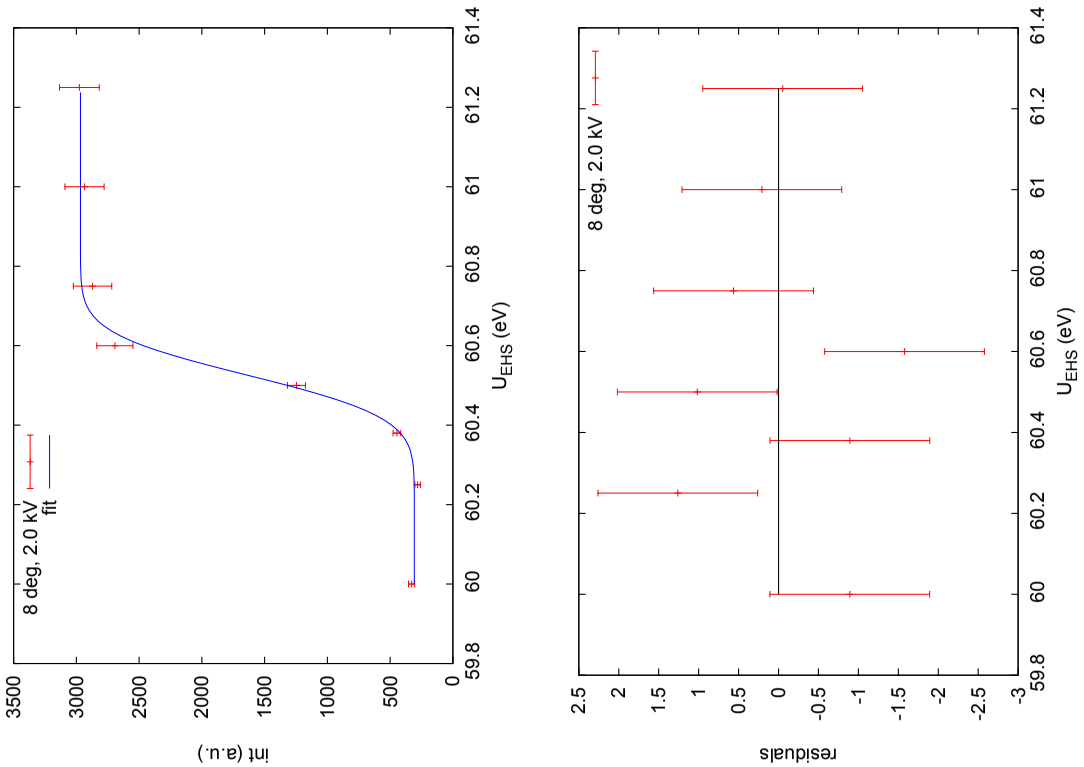

(a) fit: $\alpha = 8\ °$, $\Delta U_{\text{plate}} = 2.0\ kV$ (b) res: $\alpha = 8\ °$, $\Delta U_{\text{plate}} = 2.0\ kV$

Figure A.6.: $\alpha = 8\,°$, $\Delta U_{\text{plate}} = 2\,\text{kV}$, $\chi_r^2 = 1.8$

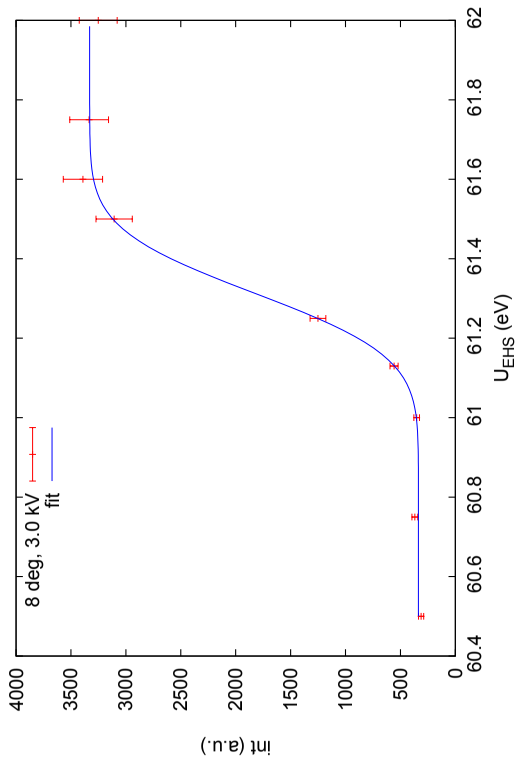

(a) fit: $\alpha = 8\ °$, $\Delta U_{\text{plate}} = 3.0\ kV$

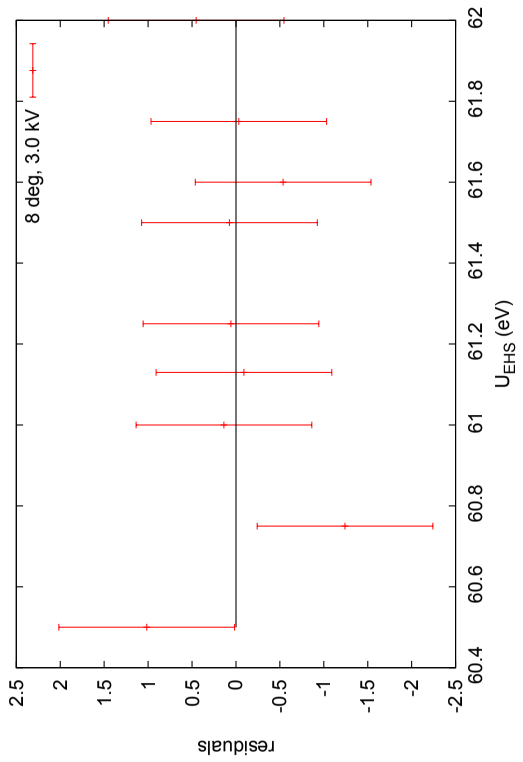

(b) res: $\alpha = 8\ °$, $\Delta U_{\text{plate}} = 3.0\ kV$

Figure A.7.: $\alpha = 8\,°$, $\Delta U_{\text{plate}} = 3\,\text{kV}$, $\chi_r^2 = 0.6$

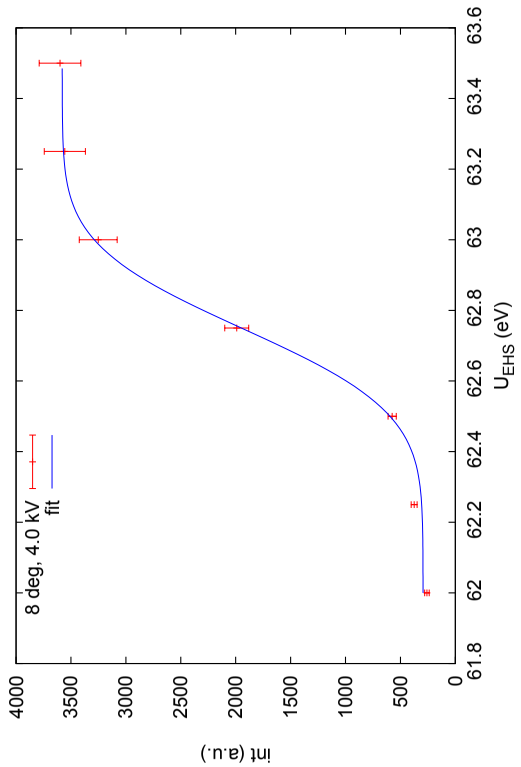

(a) fit: $\alpha = 8\ °$, $\Delta U_{\text{plate}} = 4.0\ kV$

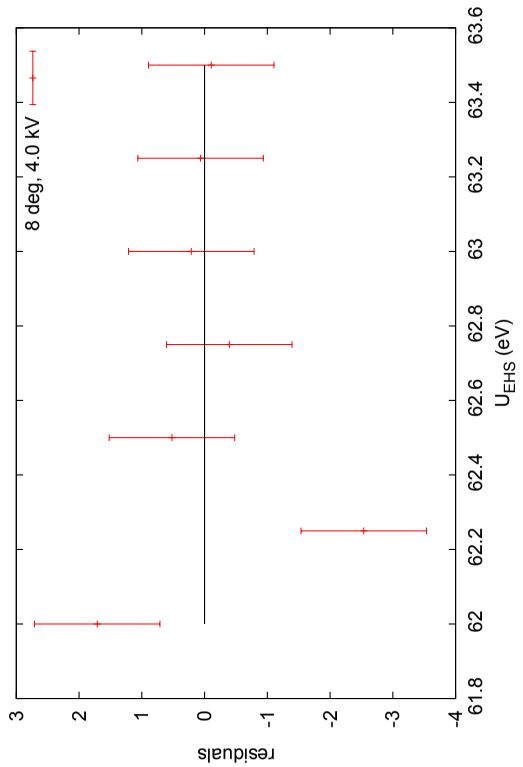

(b) res: $\alpha = 8\ °$, $\Delta U_{\text{plate}} = 4.0\ kV$

Figure A.8.: $\alpha = 8\,°$, $\Delta U_{\text{plate}} = 4\,\text{kV}$, $\chi_r^2 = 3.3$

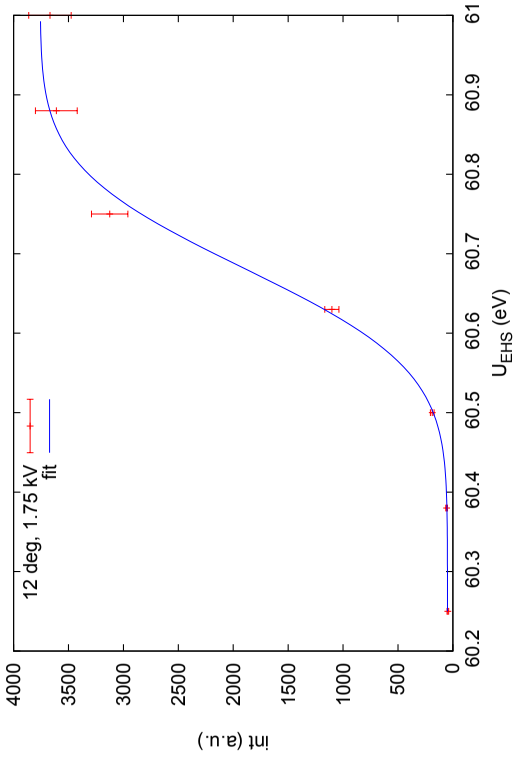

(a) fit: $\alpha = 12\,°$, $\Delta U_{\text{plate}} = 1.75\ kV$

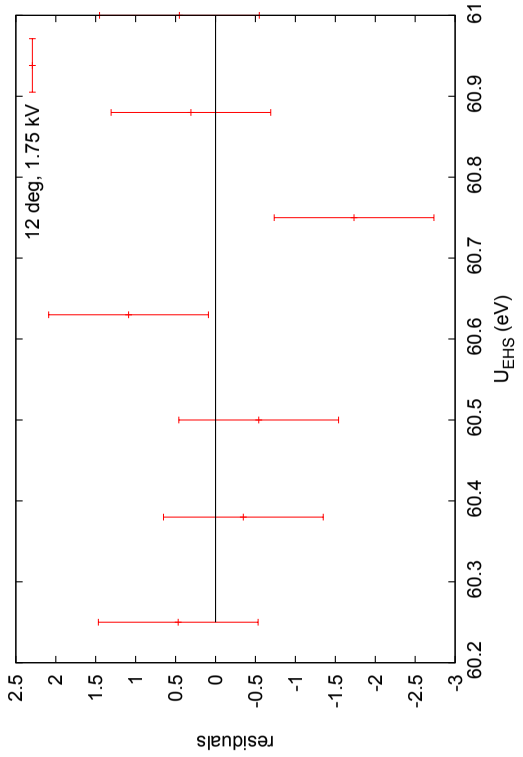

(b) res: $\alpha = 12\,°$, $\Delta U_{\text{plate}} = 1.75\ kV$

Figure A.9.: $\alpha = 12\,°$, $\Delta U_{\text{plate}} = 1.75\,\text{kV}$, $\chi_r^2 = 1.7$

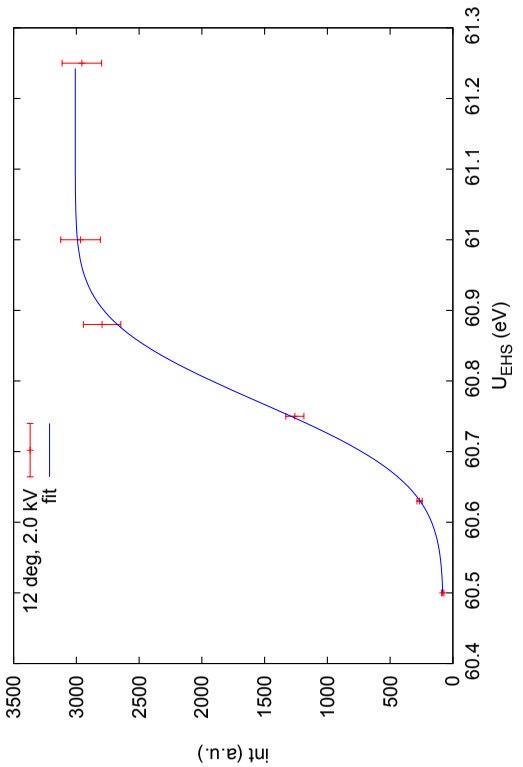

(a) fit: $\alpha = 12\,°$, $\Delta U_{\text{plate}} = 2.0\ kV$

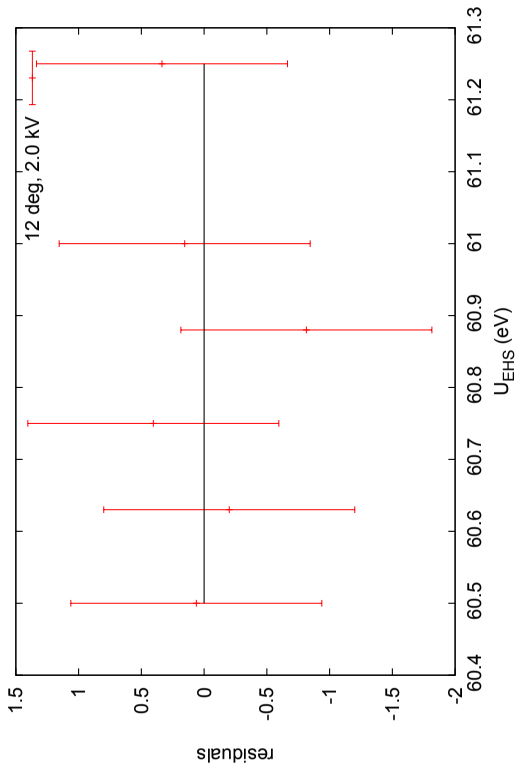

(b) res: $\alpha = 12\,°$, $\Delta U_{\text{plate}} = 2.0\ kV$

Figure A.10.: $\alpha = 12\,°$, $\Delta U_{\text{plate}} = 2\,\text{kV}$, $\chi_r^2 = 0.5$

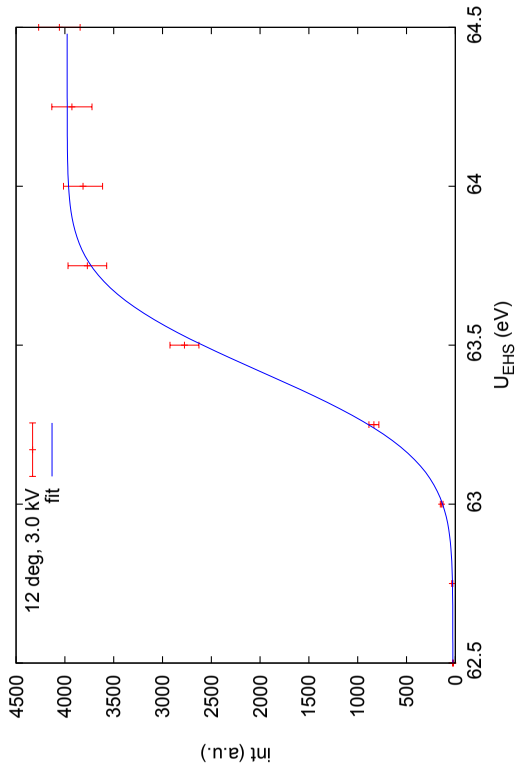

(a) fit: $\alpha = 12\ °$, $\Delta U_{\text{plate}} = 3.0\ kV$

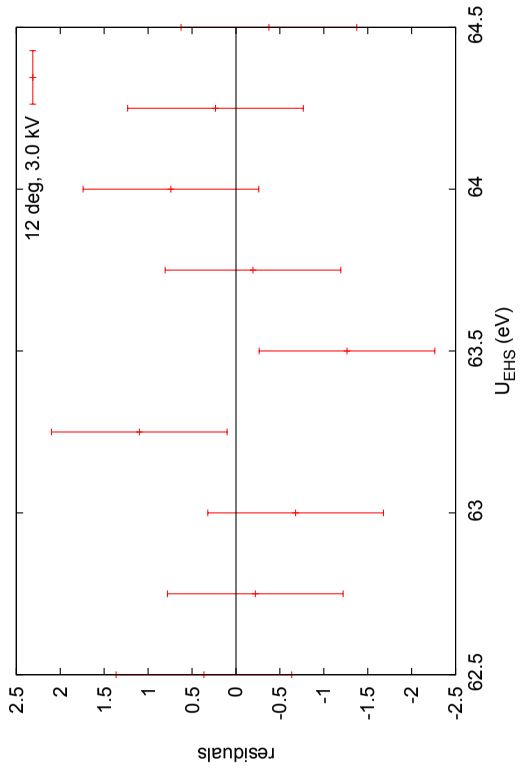

(b) res: $\alpha = 12\ °$, $\Delta U_{\text{plate}} = 3.0\ kV$

Figure A.11.: $\alpha = 12\,°$, $\Delta U_{\text{plate}} = 3\,\text{kV}$, $\chi_r^2 = 0.8$

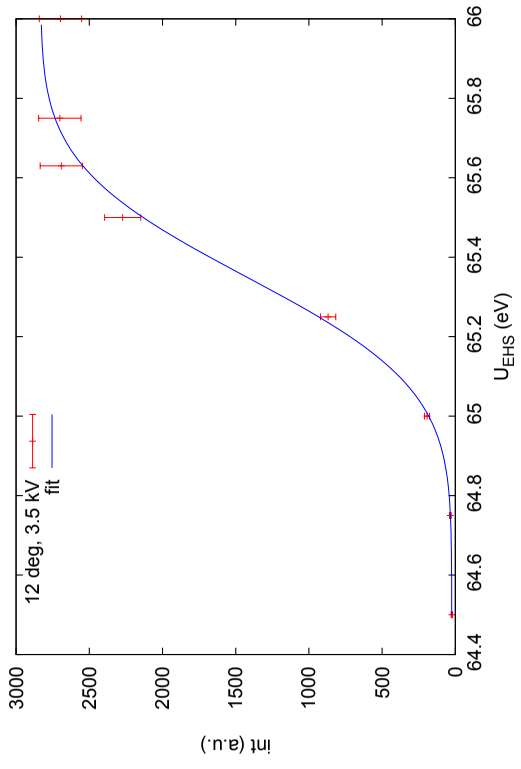

(a) fit: $\alpha = 12\ °$, $\Delta U_{\text{plate}} = 3.5\ kV$

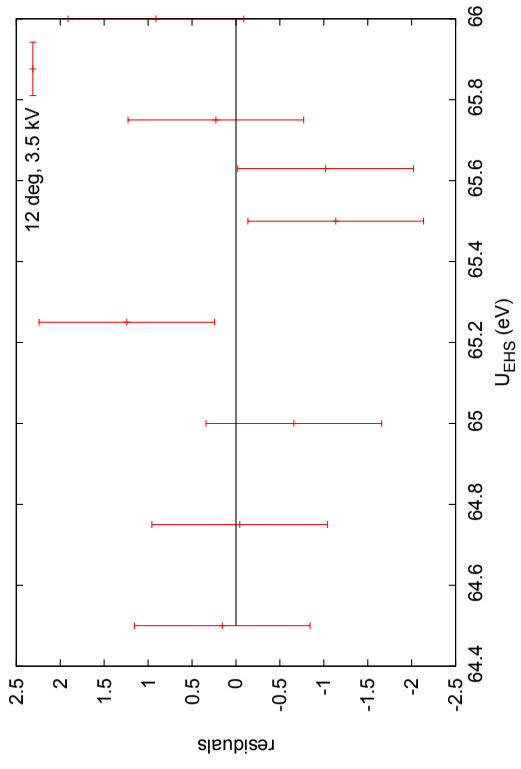

(b) res: $\alpha = 12\ °$, $\Delta U_{\text{plate}} = 3.5\ kV$

Figure A.12.: $\alpha = 12\,°$, $\Delta U_{\text{plate}} = 3.5\,\text{kV}$, $\chi_r^2 = 1.3$

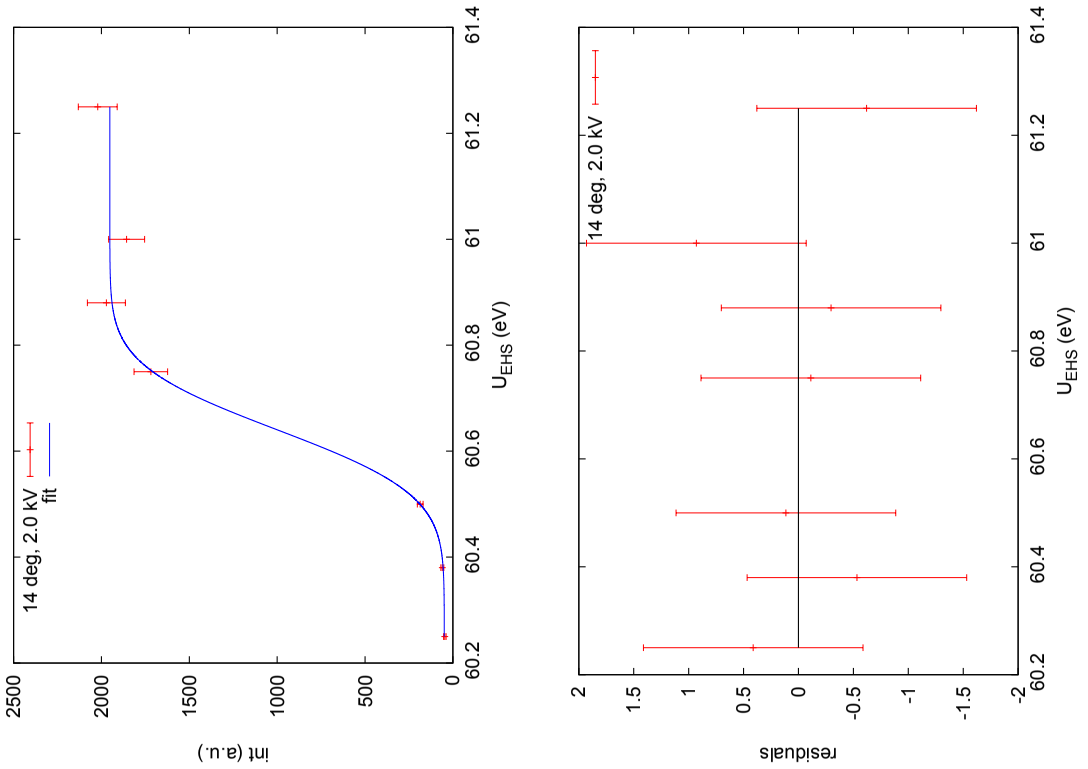

(a) fit: $\alpha = 14\ °$, $\Delta U_{\text{plate}} = 2.0\ kV$ (b) res: $\alpha = 14\ °$, $\Delta U_{\text{plate}} = 2.0\ kV$

Figure A.13.: $\alpha = 14\,°$, $\Delta U_{\text{plate}} = 2.0\,\text{kV}$, $\chi_r^2 = 0.6$

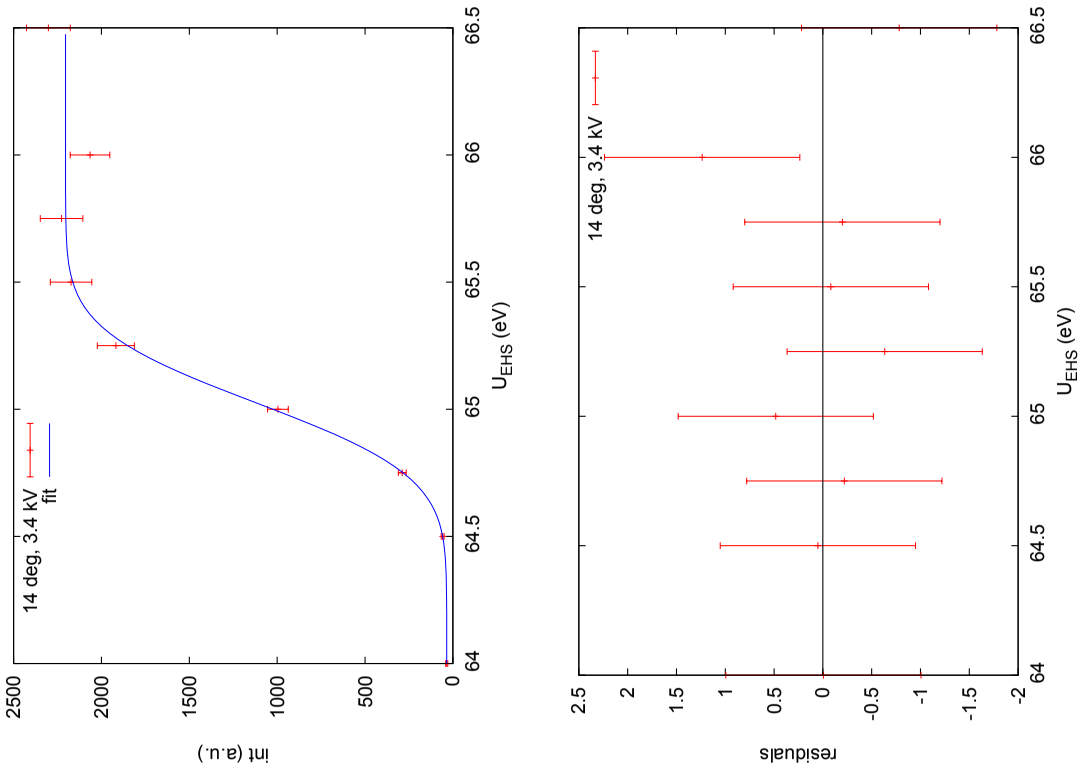

(a) fit: $\alpha = 14\ °$, $\Delta U_{\text{plate}} = 3.4\ kV$ (b) res: $\alpha = 14\ °$, $\Delta U_{\text{plate}} = 3.4\ kV$

Figure A.14.: $\alpha = 14\,°$, $\Delta U_{\text{plate}} = 3.4\,\text{kV}$, $\chi_r^2 = 0.6$

B. Calculation of angles for the reflection chamber setup

B.1. Global angles

In this section the correlations between the turnable angles in the setup $\tilde{\theta}_i$, $\tilde{\theta}_d$ and $\tilde{\varphi}_i$ (see figure B.2(a)) and the angles θ_i, θ_o and φ_o needed for the model (see figure B.2(b)) evaluation are derived.

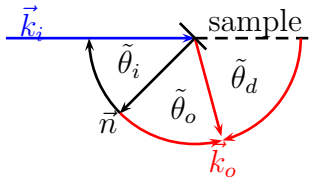

Figure B.1.: Angles in the detector plane of the setup, $\tilde{\varphi}_i = 0\,^\circ$

The detector angle $\tilde{\theta}_d$ is defined relative to the fixed entrance beam $\vec{k}_i$ (see figure B.1). The angle $\tilde{\theta}_o$ is defined with respect to the surface normal $\vec{n}$ and is connected to the experimental angles via the following relationship:

$$\tilde{\theta}_o = \tilde{\theta}_d + \tilde{\theta}_i - 180\,^\circ.$$

With basic algebra the relationship between the model angles (see figure 5.6(b)) and the experimental angles (see figure 5.6(a)) can be derived. In a first step a right handed coordinate system with center at the base of the normal vector $\vec{n}$ and the z-axis in the opposite direction of the incident light is chosen. The yz-plane coincides with the rotation plane of the detector. Choosing the normalized light vector $\vec{k}_i$ to point into the opposite direction for convenience, it is

$$\vec{k}_i = \begin{pmatrix} 0 \\ 0 \\ 1 \end{pmatrix}.$$

The vectors $\vec{n}_{\parallel}$ (the projection of the vector $\vec{n}$ into the yz-plane) and $\vec{k}_o$ are determined by the angles $\tilde{\theta}_i$ respectively $\tilde{\theta}_i$ and $\tilde{\theta}_o$ and can be calculated by rotating vector $\vec{k}_i$ with

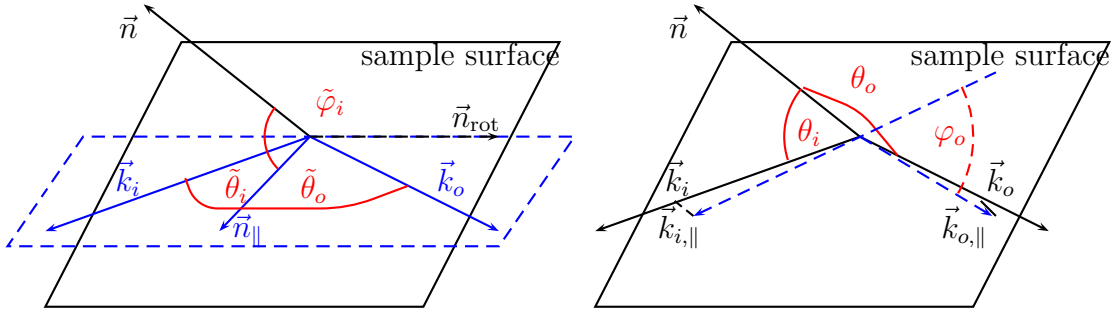

(a) Experimental angles in the setup.

(b) Angles used for the models.

Figure B.2.: Angles used in the experimental setup and in the models to describe the measured reflection.

$-\tilde{\theta}_i$ respectively $-(\tilde{\theta}_i + \tilde{\theta}_o)$ around the x-axis:

$$\vec{n}_{\parallel} = R_x(-\tilde{\theta}_i) \cdot \vec{k}_i = \begin{pmatrix} 1 & 0 & 0 \\ 0 & \cos(-\tilde{\theta}_i) & -\sin(-\tilde{\theta}_i) \\ 0 & \sin(-\tilde{\theta}_i) & \cos(-\tilde{\theta}_i) \end{pmatrix} \begin{pmatrix} 0 \\ 0 \\ 1 \end{pmatrix} = \begin{pmatrix} 0 \\ \sin\tilde{\theta}_i \\ \cos\tilde{\theta}_i \end{pmatrix}$$

$$\vec{k}_o = \begin{pmatrix} 0 \\ \sin(\tilde{\theta}_i + \tilde{\theta}_o) \\ \cos(\tilde{\theta}_i + \tilde{\theta}_o) \end{pmatrix}.$$

To derive the vector $\vec{n}$, $\vec{n}_{\parallel}$ has to be rotated around $\vec{n}_{\text{rot}}$ with the angle $-\tilde{\varphi}_i$. As $\vec{n}_{\text{rot}}$ lies in the rotation plane of the detector on the sample surface, its x-component is zero $(\vec{n}_{\text{rot}})_x = 0$. $\vec{n}_{\parallel}$ is perpendicular to $\vec{n}_{\text{rot}}$, thus

$$0 = \vec{n}_{\text{rot}} \cdot \vec{n}_{\parallel} = (\vec{n}_{\text{rot}})_y \sin\tilde{\theta}_i + (\vec{n}_{\text{rot}})_z \cos\tilde{\theta}_i \Rightarrow (\vec{n}_{\text{rot}})_y = -\frac{(\vec{n}_{\text{rot}})_z \cos\tilde{\theta}_i}{\sin\tilde{\theta}_i}.$$

$\vec{n}_{\text{rot}}$ is also a unit vector:

$$1 = \sqrt{((\vec{n}_{\text{rot}})_x)^2 + ((\vec{n}_{\text{rot}})_y)^2 + ((\vec{n}_{\text{rot}})_z)^2} = \frac{(\vec{n}_{\text{rot}})_z}{\sin\tilde{\theta}_i}$$
$$\Rightarrow (\vec{n}_{\text{rot}})_z = \sin\tilde{\theta}_i \wedge (\vec{n}_{\text{rot}})_y = -\cos\tilde{\theta}_i$$
$$\Rightarrow \vec{n}_{\text{rot}} = \begin{pmatrix} 0 \\ -\cos\tilde{\theta}_i \\ \sin\tilde{\theta}_i \end{pmatrix}.$$

The rotation matrix around $\vec{n}_{\text{rot}}$ with the angle $-\tilde{\varphi}_i$ is

$$R_{\vec{n}_{\text{rot}}}(-\tilde{\varphi}_i) = \cos(-\tilde{\varphi}_i) \begin{pmatrix} 1 & 0 & 0 \\ 0 & 1 & 0 \\ 0 & 0 & 1 \end{pmatrix} + \sin(-\tilde{\varphi}_i) \begin{pmatrix} 0 & -(\vec{n}_{\text{rot}})_z & (\vec{n}_{\text{rot}})_y \\ (\vec{n}_{\text{rot}})_z & 0 & -(\vec{n}_{\text{rot}})_x \\ -(\vec{n}_{\text{rot}})_y & (\vec{n}_{\text{rot}})_x & 0 \end{pmatrix}$$
$$+(1 - \cos(-\tilde{\varphi}_i)) \begin{pmatrix} (\vec{n}_{\text{rot}})_x^2 & (\vec{n}_{\text{rot}})_x(\vec{n}_{\text{rot}})_y & (\vec{n}_{\text{rot}})_x(\vec{n}_{\text{rot}})_z \\ (\vec{n}_{\text{rot}})_y(\vec{n}_{\text{rot}})_x & (\vec{n}_{\text{rot}})_y^2 & (\vec{n}_{\text{rot}})_y(\vec{n}_{\text{rot}})_z \\ (\vec{n}_{\text{rot}})_z(\vec{n}_{\text{rot}})_x & (\vec{n}_{\text{rot}})_z(\vec{n}_{\text{rot}})_y & (\vec{n}_{\text{rot}})_z^2 \end{pmatrix}. \tag{B.1}$$

The normal vector to the surface $\vec{n}$ is thus

$$\vec{n} = R_{\vec{n}_{\text{rot}}}(-\tilde{\varphi}_i) \cdot \vec{n}_{\parallel} = \begin{pmatrix} \sin\tilde{\varphi}_i \\ \sin\tilde{\theta}_i \cos\tilde{\varphi}_i \\ \cos\tilde{\theta}_i \cos\tilde{\varphi}_i \end{pmatrix}$$

The angles θ_i and θ_o now can be calculated from the scalar product of the normal vector $\vec{n}$ and the incoming respectively outgoing light vectors $\vec{k}_i$ respectively $\vec{k}_o$:

$$\cos\theta_i = \vec{n} \cdot \vec{k}_i = \cos\tilde{\theta}_i \cos\tilde{\varphi}_i \tag{B.2}$$

$$\cos\theta_o = \vec{n} \cdot \vec{k}_o = \cos\tilde{\theta}_o \cos\tilde{\varphi}_i. \tag{B.3}$$

The angle φ_o is enclosed by the outgoing light vector $\vec{k}_o$ projected on the sample surface $\vec{k}_{o,\parallel}$ and the negative incoming light vector $-\vec{k}_i$, also projected on the sample surface $-\vec{k}_{i,\parallel}$ (see also figure B.2(b)). The projections can be calculated with the normal vector $\vec{n}$:

$$\vec{k}_{i,\parallel} = \vec{n} \times \left(\vec{n} \times \vec{k}_i\right) = \vec{n}\left(\vec{n} \cdot \vec{k}_i\right) - \vec{k}_i\left(\vec{n} \cdot \vec{n}\right),$$

for $\vec{k}_{o,\parallel}$ analogous. This results in

$$\cos\varphi_o = \frac{-\vec{k}_{i,\parallel} \cdot \vec{k}_{o,\parallel}}{|\vec{k}_{i,\parallel}| \cdot |\vec{k}_{o,\parallel}|} = \frac{\cos\tilde{\theta}_i \cos\tilde{\theta}_o \cos^2\tilde{\varphi}_i - \cos\left(\tilde{\theta}_i + \tilde{\theta}_o\right)}{\sqrt{\left(1 - \cos^2\tilde{\theta}_i \cos^2\tilde{\varphi}_i\right)\left(1 - \cos^2\tilde{\theta}_o \cos^2\tilde{\varphi}_i\right)}}. \tag{B.4}$$

B.2. Local angles

Surface roughness can be described with micro-surfaces, whose normal vector $\vec{n}'$ is displaced from the overall surface normal $\vec{n}$ by the angle α (see figure B.3).

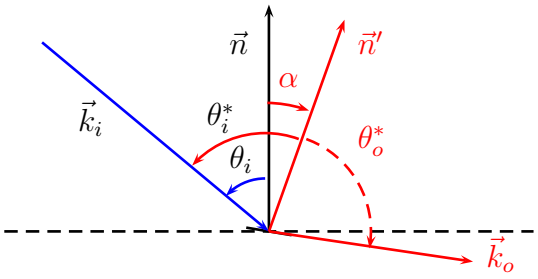

Figure B.3.: Angles to describe the micro-surface reflection

The distribution of the angle α characterizes the roughness of the surface. As the diffuse reflection is not affected by the distribution, the angle α will be calculated for the case of specular reflection from the micro-surface, thus under the condition $\theta_i^* = \theta_o^* = \theta^*$. A local coordinate system has been chosen in which the overall surface normal vector $\vec{n}$ points into the z-direction. The incident light vector is then

$$\vec{k}_i = \begin{pmatrix} \sin\theta_i \\ 0 \\ \cos\theta_i \end{pmatrix} \tag{B.5}$$

and the exit light vector is

$$\vec{k}_o = \begin{pmatrix} -\sin\theta_o \cos\varphi_o \\ -\sin\theta_o \sin\varphi_o \\ \cos\theta_o \end{pmatrix}. \tag{B.6}$$

As for specular reflection the exiting light ray $\vec{k}_o$ lies in the same plane as the incident light ray $\vec{k}_i$ and the micro-surface normal $\vec{n}'$, the angle encompassed by the light vectors $\vec{k}_i$ and $\vec{k}_o$ is equal to two times the specular angle θ^*:

$$\cos 2\theta^* = \vec{k}_i \cdot \vec{k}_o = \cos\theta_i \cos\theta_o - \sin\theta_i \sin\theta_o \cos\varphi_o. \tag{B.7}$$

The micro-surface normal vector $\vec{n}^*$ can be derived from the light vectors:

$$\vec{n}^* = \frac{a}{2}(\vec{k}_i + \vec{k}_o) = \frac{a}{2} \begin{pmatrix} \sin\theta_i - \sin\theta_o \cos\varphi_o \\ -\sin\theta_o \sin\varphi_o \\ \cos\theta_i + \cos\theta_o \end{pmatrix} \tag{B.8}$$

with the factor a normalizing the vector:

$$1 = |\vec{n}^*| = \frac{a}{2}\sqrt{(\sin\theta_i - \sin\theta_o\cos\varphi_o)^2 + (\sin\theta_o\sin\varphi_o)^2 + (\cos\theta_i + \cos\theta_o)^2}$$
$$\rightarrow a = \frac{1}{2\cos\theta^*}. \tag{B.9}$$

The angle α can then be calculated from the scalar product between the two surface normals:

$$\cos\alpha = \vec{n} \cdot \vec{n}^* = \frac{\cos\theta_i + \cos\theta_o}{2\cos\theta^*}. \tag{B.10}$$

B.3. Distribution of the angle θ_o for diffuse reflection

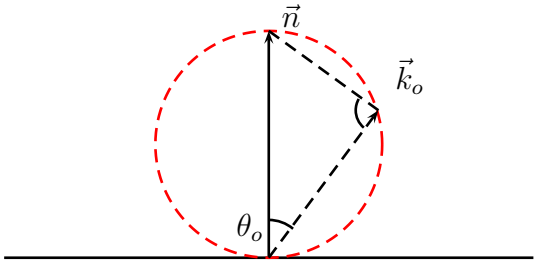

Figure B.4.: Diffuse reflection into the solid angle $\Delta\Omega$.

The diffuse reflected light into the solid angle $d\Omega$ is described by the initial intensity I_0 and the angle θ_o relative to the surface normal:

$$\frac{dI}{d\Omega} = I_0 \cdot \cos\theta_o.$$

With the solid angle $d\Omega$

$$d\Omega = d\varphi \sin\theta_o d\theta_o$$

the expression can be expanded to

$$\frac{dI}{d\theta_o} = I_0 d\varphi \sin\theta_o.$$

The normalized probability density function for $\theta_o \in [0, \pi/2]$ is

$$f(\theta_o) = 2\sin\theta_o \cos\theta_o.$$

The cumulative distribution function is then

$$\begin{aligned} F(\theta_o) &= \int_0^{\theta_o} f(\theta')d\theta' \\ &= \int_0^{\theta_o} 2\cos\theta' \sin\theta' d\theta' \\ &\overset{x=\cos\theta_o}{=} \int_1^{\cos\theta_o} -2x dx \\ &= \int_{\cos\theta_o}^1 2x dx \\ &= \left[x^2\right]_{\cos\theta_o}^1 \\ &= 1 - \cos^2\theta_o \\ &= \sin^2\theta_o. \end{aligned} \tag{B.11}$$

Using the uniform random number $r \in [0, 1[$, θ_o can be constructed to follow the $f(\theta_o)$ distribution by

$$r = F(\theta_o) = \sin^2\theta_o \Leftrightarrow \theta_o = \arcsin\sqrt{r}. \tag{B.12}$$

Bibliography

[Abe12] Y. Abe *et al.*, *Indication of Reactor $\bar{\nu}_e$ Disappearance in the Double Chooz Experiment*, Physical Review Letters **108**, 131801 (2012)

[Abe11] K. Abe *et al.*, *Solar neutrino results in Super-Kamiokande-III*, Physical Review D **83** 052010 (2011)

[Agn12] R. Agnese *et al.*, *Dark Matter Search Results Using the Silicon Detectors of CDMS II*, arXiv:1304.4279 [hep-ex]

[Aha13] B. Aharmim *et al.*, *Measurement of the ν_e and total ^8B solar neutrino fluxes with the Sudbury Neutrino Observatory phase-III data set*, Physical Review **C 87** 015502 (2013)

[Ahm02] Q. R. Ahmad *et al.*, *Direct Evidence for Neutrino Flavor Transformation from Neutral-Current Interactions in the Sudbury Neutrino Observatory*, Physical Review Letters **89** 011301-1 (2002)

[Ahn12] J. K. Ahn *et al.*, *Observation of Reactor Electron Antineutrinos Disappearance in the RENO Experiment*, Physical Review Letters **108** 191802 (2012)

[An13] F. P. An *et al.*, Chinese Physics **C 37** 011001 (2013)

[Ang08a] J. Angle *et al.*, *First results from the XENON10 Dark Matter Experiment at the Gran Sasso National Laboratory*, Physical Review Letters **100** 021303 (2008)

[Ang08b] J. Angle *et al.*, *Limits on Spin-Dependent WIMP-Nucleon Cross Sections from the XENON10 Experiment*, Physical Review Letters **101** 091301 (2008)

[Ang09] J. Angle *et al.*, *Constraints on inelastic dark matter from XENON10*, Physical Review D **80** 115005 (2009)

[Apr09] E. Aprile *et al.*, *A chamber for reflectivity and efficiency measurements*, internal note (2009)

[Apr11a] E. Aprile *et al.*, *Study of the electromagnetic background in the XENON100 experiment*, Physical Review **D 83**, 082001 (2011)

[Apr11b] E. Aprile *et al.*, *Material screening and selection for XENON100*, Astroparticle Physics **35** (2011) 43

[Apr12a] E. Aprile *et al.*, *The XENON100 dark matter experiment*, Astroparticle Physics **35** (2012) 573

[Apr12b] E. Aprile *et al.*, *Dark Matter Results from 225 Live Days of XENON100 Data*, Physical Review Letters **109** 181301 (2012)

[Apr12c] E. Aprile *et al.*, *Performance of a cryogenic system prototype for the XENON1T detector*, Journal of Instrumentation **7** (2012) P10001

[Apr12d] E. Aprile *et al.*, *Measurement of the quantum efficiency of Hamamatsu R8520 photomultipliers at liquid xenon temperature*, Journal of Instrumentation **7** (2012) P10005

[Apr13a] E. Aprile *et al.*, *Response of the XENON100 Dark Matter Detector to Nuclear Recoils*, arXiv:1304.1427

[Apr13b] E. Aprile *et al.*, *The neutron background of the XENON100 dark matter search experiment*, arXiv:1306.2303

[Ase11] V. N. Aseev *et al.*, *Upper limit on the electron antineutrino mass from the Troitsk experiment*, Physical Review **D 84** 112003 (2011)

[Bec11] M. Beck *et al.*, *Effect of a sweeping conductive wire on electrons stored in a Penning-like trap between the KATRIN spectrometers*, European Physics Journal **A 44** (2011) 499

[Bec13] M. Beck *et al.*, *An angular selective electron source for the KATRIN experiment*, to be published (2012)

[Bon99] J. Bonn *et al.*, *A high resolution electrostatic time-of-flight spectrometer with adiabatic magnetic collimation*, Nuclear Instruments and Methods in Physics Research **A 421** (1999) 256

[Cho10] B. Choi, internal document, Columbia university (2010)

[Cho12] B. Choi, phd thesis, Columbia university (2012)

[Clo06] D. Clowe *et al.*, *A direct empirical proof of the existence of dark matter*, The Astrophysical Journal, **648** (2006) L109

[Eas70] D. E. Eastman, *Photoelectric Work Functions of Transition, Rare-Earth, and Noble Metals*, Physical Review **B 2** (1970) 1

[For12] J. A. Formaggio and G. P. Zeller, *From eV to EeV: Neutrino cross sections across energy scales*, Reviews of Modern Physics **84** (2012)

[Fuk98] Y. Fukuda *et al.*, *Evidence for Oscillation of Atmospheric Neutrinos*, Physical Review Letters **81** 8 (1998) 1562

[Glu11e] F. Glück, *Axisymmetric electric field calculation with zonal harmonic expansion*, Progress in Electromagnetic Research **B 32** (2011) 319

[Glu11m] F. Glück, *Axisymmetric magnetic field calculation with zonal harmonic expansion*, Progress in Electromagnetic Research **B 32** (2011) 351

[Glu13] F. Glück, *Relativistic charged particle tracking with 8th order Runge-Kutta method*, to be published

[Hab09] F. Habermehl, *Electromagnetic measurements with the KATRIN pre-spectrometer*, phd thesis, Universität Karlsruhe (TH) (2009)

[Hea66] D. F. Heath and P. A. Sacher, *Effects of a Simulated High-Energy Space Environment on the Ultraviolet Transmittance of Optical Materials between 1050 Å and 3000 Å*, Journal of Applied Optics **5** 6 (1966) 937 - 943

[Hei10] H. Hein, *Angular defined photo-electron sources for the KATRIN experiment*, diploma thesis, Westfälische Wilhelms-Universität Münster (2010)

[Hug08] K. Hugenberg, *Design of the electrode system for the KATRIN main spectrometer*, diploma thesis, Westfälische Wilhelms-Universität Münster (2008)

[Hug10] K. Hugenberg, *An angular resolved pulsed UV LED photoelectron source for KATRIN*, Progress in Particle and Nuclear Physics **64** 2 288-290 (2010)

[Hug13] HUG Industrietechnik, *www.hug-technik.com*, Information about PTFE (2013)

[Jun96] G. Jungmann *et al.*, *Supersymmetric dark matter*, Physics Reports **267** (1996) 195

[KAT04] The KATRIN collaboration (J. Angrik *et al.*), *KATRIN Design Report 2004*, FZKA Scientific Report 7090, (2005)

[Kla06] H. V. Klapdor-Kleingrothaus and I. V. Krivosheina, *The Evidence for the Observation of $0\nu\beta\beta$ Decay: The Identification of $0\nu\beta\beta$ events from the full spectra*, Modern Physics Letters A **21** 20 (2006) 1547

[Kra05] C. Kraus *et al.*, *Final results from phase II of the Mainz neutrino mass search in tritium β decay*, European Physical Journal **C 40** 447 (2005)

[Lev13] C. Levy-Brown, phd thesis, Westfälische Wilhelms-Universität Münster, to be published (2013)

[Lew96] J. D. Lewin and P. F. Smith, *Review of mathematics, numerical factors, and corrections for dark matter experiments based on elastic nuclear recoil*, Astroparticle Physics **6** (1996) 87

[Mainz] H. Keller-Rudek and G. K. Moortgat, *MPI-Mainz-UV-VIS Spectral Atlas of Gaseous Molecules*

[McP218] McPherson, Manual for Model 218 Vacuum Monochromator

[McP632] McPherson, Manual for Model 632 Deuterium Light Source

[Mer12] S. Mertens, *Study of Background Processes in the Electrostatic Spectrometers of the KATRIN experiment*, phd thesis, KIT/IEKP (2012)

[Nic77] F. E. Nicodemus *et al.*, *Geometrical Considerations and Nomenclature for Reflectance*, NBS monograph, National Bureau of Standards, (1977)

[Ott08] E. Otten and C. Weinheimer, *Neutrino mass limit from tritium β-decay*, Reports on Progress in Physics **71** (2008) 086201

[Pic92] A. Picard *et al.*, *A solenoid retarding spectrometer with high resolution and transmission for keV electrons*, Nuclear Instruments and Methods in Physics Research **B 63** (1992) 345-358

[Pla12] G. Plante, *The XENON dark matter experiment: Design, Construction, Calibration and 2010 Search Results with Improved Measurement of the Scintillation Response of Liquid Xenon to Low-Energy Nuclear Recoils*, phd thesis, Columbia University (2012)

[Pla13] Planck collaboration, *Planck 2013 results. XVI. Cosmological parameters*, arXiv:1303.5076 (2013)

[Pla13a] ESA and the Planck Collaboration, http://sci.esa.int, Power spectrum of temperature fluctuations in the Cosmic Microwave Background, retrieved June 2013

[Ros14] S. Rosendahl, phd thesis, Westfälische Wilhelms-Universität Münster (2014)

[Rub70] V. C. Rubin and W. Kent Ford, Jr., *Rotation of the Andromeda Nebula from a Spectroscopic Survey of Emission Regions*, The Astrophysical Journal **159** (1970)

[Seo08] Seoul Semiconductors, manual (2006)

[Sil07] C. Silva *et al.*, *Measuring the angular profile of the reflection of xenon scintillation light*, Nuclear Instruments and Methods in Physics Research **A 580** (2007) 322 - 325

[Sil10a] C. Silva *et al.*, *Reflectane of polytetrafluoroethylene for xenon scintillation light*,

Journal of Applied Physics **107** (2010) 064902

[Sil10b] C. Silva *et al.*, *A model of the reflection distribution in the vacuum ultra violet region*, Nuclear Instruments and Methods in Physics Research **A 619** (2010) 59 - 62

[Sol04] V. Solovov *et al.*, *Measurement of the refractive index and attenuation length of liquid xenon for its scintillation light*, Nuclear Instruments and Methods in Physics Research **A 516** (2004) 462 - 474

[Spr11] A. Sprenger, *Construction and characterization of an experiment for reflection measurements with vacuum-UV light*, master thesis, Westfälische Wilhelms-Universität Münster (2011)

[Thü07] T. Thümmler, *Präzissionsüberwachung und Kalibration der Hochspannung für das KATRIN Experiment*, phd thesis, Westfälische Wilhelms-Universität Münster (2007)

[Tor67] K. E. Torrance and E. M. Sparrow, *Theory for Off-Specular Reflection From Roughened Surfaces*, Journal of the Optical Society of America **57** 9 (1967) 1105 - 1114

[Val09a] K. Valerius, *Spectrometer-related background processes and their suppression in the KATRIN experiment*, phd thesis, Westfälische Wilhelms-Universität Münster (2009)

[Val09b] K. Valerius, *A UV LED-based fast-pulsed photoelectron source for time-of-flight studies*, New Journal of Physics **11** (2009) 063018

[Val11] K. Valerius *et al.*, *Prototype of an angular-selective photoelectron calibration source for the KATRIN experiment*, JINST **6** P01002 (2011)

[Voe08] S. Vöcking, *Implementierung der Multipole Boundary Element Methode für das KATRIN Experiment*, diploma thesis, Westfälische Wilhelms-Universität Münster (2008)

[Wei81] V. R. Weidner and J. J. Hsia, *Reflection properties of pressed polytetrafluoroethylene powder*, Journal of the Optical Society of America, **71** 7 (1981) 856 - 861

[Wes09] J. Wessels, private communication, 2009

[Win13] D. Winzen, diploma thesis, Westfälische Wilhelms-Universität Münster, to be published

[Wol94] L. B. Wolff, *Diffuse-reflectance model for smooth dielectric surfaces*, Journal of the Optical Society of America **A 11** 11 (1994) 2956 - 2968

[Wu57] C. S. Wu *et al.*, *Experimental Test of Parity Conservation in Beta Decay*, Physical Review **105** (1957) 1413

[Wut] K. Jousten (Hrsg.), *Wutz Handbuch Vakuumtechnik*, vieweg (2006)

[Zac13] M. Zacher, phd thesis, Westfälische Wilhelms-Universität Münster, to be published

[Zbo11] M. Zbořil, *Solid electron sources for the energy scale monitoring in the KATRIN experiment*, phd thesis, Westfälische Wilhelms-Universität Münster (2011)

[Zwi33] F. Zwicky, *Die Rotverschiebung von extragalaktischen Nebeln*, Helvetica Physica Acta **6** (1933) 110

List of Figures

List of Tables